Society for Magnetic
Resonance Angiography
smrangio.com

28th Annual International Conference
Rising to New Heights
Chicago 2016

Syllabus

September 21st – 23rd
Northwestern Memorial Hospital
Chicago, Illinois, USA

President: Charles (Chuck) Dumoulin
Organizers: James Carr and Michael Markl

Session 1

Cardio-Thoracic MRA

4-Dimensional Multiphase Steady State Imaging of Contrast Enhancement (MUSIC): Dynamic MR Assessment of Neonates with Congenital Heart Disease

Kim-Lien Nguyen, MD[1,3], Fei Han, PhD[1,2], Daniel Z. Brunengraber, MD[1,2], Ziwu Zhou, BS[1,2], Ihab Ayad, MD[5], Gary M. Satou, MD[4], Brian L. Reemtsen, MD[6], Peng Hu, PhD[1,2], J. Paul Finn, MD[1,2]

[1]*Diagnostic Cardiovascular Imaging Laboratory,* [2]*Department of Radiology,* [3]*Division of Cardiology,* [4]*Division of Pediatric Cardiology,* [5]*Department of Anesthesiology,* [6]*Division of Cardiothoracic Surgery, David Geffen School of Medicine at UCLA, Los Angeles, CA*

Purpose: Although echocardiography is the clear first line test in congenital heart disease (CHD), it may not always be definitive. In these cases, MRI may play a vital role without ionizing radiation. Recently, a 4D (MUSIC) technique has been described [1,2], which generates high-resolution 3D images of the beating heart during uninterrupted ventilation. We evaluated the diagnostic performance of 4D MUSIC in a clinical cohort of neonates with congenital heart disease (CHD).

Methods: 20 neonates with CHD (age range 2 to 25 days, weight 1 to 4 kg) underwent MRI with ferumoxytol (FE) at 3.0T and were prospectively enrolled. Two readers graded the diagnostic image quality of intra-cardiac structures and vascular segments using a four-point scale. Correlation of MRA findings with other imaging modalities and/or surgery was performed.

Results: All studies were technically successful and there were no adverse events. On a four-point scale, the average FE-MUSIC image quality scores were >3.5 for intra-cardiac structures and >3.0 for coronary arteries. Intra-cardiac morphology and vascular anatomy were visualized with good interobserver agreement (r=0.46). Concordance with correlative imaging, surgical, and /or autopsy results was excellent. In two patients with discordant findings between echo and catheter angiography, findings on FE-MUSIC were shown to be accurate by surgical reports (n = 2). One patient was scheduled for single ventricular repair, but because of FE-MUSIC findings, underwent biventricular repair.

Conclusion: FE-MUSIC enables non-breath-held, high-resolution, 3D cine imaging of cardiac and vascular anatomy in neonates with CHD, providing highly diagnostic studies without the need for prospective customized imaging planes.

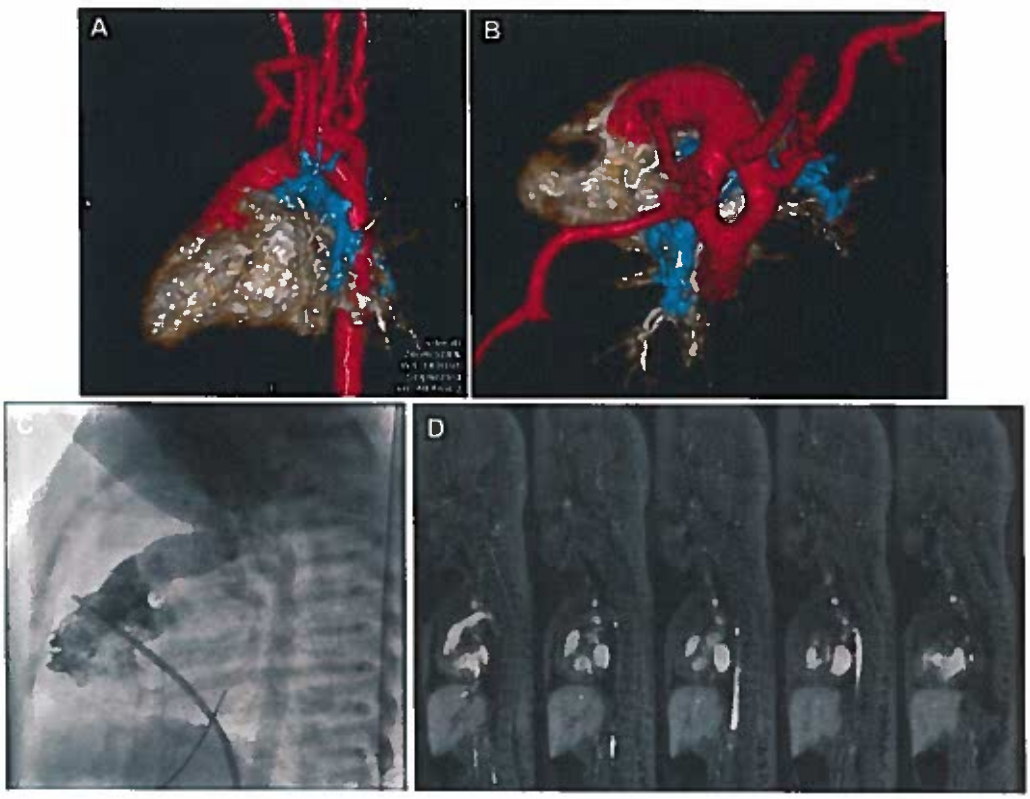

Figure 1: 7-day-old boy (3.3 kg) with D-transposition of the great arteries (TGA) and unclear anatomy on echo. FE-MUSIC shows a double aortic arch (A, B) with severe compression of the trachea and esophagus. The patient underwent cardiac catheterization (C) for atrial septostomy prior to surgery, which confirmed the FE-MUSIC findings. Pulmonic valve and subvalvar pulmonic stenosis however, were not appreciated on cath, but confirmed intra-op. Tracheal compression was shown on MRI (D). CT angiography to further characterize tracheal rings was non-diagnostic because of a heart rate 160-170s bpm. All FE-MUSIC findings were confirmed during surgical division of aortic arch and Blalock-Taussig shunt creation.

References:

1. Fei Han, et al. *4-Dimensional, Multiphase, Steady-state Imaging with Contrast Enhancement (MUSIC) in the Heart; a Feasibility Study in Children.* Mag Reson Med 2015 Oct;74(4):1042-9.

2. Fei Han, et al. *Cardiac and Respiratory Self-Gated 4D Multiphase Steady-State Imaging with Ferumoxytol Contrast (MUSIC).* ISMRM 24th Annual Conference Proceedings. May 2016. Singapore.

Circulating levels of P and E-selectin relate to magnetic resonance imaging derived aortic characteristics and cardiovascular risk factors in a general population based sample of healthy, young adults: The AMBITYON study

Anouk L.M. Eikendal[1], Michiel L. Bots[2], Esther Lutgens[3], Imo E. Hoefer[4], Hester M. den Ruijter[2] and Tim Leiner[1]

From the Departments of Radiology[1], Epidemiology[2] and Experimental Cardiology[3], Utrecht University Medical Center, Utrecht, The Netherlands, and the Department of Experimental Immunopathology[4], Academic Medical Center, Amsterdam, The Netherlands

Purpose: Circulating endothelial biomarkers are postulated to play key roles in atherosclerosis, yet have not widely been studied in young individuals. Therefore, this study evaluated whether circulating cellular adhesion molecules (CAMs) and endothelial extracellular levels (EVs) related to magnetic resonance (MR)-derived indicators of early atherosclerosis and cardiovascular risk factors in healthy, young adults.

Methods: In 131 adults (age: 25-35 years) from the general-population-based Atherosclerosis- Monitoring-and-Biomarker-measurements-In-The-YOuNg study, demography, anthropometry and a lipid spectrum was acquired. Thoracic aortic wall area, thickness and pulse wave velocity (PWV) were measured using a 3.0T MR-system. From stored blood samples, four CAMs and endothelial EV CD144+ were measured using dedicated methods. Linear mixed- effects regression analysis was used to evaluate the relation of endothelial biomarkers with aortic characteristics and cardiovascular risk factors, including the Framingham Risk Score (FRS).

Results: P-selectin related to log-aortic wall thickness (β=0.18 ln(mm) per (μg/ml) increase, p=0.007) and E-selectin to log-aortic PWV (β=3.86 ln(m/s) per (μg/ml) increase, p=0.006). Moreover, age (β=0.02 ln(μg/ml) per year increase, p=0.01) related to log-VCAM whereas smoking (β=4.26x10-3 μg/ml higher in smokers, p=0.04) and body mass index (β=8.09x10-4 (μg/ml) per kg/m2 increase, p=0.02) related to E-selectin. The FRS related to E-selectin (β=3.95x10-4 (μg/ml) per FRS point increase, p=0.02) and to log-P-selectin (β=0.04 ln(μg/ml) per FRS point increase, p=0.02). None of the CV risk factors nor the FRS related to ICAM and EV CD144+.

Conclusions: Circulating P-selectin and E-selectin levels are related to cardiovascular risk factors and early signs of atherosclerosis in healthy, young adults.

Aortic 3D Wall Shear Stress in Aortopathy in Patients with Bicuspid Aortic Valves Compared to Tri-leaflet Aortic Valve: A 4D flow MRI Study in 618 subjects

Pim van Ooij[1], Ian G. Murphy[2], Jeremy D. Collins[2], Emilie Bollache[2], James C. Carr[2], S. Chris Malaisrie[3], Patrick McCarthy[4], Aart J. Nederveen[1], Paul Fedak[5], Michael Markl[2], Alex J. Barker[2].

[1]Department of Radiology, Academic Medical Center, the Netherlands, [2]Department of Radiology, [3]Department of Medicine/Cardiology, [4]Division of Surgery/Cardiac Surgery, Northwestern University, Chicago, USA, [5]Department of Cardiac Sciences, University of Calgary, Canada

Purpose: To use 3D wall shear stress (WSS) to investigate valve mediated hemodynamics in a large cohort of aortopathy patients with bicuspid (BAV) and tri-leaflet aortic (TAV) valves sorted for valvular stenosis and morphology.

Methods: 567 patients with aortic dilation, defined as sinus of Valsalva (SOV) or mid-ascending aortic diameter (MAA) >4cm, were selected from a database of subjects who received 4D flow MRI. As summarized in table 1, patients were grouped by valve morphology: TAV (n=290), BAV with fusion of the right and left leaflets (RL-BAV, n=211), or fusion of the right and noncoronary leaflets (RN-BAV, n=61). 4D flow MRI was also performed in 56 healthy controls (mean age: 43 ± 13years, mean MAA diameter = 3.2±0.4cm). Pulse sequence parameters for 4D flow MRI were: spatial resolution: 2.2-4.2x1.7-2.9x2.2-4.0 mm^3; temporal resolution: 33-43 ms; TE/TR/FA: 2.1-2.8 ms/4.1-5.4 ms/7-15°.

Table 1. *Subject demographics and aortic dimensions*

		RL-BAV	RN-BAV	TAV	P*
All	N (% female)	211 (25%)	61 (34%)	290 (24%)	-
	Age (years)	48 ± 14	49 ± 14	58 ± 14	<0.01
No AS	N (% female)	168 (24%)	38 (42%)	269 (24%)	-
	Age (years)	46 ± 13	44 ± 12	58 ± 14	<0.01
	SOV (cm)	4.0 ± 0.5	3.8 ± 0.5	4.1 ± 0.5	<0.01
	MAA (cm)	3.9 ± 0.7	3.8 ± 0.7	3.9 ± 0.6	0.8
AS	N (% female)	43 (30%)	23 (22%)	21 (24%)	-
	Age (years)	57 ± 14	57 ± 12	62 ± 15	0.4
	SOV (cm)	3.8 ± 0.5	4.0 ± 0.6	3.7 ± 0.5	0.11
	MAA (cm)	3.9 ± 0.6	4.1 ± 0.6	4.0 ± 0.5	0.33

*Kruskal-Wallis test with P<0.05 considered significant

All scans were performed on 1.5 and 3T MAGNETOM Avanto, Espree, Aera and Skyra systems (Siemens Medical Systems, Erlangen, Germany). For all subjects, 3D segmentations of the thoracic aorta were semi-automatically created using commercial software (Mimics, Materialise, Leuven, Belgium) using 3D PC-MRA images. The peak systolic time frame was determined by isolating the time frame with the highest average velocity in the segmentation. Significant aortic stenosis (AS) was determined by extracting the systolic peak velocity in the vena contracta region (>3m/s). 3D WSS was calculated and mapped onto the segmented aorta surface for the peak systolic timeframe. Cohort averaged WSS maps for all cohorts were created according to a method that included registration to a common geometry allowing for averaging across cohorts [1]. For each group (controls, RL-BAV, RN-BAV, TAV) mean WSS in the ascending aorta was calculated in 4 regions: 1) the proximal inner curvature, 2) the proximal outer curvature, 3) the distal inner curvature and 4) the distal outer curvature (see figure 1).

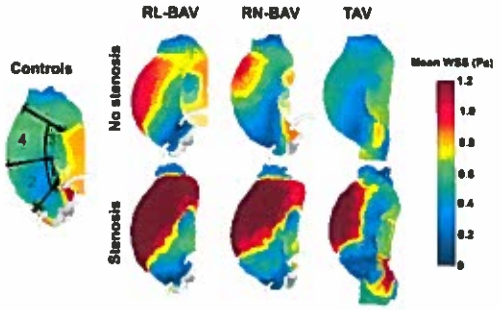

Figure 1*: WSS atlases for all study cohorts.*

Results: Table 1 lists subject demographics and aortic dimensions. In figure 1 cohort averaged 3D WSS for all cohorts are displayed. The non-stenotic RL-BAV cohort exhibited elevated WSS along the inner and outer curvature, whereas elevated WSS for the RN-BAV is found on the distal outer curvature only (which correspond to known patterns of aortopathy). In contrast, the non-stenotic TAV cohort showed decreased WSS along the entire aorta compared to the controls. Notably, cohort averaged 3D WSS in patients with AS showed substantially elevated WSS on the distal outer curvature for all patient groups. These findings are supported by the mean WSS values in the four regions reported in table 2.

Conclusion: A consistent pattern of elevated WSS was found in a large cohort of non-stenotic BAV patients, which match with regions of known dilation patterns. AS was found to reduce intergroup variability of the cohort averaged WSS maps and matches with recent evidence that dilation for BAV and TAV subjects with AS are similar [2]. The results can help understand the paradoxical findings reported earlier in literature by Tsamis et al. [3], who found asymmetric dilation of the greater curvature in BAV patients compared to symmetric dilation in TAV patients, which contrasts with Girdauskas et al. [3] reporting no difference in dilation between stenotic BAV and TAV cohorts. These results provide further supporting evidence that aortic wall remodeling is partially mediated by hemodynamics.

Table 2. *Mean WSS in the four aortic regions for the controls, the (non-)stenotic RL-BAV, RN-BAV and TAV*

Region	Controls	No stenosis							Stenosis			
		RL-BAV	P*	RN-BAV	P*	TAV	P*	P**	RL-BAV	RN-BAV	TAV	P**
1	0.8±0.2	0.8±0.2	**<0.01**	0.8±0.2	0.4	0.6±0.2	**<0.01**	**<0.01**	1.1±0.3	1.2±0.3	1.0±0.2	0.2
2	0.7±0.2	0.8±0.2	**<0.01**	0.7±0.1	0.2	0.6±0.2	**<0.01**	**<0.01**	1.3±0.3	1.0±0.2	1.0±0.2	**<0.01**
3	0.7±0.2	0.8±0.2	**<0.01**	0.7±0.2	0.8	0.5±0.2	**<0.01**	**<0.01**	1.0±0.3	1.0±0.3	0.9±0.3	0.8
4	0.6±0.2	1.0±0.4	**<0.01**	0.9±0.3	**<0.01**	0.5±0.3	**<0.01**	**<0.01**	1.7±0.4	1.5±0.4	1.4±0.3	0.1

* Wilcoxon rank sum test between controls and BAV\TAV groups, significant when P<0.05
**Kruskal-Wallis test between BAV and TAV groups, significant when P<0.05

References: [1] van Ooij et al. MRM 2015; [2] Girdauskas et al. JACC 2016; [3] Tsamis et al. JTCVS 2016;

Cost Effectiveness Analysis of Monitoring Strategies in the First Year after Cardiac Transplantation

Matthew A. Pilecki MD MBA[1] (In Progress), Asad Usman MD MPH[1,2], Gordon B. Hazen PhD[3], Amir Rahespar MD, Julie Blaisdell BA Jeremy D. Collins MD[1], Jane Wilcox MD[2], David Dranove PhD[5], Michael Markl PhD[1,4], James C. Carr MD[1]

1-Department of Radiology – Cardiovascular Imaging
2-Department of Cardiology – Heart Failure and Transplantation
3-Department of Industrial Engineering and Management Sciences
4-Department of Biomedical Engineering
5-Department of Strategy and Health Enterprise Management

Purpose: Development of acute allograft rejection is the primary cause of morbidity in the first year post cardiac transplantation. Endomyocardial biopsy (EMB) combined with echocardiography and cardiac catheterization is considered the gold standard for surveillance of rejection. EMB however remains invasive, expensive, carries risk of injury, and is uncomfortable for the patient. Validation of alternative monitoring algorithms combining clinical effectiveness with lower cost and decreased invasiveness remains a strategic priority for physicians and healthcare systems.

Methods: We developed a Markov model using cost, utility of states, sensitivity and specificity of test parameters to assess the comparative effectiveness of various monitoring strategies. We modeled the efficacy based on the utility spent in each Markov state and on reports from the literature. Cost for procedures was estimated based on Medicare reimbursement and validated against institutional data.

Results: At a 16 node level of monitoring, all monitoring strategies analyzed were similarly efficacious at 292 QALD. The average cost of invasive monitoring per patient per year is estimated to be $231,795 vs $67,287 for CMR. A mixed strategy of early EMB with subsequent CMR cost $114,573.

Discussion: Continued development and improvement of CMR in rejection surveillance for transplant patients indicates it represents a cost effective alternative to the current gold standard. Further research into combined strategies will determine not only comparative effectiveness but the possibility of improving utility of life post-transplant in the first year.. In the setting of increasing health care costs, a potential reduction of over $117,000 per patient and $146,000/QALY can result in significant value for society. We recommend a mixed strategy of early EMB with subsequent CMR after the first month post-transplant.

Monitoring Strategy:

Figure 1: Time line of Monitoring in the 1st year after transplant

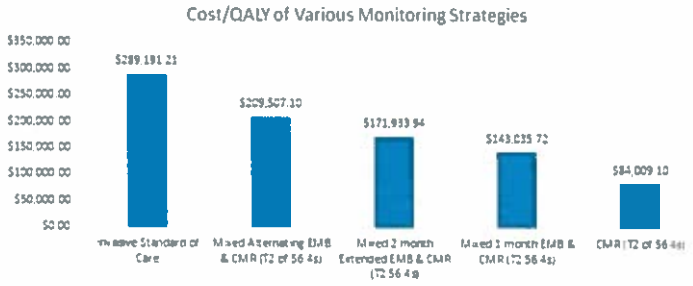

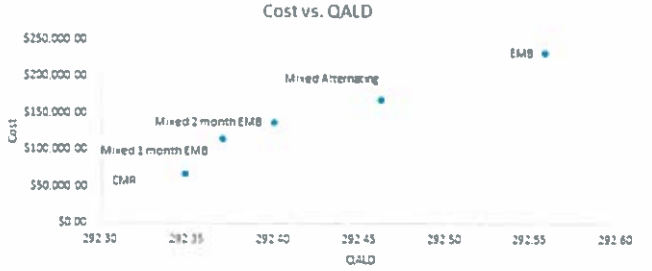

Session 2

Flow

Distinct Aortic Wall Shear Stress Alteration in Bicuspid Aortic Valve Patients with Isolated Aortic Stenosis and Insufficiency

Yongshi Wang [a], Yan Shan [a]; Boting Wu [d]; Alex J. Barker[b]; Michael Markl [b,c]; Xiaolin Wang [a]

[a]Shanghai Institute of Medical Imaging, Zhongshan Hospital Fudan University, Shanghai, China;

[b]Feinberg School of Medicine, Northwestern University, Chicago IL, USA; [c]McCormick School of Engineering, Northwestern University, Evanston IL, USA; [d]Zhongshan Hospital Fudan University, Shanghai, China

Purpose

- Bicuspid aortic valve (BAV), characterized by valve malformation and risk for aortopathy, displays profound alteration in systolic aortic outflow and wall shear stress (WSS) distribution.
- The present study performed 4-dimensional flow MRI in BAV patients with right-left (R-L) cusp fusion, focusing on the impact of valve function upon hemodynamic status within ascending aorta.

Methods

- Four-dimensional flow MRI was performed in 50 R-L BAV subjects and 15 age- and aortic size-matched control subjects with tricuspid aortic valve (TAV).
- BAV patients were categorized into 3 groups according to their aortic valve function as follows: BAV with no more than mild aortic valve dysfunction (BAV-CTL, n=20), BAV with severe aortic insufficiency (BAV-AI, n=15), and BAV with severe aortic stenosis (BAV-AS, n=15).
- Measurement planes were manually placed perpendicular to the long axis of the aorta at defined anatomic landmarks:
  - proximal ascending aorta directly distal to the sinotubular junction
  - mid-ascending aorta
  - distal ascending aorta
  - at the origin of the brachio-cephalic trunk
  - proximal descending aorta

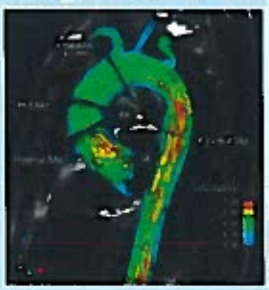

- Post-processing and data analysis was performed with customized Matlab software, and visualized on an Ensight platform.

Results

- All R-L BAV patients exhibited peak WSS at the right-anterior position of the ascending aorta (BAV vs TAV at right-anterior position: 0.91±0.23 N/m² vs. 0.43±0.12 N/m², p<0.001) with no distinct alteration between BAV-AI and BAV-AS.
- Predominance of dilatation involving the tubular ascending aorta (82%, type 2 aortopathy) persisted , with or without valve dysfunction.
- BAV-AI group displayed elevated stroke volume which led to universally elevated WSS compared to BAV-CTL subjects (0.75±0.12 N/m² vs. 0.57±0.09 N/m², p<0.01) in ascending aorta.
- BAV-AS group showed markedly increased peak aortic valve velocity, resulting in elevated flow eccentricity (increased standard deviation of averaged WSS and ratio of averaged WSS between the maximum and minimum position).

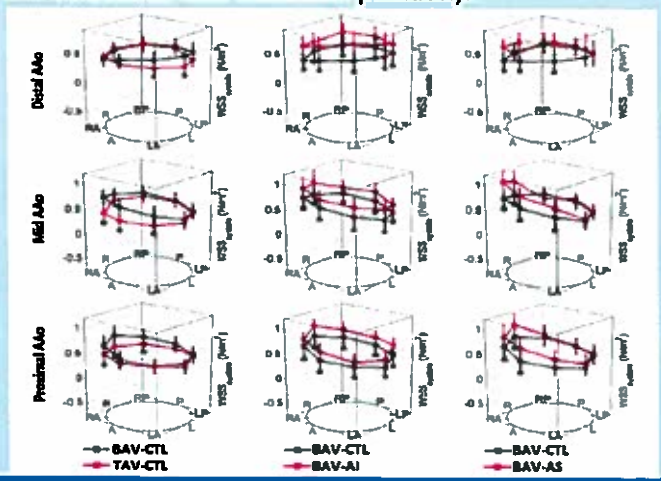

Conclusions

- The location of peak aortic WSS and type of aortopathy remained homogeneous among R-L BAV patients irrespective of valve dysfunction.
- Severe AI or AS resulted in further elevated aortic WSS and exaggerated flow eccentricity.

4-Dimensional Flow MRI of Abdominal Blood Flow Patterns in Patients with Type B Aortic Dissection

Dongting Liu MD, Jiayi Liu MD, Zhanming Fan MD

Department of Radiology, Beijing Anzhen Hospital, Capital Medical University, Beijing 100029, China.

Abstract

Purpose—The purpose of this study was evaluate alterations in abdominal flow patterns in type B aortic dissections(AD) using four-dimensional (4D) flow MRI. and to compare the changes of blood flow before and after aortic dissection operation.

Methods—Fifteen patients with AD who underwent 4D flow MRI examination using 3.0T clinical scanners before and after operation were prospectively enrolled in this study. Qualitative assessment of flow patterns in the true (TL) and false (FL) lumina was performed in consensus by two cardiovascular radiologists. Quantitative analysis included measurement of peak velocity, peak flow, average net flow, net forward volume, regurgitant fraction in the TL and FL in the four different horizontal planes of abdominal aorta. Differences in flow through TL and FL at each analysis planes were compared with the two-tailed, paired Student's t-test.

Results—Flow patterns were significantly altered in association with different lumens of AD disease and post therapeutic anatomy. Before endovascular stent-graft placement, Peak velocity，peak flow, average net flow and net forward volume were significantly higher in TL than FL ($P < 0.001$). Regurgitant fraction were less in TL than in FL ($P < 0.001$). The peak velocity, peak flow and regurgitant fraction in FL were significantly lower after endovascular stent-graft placement than that before therapy ($P<0.05$). The average net flow and forward volume were higher in FL after therapy ($P<0.05$). The peak velocity and regurgitant fraction in TL were higher ($P<0.05$) and there was no significant difference of peak flow, average net flow, net forward volume of TL（$P>0.05$）after therapy.

Discussion—4D flow MRI at 3.0T provided qualitative and quantitative information on alterations of abdominal aortic blood flow in patients with Stanford type B aortic dissections. It is important for clinical application in the diagnosis，therapeutic management and the therapeutic opponunity choice of type B aortic dissection[1,2]. Relatively easy scan prescription and retrospectiveplacement of analysis planes makes 4D Flow MRI a potentially advantageous tool in the clinical setting[3].

References

1. Dillon-Murphy D, Noorani A, Nordsletten D, Figueroa CA. Multi-modality image-based computational analysis of haemodynamics in aortic dissection. Biomech Model Mechanobiol, 2015 Sep 28. [Epub ahead of print]
2. Tolenaar JL, van Keulen JW, Trimarchi S et al. Number of entry tears is associated with aortic growth in type B dissections. Ann Thorac Surg. 2013 Jul; 96(1):39-42.
3. Dyverfeldt P, Bissell M, Barker AJ, et al. 4D flow cardiovascular magnetic resonance consensus statement. J Cardiovasc Magn Reson. 2015 Aug 10; 17:72.

Case-control Study Comparing Aortic Hemodynamics Following Aortic Root Replacement with Mechanical and Bioprosthetic Valved-Conduits

Eric J. Keller, MA[1]; Emilie Bollache, PhD[1]; S. Chris Malaisrie, MD[3]; Jane Kruse, RN[2]; Patrick M. McCarthy, MD[3]; James Carr, MD[1]; Michael Markl, PhD[1,2]; Jeremy D. Collins, MD[1]; Alex J. Barker, PhD[1,2]

[1]Department of Radiology, Northwestern University, Chicago, IL
[2]Department of Biomedical Engineering, Northwestern University, Evanston, IL
[3]Division of Surgery-Cardiac Surgery, Northwestern University, Chicago, IL

Purpose: To compare the post-operative hemodynamics of On-X mechanical and Edwards bioprosthetic valved-conduits to valve-sparing aortic root replacements (ARR).

Methods: ARRs were identified in a database of 1387 aortic four-dimensional magnetic resonance imaging (4D flow MRI) studies performed at a single institution. Cases with confounding conditions affecting aortic hemodynamics were excluded. Aortic blood flow helicity and vorticity on 4D flow MRI were graded independently by two reviewers blinded to valve type. Aortic peak and mean transvalvular pressure gradients and effective orifice areas on Doppler sonography were obtained from patients' charts at up to 4 time points: pre-ARR as well as <2 months, 1-2 years, and 2-4 years post-ARR.

Results: 86 ARRs were identified without cofounding conditions (52±16 years old, 19 women): 12 On-X ARR, 50 Bio ARR, and 24 VS-ARR. Pre-operative mean transvavular pressure gradients were higher for On-X (20.2±11.6 mmHg) and Bio ARR patients (22.3±18.3 mmHg) than VS-ARR (5.2±2.3 mmHg, p≤0.01). On-X and Bio ARR gradients were reduced post-operatively with On-X ARR gradients matching VS-ARR gradients (7.8±4.3 mmHg v. 6.1±3.0 mmHg, p=0.19) but Bio ARR gradients remaining elevated (8.7±3.6 mmHg, p<0.01) (median follow up of 702±609 days). Post-operative flow helicity and vorticity grades were similarly low for On-X ARR and VS-ARR (p>0.05) but significantly higher for Bio ARR (p≤0.02). Inter-obersever agreement was excellent for aortic flow gradings (κ≥0.85, p<0.001).

Conclusions: On-X mechanical valves may possess unique features, producing post-operative hemodynamic profiles that more closely resemble native flow patterns than Edwards bioprosthetic valves.

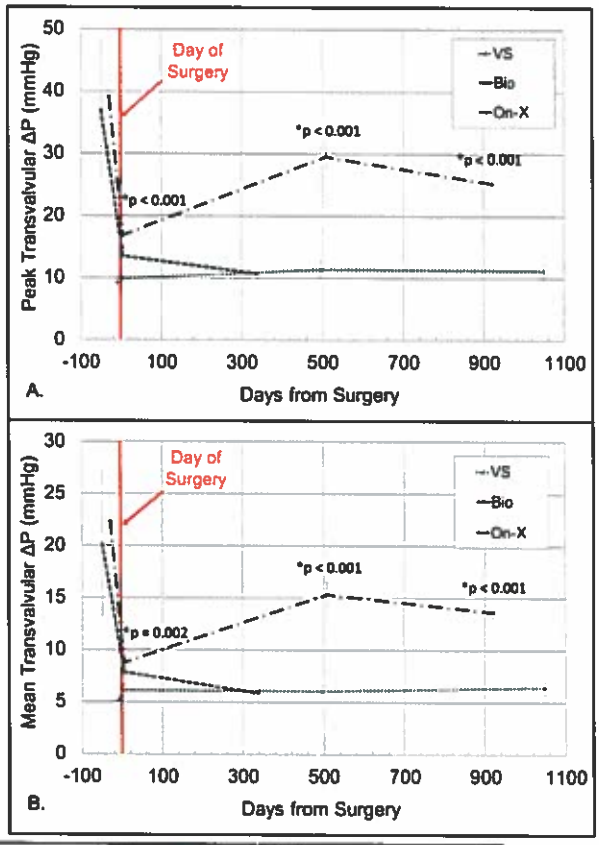

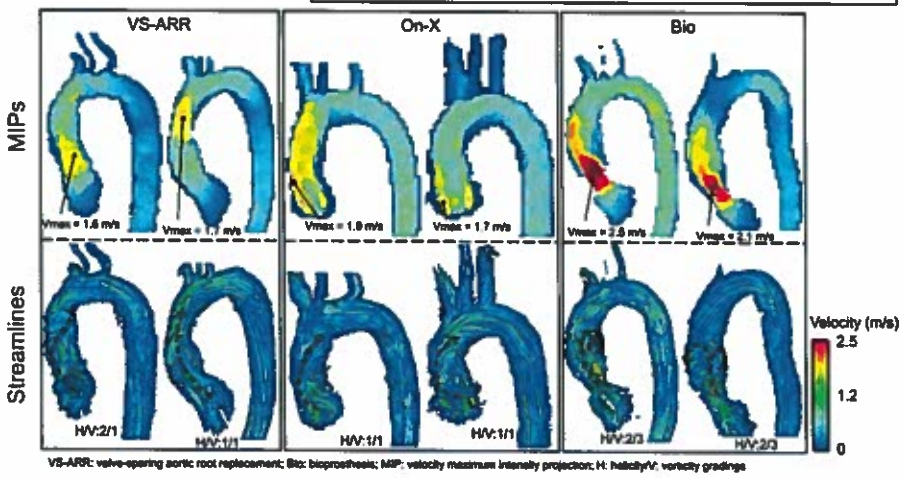

VS-ARR: valve-sparing aortic root replacement; Bio: bioprosthesis; MIP: velocity maximum intensity projection; H: helicity/V: vorticity gradings

Figure 1 (Top): Maintainance of post-operative hemodynamic patterns. Average peak (A) and mean (B) transvalvular pressure gradients (ΔP) for valve-sparing (VS), bioprosthetic (Bio), and mechanical (On-X) ARR on TTE versus median time between surgery and imaging. Error bars represent standard error. *Denotes statistically significant difference from VS (p < 0.05).

Figure 2 (Bottom): Example maximum intensity projections (top row) and flow patterns (bottom row) obtained using 4D flow MRI for two representative patients from each cohort: VS-ARR, On-X ARR, and Bio ARR (left to right)

Patient Specific Virtual Surgery Modeling Using Meal Challenge Vessel Strain Values

David R. Rutkowski[a,b], Scott B. Reeder[b,c,d,e,f], Luis A. Fernandez[g], Alejandro Roldán-Alzate[a,b]

a. Mechanical Engineering, b. Radiology, c. Medical Physics, d. Biomedical Engineering, e. Medicine, f. Emergency Medicine, g. Surgery; University of Wisconsin, Madison, WI, United States

Purpose: Hemodynamic alterations due to the mechanical changes in the hepatic vasculature of the donor after living donor liver transplant (LDLT) are not fully understood. The purpose of this study was to develop a methodology that provides further insight into the hemodynamic alterations of LDLT through the combination of in vivo patient specific 4D flow MRI, a meal challenge study, and computational fluid dynamics simulations.

Methods:

MR Imaging: In this institutional review board approved and Health Insurance Portability and Accountability Act - compliant study, one healthy subject recruited for liver donation was scanned on a clinical 3T scanner (Discovery MR 750, GE Healthcare, Waukesha, WI) both before and 14 days after surgery. 4D velocity mapping was achieved using a cardiac-gated time-resolved 3D radially undersampled phase contrast (PC) acquisition (5-point PC-VIPR) with increased velocity sensitivity performance.[1],[3]

***4D flow MRI Data Analysis*:** Data were reconstructed and PC angiograms were calculated from the velocity and magnitude data.[2] Liver vasculature was segmented from the angiograms using MIMICS (Materialise, Leuven, Belgium) and flow velocities were visualized and quantified using Ensight (CEI, Apex, NC).

Meal Challenge for Vessel Strain Determination: 4D flow MRI data from six healthy volunteers before and after meal ingestion[4] was used to determine the strain of the portal vein. The strain of the vessels was estimated as the relative change in cross-sectional area in response to the meal.

Virtual Surgery: A predictive model for post-transplant splanchnic hemodynamics of the donor was created by "virtual surgery" on the pre-surgery portal vein model using the design software 3-matic (Materialise, Leuven, Belgium). This model represented surgical resection of the right portal vein. A second virtual surgery model was prepared that accounted for the expansion of the left portal vein branch over time using strain calculated from the meal challenge. The resulting models of this virtual surgery are shown in Figure 1.

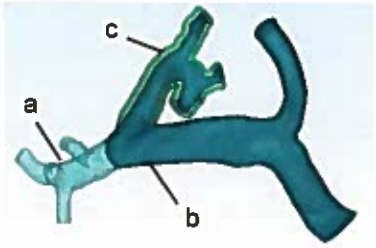

Figure 1. Virtual models representing a) pre-surgery, b) post-surgery resection, and c) strain dilated anatomies.

Computational Fluid Dynamics (CFD) Simulations: The in vivo and virtual surgery models were prepared and imported into Fluent (Ansys, inc Cannonburg, PA, USA), where steady flow simulations were performed. Flow conditions were set for the inlets with values obtained from the in vivo hemodynamic quantification from the pre-surgery donor scans.

Results: Velocity streamlines, pressure, and wall shear stress contours were produced from CFD simulation for each in vivo and predictive model. Pre-surgery CFD model results closely matched in-vivo 4D flow measurements. The model that utilized meal challenge strain values more accurately predicted actual post-surgery hemodynamics than the virtual surgery model that only accounted for surgical resection with no vessel dilation, as seen in the pressure contours of Figure 2.

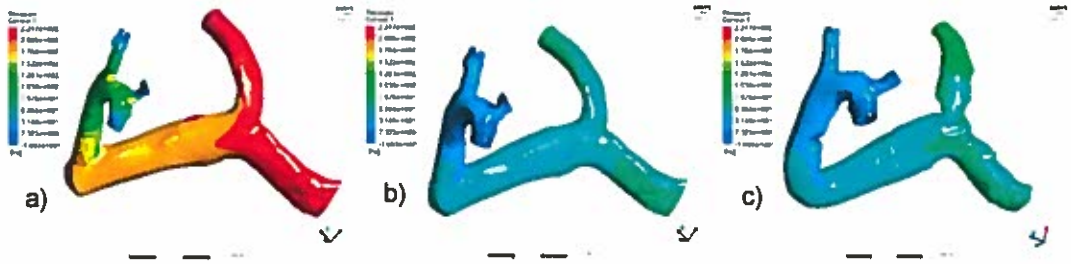

Figure 2. Pressure contours from CFD simulation of a) virtual post-surgery resection, b) post-surgery vessel strain adaptation, and c) actual post-surgery anatomies.

Conclusion: A patient specific surgical planning method based on 4D flow MRI and meal challenge data was developed that successfully quantified post-surgery hemodynamic changes that occurred in this liver donor.

References: [1] Gu T. AJNR 2005 ; [2] Johnson, K M. Magn. Reson. Med. 2008 ; [3] Johnson, K M. Magn. Reson. Med. 2010 ; [4] Roldán-Alzate, A. J. Magn. Reson. Imaging. 2015

Utility of a Non-contrast MR Angiography Protocol with 4D flow MRI in the Pre-Transplant Evaluation of the Portal and Hepatic Vasculature

Jeremy D Collins, MD[1]; Eric Keller, BS[1]; Riad Salem, MD[1]; Maria Carr, RT[1]; Rachel Davids, RT[1]; Frank Miller, MD[1]; Susanne Schnell, PhD[1]; Michael Markl, PhD[1,2]; James C Carr, MD[1]

[1]Department of Radiology, Northwestern University Feinberg School of Medicine; [2]Department of Biomedical Engineering, Northwestern University, Evanston, IL

Purpose: To assess the utility of a non-contrast MR angiography (NCMRA) protocol combined with 4D flow MRI at 3T to quantify portosystemic shunt (PSS) flow, hepatic vascular anatomy, and portal vein (PV) patency in the pre-liver transplant evaluation.

Methods: Prospective assessment of 40 patients (15 women, 52±10 years) with cirrhosis and portal hypertension were recruited under an IRB-approved protocol. All subjects underwent MR imaging at 3.0T. The NCMRA protocol was comprised of quiescent interval single shot (QISS) MR venography (MRV) and QISS MRA, native TrueFISP, and 3D short tau inversion recovery (STIR), followed by non-contrast (NC) 4D flow MRI with a flip angle of 7 degrees and a tri-directional velocity encoding gradient (VENC) of 50 and 100 cm/sec for arterial and venous flow quantification, respectively. Conventional contrast-enhanced MRA (CEMRA) was performed with arterial and venous phases following administration of 0.03 mmol/kg Gadofosveset trisodium. Post-contrast 4D flow MRI was performed with identical velocity encoding gradients and a FA of 15 degrees. The visibility of the vasculature was graded by a single blinded observer; the presence of PSS < or >=10 mm in size and hepatic arterial variants were noted. Cavernous transformation of the portal vein and the presence of thrombus was noted. Flow quantification was compared between non- and post-contrast 4D flow MRI techniques for arterial and venous flow quantification respectively. The PSS fraction (%) was calculated from 4D flow MRI data by dividing variceal flow by main PV flow. Quantitative data between groups was compared using a paired student's t-test.

Results: The NCMRA protocol enabled assessment of the liver and portal vasculature in 37 subjects (93%). Taken separately, QISS MRV performed the best enabling assessment of the vascular anatomy in 29 (73%) of subjects. 26 of 28 (93%) and 18 of 18 (100%) of PSS < and >=10 mm in size were identified at NCMRA. Variant hepatic arterial anatomy was identified correctly in 10 of 11 subjects (91%), failing in one patient with an irregular breathing pattern. The PV was patent in all subjects; mural PV thrombus was identified at NCMRA in 1 patient. Post-contrast 4D flow MRI demonstrated an average 11.5% and 9.5% greater flow values than non-contrast 4D flow datasets. The PSS fraction was higher for NC 4D flow MRI acquisitions (48±41% vs 43±38%, p=0.04). Representative images from a patient with a recanalized umbilical vein are provided in Figure 1.

Conclusion: NCMRA demonstrated excellent performance in the pre-transplant assessment of the PV and hepatic vasculature. The addition of 4D flow MRI enabled quantification of hepatic and portal hemodynamics without contrast, diverging from measurements on contrast-enhanced 4D flow MRI between 9.5-11.5%.

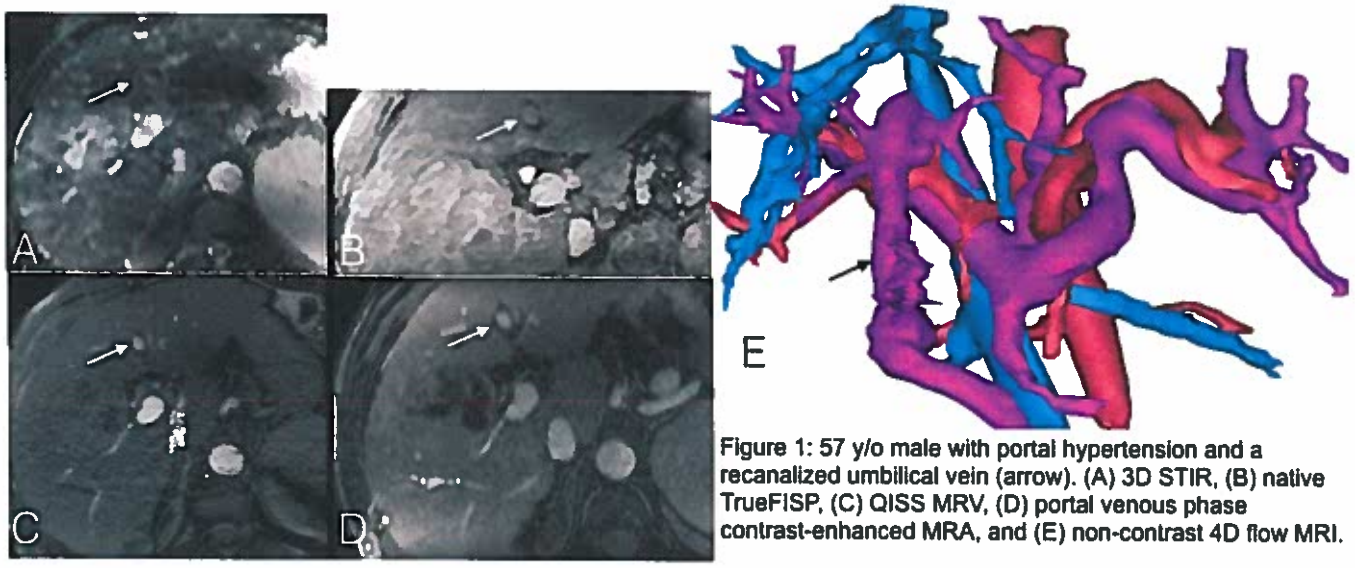

Figure 1: 57 y/o male with portal hypertension and a recanalized umbilical vein (arrow). (A) 3D STIR, (B) native TrueFISP, (C) QISS MRV, (D) portal venous phase contrast-enhanced MRA, and (E) non-contrast 4D flow MRI.

BIAS IN VELOCITY ESTIMATES OBTAINED FROM 2D PC-MRI OF AQUEDUCTAL CSF FLOW

Sudarshan Ragunathan[1,2], and James G. Pipe[1]
[1]Barrow Neurological Institute, Phoenix, Arizona
[2]School of Biological Health and Systems Engineering, Arizona State University, Tempe, Arizona

PURPOSE: The accuracy of phase contrast (PC) based quantitative flow measurements is an important factor, when used to study flow dynamics in cerebrovascular pathological conditions such as hydrocephalus[1]. There is established research quantifying bias in flow due to effects of resolution, partial volume and intra-voxel flow dephasing[2,3,4]. However, RF saturation effects on velocity estimates is not clearly defined. Flow regions, as in a vessel, encounter varying amounts of RF pulses due to the velocity distribution of spins across the vessel. The slower spins are therefore expected to be saturated to a greater extent than the faster spins in a pixel, inducing changes to the average velocity estimate of the pixel. The focus of this study was to determine if RF saturation introduced a significant bias in velocity estimates for 2D PC-MRI of cerebrospinal fluid (CSF) flow in the aqueduct.

METHODS: A mathematical model describing RF saturation was developed for flow through the center of a circular cross section. The bias introduced is reflected in the magnitude and phase of the MR signal, and is dependent on variation in slice thickness (dz), and flip angle (FA). Accounting for RF saturation, the MR signal S(x) was calculated as

$$S(X) = K\int_0^{\Delta x} x(2R-x)[1 - S1^{(\frac{1}{x(2R-x)})}]e^{ix(2R-x)CE}dx,\ K = -\frac{T_R V_M}{\Delta x \Delta z R^2 \ln(cos\theta)},\ S1 = (cos\theta)^{\frac{\Delta x R^2}{T_R V_M}}, CE = \frac{\pi V_M}{R^2 V_{enc}} \quad (1)$$

where x is the distance from the vessel wall, R is the radius of the vessel, V_M, the peak velocity, and V_{enc}, the aliasing velocity.

Numerical Simulation: Laminar flow was simulated using the model described for 0.5x0.5mm in-plane resolution, V_M=8cm/s, FA = (10,30) degrees, and dz=(2,10)mm. Relative bias was calculated across the vessel diameter. **Phantom Experiments:** A flow phantom was used with 2D PC-MRI (0.5x0.5mm in-plane resolution, V_M=8cm/s), to obtain data. FA of 10 and 30 degrees (dz=2mm), and dz of 2mm and 10mm (FA=10 deg) datasets were obtained. **In vivo Experiments:** Five volunteers were scanned (3 repeated measures per volunteer) using 2D cardiac gated PC-MRI (0.6 x 0.6 mm in-plane resolution, V_M=5cm/s). FA was varied between 10 and 30 degrees. **Data Analysis:** A paired t test was performed on the flow phantom data to identify regions with significant changes in velocity estimates, due to variations in FA and dz. The aqueduct in the in vivo data was segmented using thresholding of the magnitude images. Velocity difference and spatial velocity gradient maps were computed for each cardiac phase. Linear regression analysis was performed to determine correlation between bias and the spatial velocity gradient. The implementation was performed using GPI[5] (Graphical Programming Interface).

RESULTS: Figure 1 shows the relative bias (%) as a function of distance from the vessel wall for simulations. The bias measurements were obtained for variations in FA (Fig.1A), and dz (Fig.1B). The results from the phantom and in vivo data are shown in Fig.2, and Fig.3 respectively. The p-value maps indicate regions with significant change in velocity estimates ($p<0.05$). Signed mean difference velocity maps obtained for FA variation in the case of in vivo data, are shown in Fig. 3B. Figure 4 shows a scatter plot between the velocity difference maps and spatial velocity gradient.

DISCUSSION: The simulated bias increased with increasing FA, and dz at the vessel wall. The p-value maps generated for the flow phantom, indicated that slow flow regions incurred greater bias. The signed velocity difference maps from in vivo data, indicated higher bias at the aqueduct periphery during systole, but not consistent during diastole. It is important to note here that temporal variation was not accounted for while computing the velocity gradient. Regression analysis for a single cardiac phase from a single dataset, during systole, indicated that 48% of the velocity variations could be explained by variations in the spatial velocity gradient. This observed correlation is consistent with the expectation that RF saturation effects are more prominent at the vessel periphery, where the velocity gradient is the higher than the vessel interior. Initial results are indicative that flip angle variation could bias velocity estimates in the aqueduct. Further work, with the inclusion of the temporal velocity gradient, has to be performed to show repeatability of this effect in the aqueduct

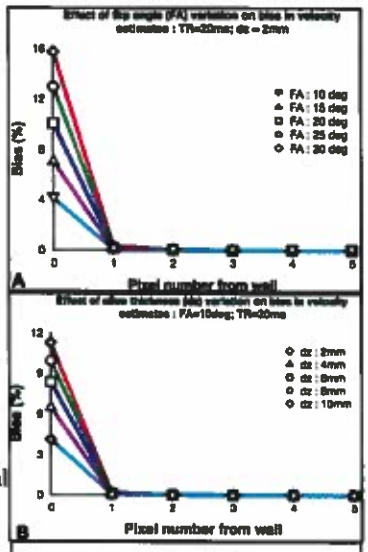

Fig. 1: Bias in velocity estimates from numerical simulation due to (A) FA variation, and (B) dz variation.

Fig.2:(A)Phantom axial slice velocity map; (B)$p<0.05$ regions for FA variation: (C)$p<0.05$ regions for dz variation.

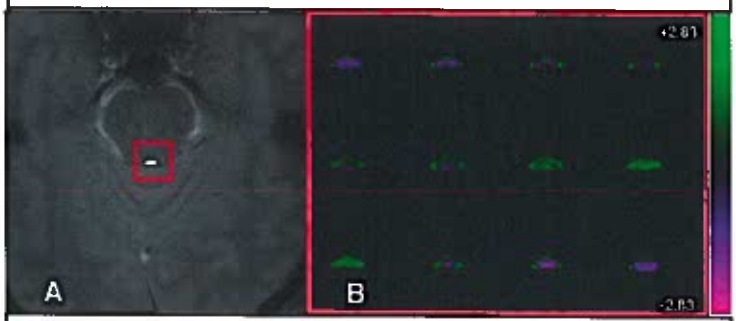

Fig.3:(A)Axial gradient echo image of aqueduct (red square);(B) Signed mean difference velocity maps (FA30 - FA10) for 12 cardiac phases of the red square in (A)

REFERENCE:[1] J.F. Giner et.al, Neurologia, 2014: 29, 68-75. [2] C.Tang, et.al., JMRI, 1993:3, 377-385. [3] D.N. Ku, et al., Journal of biomedical engg., 1990:112(4), 464-472. [4] Y Papaharilaou, et al., JMRI 2001, 14:714-723. [5] N.R.Zwart and J.G.Pipe, MRM, 2014, doi:10.1002/mrm.25528

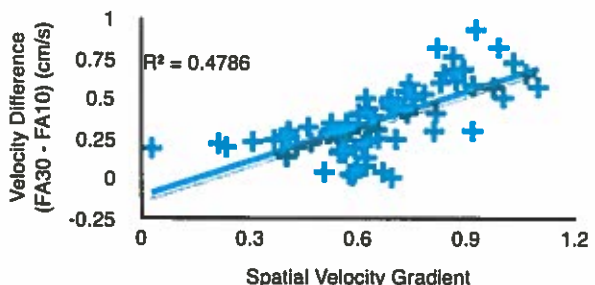

Fig 4: Correlation between spatial velocity gradient and velocity difference due to change in FA

4D Flow and Cardiac MR imaging in Patients with Chronic Thromboembolic Pulmonary Hypertension treated by Balloon Pulmonary Angioplasty

Hideki Ota[1], Koichiro Sugimura[2], Haruka Sato[2], Yuta Urushibata[3], Yoshiaki Komori[3], Hiroaki Shimokawa[2] and Kei Takase[1].
[1]Diagnostic Radiology and [2]Cardiovascular Surgery, Tohoku University Hospital, Sendai, Japan.
[3]Siemens Japan K.K., Tokyo, Japan.

Purpose: Chronic thromboembolic pulmonary hypertension (CTEPH) is a distinct disease entity of pulmonary hypertension (PH) with a mean pulmonary arterial pressure (mPAP) greater than 25mmHg for more than 6 month. Recent advancement of balloon pulmonary angioplasty (BPA) procedure improved right ventricular (RV) function and long-term prognosis in patients with inoperable CTEPH [1,2]. Past studies indicated conventional cardiac and 4D flow MR imaging parameters were correlated with mPAP[3,4]. However, longitudinal studies to correlate mPAP and MR imaging during follow-up for CTEPH are sparse. The purpose of this study was to examine whether the changes of PA flow patterns on 4D flow MR and parameters of cine MR imaging are correlated with the change of mPAP in patients with CTEPH treated by BPA.

Methods: This study included 32 patients with CTEPH who were scheduled for BPA. All patients underwent serial MR scans using a 3.0T whole body scanner before and after completion of BPA procedures. MR scan protocols included standard cardiac cine MR imaging and 4D flow MR imaging of the pulmonary trunk. 4D flow MR imaging parameters were in the following: 3 dimensional phase-contrast MR imaging with 3-directional velocity encoding in transverse acquisition; ECG-gating; respiratory-gating; TR/TE, 52.4ms/3.43ms; flip angle, 15 degrees; VENC, 50-110cm/sec; matrix size, 2.4mm x 1.8mm x 3.5mm.

Cine MRI measurements included left ventricular ejection fraction (LVEF), LV cardiac index (LVCI), RVEF, RVCI, RV end-diastolic and end-systolic volume index (RVEDVI, RVESVI) and pulmonary trunk diameter to ascending aortic diameter ratio (PA/AA ratio). 4D flow MR images were analysed with standalone software (4D FLOW Demonstrator, ver. 2.3, Siemens, Erlangen, Germany). On 4D flow MRI, the degree of vortex flow in the pulmonary trunk in the end-systolic phase was evaluated in the following manner: a cross-section that contains the largest vortex flow diameter was extracted; on the cross-section, a ratio of area with backward flow to total cross-sectional area in the end-systolic phase was calculated (backward flow area ratio). Mean and maximal PA flow velocities on the cross-section were also obtained.

Each MR imaging parameter was compared with catheter-driven mPAP using Pearson's correlation coefficient. 0.05 was used to designate statistical significance.

Results: Vortex flow in the pulmonary trunk was observed in all patients prior to BPA. The mean of mPAP was significantly decreased after BPA in all patients (37.7±10.0 mmHg vs 23.4±6.8 mmHg, $p<0.01$). Significant correlations with pre-BPA mPAP were observed in RVEDVI ($r=0.42$, $p=0.02$), RVESVI($r=0.42$, $p=0.02$) and backward flow area ratio ($r=0.59$, $p<0.01$). None of the other MR imaging parameters was correlated with mPAP. All MR parameters except for LVEF demonstrated significant improvement after BPA. The difference of mPAP before and after BPA were significantly correlated with the difference of backward flow area ratio ($r=-0.50$, $p<0.01$) and difference of RVESVI ($r=-0.38$, $p=0.04$) (Figure). On multivariate linear regression analysis, both differences of backward flow area ratio and RVESVI were independently correlated with the difference of mPAP.

4D Flow MRI before and after BPA

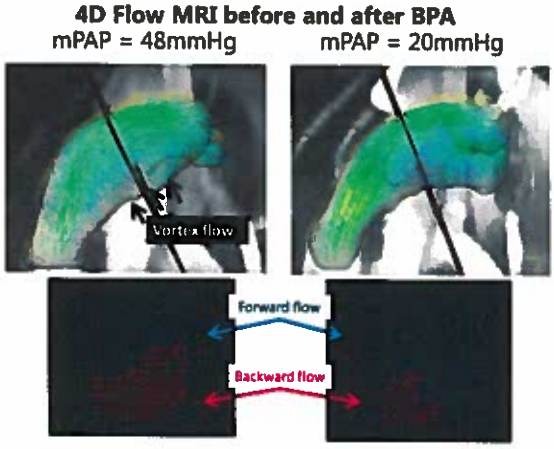

Vortex flow may be a characteristic finding of PH. The degree of backward flow ratio as well as RVESVI were improved along with improvement of mPAP after BPA. These results indicated potential importance of evaluating both right ventricular function and pulmonary arterial hemodynamics in follow-up MR studies for effective treatment of CTEPH.

Conclusion: 4D flow MRI can visualize vortex flow in the pulmonary trunk in CTEPH patients. Adding 4D flow MRI to cardiac MR protocols may provide better estimation of mPAP after effective BPA on CTEPH.

References:

1. Sato H, Ota H, Sugimura K, et al. Balloon Pulmonary Angioplasty Improves Biventricular Functions and Pulmonary Flow in Chronic Thromboembolic Pulmonary Hypertension. Circ J. April 2016. doi:10.1253/circj.CJ-15-1187.
2. Sugimura K, Fukumoto Y, Satoh K, et al. Percutaneous Transluminal Pulmonary Angioplasty Markedly Improves Pulmonary Hemodynamics and Long-Term Prognosis in Patients With Chronic Thromboembolic Pulmonary Hypertension. Circ J. 2012;76(2):485-488.
3. Swift AJ, Rajaram S, Hurdman J, et al. Noninvasive Estimation of PA Pressure, Flow, and Resistance With CMR Imaging: Derivation and Prospective Validation Study From the ASPIRE Registry. J Am Coll Cardiol Img. 2013;6(10):1036-1047. doi:10.1016/j.jcmg.2013.01.013.
4. Reiter G, Reiter U, Kovacs G, Olschewski H, Fuchsjäger M. Blood Flow Vortices along the Main Pulmonary Artery Measured with MR Imaging for Diagnosis of Pulmonary Hypertension. Radiology. 2014;275:71-79.

More accurate velocimetry for high-moment phase contrast using weighted non-convex optimization

Michael Loecher[1], Daniel Ennis[1,2]

[1]Department of Radiological Sciences, [2]Biomedical Physics, University of California, Los Angeles, CA, United States

INTRODUCTION: Phase contrast MRI is a powerful non-contrast angiographic tool. Properly scaled bipolar gradients enable velocity quantification on a voxel-by-voxel basis, which is useful for a wide range of diagnostic cardiovascular applications. High-moment bipolar gradients improve angiographic quality and velocity accuracy, but are limited by velocity wrapping. Phase unwrapping methods can correct these errors up to a point, but to raise gradient moments significantly, alternative velocity encoding strategies must be used (e.g. dual-venc [1] or multi-directional [2]).

The ***objective*** of this work was to use a weighted non-convex optimization method to make high-moment acquisition schemes more effective and robust. This was accomplished by including more information about the prescribed gradient moments and signal estimates to reconstruct: 1) angiograms with better vessel depiction; and 2) un-aliased, more accurate velocity data.

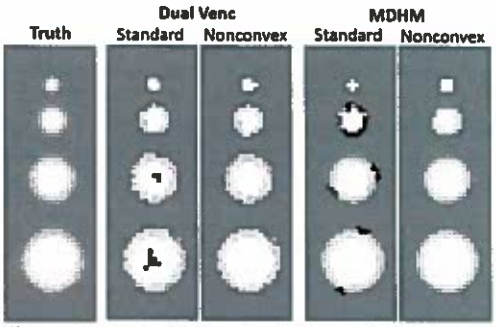

Figure 1: Simulation results during peak systole with Dual venc and MDHM methods using 4x gradient moments. Errors are seen with both methods for the standard reconstructions, which are not present in the weighted non-convex optimized method.

THEORY: We solve for velocity (v) by optimizing this non-convex equation: $\underset{v}{\operatorname{argmin}} \left\|we^{iAv} - y\right\|_2^2 + \lambda\nabla^2 v \; subject\ to\ |v| < v_{max}$ where y is the magnitude normalized data, A is the encoding matrix, v_{max} is the user defined search radius (similar to VENC), w is a data weighting vector, and $\nabla^2 v$ represents a multidimensional Laplacian regularizer [3]. w is the velocity variance σ_v^2 with constant factors removed and calculated based on signal magnitude.

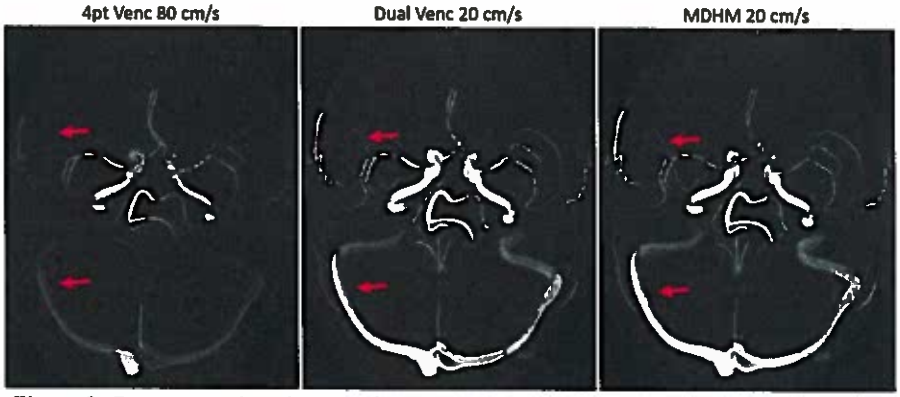

Figure 2: Reconstructed angiograms from a 3D-PC acquisition using the different encoding strategies. The higher moment acquisitions (Dual VENC and MDHM) show significantly better small vessel and venous signal, as shown with the arrows

METHODS: Computational fluid dynamics was used to simulate 20 phases of pulsatile blood flow through straight tubes of various diameters (2, 4, 6, and 8 mm) with a peak velocity arbitrarily set to 100 cm/s. Intravoxel dephasing was simulated by spatially oversampling the velocity profiles by 32x, encoding the velocity into a complex signal using a dual-venc (DV) or a 6-point multi-directional high moment (MDHM) strategy, then cropping in k-space. Velocities were solved using standard methods and weighted non-convex optimization, which was implemented using a multistart conjugate gradient descent method. Velocity error vectors were computed between the reconstructed and true velocity vectors. The mean magnitude of this error was reported. The method was evaluated using *in vivo* human head datasets (IRB approved with consent) using a standard 4-pt (VENC=80 cm/s) acquisition, and DV and MDHM acquisitions with 20 cm/s. Scan time was held constant, so fewer projections were used with 7 encoding directions.

RESULTS: Figure 1 shows velocity images in a single direction of the 2D cine simulation. Velocity errors can be seen for the standard methods, which are not present in the non-convex optimization method. In the simulation, the normalized RMSE of the velocity vectors was decreased by using the nonconvex method as compared to standard methods from 15.2% to 5.7% with DV, and from 4.3% to 1.8% with MDHM. Figure 2 shows the improvement in angiogram quality with high moment acquisitions. Figure 3 shows *in vivo* results where the nonconvex method shows more consistent velocity values than standard reconstructions.

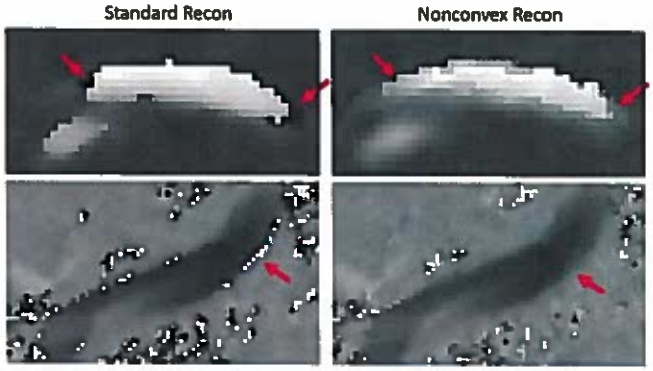

Figure 3: Single *in vivo* axial slices of velocity data from a volunteer in a region of the basilar artery (top row) and internal carotid artery (bottom row) with the MDHM acquisition. Significant errors are seen at vessel walls that are better handled with the nonconvex optimization

CONCLUSION: The weighted non-convex method leverages the use of additional information when solving for velocities with any type of high moment acquisition. By adding weighting factors and a regularization parameter, velocities are more accurately reconstructed, allowing for more robust use of high-moment acquisitions, significantly higher velocity to noise ratios, and improved angiograms.

REFERENCES: [1] Nett EJ *et al. JMRI* 35.6 (2012): 1462-1471. [2] Zwart NR and Pipe JG. *MRM* 69.6 (2013): 1553-1563. [3] Loecher M *et al. JMRI* (2015).

Session 3

Power Pitch!

Vascular injuries in elite volleyball players: imaging modalities and findings

Nils Planken[1], Daan van de Pol[1], Marja Pannekoek[1], Aart Terpstra[1], Paul Kuijer[2], Mario Maas[1]
Departments of Radiology[1], Coronel Institute of Occupational Health[2]
Academic Medical Center, University of Amsterdam, The Netherlands

Purpose: Elite overhead athletes, like volleyball players, are at risk of finger ischemia due to arterial emboli originating from an injured and degenerated proximal posterior circumflex humeral artery (PCHA) in the dominant shoulder. Contrast enhanced magnetic resonance angiography (CE-MRA) revealed to be of additional value for diagnosis by visualization of both the culprit PCHA aneurysm and digital embolization in a symptomatic elite volleyball player. The purpose of this abstract is (1) to describe the diagnostic yield of time resolved – and high resolution steady state CE-MRA when compared to vascular ultrasound for detection of PCHA aneurysm and digital embolization. Additionally we aimed (2) to determined the prevalence of PCHA aneurysms in elite volleyball players and relate the presence of aneurysms to anatomical variants.

Methods: (1) In an elite volleyball player with ischemic symptoms of his spiking hand, time resolved and high-resolution steady state CE-MRA was acquired (0.3x0.3x0.3 mm voxel size) using a 1.5T MR system, a blood pool contrast agent and a 15-channel knee coil, in addition to physical examination, finger pressure measurement and vascular ultrasound. (2) A cohort of 280 elite volleyball players (national and international top level) was screened for PCHA aneurysms, anatomy, branching pattern, vessel course and diameter using vascular ultrasound.

Results: (1) In the symptomatic elite volleyball player ultrasound detected a proximal PCHA aneurysm. However, ultrasound was inconclusive for the assessment of the palmar arch and digital arteries. Non-invasive digital arterial blood pressure evaluation revealed abnormal pressure values at the level of the proximal phalanx (digit I-V: 159, 144, 149, 159, 0 mmHg) and mid phalanx (digit II-IV: 85, 97, 81 mmHg). Multiple filling defects / emboli were detected by time-resolved and high-resolution CE-MRA in the distal radial artery, palmar arch, common palmar artery and digital arteries (figure 1, first pass MIP left panel, steady state MPR right panel). These lesions corresponded to the abnormal non-invasive digital arterial pressure values. In addition CE-MRA depicted the PCHA aneurysm (diameter 8mm, length 25mm, at 8 mm from the PCHA origin) in supine anatomic position (figure 2 right panel). During abduction and external rotation (ABER provocation) the aneurysm was largely compressed (figure 2 left panel). The remaining vascular tree showed no abnormalities.
(2) The prevalence of PCHA aneurysms was 4.6 % (13/280) in the cohort of elite volleyball players. All aneurysms were detected in proximal PCHAs that originated from the axillary artery (AA). The PCHA originated from the AA in 81 % of cases (228/280), and showed a curved course dorsally towards the humeral head in 93 % (211/228).

Figure 1

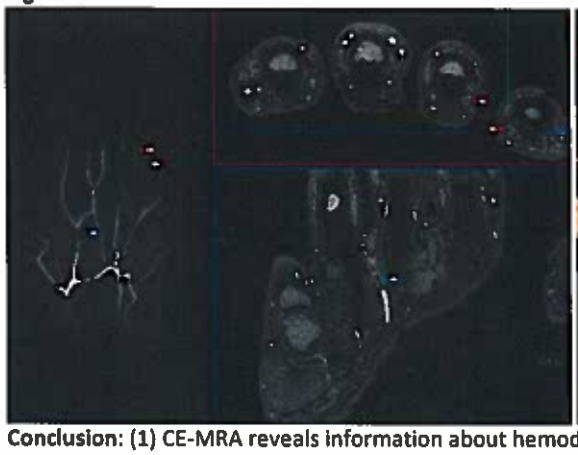

Figure 2

Conclusion: (1) CE-MRA reveals information about hemodynamics as well as detailed anatomical and pathological information. Thereby CE-MRA enables visualization of small vessel pathology, such as symptomatic emboli, that are not detected by vascular ultrasound, and that are in agreement with symptoms and non-invasive hemodynamic measurements. Additionally, this comprehensive approach also enables identification of the culprit, the PCHA aneurysm, a known source of digital embolization in the spiking arm of elite volleyball players. (2) The prevalance of PCHA aneurysms in elite volleyball players is high and associated with a specific branching type: a PCHA that originates from the axillary artery.

Initial Results with ASL-FAIR Perfusion MRI in the Rhesus Macaque Placenta

Kai D. Ludwig[1], Kevin M. Johnson[1], Scott B. Reeder[1,2,3,4,5], Thaddeus G. Golos[6,7], Ian M. Bird[7], Oliver Wieben[1,2], Dinesh M. Shah[7], Sean B. Fain[1,2,3].

Departments of Medical Physics[1], Radiology[2], Biomedical Engineering[3], Medicine[4], Emergency Medicine[5], Comparative Biosciences[6], and Obstetrics & Gynecology[7] at the University of Wisconsin-Madison, Madison, WI

Purpose: Perfusion is an essential physiological function for a healthy placenta and fetal development. Poor placental perfusion is related to adverse outcomes such intrauterine growth restriction[1] associated with conditions including maternal diabetes and obesity. Recently, the NIH launched the Human Placenta Project to develop non-invasive methods and markers of placental health to understand the role of placental development and function in normal and abnormal pregnancies without the use of ionizing radiation[2]. Here, we investigate the feasibility of arterial spin labeled (ASL) perfusion MRI using a flow-sensitive alternating inversion recovery (FAIR) sequence, as a means of assessing placental perfusion in the rhesus macaque. ASL-FAIR does not require exogenous contrast, has low SAR deposition, and can quantitatively assess tissue perfusion. The rhesus macaque is a suitable experimental model as its placenta has anatomical and physiological similarities to that of a human[3,4].

Methods: Three pregnant rhesus macaques were imaged at 3.0T (Discovery MR750, GE Healthcare, Waukesha, WI) with a 32 channel coil. The macaques had gestational ages of 66, 69, and 106 days. The animal was sedated with isoflurane. Placental imaging was performed using a 2D respiratory-triggered ASL-FAIR acquisition with a single-shot FSE readout with an inversion time (TI) of 2.0s (TR/TE = 4.0s/49.2ms; FOV =18x18cm^2; matrix=128x128; 4mm slice; BW=83.3kHz; and 32 control/tag pair images). Images were acquired under free breathing conditions with the 2.0s TI chosen such that tagging and imaging both occurred in end expiration. A proton density image (M_0) was obtained prior to control/tag imaging. ASL post-processing and placental segmentation was performed using MATLAB (R2014b, MathWorks, Natick, MA). Averaged control and tag images were subtracted to produce a difference image (ΔM). Perfusion was estimated with a one compartment model:

$$f = \frac{\lambda}{2\alpha \cdot TI} \cdot \frac{\Delta M}{M_0} \cdot \exp\left(\frac{TI}{T_1}\right)$$

Where $f \equiv$ perfusion, $\lambda \equiv$ partition coefficient = 80mL/100g, $\alpha \equiv$ inversion efficiency = 1.0, $TI \equiv$ inversion time, and $T_1 \equiv$ longitudinal relaxation time of placenta. Perfusion values were then normalized ($\hat{f}$) to the maximum perfusion value.

Results: Fig. 1A and 1B show the averaged global inversion and slice-selective inversion images from the ASL-FAIR acquisition. The difference image in Fig. 1C shows focal signal enhancements within the placenta and in its surrounding vasculature. An overlay of the normalized placental perfusion map (color) on the proton density image (Fig. 1D) depicts localized regions of high perfusion. A histogram distribution of the normalized perfusion values for voxels within the placenta is displayed in Fig. 2 for all three macaques. Table 1 contains the estimated mean and maximum perfusion values compared to the gestational age of the macaques.

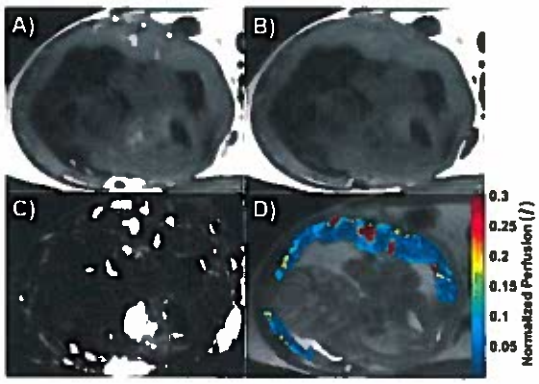

Figure 1: Representative global inversion (tag) **(A)** and slice-selective inversion (control) **(B)** MR images from ASL FAIR sequence. Resulting difference image **(C)** and placental perfusion map (color) overlaid on M_0 image (gray) **(D)** show localized enhancement within the placenta.

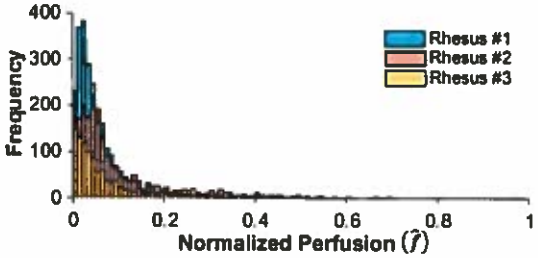

Figure 2: Histogram distribution of normalized placental perfusion values for all three animals.

Table 1: Placental Perfusion Statistics

Rhesus	Gestational Age [days]	Perfusion (f) Values [ml/100g/min]	
		Mean	*Max*
#1	106	123	1588
#2	69	105	1017
#3	66	59	623

Conclusion: While placental perfusion has been investigated in several human studies, this is the first attempt to measure perfusion in the placenta of the rhesus macaque with ASL FAIR. Mean placental perfusion values presented here are below those reported for normal pregnancy in humans (176±91 mL/100g/min)[5]. A 2.0s TI resulted in minimal respiratory motion artifact; in addition, sedation of the mother resulted in minimal fetal movement. The heterogeneous nature of the intra-placental perfusion values remains unclear but suggests an extended transit time across the placenta. Additional studies are ongoing to further investigate the utility of this approach, compare values to those acquired with DCE-MRI, and apply modified tagging to reduce residual blood signal from within macrovasculature.

References: **1.** Anblagan et al. *Proc. Intl. Soc. Mag. Reson. Med.* 2011;19:151. **2.** nichd.nih.gov/research/HPP **3.** Dambaeva et al. *Biology of reproduction.* 2012;86(1):1-10. **4.** Golos et al. *International J Developmental Bio.* 2010;54(2-3). **5.** Gowland et al. *MRM.* 1998;40:467-473.

Acknowledgements: We thank NIH awards CHD U01 HD087216, UL1TR000427 and TL1TR000429 for funding and GE Healthcare for research support.

Cardiac MRI heart deformation analysis demonstrates differences in circumferential strain between amyloid and non-amyloid infiltrative cardiomyopathy.

Bradley Allen, MD[1]; Marcos P Ferreira Botelho, MD[1]; Eric Keller[1]; Benjamin Freed, MD[2]; Daniel Lee, MD[2]; Bruce Spottiswoode, PhD[3]; Maria Carr[1]; James C Carr, MD[1]; Jeremy D Collins, MD[1]

Departments of [1]Radiology and [2]Cardiology, Northwestern University, Chicago, IL;
[3]MR Collaborations, Siemens Medical Solutions USA Inc., Malvern, PA

Purpose: Cardiac MR (CMR) derived strain parameters have been studied in both ischemic and non-ischemic cardiomyopathies (NICM) (1,2). It is established that differences in longitudinal strain exist in patients with cardiac amyloidosis (3,4). The purpose of the current analysis was to explore the utility of CMR standard balanced steady-state free precession (bSSFP) cine imaging deformation analysis quantification of regional and global circumferential, radial, and longitudinal LV myocardial strain parameters for the stratification of patients with amyloid and non-amyloid NICM.

Methods: Fifteen patients (12 men, 65.5 ± 17 years) with biopsy proven cardiac amyloidosis (A), 9 patents (6 men, 46.7 ± 16 years) with biopsy proven fibrotic NICM (NA), and 8 healthy volunteers (6 men:, 47.0 ± 5.3 years) were included. All subjects underwent CMR at 1.5 T with bSSFP segmented cine imaging with a temporal resolution of 25-40 msec. Images were retrospectively evaluated using prototype software employing deformation field analysis to generate Lagrangian strain values for the left ventricle (LV- radial, circumferential, longitudinal) (5,6). Radial and circumferential strain values were generated for base, mid, and apex regions using the AHA 17 segment model, and global radial and circumferential strain were averages of segments 1 through 16. Longitudinal strain was assessed at base, mid, and apex and appropriate segments were averaged to derive a LV free wall longitudinal strain. LV ejection fraction (LVEF) was calculated on a dedicated workstation. Analysis of variance was used to compare parameters for the three groups and post-hoc Bonferroni correction was applied for between group comparisons.

Results: Global circumferential strain was the only parameter that accurately stratified the three groups with significant differences between A, NA, and V cohorts. Apical circumferential strain and mid-LV radial strain was significantly reduced in the NA cohort relative to both A and V cohorts, but there was no difference between A and V groups. Global radial strain as well as the majority of regions for longitudinal strain were significantly decreased in both NICM cohorts relative to V, but there was no difference between A and NA groups. See Table 1 for a complete numeric and statistical summary. There was a significant difference in LVEF between A and NA group (49 ± 18% vs. 26 ± 17%, p = 0.001).

Conclusions: The current study demonstrates that CMR cine deformation analysis quantification of circumferential strain may help in discriminating cardiac amyloidosis from other NICM. Additional derived global and regional strain parameters are generally decreased relative to normal volunteers, but were unable to distinguish NICM groups. An important limitation in the current study was the difference in LVEF between NICM groups which may result in overestimation of between group differences that may not be present in patients with similar function.

References: 1. Young et al. CV Res 2001. 2. Neizel et al. Circ CV Imag 2009. 3. Koyama et al. Circulation 2003. 4. Senapati et al. Heart 2016. 4. Guetter et al. Proc. ISBI, 2011.5. Jolly et al. Proc. ISBI, 2010.

	Region	Amyloid	Non-Amyloid	Volunteer	p-value			
					ANOVA	A vs NA	A vs V	NA vs V
Circumferential	Base	-14.4 ± 4.0	-13.6 ± 4.5	-16.3 ± 1.3	.31	-	-	-
	Mid	-17.5 ± 3.1	-14.5 ± 5.4	-17.1 ± 1.6	.16	-	-	-
	Apex	-17.0 ± 4.8	-11.5 ± 5.7	-20.8 ± 2.2	.001	***.03***	.22	***.001***
	Global	-12.1 ± 2.5	-9.0 ± 3.2	-17.7 ± 1.3	<.001	***.021***	***<.001***	***<.001***
Radial	Base	27.3 ± 10.3	35.9 ± 19.6	41.0 ± 11.6	.09	-	-	-
	Mid	42.5 ± 11.1	27.5 ± 12.6	47.7 ± 11.1	.003	***0.02***	0.96	***0.004***
	Apex	32.2 ± 15.5	25.2 ± 17.6	41.7 ± 17.4	.14	-	-	-
	Global	23.3 ± 7.8	17.7 ± 8.5	43.7 ± 12.1	<.001	0.46	***<.001***	***<.001***
Longitudinal	Base	-13.9 ± 5.3	-10.2 ± 3.6	-20.0 ± 5.0	<.001	0.18	***0.02***	***<.001***
	Mid	-11.7 ± 5.4	-10.4 ± 3.4	-15.5 ± 2.4	0.04	1.00	0.15	***0.04***
	Apex	-8.3 ± 3.9	-9.6 ± 4.0	-15.5 ± 4.2	<.001	1.00	***0.001***	***0.01***
	Free Wall	-11.4 ± 4.2	-10.0 ± 3.7	-17.0 ± 3.6	.001	1.00	***.007***	***<.001***

Table 1: Regional Strain. Units are %. A – Cardiac amyloidosis, NA – non-amyloid NICM, V – volunteers.

MRI-Derived Coronary Fractional Flow Reserve: Preliminary Results

Jackson B. Hair[1], Lucas H. Timmins[2], John N. Oshinski[1,2]

[1]Wallace H. Coulter Department of Biomedical Engineering, Georgia Institute of Technology and Emory University, Atlanta, GA, USA
[2]Department of Radiology & Imaging Sciences, Emory University School of Medicine, Atlanta, GA, USA

Purpose: The gold standard for determining the functional severity of coronary artery stenosis is fractional flow reserve (FFR). FFR is defined as the pressure distal to the stenosis divided by the proximal pressure under hyperemic conditions and FFR is measured through percutaneous insertion of a pressure wire. Recently, it has been shown that FFR can be approximated noninvasively through CT imaging and computational fluid dynamics (CFD) [1]. Due to limitations associated with CT (ionizing radiation, inability to measure flow, issues imaging calcium), we developed a methodology using MRI and CFD to estimate FFR and display it as a function of vessel position.

Methods: We evaluated patients (n = 2) who presented with class III ischemic heart failure and were undergoing a cardiac MRI exam prior to cardiac resynchronization therapy. MRI exams were performed on a 3 T MRI (Trio, Siemens Medical Systems) system using a six-element phased-array cardiac coil. A 3D, whole-heart, navigator and EKG-gated inversion-recovery FLASH sequence with a centric k-space trajectory was used to acquire coronary images at a resolution of 0.64 x 0.64 x 0.75 mm^3 in diastole during the slow infusion of a Gadolinium-based contrast agent. On the acquired images, a Frangi vessel enhancement filter was applied to extract the lumen contours of the left main (LM), left anterior descending (LAD), and left circumflex coronary arteries in vmtk (Vascular Modeling ToolKit), Figure 1A. A surface was fit to the contours in Geomagic (Geomagic, Inc.), and flow extensions were added to the inlet and each outlet followed by discretization of the geometry in ICEM (Ansys, Inc.). Applied boundary conditions included an inlet velocity of 0.2 and 0.7 m/s for basal and hyperemic flow, respectively, and an inlet pressure of 100 mmHg. Murray's Law was used to approximate the flow split through each branch [2]. CFD simulations were run in Fluent (Ansys, Inc.) to quantify velocity and pressure values across the computational domain. Following solution convergence, pressure values were extracted within 5 μm of each centerline location and averaged along the LM and LAD. Both patient image sets analyzed contained a focal stenosis in the proximal LAD, so "healthy" vessels were created by widening the lumen at the site of stenosis in Geomagic.

Results: The color map representation of FFR for the LM and LAD in Patient 1 is shown in Figure 1B, and the FFR evaluated along the centerline for Patient 1 is shown in figure 1C. In the artificially created healthy vessels, FFR was seen to gradually decrease along the length of the vessel, which is consistent with experimental results [3]. In the diseased cases under basal conditions, FFR dropped more rapidly across the lesion (0.95 and 0.98 for patients 1 and 2, respectively) as compared with the healthy vessels (0.99 for both patients). FFR was further reduced under hyperemic conditions (0.54 and 0.87 for patients 1 and 2, respectively), which is consistent with experimental results [3].

Conclusion: Preliminary results using a 3D, contrast-enhanced, whole heart, coronary artery imaging sequence coupled with CFD indicate that the methodology is able to non-invasively quantify FFR *in vivo*.

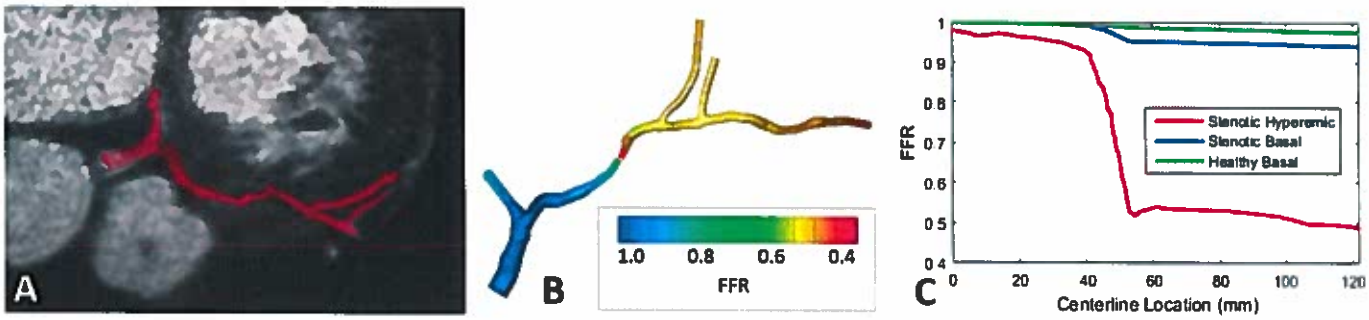

Figure 1. *(A) Segmented lumen contour surface from MR image data. (B) FFR color map of coronary artery. (C) FFR values as a function of centerline locations.*

References: [1] Taylor (2013) *JACC.* [2] Murray (1926) *Proc Natl Acad Sci USA.* [3] Pijls (1993) *Circulation.*

Pulmonary embolus workup in the emergency room: Can we avoid exposure to radiation by using a dedicated magnetic resonance imaging strategy?

Irislimane Y[1], Toporowicz AK[1],Maki JH[2], Finn JP[3], Lambert J[1], Lanthier C[1], Chauny J-M[1], Desjardins A[1], Papas K[1], Samson P[1], Desnoyer M[1], Pressacco J[1]

[1]University of Montreal, [2]University of Washington, Seattle, [3]University of California, Los Angeles

Introduction: Pulmonary embolus (PE) is a potentially fatal condition associated with substantial morbidity and mortality in untreated patients. The incidence rate for PE in the U.S. and Canada (1) is approximately 1 in 418 or 0.24% of the population. As many as 90% of tests for PE detection are negative (2), as the clinical presentation of patients with PE is also common among patients without PE. Computed tomography pulmonary angiography (CTPA) is considered the "modern gold standard" non invasive imaging modality for PE. The main drawback of CTPA is ionizing radiation, with average doses in the range of 12.4-31.8 mSV. As a result, a relatively large number of patients without PE are exposed to ionizing radiation, putting them at a higher risk for developing a malignancy in the future. This study evaluated the possibility of replacing CTPA by MRA in the diagnostic workup of the ED patient with suspected PE. This is highly clinically relevant, as extrapolating ED data obtained in a large multicenter diagnostic study (3), approximately 1 to 2% of all ED patients undergo CTPA to rule out a PE, making this one of the most commonly ordered CT scans in the ED.
Methods: 41 patients admitted to the Montreal Sacre-Coeur Hospital (HSCM) ED who underwent clinically indicated CT for PE (+/- lower limb ultrasound (US)) were recruited for this study. Contrast-enhanced MRA (CE-MRA) was performed within 24 hours of CT using a simultaneous technique to evaluate the pulmonary arteries and lower extremity veins to rule out deep venous thrombosis (DVT). Imaging was performed using and comparing two gadolinium blood pool contrast agents, gasdofosveset trisodium (Ablavar, N=30) and gadobenate dimeglumine (MultiHance, N=11). Both agents were diluted with saline in order to achieve a bolus length matching first pass acquisition. MRA was performed at 3T using first pass and immediate dealy 3D T1 FFE pulmonary artery angiography of the thorax and 3D T1 FFE steady state / VIBE pulmonary artery MRI angiography of the thorax (Figure 1). This was followed by vena cava and lower limb 3D MR venography (Figure 2).
Results: MRA exam success was 95%, with 2 panic/claustrophobic patients out of the total 41 patients. The sensitivity and specificity for the detection and exclusion of PE by MRI was greater than 90% for identifying thrombi in the main, lobar and segmental pulmonary arteries. As has been reported by other investigators, CE-MRA appeared inferior to CTPA for the visualization of thrombus in the subsegmental pulmonary arterial branches

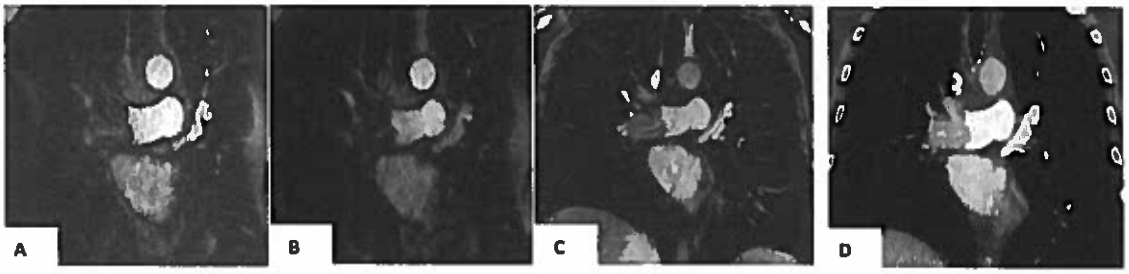

Figure 1: PE shown by CE-MRA (A) 3D T1 FFE first-pass and (B) second-pass MRI angiography, (C) 3D T1 FFE steady state / VIBE MRI sequence and (D) CTPA.

Figure 2: DVT shown by (A) 3D T1 FFE steady state / VIBE MRI sequences and correlated by (B) Doppler echography.

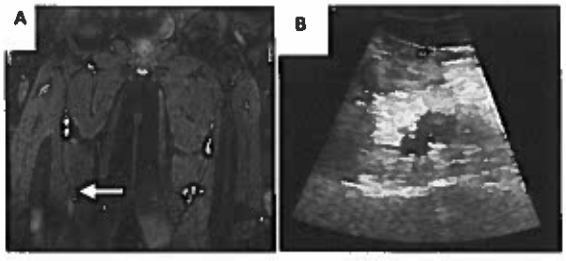

Conclusion: CE-MRA was sensitive and specific compared to CTPA in the workup of PE, thereby being a potential alternative imaging modality of choice on radiation protection grounds alone. The MRA protocol developed was rapid, performed within 15 min. In addition, both protein-binding contrast agents, gasdofosveset trisodium and gadobenate dimeglumine, were similarly effective, giving centers an option of contrast agents for pulmonary MRA.Further large-scale multicenter studies are clearly needed to determine whether and under what circumstances MRA could replace CTPA for the workup of PE. Should MRA be able to replace CTPA, as suggested by this small study, it would decrease exposure to ionizing radiation in the 1 to 2% of all patients presenting ED annually with suspicion of PE. In the US alone, there are an estimated 110 million ED visits per year (4). As radiologists, we have the obligation to evaluate MRA as a potential first-line alternative to CTPA in order to decrease medical radiation exposure in patients, and thus decrease future radiation induced cancers.

References:

1. US Census Bureau R. Population estimates. US Census Bureau. 2004.
2. Anderson DR et al, JAMA : the journal of the American Medical Association. 2007;298(23):2743-53.
3. Kline JA, et al, J Thromb Haemost 2008;6(5):772-80.
4. McCaig LF, Nawar EW. National Hospital Ambulatory Medical Care Survey: 2004 emergency department summary. Advance data. 2006(372):1-29.

The Influence of Field Strength on High Resolution 4D-Flow Imaging

Sarah Kefayati[†], Henrik Haraldsson[†], Chengcheng Zhu[†], Evan Kao[†],Sinyeob Ahn[‡], Gerhard Laub[‡], David Saloner[†§]

†Department of Radiology & Biomedical Imaging, UCSF, San Francisco, CA, USA
‡ Siemens Healthcare, CA, USA
§Radiology Service, VA Medical Center, San Francisco, USA

Abstract:

Purpose: The main goal of this study was to compare the relative abilities of 7T and 3T imaging to capture structural features of complex flow using 4D flow methods within a clinically relevant imaging range.
Materials and Methods: An in vitro study was performed in a jugular vein model and a total of seven imaging protocols were applied and matched for both 3T and 7T. The imaging criteria were selected to create a range of (signal-to-noise ratio) SNRs by alteration in the imaging volume and flip angles. A quantitative measure based on quantifiable flow voxels was applied to compare the level of capturing flow features across field strengths and imaging settings.
Results: Complex helical features were captured in all applied imaging settings at 7T while at 3T only the two imaging protocols with larger volume and highest flip angle (24°) exhibited expected flow features. The variation mean of quantifiable flow voxels was about three times higher in 3T compared to 7T for the highest SNR case.
Conclusion: 4D flow imaging at 7T enables improved capability in capturing complex flow features compared to 3T and provides the essential boost in SNR that is needed for improvement of temporal resolution or imaging of the complex geometries.

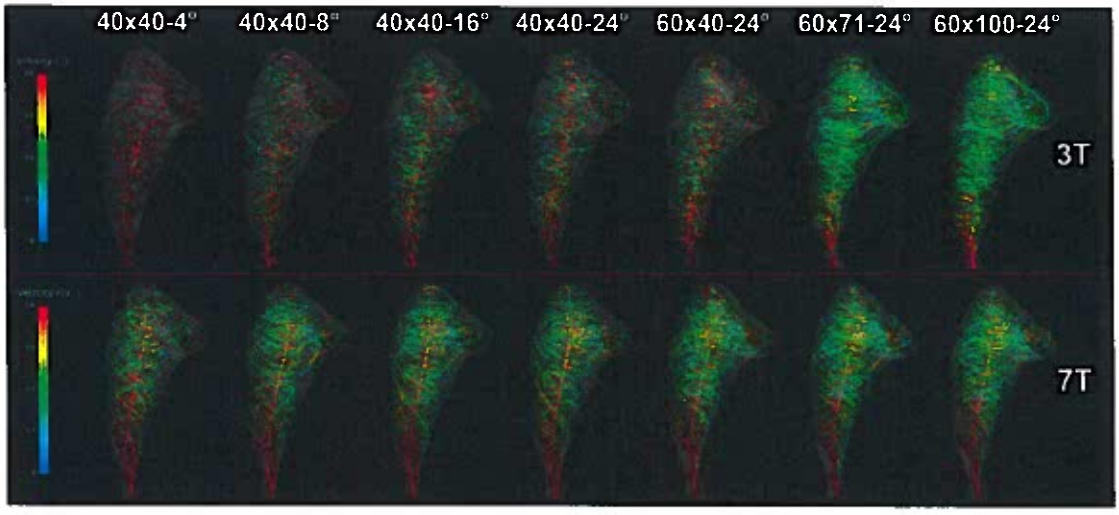

Patient-Specific vs. Population-based Arterial Input Function in Perfusion Estimation for DCE-MRI of the Prostate

Soudabeh Kargar[1], Eric G. Stinson[2], Eric A. Borisch[2], Adam T. Froemming[2], Akira Kawashima[3], Lance A. Mynderse[2], Joshua D. Trzasko[2], Stephen J. Riederer[2]

[1]Biomedical Engineering and Physiology, Mayo Graduate School, Mayo Clinic, [2]Rochester, MN, [3]Scottsdale, AZ, USA

Purpose: Dynamic Contrast Enhanced MRI (DCE-MRI) is a vital component of a multi-parametric MRI exam, the usage of which has increased remarkably in the past several years. Specifically, DCE-MRI is important in the evaluation of local recurrence, particularly after radiotherapy and radical prostatectomy[1]. Pharmacokinetic parameter estimation derived from DCE-MRI is used to differentiate characteristics of cancerous vs. normal tissue. The Arterial Input Function (AIF) plays an important role in perfusion estimation and a patient specific (PS) AIF is ideal[2] because it is a function of the individual patient's physiology and anatomy. The goal of this study is to compare the perfusion parameters estimated by using (i) the PS AIF, (ii) a 10-patient averaged (10-PA) AIF, (iii) the original Parker model with adjusted delay (Pa-O) AIF, and (iv) the Parker[2] model fitted to PS AIF with adjusted delay (Pa-PS) AIF.

Methods: *AIF estimation:* For cases (i) and (ii), the AIF is determined from the DCE-MRI acquisition in which a total of 55 time frames are acquired using an accelerated 3D time-resolved sequence[3] (256×384×38, 0.86×1.15×3.0 mm^3). For case (i), the PS AIF is the average of 9 (3×3) adjacent voxels selected from the L iliac artery for each individual from our prostate MRI patient population. For case (ii), the 10-PA AIF is the average of 10 individual AIFs from the patient population used for case (i). For case (iii), the Pa-O AIF is adjusted with individualized delay of the contrast arrival, and for case (iv) the Pa-PS AIF shown in Eq. 1 is fitted to PS AIF using non-linear least squares via MATLAB's built-in Levenberg-Marquardt algorithm.

$$C_b(t) = \sum_{n=1}^{2} \frac{A_n}{\sigma_n\sqrt{2\pi}} e^{\left(-\frac{(t-T_n)^2}{2\sigma_n^2}\right)} + \frac{\alpha e^{-\beta t}}{\left(1+e^{(-s(t-\tau))}\right)} \quad (1)$$

$$S_n(t) = M_0 \sin\theta_n \frac{1-e^{-TR.R_1(t)}}{1-\cos\theta_n\, e^{-TR.R_1(t)}} \quad (2)$$

$$R_1(t) = R_{10} + r_1.C_b(t) \quad (3)$$

$$C_p = C_b/(1-Hct) \quad (4)$$

Pharmacokinetic modeling: The perfusion model (Tofts[4]) is fitted to the acquired signal for each voxel in the region of interest (ROI) for all 4 cases of AIF. A robust and efficient non-linear least squares technique[5] derived with VARPRO[6] is used for pharmacokinetic modeling. This analysis (fitting) was performed on non-motion corrected data. The signal intensity is converted to contrast concentration by using the spoiled gradient echo signal model (Eq. 2), relaxivity (r_1), and constant pre-contrast R_{10} for blood and prostate tissue (Eq. 3-4). The blood concentration curve vs. time is normalized individually by matching the area under the curve (first-pass) to the total concentration based on the weight of the patient. The blood volume is roughly estimated as 5 liters for a 70 kg man and extrapolated for lower or higher weights.

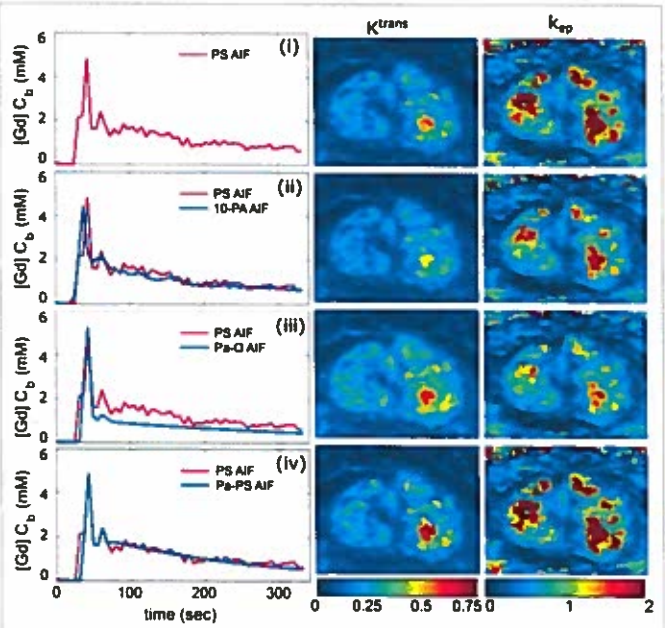

Fig. 1: Patient specific AIF compared with 3 other methods (left) and their respective K^{trans} and k_{ep} maps (right).

Results: The perfusion maps are compared qualitatively for the 4 cases of AIF in Fig. 1. It is observed that the Pa-O AIF peaks higher and drops lower than the PS AIF. As a result, the values of K^{trans} are usually (for 13 cases analyzed in this study) over- and k_{ep} under- estimated as shown in Fig. 2. However, the perfusion results from Pa-PS AIF agree well with the PS AIF results. The 10-PA results show relatively good agreement with PS possibly due to similarity of data acquisition among those 10 averaged cases and the PS AIF.

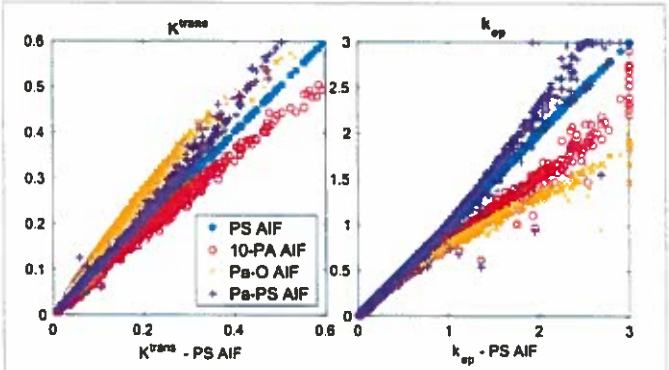

Fig. 2: Perfusion parameters (K^{trans} and k_{ep}) for all the voxels in the ROI plotted vs. those from patient specific AIF.

Conclusion: In conclusion, if no PS AIF or only a low temporal resolution PS AIF is available, using a population-based AIF is sufficient for qualitative assessment of perfusion maps. The Parker model illustrates the first pass and the recirculation peak of the PS AIF and if used, it should be adjusted for the delay to ensure consistency with the PS AIF.

References: **[1]** Kitajima K., *J Nucl Med*, 55(2):223 (2014) **[2]** Parker GJM, *MRM*; 56(5):993 (2006). **[3]** Froemming A.T., *ISMRM* #1169 (2015) **[4]** Tofts P.S., *JMRI*.10:223 (1999) **[5]** Kargar S., *MRA club*, 2015. **[6]** Golub, G.H., *SIAM J. Numer. Anal.* 10(2):413 (1973).

Assessing regionally heterogeneous aortic wall strain in vivo using DENSE MRI

John S. Wilson[1], W. Robert Taylor[2,3,4], John Oshinski[1,2]

[1]Department of Radiology, Emory University, Atlanta, GA, USA
[2]Wallace H. Coulter Department of Biomedical Engineering, Georgia Institute of Technology and Emory University, Atlanta, GA, USA
[3]Division of Cardiology, Department of Medicine, Emory University, Atlanta, GA, USA
[4]Division of Cardiology, Atlanta Veterans Affairs Medical Center, Decatur, GA, USA

Purpose: Mechanics plays a key role in both homeostatic maintenance and pathologic remodeling of the aortic wall. However, there is no reliable quantitative method for determining patient-specific regional aortic kinematics. Thus, we explored the use of cine DENSE (Displacement Encoding with Stimulated Echoes) MRI, which has previously been used to assess myocardial motion, to quantify regional aortic wall strain in vivo.

Methods: Spiral cine DENSE images were acquired on a 3T Siemens Trio in the transverse plane, perpendicular to the infrarenal abdominal aorta in 3 healthy subjects. The sequence used ECG and navigator-gating to acquire 20 images across the first half of the cardiac cycle with a voxel size of 1.3 x 1.3 x 8 mm. Similar to phase contrast MR, DENSE acquires magnitude and phase images; however, in DENSE, phase is proportional to the displacement since the tagging pulse at the r-wave. Using custom Matlab code, wall motion in the transverse plane was tracked through systole, and aortic wall strains were calculated using a quadrilateral interpolation function. After optimizing quadrilateral size, post-processing techniques (reference point averaging, weighted spatial averaging, and time smoothing) were developed to reduce noise while preserving regional strain variations.

Results/Discussion: Defining a quadrilateral size corresponding to 12 equi-spaced 30° sectors around the vessel was found to significantly reduce noise artifacts compared to smaller quadrilaterals. By neglecting the minimal motion at end diastole, noise was further reduced by averaging the strain from up to 4 pre-systolic reference time points. Weighted spatial averaging using two overlapping 12 sector maps (rotated by 15°) reduced noise without overly homogenizing inherent spatial heterogeneities of strain. Fitting a fourth order polynomial to the temporal data for each sector reduced strain variations in time, while preserving a normal aortic pulsatile strain pattern. Preliminary results suggest regional heterogeneities in the magnitude of displacement and in circumferential strain in the healthy infrarenal aorta, with the largest strain in the lateral walls (Figure 1). Lower strains anteriorly and posteriorly may reflect external constraints due to surrounding structures and/or inherent regional differences in aortic structural stiffness. The absolute difference in mean circumferential strain by DENSE compared to homogenized strain by cine MR was less than 1.5% (n=2).

Conclusion: Patient-specific regional circumferential aortic wall strain can be reasonably quantified in vivo using spiral cine DENSE. Healthy infrarenal aortic wall displacement and strain are circumferentially heterogeneous. The displacement is greatest along the anterior wall; however, the greatest circumferential strain is present in the lateral walls. These heterogeneities could have important implications in terms of regional cellular mechanobiology and patient-specific aortic wall remodeling and vulnerability.

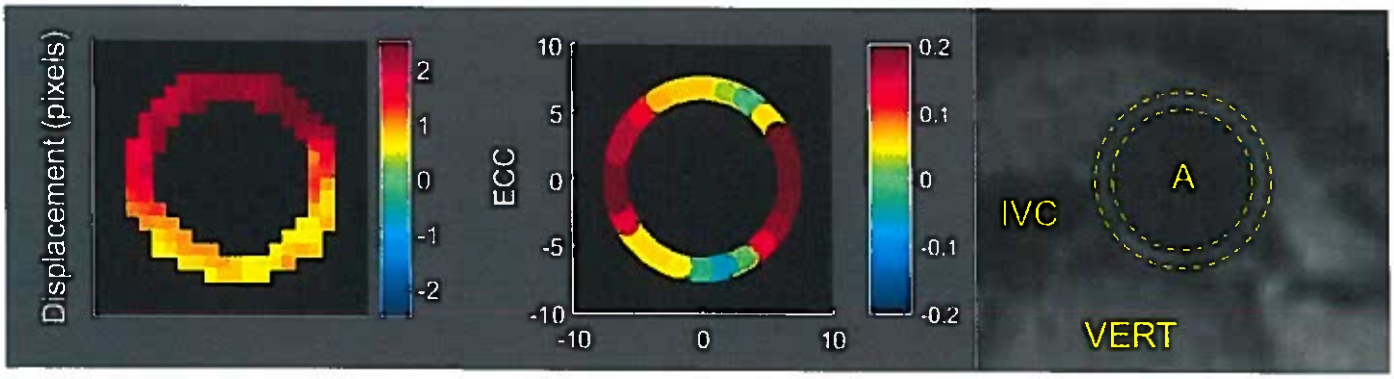

Figure 1. (*Left*) Displacement map of the abdominal aortic wall from end diastole to systole in a young healthy control. (*Middle*) Circumferential Green strain (ECC) map at the same location and time. (*Right*) Reference aortic cross-section for anatomical comparison [A – aorta, IVC – inferior vena cava, VERT – vertebra].

Effect of Contrast Dilution and Bolus Length in Breathhold MRA Exams – the Longer the Bolus, the Better?

[1] T. Schubert, [1] S. Kinner, [1] U. Motosugi, [2] S. Sharma, [1,2] S.B. Reeder

Departments of [1]Radiology and [2]Medical Physics, University of Wisconsin – Madison, USA

Purpose: Uniform intravascular contrast bolus during first-pass MRA may be beneficial for image quality due to steady signal enhancement during the k-space acquisition. This can be achieved with a slower or diluted contrast bolus. The purpose of this study was to prospectively compare the image quality and contrast to noise ratio (CNR) for a short (undiluted) and long (diluted) bolus of a gadolinium based contrast agent.

Methods: After IRB approval and informed consent, twelve healthy volunteers (6 female, mean age 44.3y) were recruited for this study. Imaging was performed on a clinical 3T MRI system (MR750, GE Healthcare). Contrast enhanced first-pass MRA and portal venous phase imaging was performed using either a non-diluted bolus (n=6) of gadobenate-dimeglumine (0.1 mmol/kg), or a bolus (0.1 mmol/kg) diluted up to 40 ml with saline (n=6). Injection rate was 2ml/s for all studies.

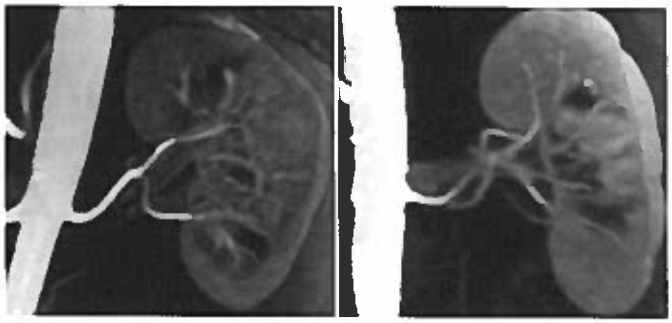

Fig. 1: Renal aortogram acquired with a diluted bolus (**left**) and with a non-diluted bolus (**right**). Higher image quality and lesser edge blurring were observed using a diluted bolus.

Acquisition parameters included: TR/TE = 4.54/1.40ms, BW = +/- 127 kHz, FOV = 400 x 360 x 320mm3, 224 x 160 x 160 matrix for true spatial resolution interpolated to 0.8 x 0.7 x 1.1 mm3 through zero-filling.

Quantitative analysis included contrast-to-noise (CNR)-ratio measurements for all acquisitions, comparing the signal enhancement in the arteries relative to muscle. Results were compared using repeated measures ANOVA.

Qualitative analysis included the evaluation of first pass MRA images in a blinded fashion with respect to vessel contrast, artifacts and image quality on a 5-point-scale (5=best-1=worst) by two radiologists with 11 and 8 years of experience, respectively.

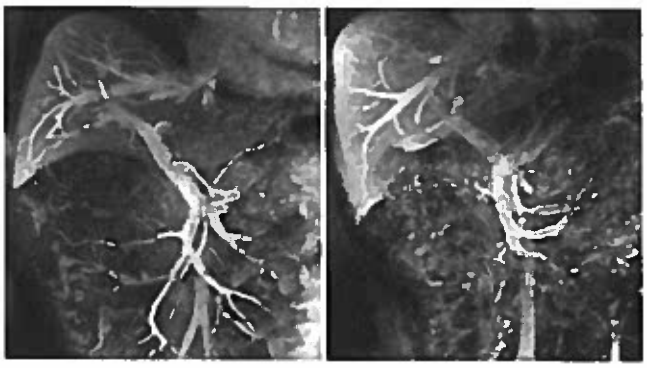

Fig 2: Portal venous MR-venography using a diluted bolus (**left**) and non-diluted bolus (**right**). Higher relative CNR was observed with the diluted bolus.

Results: Quantitative evaluation revealed a significantly higher relative CNR during first pass with non-diluted relative to diluted contrast (p=0.027). Surprisingly, 50s after injection (portal venous phase), the relative CNR was significantly higher for diluted compared to non-diluted (p=0.04).

Qualitative evaluation revealed a significantly higher image quality scoring for diluted (score 5 in 79% of vessel segments) compared to non-diluted (score 5 in 54% of vessel segments, p=0.013), with less blurring and overall superior image quality.

Conclusion: Our results indicate that dilution of a gadolinium based contrast agent results in improved image quality, most likely due to reduced temporal variation of the intravascular signal during the k-space acquisition. The resulting lower relative CNR of the diluted bolus during first pass does not affect image quality. Surprisingly, dilution of the contrast bolus results in higher CNR during the portal venous phase.

Comparison between symptomatic and asymptomatic carotid plaques in patients with bilateral intraplaque hemorrhage

Xianling Wang[1], Jie Sun[1], Xihai Zhao[2], Daniel S. Hippe[1], Jin Liu[1], Thomas S. Hatsukami[1], Rui Li[2], Gador Canton[1], Yan Song[1], Chun Yuan[1,2]

[1]University of Washington, Seattle, WA, Unites States; [2]Tsinghua University, Beijing, China

Purpose

Meta-analyses of prospective carotid MRI studies have demonstrated a strong association between intraplaque hemorrhage (IPH) and increased risk of cerebrovascular ischemic events [1,2].However, IPH is also seen in a substantial number of asymptomatic patients [3,4]. Furthermore, natural history studies with serial MRI indicate that IPH can occur silently and persist for years before causing clinical symptoms [5,6].As such, identifying the mere presence of IPH may be insufficient to precisely identify the patient at greater risk for cerebrovascular ischemic events. The goal of this study is to examine whether there are differences in the characteristics of IPH plaques associated with recent cerebrovascular ischemic events, compared to IPH plaques not associated with recent symptoms.

Methods

The Carotid Atherosclerosis Risk Assessment (CARE-II) Study(NCT02017756) is a multicenter carotid MRI study of Chinese patients with recent (≤2 weeks) cerebrovascular ischemic events. Images were acquired at 3T using a standardized multicontrast protocol, including time-of-flight, T1-weighted, proton-density-weighted, T2-weighted, and magnetization prepared rapid acquisition gradient echo (MPRAGE). Subjects were screened to identify those showing IPH bilaterally on MPRAGE [7]. Multicontrast images were reviewed to obtain information of bilateral IPH plaques on plaque morphology and coexisting plaque characteristics. Additionally, quantitative measurements on IPH signals were performed on MPRAGE, including signal-intensity-ratio as compared to adjacent sternocleidomastoid muscle, longitudinal length, cross-sectional area, and total volume. Imaging measurements were compared between the symptomatic and asymptomatic side using the paired t-test for continuous variables or the sign test for binary variables.

Results

Thirty-one subjects were identified to have bilateral carotid IPH. The study cohort was predominantly males (96.8%), with a mean age of 67±9 years (range: 43-83 years). IPH+ plaques on the symptomatic and asymptomatic side showed similar degree of luminal stenosis (Table). IPH signals on the symptomatic side were stronger(p=0.004 for maximum signal-intensity-ratio) and tended to be more extensively distributed (p=0.071 for IPH volume). Plaque length was significantly longer (p=0.026) and focal plaque burden tended to be larger (p=0.071 for maximum percent wall area) on the symptomatic side. Coexisting plaque characteristics were generally similar between the symptomatic and asymptomatic side, except that the symptomatic side had larger lipid-rich necrotic core volume (p=0.039) and a trend towards higher prevalence of mural thrombus (p=0.11).*Interpretation:* IPH+ plaques in symptomatic patients with bilateral carotid IPH demonstrated advanced features whether or not they were on the side of the recent cerebrovascular ischemic event. The major difference between the symptomatic and asymptomatic side was in MR signals of IPH. Stronger and more extensive IPH signals may indicate more accumulative IPH on the symptomatic side, which are likely from repeated IPH and reflect the activity of the underlying process. Differences in plaque morphology and coexisting plaque characteristics could be the outcomes of plaque progression driven by IPH.

Conclusion

Despite comparable luminal stenosis, IPH+ plaques on the symptomatic side showed stronger MR signals compared to those on the asymptomatic side in patients with bilateral carotid IPH. Quantitative characterization of IPH signals on MRI may be useful as novel imaging markers in refining clinical risk and understanding plaque progression.

References

[1] Saam T, et al. J Am Coll Cardiol. 2013;62(12):1081-1091.
[2] Hosseini AA, et al. Ann Neurol. 2013;73(6):774-784.
[3] Saam T, et al. J Am Coll Cardiol. 2008;51(10):1014-1021.
[4] Singh N, et al. Radiology. 2009;252(2):502-508.
[5] Sun J, et al. J Am Coll Cardiol Img. 2012;5(8):798-804.
[6] Underhill HR, et al. J Am Coll Cardiol Img. 2009;2(12):1381-1389.
[7] Moody AR, et al. Circulation. 107(24):3047-3052.

Table. Comparing IPH+ plaques between the symptomatic and asymptomatic side.

	Carotid plaques with IPH		
	Symptomatic side	Asymptomatic side	p-value
Percent luminal stenosis, %	53±42	53±39	0.99
Plaque morphology			
Maximum wall thickness, mm	5.3±1.6	4.7±1.7	0.11
Plaque length, mm	**24±6**	**21±7**	**0.026**
Mean wall thickness, mm	2.1±0.5	2.0±0.5	0.43
Maximum percent wall area, %	77±12	73±11	0.071
Percent wall volume, %	60±8	59±9	0.62
Coexisting plaque characteristics			
LRNC volume, mm^3	**406±354**	**291±293**	**0.039**
Calcification volume, mm^3	54±51	55±95	0.90
Thin/ruptured fibrous cap, n (%)	24 (77.4)	21 (67.7)	0.55
Surface ulceration, n (%)	13 (41.9)	10 (32.3)	0.55
Mural thrombus, n (%)	9 (29.0)	3 (9.7)	0.11
IPH characteristics			
Maximum signal-intensity-ratio	**5.8±2.4**	**4.7±1.8**	**0.004**
IPH length, mm	14±7	12±8	0.12
Maximum IPH area, mm^2	17±17	13±10	0.21
IPH volume, mm^3	150±199	88±106	0.071

IPH : intraplaque hemorrhage; LRNC: lipid-rich necrotic core.

Aortic Hemodynamics in Patients with Repaired Aortic Coarctation – Serial Analysis by 4D Flow MRI

Geiger J[1], Romberg J[2], Hirtler D[2], Gottfried K[3], Stiller B[2]

[1] Northwestern University, Feinberg School of Medicine, Dept. of Radiology, Chicago/USA
[2] University Hospital Freiburg, Dept. of Pediatric Cardiology and Congenital Heart Disease, Freiburg/Germany
[3] University Hospital Mainz, Dept. of Anaesthesiology, Mainz/Germany

Purpose: Aortic coarction (CoA) is one of the most common congenital heart defects [1]. The majority of patients needs surgical or endovascular repair; however, potential complications such as aneurysm formation and recoarctation should be identified in the follow-up [2]. A previous study applying 4D flow MRI on CoA patients revealed abnormal flow patterns throughout the thoracic aorta as well as increased wall shear stress (WSS) [3]. The aim of this study was to analyze the evolution of aortic hemodynamics in adolescent patients with repaired CoA while aiming to detect specific characteristics of patients with coexistent bicuspid aortic valve (BAV).

Methods: 4D flow MRI of the thoracic aorta was performed in 28 CoA patients on two occasions: the mean age at first scan (t1) was 14.6±7.9 years, at second scan (t2) 19.0±8.3 years. All patients were examined on a 1.5T MRI scanner using prospective ECG and diaphragm navigator gating (Avanto, Siemens, Germany). The MR sequence consisted of a k-space segmented rf-spoiled 3D phase contrast gradient echo sequence with 3D velocity encoding (TE = 2.4-2.7ms, TR = 4.8-5.0ms, spatial resolution = (1.7-2.9)x(1.5-2.4)x(2.2-3.5) mm³, temporal resolution = 38.4-48.8ms, field of view = 210-270mm x 275-360mm, venc = 200cm/s) [4]. Wall shear stress (WSS), peak velocities and oscillatory shear index (OSI) were calculated at 9 defined levels of the thoracic aorta, and aortic diameters (ascending/descending aorta (AAo/DAo), arch, CoA) were measured (see figure). Blood flow visualization was performed by 3D pathlines colored according to local blood flow velocity (EnSight, CEI, Apex, USA). For statistical analysis, patients who underwent re-intervention (12/28) and BAV patients (7/28) were evaluated separately. Continuous variables were compared using a paired two-sided t-test. All tests used a significance level of 5%.

Results: Quantitative analysis showed an overall decrease in WSS (mean at t1: 0.48±0.18 N/m², t2: 0.33±0.13 N/m²; $p<0.005$) and an increase in OSI (t1: 7.16±4.05, t2: 9.98±4.76; $p<0.05$). The significant quantitative changes were even more pronounced in the group without re-intervention. AAo/DAo ratio decreased in all subgroups (t1: 1.44±0.29, t2: 1.34±0.18; $p=0.017$). We detected no significant changes in relative diameters of the aortic arch and at the CoA site. Peak velocities decreased significantly in the AAo (t1: 1.42±0.37m/s, t2: 1.27±0.37m/s; $p<0.001$). BAV patients revealed lower OSI and higher WSS in the AAo ($p>0.05$), and lower peak velocities in the aortic arch, the CoA site and the DAo ($p<0.05$). The total number of secondary flow patterns decreased, whereas additional localized helices in the AAo increased (see figure).

Discussion: Aortic hemodynamics normalized in patients with repaired CoA in the follow-up independently of re-intervention. BAV patients showed specific characteristics in quantitative parameters and should be assessed separately. 4D flow MRI permits the evaluation of qualitative and quantitative aortic changes in CoA patients over time which are not limited to the CoA site.

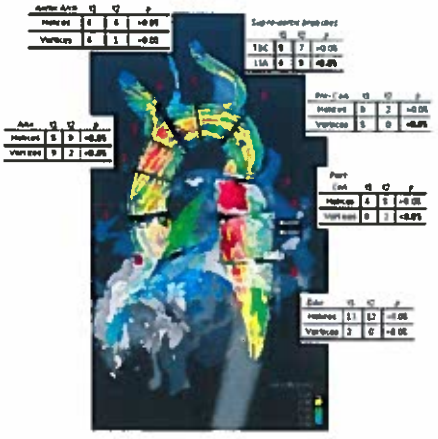

References:
1. Abbruzzese PA, Aidala E. J Cardiovasc Med 2007;8:123-128.
2. Brown ML, et al. J Am Coll Cardiol 2013;62:1020-1025.
3. Frydrychowicz A, et al. Invest. Radiol 2011;46:317-325.
4. Markl M, et al. J Magn Reson Imaging 2007;25:824-831.

Fig. Red numbers represent 9 defined levels for calculation of quantitative parameters. Tables show presence of secondary flow patterns for the non-intervention group (n=16).
TBC = brachiocephalic trunk, LSA = left subclavian artery.

Comprehensive MRI Evaluation of Potential Renal Donors – Addition of Renal Functional Assessment to MRA. Clinical Pilot Study Assessing Comparative Performance of 1.5 T DCE-MRI Perfusion versus Nuclear Medicine

MR Lopez-Gonzalez[1], SL Chang[2], G Roditi[2]
[1]Department of Clinical Physics and Bioengineering & [2]Department of Radiology, NHS Greater Glasgow and Clyde, Glasgow, Scotland, UK.

Purpose/Introduction
Dynamic Contrast Enhanced MRI (DCE-MRI) has been used in research for characterisation of renal function. Clinically relevant parameters can be quantified using tracer kinetic models to estimate blood flow, blood volume, mean transit times and glomerular filtration rate. Morphological assessment can accurately evaluate renal volume and mass. The aim of this study is to compare the accuracy of DCE-MRI derived renal function with Nuclear Medicine (NM) Renogram and Single Kidney Glomerular Filtration Rate (SK-GFR) estimation as gold standard, in a population of healthy living potential kidney donors undergoing contrast-enhanced MRA as part of surgical work-up.

Subjects and Methods
MRI datasets were obtained from potential donors undergoing renal MRA and all Nuclear Medicine tests. DCE-MRI was performed prior to MRA at 1.5T using a fast low angle shot (FLASH) sequence continuously sampling - 64 volumes obtained in 255s, TE/TR = 1/190ms; FoV = 420mm; matrix = 124x128; slice thickness = 8mm.
Kidney volumes were calculated, from a 3D T1w VIBE acquisition post-contrast, comparing the segmentation tools Osirix 3.8.1 versus Philips Extended MR workspace using a combination of threshold and manual segmentation techniques. Kidney function evaluated using PMI 0.4 software (1). A ROI-based two-compartment renal filtration model was applied for quantification of the four single kidney parameters of blood volume, blood transit time, tubular flow and tubular transit time. Two observers measured kidney volumes and MRI-derived GFR values independently and blind to the NM results.

Results
Inter-observer variations of the kidney volumes using the Philips workstation and Osirix were 7.9% and 11.9%, respectively. The DCE-MRI measurements were analysed with motion correction and single kidney derived of GFR and transformed in percentages to compare with the split divided function as reported in the NM Renograms. Preliminary comparisons show a positive covariance for the split divided renal function when using the standard volume of 200 cm^3 and when using the measured individual volumes.

Conclusions
Addition of DCE-MRI for functional assessment to a renal MRA protocol is feasible for comprehensive evaluation of possible kidney donors providing all the information required to plan potential donor nephrectomy in a single examination.

References
1. PMI: Platform for Research in Medical Imaging. S. Sourbron, A Biffar, M. Ingrisch, Y Fierens, R Luypaert. ESMRMB 2009.

Session 4

Cardiac Structure and Function

High Resolution Mapping of Myocardial Motion with Spiral SPIRIT Tissue Phase Mapping

J. Hennig, B. Jung, D. Föll, M .Menza

Introduction

MR Tissue Phase Mapping (TPM) is a powerful approach to assess left ventricular (LV) function. Cartesian acquisition-strategies with k-t-based parallel imaging acceleration allow the acquisition of a single slice within a breath-hold period with high temporal resolution of about 20 ms using a k-t undersampling factor of R=5 at 2-3 mm spatial resolution. The aim of this study was to develop an undersampled spiral imaging method in combination with SPIRIT -reconstruction to enable the acquisition of three-directional velocity encoded TPM in a single slice during breath-hold, while maintaining high temporal and spatial resolution.

Methods

Spiral trajectories with 8 Interleaves were designed and optimized to support a field of view (FOV) of 32 cm. Different types of spiral trajectories were implemented and compared. All contained a fully sampled SPIRIT calibration area around the k-space center (FOV 32cm, 1/8 radius). Outside the calibration area FOV was reduced to 16 cm and 10 cm for dual density (DD) spirals (2-fold, DD 2; 3-fold, DD 3). For variable density (VD) an iterative method was used to linearly decrease the FOV outside the calibration area proportional to the radius in k-space until the readout duration reaches half (VD 2) and one third (VD 3) of the fully sampled k-space. Measurements in 10 healthy volunteers (age 31±5 years) were performed on a 3TPrisma-system (Siemens).For spiral TPM measurements a basal slice was acquired during 16 heartbeats using three-directional velocity encoded black-blood prepared off-centre spiral gradient echo sequence with prospective ECG gating and water excitation in breath-hold. For comparison a Cartesian gradient echo sequence was used with navigator respiration control, water excitation and PEAK-GRAPPA with R=5 .Spiral images were iteratively reconstructed using conjugate gradients SPIRIT with a kernel size of 7x7.

Results

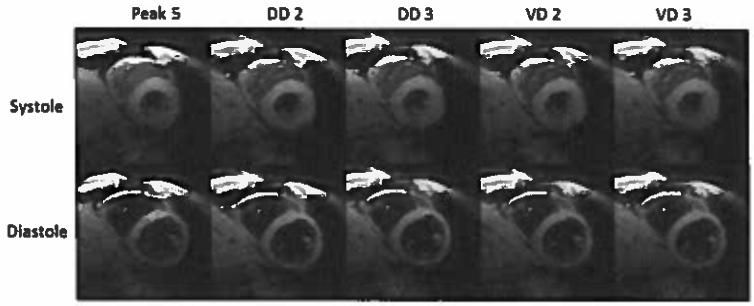

Spiral images for all trajectory designs exhibit excellent image quality (see Fig.). Despite longer spiral readout durations no significant signal voids caused by susceptibility artefacts can be observed. Undersampling artefacts are removed by SPIRIT reconstruction. Global velocity time courses of Vz and Vr agree well for all spirals and PEAK with no significant differences for global and segmental as well as systolic and diastolic Vz peak velocities. Systolic global and lateral segmental Vr peak velocities show significant differences between PEAK and all spirals, whereas no significant differences could be observed in diastole. All global and segmental TTP in systole and diastole for both velocities correlate well.

Discussion

Using spiral SPIRIT TPM with undersampling factors of 2 and 3 for DD and VD provide excellent image quality and agreement of peak velocities and TTP for Vz and Vr with k-t-accelerated Cartesian acquisition.

References

1. Menza M., et al. Proc. 24th Annual Meeting ISMRM, Singapore, 2016, p.3131
2. Bauer et al. J Magn Reson Imaging. 2013 38(5):1054-62.
3. Jung B et al. J Magn Reson Imaging. 2008 Nov;28(5):1226-32.
3. Lustig et al. Magn Reson Med. 2010 Aug; 64(2):457-71.

Title: diagnosis of chronic allograft vasculopathy using Semiquantitative stress perfusion CMR in heart transplant patients

Authors: Madeline Schwid, Hannah Recht, Amir Rahsepar, Kai Lin, Jeremy Collins, Michael Markl, Dan Lee, James Carr

Institution: Northwestern University, Department of Radiology

Background: Patients with heart transplant are susceptible to developing chronic allograft vasculopathy (CAV), the prevalence of which increases in frequency over time. Traditional methods for diagnosing CAV rely on invasive catheter based angiography and intravascular ultrasound (IVUS). Stress perfusion cardiac MRI (CMR) is frequently used to noninvasively diagnose ischemic heart disease and has also been used to assess CAV in heart transplant patients.

Purpose: To evaluate semiquantitative measures of ischemia using noninvasive stress perfusion CMR in the detection of CAV using invasive coronary angiography as the standard reference.

Methods: A cohort of 43 chronic heart transplant patients was studied using both stress CMR and coronary angiography. Stress CMR was performed in the standard manner using an IV injection of regadenoson and 0.2 mM/kg of a gadolinium based contrast agent. Based on the coronary angiogram, the patients were divided into groups of no disease (group 1), mild chronic allograft vasculopathy (CAV) (group 2), and moderate to severe CAV (group 3), based on the International Heart Lung Transplantation (IHLT) guidelines for diagnosis of CAV. The time between the angiogram and perfusion results varies from less than 6 months to just over 2 years, with an average of about 1 year between studies. The rest and stress perfusion images were analyzed by segment based on the AHA 16 segment model of the heart using dedicated myocardial perfusion software (Circle). The upslope was measured for each segment as well as for the blood pool on both stress and rest images and then an average upslope value was calculated for each patient. The myocardial perfusion reserve was calculated by divided the upslope values of rest and stress images. The semiquantitative results of the perfusion studies, both stress perfusion upslope values and myocardial perfusion reserve, were then correlated to the angiogram results on a global basis.

Results: There were 18 patients with no evidence of CAV on angiogram (group 1), 23 patients with mild CAV (group 2), and 2 patients with moderate to severe CAV (group 3). Both stress perfusion upslope and myocardial perfusion reserve tend to decrease with increasing disease severity. For the myocardial perfusion reserve, group 1 had an average of 1.89, group 2 had an average of 1.58, and group 3 had an average of 1.23. Using a t-test, there was no statistical difference between the group 1 and 2 for the myocardial perfusion reserve index (p=0.03), but there was a statistical difference between group 1 and 3 (p=0.0001), 2 and 3 (p=0.001), and when comparing patients with no evidence of disease versus patients with any evidence of disease (group 1 vs 2+3, p = 0.02). For the stress perfusion upslopes, group 1 had an average of 5.63, group 2 had an average of 4.76, and group 3 had an average of 1.92. There was no difference between the groups, with a p values from 0.06 for disease versus no disease (group 1 vs group 2 and 3).

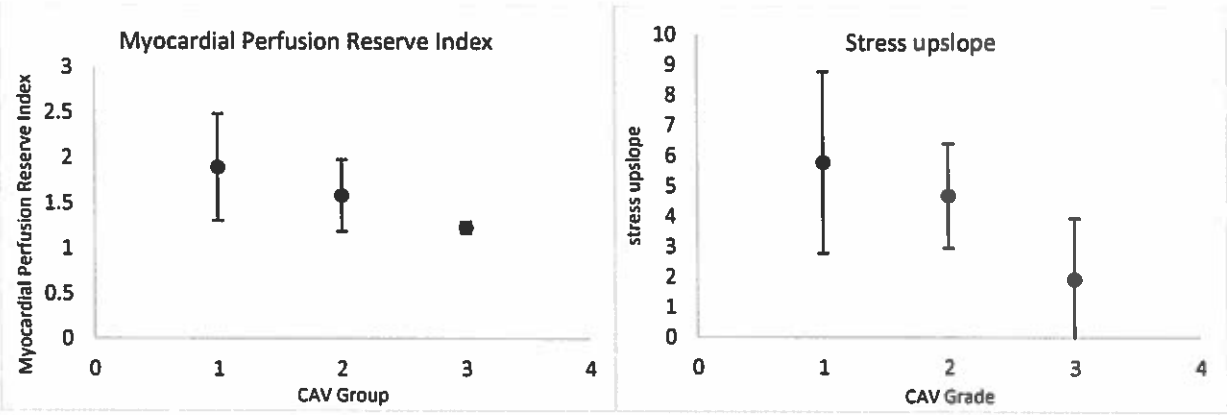

Conclusions: Semiquantitative parameters of upslope and myocardial perfusion reserve as measured from stress perfusion CMR can detect CAV in heart transplant patients. Stress perfusion CMR is a promising noninvasive tool for detecting CAV potentially obviating the need for regular invasive coronary angiography.

Low-Rank Tensor Imaging for Non-ECG Multidimensional Cardiovascular MRI

Anthony G. Christodoulou[1,2], Jaime Shaw[1,3], Behzad Sharif[1,4], and Debiao Li[1,3]
[1]Biomedical Imaging Research Institute, Cedars-Sinai Medical Center, Los Angeles, CA, USA;
[2]Cedars-Sinai Heart Institute, Cedars-Sinai Medical Center, Los Angeles, CA, USA; [3]Department of Bioengineering, UCLA, Los Angeles, CA, USA;
[4]Department of Biomedical Sciences, Cedars-Sinai Medical Center, Los Angeles, CA, USA

Purpose: Cardiovascular MRI suffers from the curse of dimensionality in its many applications, from angiography to myocardial perfusion to T_1 mapping. This results in dependence on inefficient "freezing" mechanisms to isolate different sources of image dynamics: ECG gating to freeze cardiac motion, breath-holding to freeze respiratory motion, steady-state imaging or limited acquisition windows to freeze image contrast, etc. Here we present a new framework for cardiovascular MRI—*low-rank tensor imaging*—that expands spatiotemporal low-rank imaging [1] to handle multiple time dimensions (i.e., multiple sources of image dynamics), yielding high-quality images from very sparsely sampled data. The method has many different capabilities, e.g. non-ECG, free-breathing, multi-contrast imaging. We demonstrate this framework on non-ECG T_1-mapped quantitative myocardial perfusion and non-ECG, free-breathing myocardial T_1 mapping.

Methods: We performed low-rank tensor imaging to exploit the correlation along each dimension of a multidimensional cardiovascular image $a(\mathbf{x}, t_c, t_r, \tau, t)$, which has time dimensions indexing cardiac phase t_c, respiratory phase t_r, sequence timing parameter τ (e.g., inversion time) and cardiac cycle t. Representing this image as a 5-way tensor $\mathcal{A}$ with elements $A_{ijk\ell m} = a(\mathbf{x}_i, t_{c,j}, t_{r,k}, \tau_\ell, t_m)$, the proposed method models $\mathcal{A}$ as low-rank, i.e., as the product of a small core tensor $\mathcal{C}$ and matrices $\mathbf{U_x}$, $\mathbf{U_c}$, $\mathbf{U_r}$, $\mathbf{U_\tau}$, and $\mathbf{U_t}$ containing basis functions for each dimension [2].

All data were acquired on a 3T Siemens Verio scanner using a continuous-acquisition SR-prepared (for myocardial perfusion) or IR-prepared (for native myocardial T_1 mapping) radial FLASH sequence. Odd-numbered readouts collected spokes in golden-angle increments (for determining $\mathbf{U_x}$); even-numbered readouts collected the 0° spoke (for determining $\mathcal{C}$ and the temporal bases). Data were collected for 30–45 s for myocardial perfusion and 1 min for native T_1 mapping.

The relaxation basis in $\mathbf{U_\tau}$ was pre-estimated from a dictionary of relaxation curves factoring in potential B_1 inhomogeneity and inefficient inversion. The core tensor $\mathcal{C}$ and the temporal bases in $\mathbf{U_c}$, $\mathbf{U_r}$, and $\mathbf{U_t}$ were jointly estimated via low-rank tensor completion [3] of the 0° spoke data constrained to the relaxation subspace described by $\mathbf{U_\tau}$. The remaining unknown, $\mathbf{U_x}$, was estimated by fitting the core tensor and temporal bases to the golden-angle data $\mathbf{d}$, according to $\mathbf{U_x} = \arg\min_{\mathbf{U_x}} \|\mathbf{d} - E\{\mathbf{U_x}\mathbf{C}_{(1)}(\mathbf{U_t} \otimes \mathbf{U_\tau} \otimes \mathbf{U_r} \otimes \mathbf{U_c})^T\}\|_2^2 + \mathrm{TV}(\mathbf{U_x})$, where $\mathrm{TV}(\cdot)$ is a spatial total variation functional, $\mathbf{C}_{(1)}$ is the mode-1 unfolding of $\mathcal{C}$, and E is the MRI encoding operator.

Results: Figure 1 shows first-pass perfusion images as well as baseline-corrected signal intensity curves and R_1 curves for the LV blood pool and septal myocardial segment at end-diastole. Signal intensity at a saturation time of 280 ms underestimates the arterial input function (AIF) due to a nonlinear response to contrast agent concentration; however, the R_1 curve has a linear response. For the myocardial T_1 mapping application, Figure 2 depicts three of the 345 IR-FLASH contrasts, a T_1 relaxation profile, and a T_1 map (all displayed for end-diastole), as well as a T_1 profile over the full cardiac cycle. This demonstrates the ability to retroactively choose the inversion time and to map T_1 at any cardiac phase. Figure 3 depicts voxelwise Bland-Altman plots of myocardial T_1 and LV blood pool T_1* (less sensitive to inflow), comparing the proposed IR-FLASH-based method, MOLLI [4], and ShMOLLI [5]. Of the three pairings, the proposed method vs. MOLLI shows the smallest mean difference and closest myocardial limits of agreement; ShMOLLI vs. MOLLI shows the closest blood pool limits of agreement. Only the proposed method was performed without using breath holding or ECG.

Conclusion: We have presented a novel framework exploiting the low-rank tensor structure of multidimensional cardiac images, demonstrating its use for two challenging applications. The framework enhances the practical utility of T_1 mapping—using efficient, continual acquisition and advanced reconstruction techniques to overcome the practical limitations of ECG and breath-holds—and demonstrates time-resolved mapping during first-pass perfusion, which may allow direct quantification of tissue contrast agent concentration with a single bolus. Future work includes an extension to 3D (expected to improve blood pool inflow properties), quantitative evaluation and validation of these applications, and exploration of other high-dimensional applications such as non-ECG, free-breathing, multi-contrast angiography.

References: [1] Liang ISBI 2007
[2] Christodoulou ISMRM 2016 [3] Liu TPAMI 2013
[4] Messroghli MRM 2004 [5] Piechnik JCMR 2010

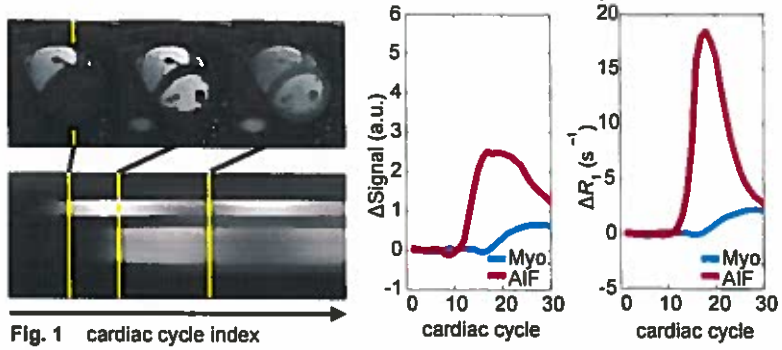

Fig. 1 cardiac cycle index

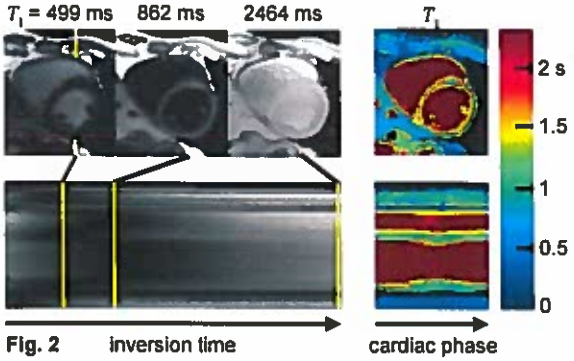

Fig. 2 inversion time cardiac phase

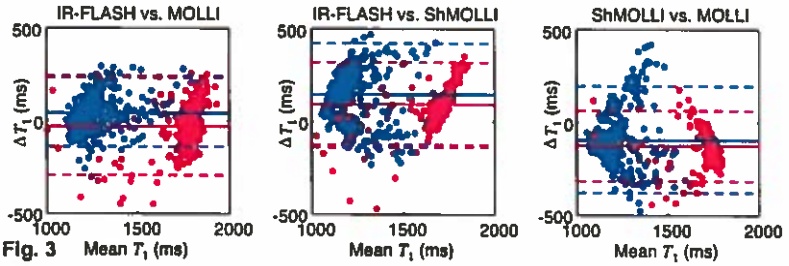

Fig. 3

T1-refBlochi: High resolution 3D cardiac T1 mapping methods based on 3D late gadolinium enhancement, Bloch equations, and a reference T1.

Dana C. Peters Albert J. Sinusas, Steffen Huber, Hamid Mojibian, Chenxi Hu,
Yale School of Medicine, New Haven CT, USA

Introduction: Our goal was to investigate the accuracy of the method we call T1-refBlochi, for high resolution 3D T1-mapping. The method uses a single 3D late gadolinium enhancement (LGE) volume to generate a T1-estimate, based on i) the Bloch equations, and on ii) an a priori reference T1 and its mean signal in the image. This could enable high resolution T1-mapping for applications such as left atrial fibrosis assessment.

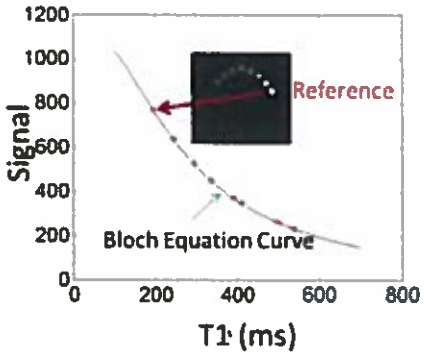

Figure 1: The refBlochi method uses Bloch equations to model the signal vs. T1 curve. A single reference T1 and its corresponding signal in the 3D LGE image is used to scale this curve, thereby mapping each signal in the 3D LGE image to a T1 value, assuming pure T1-weighting.

Methods: The T1-refBlochi method (Figure 1) uses the exact Bloch equations to model for the signal vs. T1 prior to the 1st alpha pulse, in an LGE sequence, at steady state, using the scan parameters, TR, θ, views per segment, (vps), inversion time (TI) and RR interval. The signal measured in the image from the known reference T1 (e.g. blood—measured on a breathold scan) than rescales the relationship, and from this curve, all T1s in the image are estimated. We hypothesize that the signal is mainly T1-weighted, and any effects of coil-sensitivity, T2* and proton density weighted are small or can be minimized. Phantom studies, with known T1s ranging from 200-560ms, and multiple scan protocols were performed. The basic LGE protocol parameters were: TR/TE/θ/TI/RR/vps=3.8ms/2ms/15°/TI=300ms/800ms/37. In vivo imaging in 8 pigs (4 with infarction) was performed, comparing refBlochi with T1-mapping using multiple TIs. Using multiple TI approach, the non-T1 related weightings were also mapped, to analyze our hypothesis that coil-sensitivity, T2* and proton density are minor effects. The T1s and non T1 weightings were measured in identical ROIs (in myocardium, blood, and scar) for both multi-TI mapping and refBlochi.

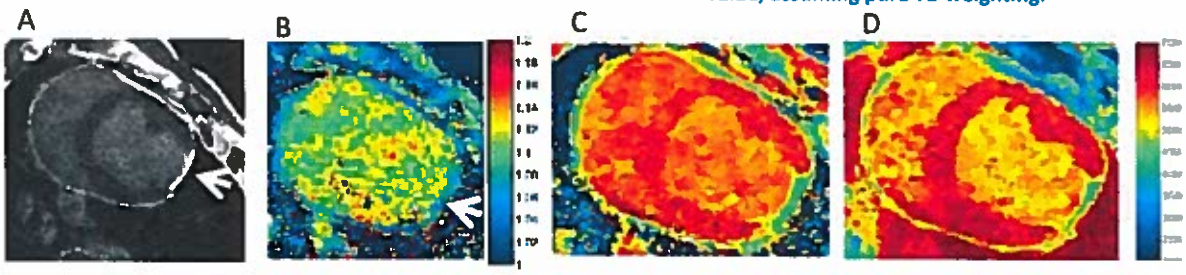

Figure 2: A) The 3D LGE image, showing an infarction (arrow). B) The combined T2* and PD weighting map. The mean ratio of blood to myocardium was 1.03±0.02, blood to scar 0.94±0.01. C) The T1 map using multi-TIs. D) T1-mapping with refBlochi. Overall T1 agreement was good compared to multi-TI methods, with bias ±2SDs of -10 ±42ms.

Results: In phantoms, over all protocols and T1 ranges, the mean bias and standard deviation was -3ms ± 11ms (refBlochi), and the correlation coefficient was R^2=0.99. The combined weightings of T2*, proton density and coil sensitivity generated maps with a mean scar to blood ratio of 0.94±0.01 and for myocardium/blood: 1.03±0.02 (p=0.02) (Figure 2B). T1-maps with refBlochi agreed well with multiple TI T1mapping (Figure 2C, D). Comparing T1s in matched ROIs in myocardium and scar, the quantitative in vivo agreement was good (R^2=0.94, slope =0.99) between T1s measured by T1-refBlochi and the multi-TI method (bias ±2Ds of -10 ±42ms).

Conclusions: In conclusion, we present a method for high resolution T1-mapping method that exhibits accuracy and limitations. Some steps to overcome these limitations include shorter TEs and reduction of coil sensitivity variations. Even with its limitations, refBlochi provides the possibility of high resolution T1-mapping in feasible scan times.

K-t Accelerated 3D CINE bSSFP for improved 4D Flow MRI Visualization

Kelly Jarvis MS[1,2], Bradley Allen MD[1], Can Wu PhD[1], Susanne Schnell PhD, Alex J. Barker PhD[1], Shivraman Giri PhD[3], Marcos Botelho MD[1], James Carr MD[1], Jeremy Collins MD[1], Michael Markl PhD[1,2]

Dept. of [1]Radiology, [2]Biomedical Engineering, Northwestern University, Chicago, USA. [3]Siemens Healthcare, Chicago, IL, USA

Purpose: 4D flow MRI magnitude images are shown during blood flow visualization to give dynamic reference to the surrounding anatomy. However, this approach is limited by the low blood-tissue contrast of the magnitude images, acquired with 3D RF-spoiled gradient echo imaging. Fast 3D time-resolved balanced steady state free precession (*k-t* 3D CINE bSSFP) offers a promising alternative (1-4) providing anatomical images with improved blood-tissue contrast. The aim here is to use co-registered *k-t* 3D CINE bSSFP with superior contrast to improve anatomic orientation and joint visualization of anatomy, cardiovascular function (e.g. vessel motion), and flow.

Methods: Non-contrast free-breathing *k-t* 3D CINE bSSFP and 4D flow MRI were acquired in 10 controls (6 females, age = 44 +/- 18 [21-68] years) with the same spatial resolution (2.3-2.5 x 2.3-2.5 x 2.4 mm^3) and volumetric coverage (FOV = 360-400 x 270-300 mm^2, slab thickness = 72 mm). Three averages were acquired for 3D CINE bSSFP to mitigate breathing effects (outer mode averaging, TE = 1.6 ms, TR = 3.2 ms, temp res = 38.4 ms, flip angle = 47-90 deg, R = 5, average scan time = 2.6 min), and interpolated along the temporal domain for integration with 4D flow MRI (TE = 2.4-2.5 ms, TR = 4.8-4.9 ms, temp res = 38.4-39.2 ms, flip angle = 7°, R = 2, average scan time = 11 min). A phase contrast MR angiogram was calculated from the 4D flow MRI data and used to segment a mask of the aorta and emit pathlines within the mask for flow visualization. Analysis planes were placed by the left ventricular outflow tract and aortic arch for dynamic viewing of structures during one cardiac cycle. Two videos were prepared for each subject (Figure 1a-b). A radiologist assessed the images for overall image quality, presence of noise, severity of artifact and joint visualization of anatomy and flow. Areas of the sinuses, aorta and heart were evaluated for vessel wall depiction and blood signal homogeneity.

Results: See table 1. We found significantly improved overall image quality, presence of noise and joint visualization of anatomy and flow with *k-t* 3D CINE bSSFP compared to the 4D flow MRI magnitude images. Vessel wall depiction was significantly improved for all regions of interest. Blood signal homogeneity in the mid-ascending aorta and distal arch was also significantly improved.

Discussion: Acquiring *k-t* 3D CINE bSSFP together with 4D flow MRI provides improved anatomical images compared to 4D flow magnitude images and an overall better dynamic depiction of the surrounding cardiovascular anatomy for flow visualization. Future work will focus on the combination of *k-t* 3D CINE bSSFP with 4D flow MRI for improving vessel segmentation.

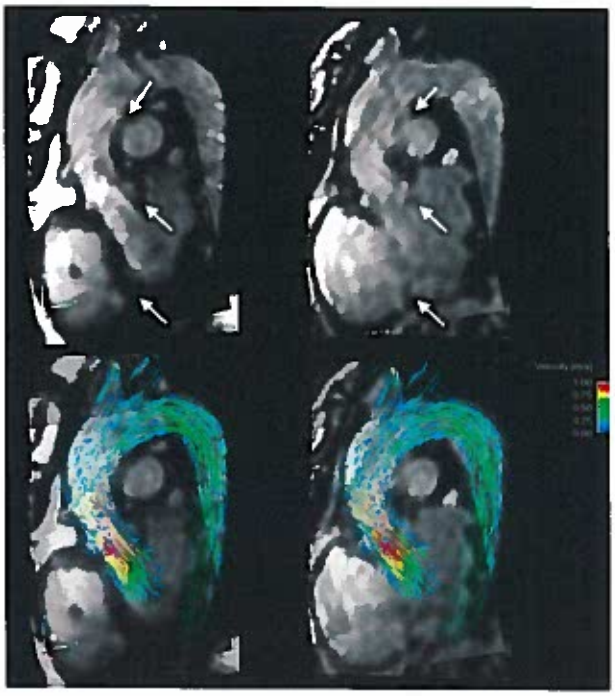

Fig. 1: Systolic time-point from two movies (top: anatomy only, bottom: anatomy & 3D pathline visualization) depicting aorta, surrounding structures, and flow. Left: *k-t* 3D CINE bSSFP. Right: 4D flow MRI magnitude. Arrows indicate locations where the superior contrast of bSSFP has improved visualization of the blood-tissue interface.

	4D flow MRI magnitude	*k-t* 3D CINE bSSFP MRI	Wilcoxon Signed-Rank test P value
Overall image quality scale: 1 (poor) to 5 (excellent)	2.7±0.5 [2-3]	4.0±0.5 [3-5]	0.004*
Presence of noise scale: 1 (non-diagnostic secondary noise) to 5 (little to no appreciable noise)	2.6±0.5 [2-3]	4.2±0.4 [4-5]	0.005*
Severity of artifact scale: 1 (non-diagnostic secondary to artifact) to 5 (no appreciable artifact)	3.4±0.7 [2-4]	3.6±0.5 [3-4]	0.424
Joint visualization of anatomy & flow scale: 1 (poor) to 5 (excellent)	3.7±0.7[3-5]	4.6±0.5[4-5]	0.018*
Vessel wall depiction scale: 1 (poor) to 5 (excellent)			
Sinuses of Valsalva	2.9±0.7[2-4]	3.6±0.7 [3-5]	0.048*
Mid-ascending aorta	2.3±0.7 [1-3]	4.0±0.9 [2-5]	0.008*
Distal arch	3.5±0.8 [2-5]	4.6±0.8 [3-5]	0.033*
Left Ventricle	1.5±0.7 [1-3]	3.9±0.7 [3-5]	0.005*
Blood signal homogeneity scale: 1 (poor) to 5 (excellent)			
Sinuses of Valsalva	2.5±0.8 [1-3]	3.4±0.5 [3-4]	0.057
Mid-ascending aorta	2.8±0.4 [2-3]	3.7±0.7 [3-5]	0.031*
Distal arch	2.8±0.8 [2-4]	3.4±0.5 [3-4]	0.048*
Left ventricle	2.3±0.8 [1-3]	2.9±0.7 [2-4]	0.141

Table 1: Results for visual assessment. *p<0.05

References: 1. Scheffler K, Lehnhardt S. Eur Radiol 2003;13:2409-2418. 2. Barkhausen J, et al. Radiology 2001;219:264-269. 3. Jung BA, et al. Magn Reson Med 2002;48:921-925. 4. Markl M, Leupold J. J Magn Reson Imaging 2012;35:1274-1289.

Funding Sources: AHA Predoctoral Fellowship 14PRE18620016

High Precision Free-Breathing SASHA T_1 Mapping Using High-Contrast Image Registration

Kelvin Chow, Yang Yang, Michael Salerno
Departments of Medicine and Biomedical Engineering, University of Virginia

Purpose: T_1 mapping has been used to assess diffuse myocardial fibrosis in a variety of cardiac diseases, but increased accuracy and precision are needed to confidently measure subtle changes in sub-clinical diseases. The SASHA technique (1) is accurate and robust to systematic confounders, but it has low precision compared to MOLLI (2). Motion-corrected free-breathing acquisitions (3) can improve precision, however robust motion correction is challenging for SASHA images due to poor blood-tissue contrast. We present a novel approach for generating co-registered high-contrast images that improve the robustness of image registration and enable free-breathing SASHA T_1 mapping.

Methods: Variable flip angle (VFA) SASHA (4) images have poor blood-tissue contrast because the center of k-space is acquired early on in the bSSFP image readouts. Additional low frequency k-space lines acquired immediately following the primary SASHA-VFA image can be used to generate a secondary image with high contrast (HC) due to intrinsic bSSFP T_2/T_1 weighting. High-frequency k-space data can be shared from the primary image to reduce the acquisition time of the HC image (Fig. 1). As the HC images are intrinsically co-registered with the primary images, registration performed on the HC can be used to directly motion correct the primary images used to calculate T_1 maps.

SASHA sequence parameters included: 120° maximum flip angle, 360×270 mm FOV, 256×150 matrix, 78% phase resolution, 7/8ths partial Fourier, 1.19/2.76 ms TE/TR, and GRAPPA R=2 acceleration, with 65 phase encodes for the primary image. High-contrast acquisitions consisted of 15 low-frequency lines at R=3 and were reconstructed using GRAPPA prior to combination with primary k-space data. POCS reconstruction was used on the combined primary and high-contrast k-space data.

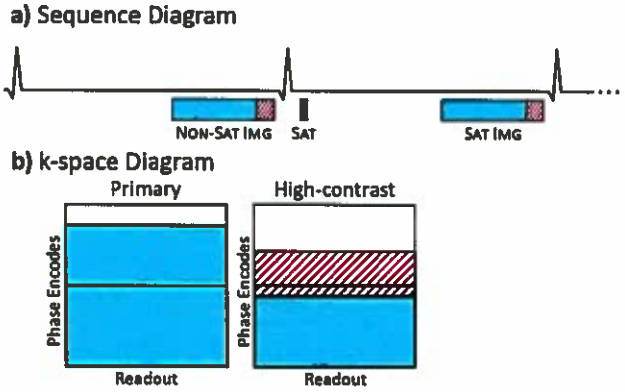

Fig. 1. Sequence and k-space diagram for SASHA-HC

10 healthy volunteers (6 male, 33±9 yrs) were imaged on a Siemens 1.5T Avanto scanner with written informed consent. Breath-hold T1 data were acquired in a short-axis slice using 5(3)3 MOLLI and SASHA-VFA. The MOLLI sequence used 1.04/2.68 ms TE/TR and other parameters matched to SASHA. Free-breathing SASHA-VFA data was acquired with 10 non-saturated images separated by >5 seconds and 50 saturation recovery images for a total imaging time of 108±7 seconds. Free-breathing images where the average displacement of the heart was within a ±4 mm window were automatically selected and aligned with a non-rigid image registration algorithm (5) using information from difference and primary images. Conventional registration was also performed using the primary images only. The mean and standard deviation of myocardial T_1 values were calculated for each T_1 map.

Results: T_1 maps from one subject are shown in Fig. 2. Free-breathing acquisitions have higher precision, but misregistration of the septum with normal registration results in appreciable blurring. The myocardial T_1 standard deviation for free-breathing SASHA with HC registration (36±3 ms) and normal registration (46±7 ms) were lower than breath-hold MOLLI (55±6 ms) and breath-hold SASHA (69±6 ms). Mean myocardial T_1 values were not different between free-breathing SASHA-HC (1156±28 ms) and breath-hold SASHA (1148±22 ms, $p>0.05$), but elevated T_1 values with normal registration of free-breathing SASHA (1167±28 ms, $p<0.05$) are consistent with blood pool contamination.

Fig. 2. T1 maps using MOLLI and SASHA in a healthy volunteer

Conclusions: High-contrast images with improved blood-tissue contrast can be acquired in ~40 ms using keyhole sharing, enabling robust free-breathing SASHA T_1 mapping. Myocardial SASHA-VFA T_1 values were similar between free-breathing with high-contrast registration and standard breath-hold acquisitions, but with a 48% reduction in standard deviation. Free-breathing SASHA-HC is an accurate T_1 mapping technique with lower 34% variability than the reference MOLLI sequence in a <2 minute acquisition.

References:
1. Chow K *et al.* MRM 2014;71:2082-2095
2. Messroghli DR *et al.* MRM 2004;52:141-146.
3. Kellman P *et al.* JCMR 2015;17:3.
4. Chow K *et al.* JCMR 2014;16(Suppl 1):M9.
5. Avants BB *et al.* NeuroImage 2011;54:2033-2044.

REPAIR: improving late gadolinium enhancement images under arrhythmia by RR dependent pre-saturation

Chenxi Hu, Steffen Huber, Maolin Qiu, Gigi Galiana, Hamid Mojibian, Lauren Baldassarre, Dana C. Peters, Yale School of Medicine, Yale University

Purpose: High resolution 3D late gadolinium enhancement (LGE) is commonly used to detect myocardial scar in the left atrium in atrial fibrillation (AF) patients[1]. However, arrhythmia impairs the image quality due to the variable time between inversion pulses (based on variation of RR intervals), which generates ghosts in the phase-encoding direction, as well as motion-blurring. Acquiring data every second RR—which reduces ghosts-- is unrealistic for 3D navigated LGE due to the increased scan time. Previous solutions explored using 90° saturation before the inversion[2], or changing TI dynamically to compensate for the RR variation[3]. In this work, we propose to insert a saturation pulse with a dynamic flip angle before the inversion pulse to improve the image quality. The saturation pulse, referred to as Regrowth Equalization Pulse for Arrhythmias in Inversion Recovery (**REPAIR**), changes its flip angle dynamically based on the previous RR interval.

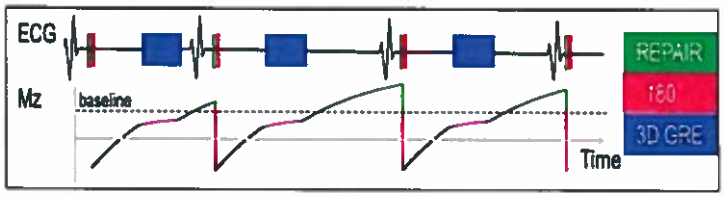

Figure 1: Illustration of the REPAIR LGE sequence and Mz evolution. The REPAIR pulses tip down Mz to the baseline by dynamic flip angles in response to the changing RR intervals.

Methods: Figure 1 illustrates the REPAIR LGE sequence and corresponding longitudinal signal. A minimal RR interval is specified for each subject. A longer RR interval causes an increased signal (Mz) compared to the minimal RR. A saturation pulse is applied before the inversion to tip down Mz to the signal level corresponding to the minimal RR (baseline) (for a target T1). Since the RR interval always changes, the saturation flip angle is dynamically changed. After each ECG trigger, the sequence obtains the length of the previous RR interval to calculate the saturation flip angle that saturates Mz to the baseline. The calculation is sufficiently simple to be performed in real time. The saturation (REPAIR) pulse is then applied, followed by the 180° pulse. We derived an analytical equation for calculation of the REPAIR flip angle θ_l for the lth RR based on Bloch equation:

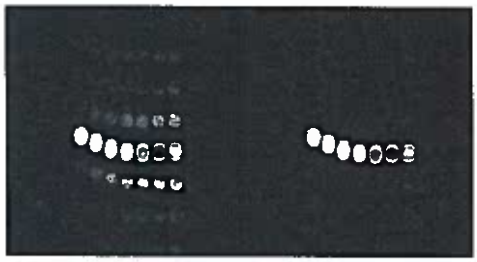

Figure 3: Seven bottles with T1s ranging from 200-600ms, imaged during programmed arrhythmia, with LGE (left) and with LGE REPAIR (equally scaled for display).

$$\cos(\theta_l) = \frac{1-exp\left(\frac{RR_{min}-N\cdot TR-TI}{T_1}\right)(1-M_{z_{ss}})}{1-\exp\left(\frac{RR_{l-1}-N\cdot TR-TI}{T_1}\right)(1-M_{z_{ss}})}, \text{ where } M_{z_{ss}} = \frac{1-\cos(\alpha)}{1-\cos(\alpha)\exp\left(-\frac{TR}{T_1}\right)}\left(1-\left(\cos(\alpha)\exp\left(-\frac{TR}{T_1}\right)\right)^N\right),$$

N is views per segment (VPS), TR the gradient-echo repetition time, and α the gradient-echo flip angle. T_1 can be freely chosen (here 350 ms, representative of blood T1 post-contrast).The REPAIR LGE was studied in phantoms and AF patients on a 1.5 T Siemens scanner. The phantom study used following parameters: TR/FA/VPS/BW/RRmin/RRmax = 8.06ms/10°/33/200Hz/Px/400ms /1900ms. An AF patient with an average heart rate of 60 bpm and mild arrhythmia was imaged with both standard and REPAIR 3D LGE after providing informed consent. The parameters for the patient study are TR/FA/VPS/BW = 5.12ms/15°/27/399Hz/Px.

Results: Figure 3 shows that in phantoms, REPAIR dramatically reduces the amount of ghosting artifacts compared to standard LGE while maintaining a similar contrast. Signal-to-ghost ratio, defined by the ratio of the maximal signal to the maximal ghost in the image, is 8.9 and 26.5 for the standard LGE and REPAIR, respectively. Figure 4 demonstrates the reduced ghosting artifact and blurring with REPAIR LGE.

Figure 4: The standard LGE (left) and REPAIR LGE (right) images. Reduction of ghosts and blurring are indicated by the arrows.

Conclusions: The phantom and patient data have demonstrated that LGE with REPAIR is more insensitive to arrhythmia and leads to better image quality, enabling assessment of left atrial scar in patients with ongoing arrhythmia.

References: 1. Marrouche NF. et al., JAMA 2014; 2. Weingartner S. et al., MRM 2014; 3. Keegan J. et al., MRM 2015

Session 5

Neuro MRA

Flow quantification in cerebral aneurysms: CFD, 4D Flow MRI, and DSA

A. Vali[1], B. Dickerhoff[1], R. Sacho[1], R. Prost[2], S. Schnell[3], M. Markl[3] and V.L. Rayz[1]

[1]Neurosurgery, Medical College of Wisconsin, [2]Radiology, Medical College of Wisconsin,
[3]Radiology, Northwestern University Feinberg School of Medicine.

Purpose: Quantitative characteristics of cerebral blood flow can provide valuable information for diagnostic and treatment of cerebral aneurysms. The flow velocities can be measured in vivo with time-resolved 3D PC-MRI (4D Flow MRI) or computed using CFD models based on MRA/MRI data. In clinical practice, however, clinicians rely mostly on x-ray angiography/digital subtraction angiography (DSA) to determine the flow characteristics in aneurysmal vasculature. In this study, we compare these different methods of flow analysis in order to determine their relative advantages and limitations in assessing the actual flow velocities and residence time. An accurate estimation of the filling and wash-out patterns can help predict intra-aneurysmal regions prone to thrombus deposition. The flow analysis can be particularly helpful in treatment of complex cerebral aneurysms, which cannot be coiled or clipped. In such cases, flow-altering options such as clipping of some of the distal and/or proximal vessels or deploying flow diverters may be considered in order to reduce the flow through the aneurysmal vessel. A thorough understating of the patient-specific flow features is required prior to these procedures in order to mitigate the risk of postoperative thrombosis of vital arteries distal to aneurysm or branching off the aneurysm pouch. While each of the aforementioned flow analysis techniques has its own limitations, their combination may overcome these limitations and could serve as a predictive tool for making clinical decisions.

Methods: A comprehensive flow study was conducted on two patients diagnosed with internal carotid artery aneurysm. In vivo flow data was obtained from 4D Flow MRI and DSA. For the computational model, patient-specific vascular geometries were generated from time-of-flight MR angiography (TOF-MRA) data. Computational modeling of the flow was achieved by solving the transient Navier-Stokes equations using a finite-volume solver and patient-specific boundary conditions obtained from 4D flow MRI. In order to estimate the flow residence time an injection of virtual contrast agent was simulated by solving the advection-diffusion equations. The computational model was compared against in vivo flow measurements from PC-MRI and DSA. Furthermore, a 3-D printed model of the aneurysmal ICA was generated for one of the patients in order to conduct in vitro 4D Flow MRI measurements. CFD and 4D Flow MRI data were interpolated on the same grid to obtain quantitative comparison of the velocities.

Results: The results obtained from two CFD models are compared to in vivo 4D Flow MRI data in Fig. 1. The initial model (a) overestimates the flow velocities, indicating inadequate segmentation of the TOF MRA data. The corrected model (b) shows substantially better agreement between the CFD and PC-MRI velocities. Comparison of the virtual contrast filling and wash-out patterns obtained from the computational model and in vivo DSA is shown in Fig. 2 for one of the patients. As shown in Fig. 2 there is a good agreement between the actual contrast injection images and the simulated tracer advection. The results show that 4D Flow MRI data can verify and improve numerical models by providing patient-specific boundary conditions. However, the MR-based CFD solution provides much better temporal and spatial resolution required for accurate estimation of the relevant flow variables, which cannot be measured directly, such as wall shear stress, flow residence time, and pressure distribution. In addition, it can be used to assess the changes of flow for alternative surgical options.

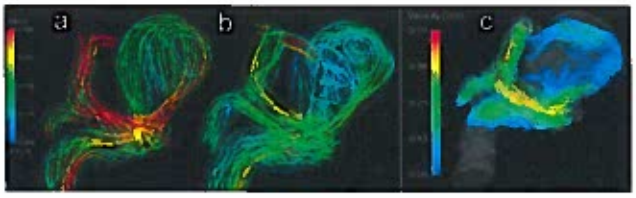

Fig. 1 Flow streamlines (a) and (b) computed from CFD simulation and (c) measured with 4D Flow MRI

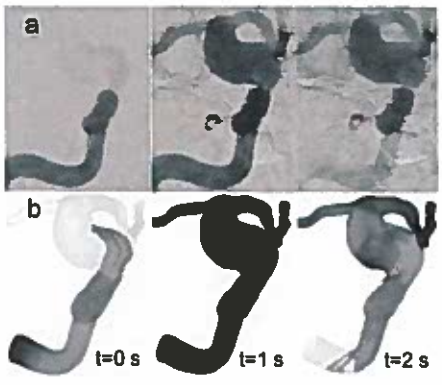

Fig. 2 Filling and wash-out patterns of an ICA aneurysem with the contrast agent (a) DSA image (b) CFD model

Conclusion: MR-based CFD modeling and in vivo flow measurements such as 4D Flow MRI and DSA can provide crucial information on patient-specific flow fields in aneurysmal blood vessels. The results indicate that 4D Flow MRI can be used to improve the accuracy of CFD models, while image-based CFD can determine important flow-derived variables such as flow residence time. This information, available prior to surgery, may help improve the outcome of surgical procedures.

Super-Resolution Quiescent-Interval Slice-Selective Magnetic Resonance Angiography of the Intracranial Circulation

Ioannis Koktzoglou[1,2], Marcos P.F. Botelho[1,3], Shivraman Giri[4], Robert R. Edelman[1,3]

[1]Radiology, NorthShore University HealthSystem, Evanston, IL, [2]University of Chicago Pritzker School of Medicine, Chicago, IL, [3]Northwestern University Feinberg School of Medicine, Chicago, IL, [4]Siemens Healthineers, Chicago, IL

Purpose: Quiescent interval slice-selective (QISS) magnetic resonance angiography (MRA) is a multi-slice 2D technique that can be used to evaluate the peripheral, renal, carotid and coronary arteries[1-3]. However, a drawback of 2D MRI methods such as QISS is limited slice resolution due to practical constraints of gradient slew rates, signal to noise ratio and artifacts from out-of-slice spins. Typical slice thickness used with QISS MRA range from 2-3 mm. Well-established in the signal processing literature, "super-resolution" is an approach for creating a higher resolution image from a series of overlapping and offset lower resolution images[4]. We hypothesized that super-resolution reconstruction could be used to improve the slice resolution of QISS MRA, and sought to apply this strategy for imaging the intracranial circulation.

Methods: This study was IRB approved and used informed consent. QISS MRA was used to image the intracranial arteries on 1.5T and 3T MR systems (MAGNETOM Avanto and Verio, Siemens Healthcare). To facilitate super-resolution reconstruction, QISS slices were acquired with either 50% or 67% overlap. Super-resolution reconstruction was done using the Irani-Peleg algorithm[5]. Limited comparisons were made with 3D time-of-flight (TOF) MRA.

Results: The figure below shows the impact of super-resolution as applied to QISS MRA of the intracranial circulation, as well as a comparison with 3D TOF MRA. With super-resolution reconstruction, there was visible improvement in arterial detail in the slice direction (blue arrow, panel a). Intracranial QISS MRA demonstrated similar to more intracranial arteries than 3D TOF MRA, with an improved degree of background signal suppression (Figure, panels b & c).

Discussion: Super-resolution reconstruction is a promising method to improve the reconstructed slice resolution of QISS MRA of the intracranial circulation. Preliminary results suggest that it can be used to improve arterial detail without the signal-to-noise ratio penalty of directly acquiring thin-slice images. Although the present study focused on the intracranial circulation, we anticipate that super-resolution reconstruction can be applied to QISS MRA of other vascular territories, including the carotid, renal and coronary arteries.

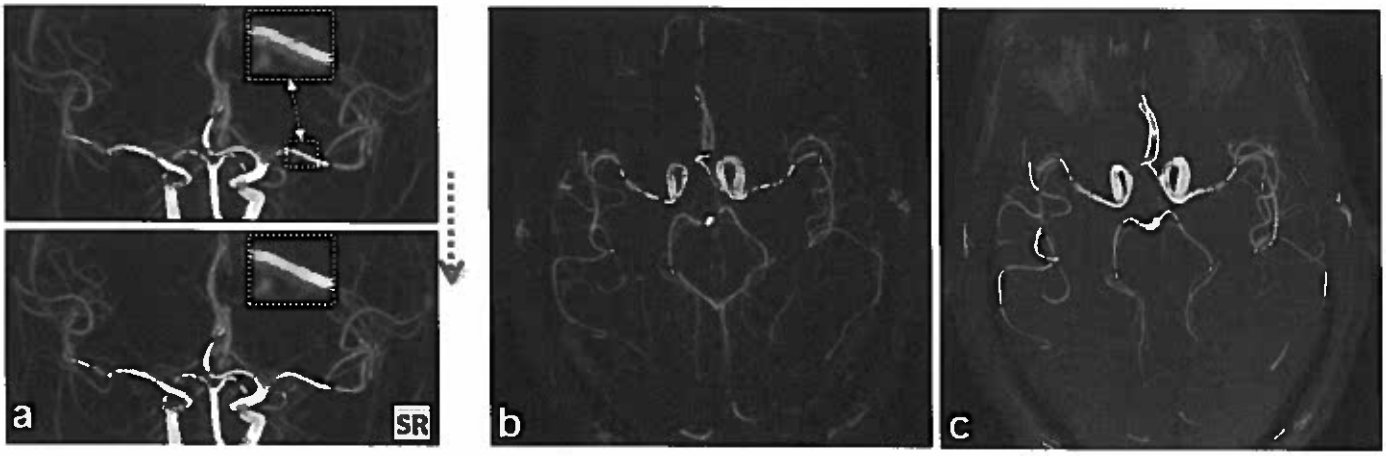

Figure. *Super-resolution intracranial QISS MRA.* ***(a)*** *Impact of super-resolution (SR) compared with standard reconstruction in QISS MRA in the slice direction (blue arrow) at 3T. Axial maximum intensity projections of the intracranial arteries obtained at 1.5T with* ***(b)*** *super-resolution QISS MRA and* ***(c)*** *3D TOF MRA.*

References: **1.** Edelman RR et al. Magn Reson Med. 2010;63:951-8. **2.** Koktzoglou I et al. Magn Reson Med. 2016;75:2072-7. **3.** Edelman RR et al. J Cardiovasc Magn Reson. 2015;17:101. **4.** Park SC et al. Signal Processing Magazine, IEEE. 2003;20:21-36. **5.** Irani M and Peleg S. CVGIP: Graphical models and image processing, 1991;53:231-9.

Intracranial venous blood flow and pulsatility in Alzheimer's disease with 4D flow MRI

Leonardo A. Rivera[1], Patrick Turski[1,3], Kevin M Johnson[1], Sterling C. Johnson[2], Oliver Wieben[1,3] and Tilman Schubert[3]
[1]Medical Physics, [2]Medicine, [3]Radiology, University of Wisconsin-Madison, Madison, WI, United States

Purpose: It has been shown that arterial pulsatility is increased in AD [1]; however, less information is available about changes in venous flow and venous pulsatility in individuals with AD [2]. In this study, using 4D flow MRI, we investigated intra-cranial flow features; particularly mean flow, pulsatility index (PI), PI ratios and transit time of the pulse wave from arteries to veins in patients with AD, mild cognitive impairment (MCI), healthy age matched controls and middle-aged with parental history of sporadic AD (MAPHSA).

Methods: *Subjects*: The study population consisted of 104 subjects: 26 AD patients (age 57-91y, mean=71y, 11 F), 26 MCI patients (age 52-87y, mean=73y, 13 F), 26 normal old (age 66-85y, mean=73y, 12 F) and 26 MAPHSA (age 45-64y, mean=57y, 22 F). With IRB approval and HIPAA compliance, informed consent was obtained for all study subjects. *MRI:* Volumetric, time-resolved PC MRI data with 3-directional velocity encoding were acquired on a 3T clinical MRI system (MR750, GE Healthcare,) with a 3D radially undersampled sequence, PC VIPR [3] with the following imaging parameters: V_{enc} = 80 cm/s, imaging volume = 22x22x10 cm^3, (0.7 mm)^3 acquired isotropic spatial resolution, TR/TE=7.4/2.7ms, scan time ~ 7 min, retrospective cardiac gating into 20 cardiac phases with temporal interpolation [4]. *Flow analysis:* Automatic vessel segmentation and flow quantification was performed in a customized post-processing tool (MATLAB, Mathworks, Natick, MA) [5] from time maximum intensity projection (tMIP) dynamic PC MRAs reconstructed from the 4D flow data. The complete vascular tree was extracted using a centerline process, recording coordinates and labels for every branch. A centerline guided flow tracking algorithm was used to visualize and select the venous segments for further analysis. Flow rates were calculated for every selected branch by averaging flow data obtained in local cross-sectional cut-planes automatically placed in every centerline point perpendicular to the axial direction of the vessel. For this purpose 4 venous segments were selected (Fig. 1) (d, e, f): posteroinferior portion of the Superior Sagittal Sinus (SSS), middle segment of the Straight Sinus (STS), and the Transverse Sinus (TS)(left and right) segment just before the Sigmoid Sinus. Additionally the internal carotids and middle cerebral arteries were also segmented. Mean flow, PI, transit time of the pulsatile flow from MCA to SSS, MCA/ICA and SSS/ICA PI ratios, were calculated and groups were compared with ANOVA followed by post hoc tests.

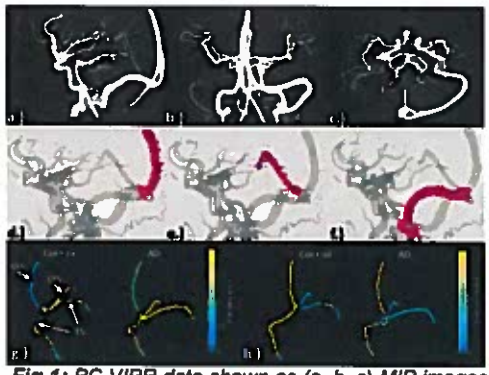

Fig 1: PC VIPR data shown as (a, b, c) MIP images of the PC angiogram and the segmented 3D vessels with centerline points labels for the d.) superior sagittal sinus, e.) Straight sinus and f.) transverse sinus extracted from the PC VIPR data. g.) Pulsatility index and h.) mean blood flow (mL/s) throughout the major venous segments shown as color maps for one aged matched control and one AD subject.

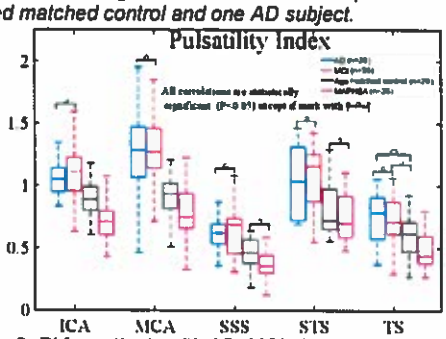

Fig 2: PI for patients with AD, MCI, the control group and MAPHSA. For each vessel segment, the PI is statistically different among all cohorts, with exception of the 9 pairs indicated with brackets.

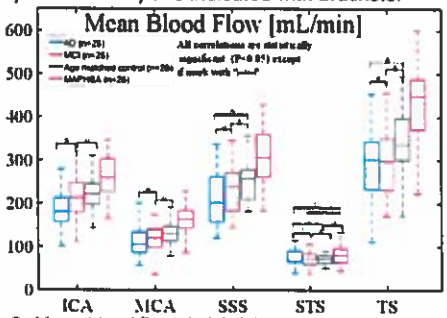

Fig 3: Mean blood flow. (mL/min)

Results: Results for the analysis are summarized for all in Figures 2 & 4. There is statistically significant difference in PI and mean flow between all groups for each segment except those marked with a bracket (21 out of 30 statistically significant pairs for PI and 14 out of 30 pairs for mean flow). Statistically significant differences were also found on the MCA/ICA and SSS/ICA PI ratios and on the pulsatile flow transit time between AD and controls. These results are in accordance with other studies [6] and a relationship between AD and the destructive impact of the pulse on the cerebral vasculature has been suggested to drive these hemodynamic changes [7].

Time (ms)	AD (n=26)	MCI (n=26)	Age matched control (n=26)	MAPHSA (n=26)
Pulsatile flow transit time from MCA to SSS	99 ± 93	108 ± 57	171 ± 77	106 ± 91

Fig 4: Pulsatile wave transit time (ms)

Discussion: New characteristics of the hemodynamic parameters of both arterial and venous vasculature as well as the transit time of the pulse wave are presented. The reduced mean blood flow in the SSS but similar values in the STS in AD patients when compared with age match controls might reflect a relative decrease in cortical cerebral blood volume. The significantly faster translation of the peak of the flow waveform from the MCA to the SSS in the AD and MCI groups when compared to the age matched controls is in line with the hypothesis of a generally reduced cerebrovascular compliance. To our knowledge, this finding has not been reported previously. MCA/ICA PI ratios showed a gradual increase from healthy aging over MCI to AD subjects with a significant difference between AD subjects and healthy age matched individuals. This finding is in accordance with a reduced dampening of the pulse wave in AD and MCI patients. With the large volume coverage and high temporal and spatial resolution demonstrated here, 4D flow MRI can provide additional biomarkers of vascular health that can contribute to increase understanding of the pathogenesis of AD and help in the treatment of AD patients.

References: [1] Roher J Internal Medicine. 2015; 277(4): 426-28. [2] Bateman et al.,Neuroradiology 50:491-497 (2008). [3] Gu et al. AJNR 26(4):743-9 (2005). [4] Liu et al., IEEE TMI 25(2):148-57 (2006). [5] Schrauben et al., J MRI. 2015 Nov;42(5):1458-64.[6] Henry-Feugeas et al., Clin Interv Aging 2008, 3, 187-199. [7] Stone et al., J Alzheimers Dis. 2015;44(2):355-73.

Accelerated Intracranial Vessel Wall Imaging using Compressed Sensing

Chengcheng Zhu[1], Sinyeob Ahn[2], Esther Raithel[3], Gerhard Laub[2], David Saloner[1]

1. Department of Radiology and Biomedical Imaging, UCSF, San Francisco, CA, USA
2. Siemens Healthcare, California, USA; 3. Siemens Healthcare, Erlangen, Germany

Purpose: 3D high resolution black blood MRI has been widely used for imaging of vessel wall pathology of intracranial vascular diseases, including atherosclerotic plaques, aneurysms and vasculitis. High isotropic resolution (0.4mm to 0.6mm) has been achieved with good blood suppression and image quality. However, these protocols often need a long scan time of around 10 minutes, which is poorly tolerated by patients[1-2]. Acceleration techniques that significantly reduce the scan time while maintaining the image quality would be very valuable. This study aims to evaluate and optimize compressed sensing methods for fast intracranial vessel wall imaging.

Methods: A compressed sensing fast-spin-echo sequence (CS-SPACE) was implemented on a Siemens 3T scanner. A Poisson-disk k-space pattern and symmetric radial k-space sampling trajectory were used. Online reconstruction was implemented and took ~2 minutes (20 iterations) for current CS-SPACE protocols. 3 healthy volunteers and 2 patients (one with an internal carotid artery aneurysm, one with a vertebral artery dissection) were recruited for preliminary testing. The effect of under-sampling factors (10% to 50% of k-space), regulation factors (0.005 to 0.04) and iteration times (10 to 40) on image quality were evaluated, and the optimized values were assessed. Subjects were scanned with a previously optimized whole brain SPACE protocol (0.5mm isotropic, 9:47s)[2] and two CS-SPACE protocols (0.5mm isotropic, 5:47s and 0.6mm isotropic, 4:08s). Scanning parameters were: TR/TE = 900ms/13ms, 320 slices with 0.5mm/0.6mm thickness; 16-18cm FOV; echo train length 52 to 60. Conventional SPACE used GRAPPA 2 (phase direction) and 6/8 partial Fourier (slice direction). Patients were scanned both pre- and post-contrast injection. Image quality, specifically contrast-to-noise ratio and vessel wall sharpness, was compared among protocols.

Results: Results indicated that 20% k-space coverage, with 20 iterations and a regulation factor of 0.002 achieved the best image quality and scan efficiency. Images are shown for the patient with an aneurysm (Fig. 1) and the dissection (Fig 2.) CS-SPACE achieved similar resolution and comparable image quality to SPACE, with a scan time reduction of 41%. A 0.6mm isotropic CS-SPACE protocol provided good image quality and visualization of vessel wall in ~4 minutes. Vessel wall boundaries and contrast enhancement were clearly delineated by SPACE and CS-SPACE in patient scans.

Discussion and Conclusions: To our knowledge, this is the first study to apply compressed sensing in 3D black blood intracranial vessel wall imaging. Our preliminarily optimized CS-SPACE protocol shows good image quality compared to SPACE, in a scan time of less than 6 minutes. 0.6mm isotropic imaging is possible with CS-SPACE in as little as 4 minutes. Fast imaging of intracranial vessel wall using CS-SPACE is a promising tool to evaluate patients with intracranial vascular disease in the clinical setting, and has the potential to improve risk stratification in these patients.

References: 1. Fan Z et al, MRM 2016. 2. Zhu C et al, MAGMA 2016

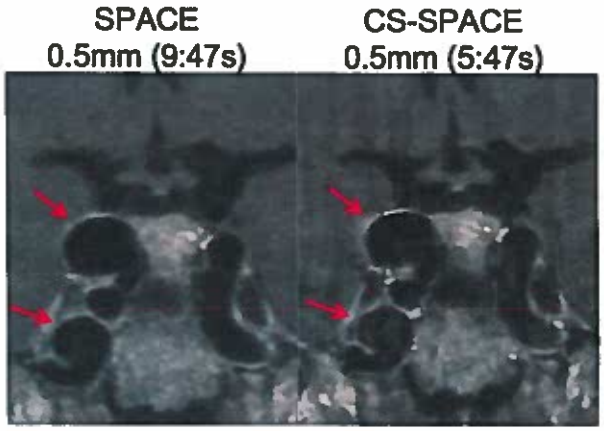

Figure 1. Multiple ICA aneurysms (post-contrast).

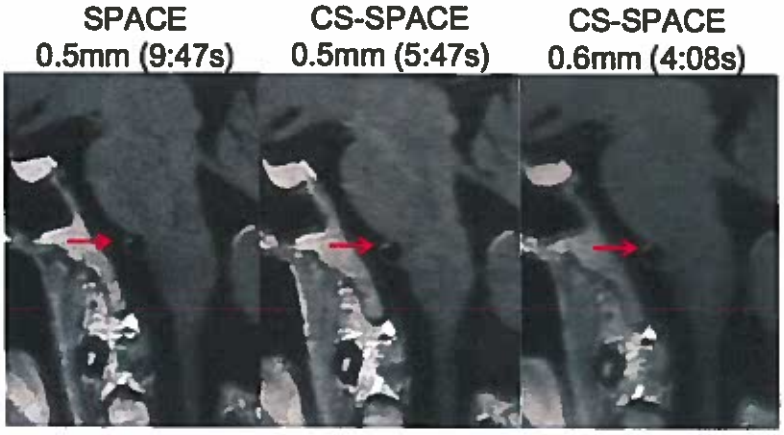

Figure 2. A patient with vertebral artery dissection (post-contrast).

Vascular TTP map of the brain acquired from time-resolved contrast-enhanced MR angiography: comparison with brain SPECT

Jin-hee Jang[1], Yoon-ho Nam[1], Bum-soo Kim[1], Song Lee[1], Hyun Suk Choi[1], So-Lyung Jung[1], Kook-Jin Ahn[1], Taesub Chung[2]

The Catholic University of Korea[1], Yonsei University Medical College[2], Seoul, Korea

Purpose: We explored the feasibility of a time-to-peak (TTP) map from time-resolved contrast-enhanced MRA (TRCEMRA) for detection of perfusion deficits in patients who were suspected to have steno-occlusive lesions in head and neck arteries, as compared with single-photon emission computed tomography (SPECT).

Methods: Twenty-seven patients who underwent both TRCEMRA and brain SPECT were included in this study (14 men and 13 women, median age 61). TRCEMRA was performed using the time-resolved angiography with stochastic trajectories (TWIST) technique after intravenous injection of a low dose (0.03 mmol/kg bolus at a flow rate of 1.5 mL/sec followed by a 20 cc saline flush at the same rate) of gadobutrol. A total of 60 seconds was covered with a temporal resolution of 0.98 seconds after interpolation. TTP map of the brain was generated from source images of TRCEMRA using in-house software. Detection of hemodynamic changes were compared, in time-series of in-line generated MIP images, TTP map and SPECT. Quality and perfusion abnormality of TTP map was assessed. Perfusion deficit of predefined 7 areas of the middle cerebral artery (MCA) territory were assessed in TTP map and SPECT using modified ASPECT scores.

Results: Quality of the TTP map was good or excellent in 81.5 % (22/27). Agreement of modified ASPECT scores between TTP maps and SPECT were substantial (Kappa 0.66 95% CI 0.46 -0.85). TTP map showed significantly high sensitivity than the review of serial MIP images (P=0.04 for sensitivity) for diagnosis of perfusion deficit.

Conclusion: Generation of TTP map from TRCEMRA is feasible, and it has acceptable image quality and diagnostic performance to detect the perfusion abnormality associated with neurovascular steno-occlusive lesion.

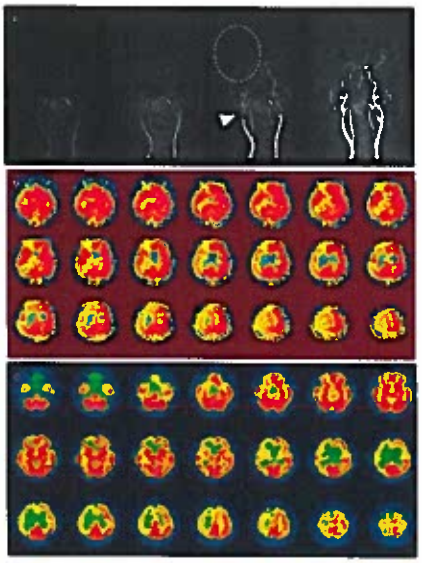

Figure. A 75 year-old female with left arm weakness. MIP images of TRCEMRA (A) shows delayed perfusion of right MCA territory (dashed circle). Note the stenosis of right proximal ICA (arrowhead). On TTP map from TRCEMRA (B), Perfusion abnormality in right MCA territory is clearly visualized. Note the same perfusion abnormality on SPECT (C).

Longitudinal Surveillance of Intracranial Aneurysms with Contrast-Enhanced MRA: Estimation of Volumetric Measurement Error at 1.5 and 3T

Farshid Faraji, Evan Kao, Megan Ballweber, Alastair Martin, David Saloner
UCSF Department of Radiology and Biomedical Imaging, SF Veterans Affairs Medical Center

INTRODUCTION: We report on an ongoing longitudinal study of unruptured intracranial aneurysms. Intracranial aneurysms pose a considerable risk for subsequent neurological events, such as aneurysmal rupture resulting in hemorrhagic stroke or mass effect from the growing aneurysm pressing on critical brain structures. This analysis reports on measurement error of 3D MRI/MRA methods used to evaluate the progression of vascular disease in patients with intracranial aneurysms where no intervention was planned, either because of size, unfavorable treatment options, or patient choice. This analysis also extends our previous findings from imaging with 1.5T MRI to include imaging at 3T.

METHODS: 87 patients with 100 aneurysms of the intracranial circulation were recruited for serial imaging using an IRB-approved protocol. Patients were imaged at baseline and followed in intervals ranging from 6 months to 1 year. All patients were imaged on a Philips 1.5T Achieva (n = 72 patients with 365 studies), or Siemens 3T Skyra (n = 60 patients with 175 studies). 54 patients were imaged on both MRI scanners. Patients were categorized by territory of the aneurysm, with 62 aneurysms of the Internal Carotid Artery, 12 of the Middle Cerebral Artery, 8 of the Anterior Cerebral Artery, and 18 aneurysms found to be of the posterior circulation. Of 100 aneurysms, 2 had 12 follow-up studies, 2 had 11 follow-up studies, 2 had 10 follow-up studies, 3 had 9 follow-up studies, 8 had 8 follow-up studies, 7 had 7 follow-up studies, 9 had 6 follow-up studies, 10 had 5 follow-up studies, 11 had 4 follow-up studies, 9 had 3 follow-up studies, 17 had 2 follow-up studies, and the remaining 18 had one follow-up study. This results in a total of 540 interval measurements. At each imaging session MRI and MRA were conducted to assess lumenal volume and presence of thrombus. A 3D balanced steady-state free precession pulse sequence was acquired (bFFE on Philips and TrueFISP on Siemens) with orientation and resolution matching the CE-MRA study to check for the presence of thrombus. If thrombus was present, the patient was excluded from this analysis, as longitudinal changes could be due to reduction and expansion of the lumen from layering of thrombus rather than dilation of the vessel wall. The MRA study used was a contrast-enhanced 3D acquisition with a parallel acceleration factor of 2 resulting in high-resolution CE-MRA images of the intracranial vessels (0.6 x 0.63 x 1.2mm at 1.5T and 0.7mm isotropic resolution at 3T). Serial MR studies were co-registered using anatomical features. Consistent intensity-based thresholding was imposed, requiring that a reference segment of undiseased vessel maintain the same lumenal volume over time. The lumenal volume of the aneurysmal segment was subsequently assessed on the follow-up CE-MRA studies for regional and global changes. Changes in volume of the aneurysmal segment were calculated as a percentage of the baseline volume and were normalized on an annualized basis. Measurement error was calculated as the residual (normalized to the mean aneurysm volume) after performing a linear regression.

RESULTS: Measurement error was calculated as 4.6% for studies performed at 1.5T, and 3.2% for studies performed at 3T. Of the aneurysms that were followed, 11 of 100 showed growth that was significant beyond measurement error. Interestingly, small aneurysms demonstrate a marked increase in volume upon first imaging at 3T. These volumetric changes were most likely due to a reduction in partial volume effect resulting from the increase in spatial resolution, since any changes in volume and shape noted when imaging at 3T disappeared when patients were re-imaged at 1.5T.

CONCLUSION: MRI provides a minimally invasive method to monitor intracranial aneurysms, allowing for the investigation of their natural history in ways that have not been possible before. In particular, 3D analyses remove the limitations of traditional methods that utilize measurements of linear dimensions. Here we further analyze methodology that allows for longitudinal assessment of growth using contrast-enhanced MRA. Our results demonstrate less than 5% measurement error at 1.5T. Additionally, we found that imaging at 3T allows for more than 1% reduction in measurement error, which gives greater sensitivity and specificity to detect aneurysm growth. This is important considering that growing aneurysms are at greater risk for rupture, and will better inform physicians as to which patients should go on to have an intervention due to re-stratification of risk. Measurement error reduction also allows for significant sample size reduction to detect statistical significance in longitudinal studies.

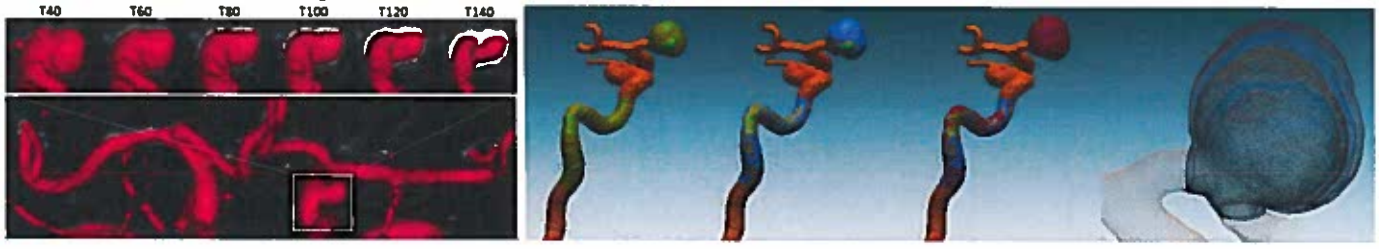

Figure 1 (left) shows the effect of different threshold values on volume and shape, and demonstrates the need for a method to normalize serial studies
Figure 2 (right) displays 3 studies for one patient. The reference vessel (proximal carotid) has been matched, and the ACA aneurysm shows growth

REFERENCES: [1] Dispensa, BP et al JMRI 2007; 26:177–183 [2] Boussel et al. JVIR 2011; 22(7):1007-11

Session 6

Non-contrast MRA

Selective pulmonary MR venography using radial QISS

Robert R. Edelman[1,2], Amit Pursnani[3], Shivraman Giri[4], Ioannis Koktzoglou[1,5]

[1]Radiology, NorthShore University HealthSystem, Evanston, IL, [2]Radiology, Northwestern University, Chicago, IL, [3]Medicine, NorthShore University HealthSystem, Evanston, IL, [4]Siemens Healthcare, Chicago, IL, [5]Radiology, University of Chicago, Chicago, IL.

Purpose: Atrial fibrillation is the most common sustained cardiac arrhythmia and entails the risk of serious morbidities including stroke. Pulmonary vein isolation provides an important treatment option for this condition. The procedure is carried out under fluoroscopy, with catheter guidance based on integration of 3D electro-anatomical maps with pre-procedural CTA or contrast-enhanced MRA [1]. CTA entails exposure to ionizing radiation and iodinated contrast agents, whereas CEMRA requires administration of a gadolinium-based contrast agent and spatial resolution may be restricted by the need to complete imaging during the first pass of the contrast agent. Non-contrast MRA using navigator-gated 3D bSSFP is unpredictably time-consuming and vessel detail may be degraded by respiratory artifact. We therefore explored the feasibility of using QISS MRA, which has previously been applied to peripheral MRA and more recently to carotid and coronary MRA, to image the pulmonary veins. A radial variant of the technique was furthered modified to incorporate pseudocontinuous arterial spin labeling (pCASL) RF pulses so as to create selective MR angiograms that only displayed the pulmonary veins.

Methods: Subjects were scanned on a 1.5 Tesla MR system (MAGNETOM Avanto, Siemens Healthcare, Erlangen, Germany) with IRB approval. The prototype radial QISS sequence [2] applies a slice-selective FOCI pulse followed by a user-defined quiescent interval, alpha/2 catalyzation, and bSSFP diastolic readout with equidistant azimuthal radial view angle increments. Using a single-shot acquisition with ~98 views, ~20 contiguous slices (1.5 to 3-mm slice thickness) were acquired, spanning the left atrium and proximal pulmonary veins in a coronal or axial orientation. Images were acquired in a single breath-hold, thereby minimizing the likelihood of misregistration artifact. The pCASL RF pulses were applied along a plane separating the right and left lungs and passing through the central portion of the left atrium as well as the ascending aorta. In addition, spatial saturation was applied through the sub-diaphragmatic portion of the inferior vena cava to further suppress the signal intensity of the right atrium. QISS MRA was compared with CT pulmonary venography when available and in one subject it was compared with dynamic CEMRA.

Results: Single breath-hold radial QISS MRA depicted the entire left atrium and proximal pulmonary veins with excellent conspicuity and without obvious degradation from respiratory or cardiac motion. Banding artifacts from off-resonance effects that are typically seen with a bSSFP readout when imaging the pulmonary veins were avoided by manually shimming to the region of the heart and proximal pulmonary veins, and by the combined use of a high-bandwidth readout (e.g. 1347 Hz/px) and short RF pulses (e.g. 600 us). Concurrent application of pCASL and spatial saturation was highly effective at suppressing background blood pool signal for selective pulmonary venography (Figure). In the one subject where a comparison with CEMRA was available, QISS MRA outperformed the contrast-enhanced exam with respect to vascular detail.

Discussion: We have demonstrated the feasibility of single breath-hold selective pulmonary venography using pCASL radial QISS. With further study, it could provide a useful alternative to CT and CEMRA for pre-procedural evaluation of the pulmonary veins.

References: 1. Haegeli LM, Calkins H. Eur Heart J. 2014 21;35(36):2454. Edelman RR et al. J Cardiovasc Magn Reson 2015 23;17:101.

MR Imaging for aortic annular sizing

Ferreira Botelho, Marcos P. [1]; Jarvis, Kelly B[1]; Collins, Jeremy D. [1]; Markl, Michael[1]; Mohiuddin, Sohaib A[1]; Carr, James C. [1]

1. Radiology, Northwestern University, Chicago, IL, United States.

Introduction:
Aortic annulus sizing is a crucial part of pre-procedural planning for transcatether aortic valve replacement (TAVR). Undersizing annular measurement may lead to paravalvular leak and oversizing increases the risk of annular rupture. Annular measurement has traditionally relied on CT angiography with retrospective ECG gating, which can provide reliable systolic and diastolic annular measurements. In the last few years, some authors have tried annular sizing using MRI with promising results. Besides avoiding radiation, these techniques normally do not need any type of contrast injection. The purpose of this study was to compare MR techniques for annular sizing in volunteers and to evaluate precision and reliability of the techniques in TAVR patients that had a CTA as the gold standard.

Methods:
6 volunteers and 2 TAVR candidates were prospectively enrolled and scanned at 1.5T. The non-contrast MR sequences compared for annular sizing were: breath held 5mm 3D cine bSSFP, navigator gated 1.4 mm T2 Prep 3D bSSFP and a newly developed breath held 3D cine bSSFP k-t accelerated sequence, with 1.5 and 1.3 mm slices. Quiescent interval slice selective (QISS) non-contrast MRA was also acquired in the 2 patients to evaluate for coronary artery heights. A single observer measured annular areas and coronary heights using dedicated software.

Results:
Average annular sizes were (mm^2): 497 (+/- 69) for the 5 mm 3D cine, 502 (+/- 78) for the nav T2 prep sequence and 497 (+/- 78) for the k-t accelerated sequences, with no statistical difference among techniques ($p>0.05$). There was good agreement between the MRI methods with Bland-Altman results showing no sizeable bias (1% or less of the average value) and limits of agreement within 18%. In the 2 patients with CT imaging, the MRI methods showed excellent agreement with CTA with absolute differences of 6%, 5%, and 2% for the 3D cine, nav T2 Prep and k-t accelerated methods, respectively. The newly developed 3D cine bSSFP k-t sequences showed the best agreement with CTA with an average absolute difference of 2%. Compared to CTA, QISS provided similar coronary heights in both patients, with a maximum difference of 2 mm.

Conclusion:
The techniques studied demonstrated excellent correlation with CTA in patients. Newly developed 3D cine bSSFP k-t sequences provided reliable annular sizing compared to CTA. QISS provided reliable information regarding coronary heights. These techniques have great potential as alternatives for patients undergoing pre-TAVR assessment of annular sizing.

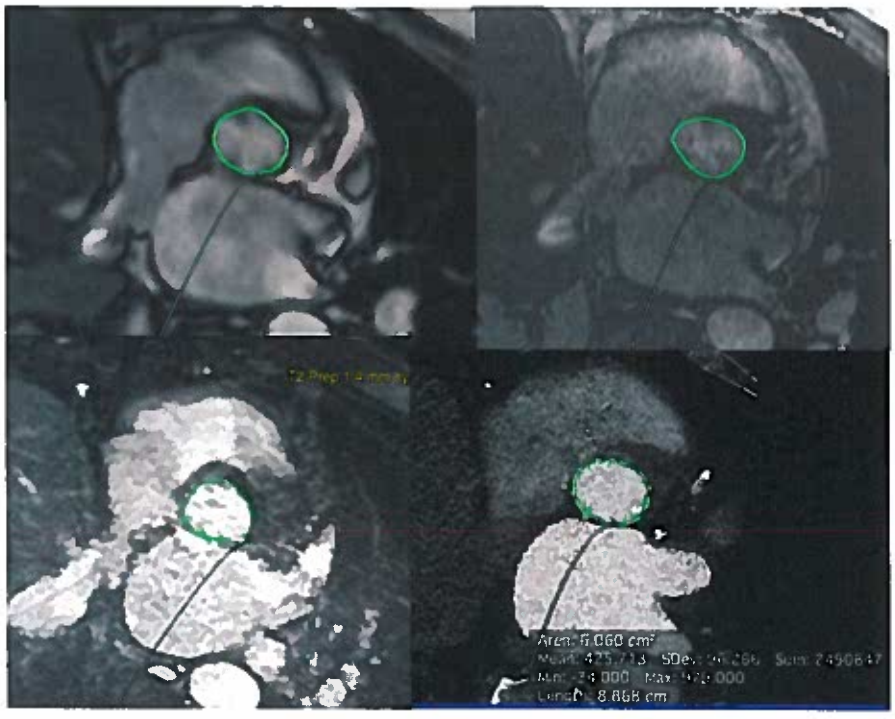

Image examples of the techniques studied. Upper left 3D cine, lower left navigator gated 3D bSSFP, upper right 3D cine bSSFP with k-t acceleration and lower right, the gold standard, CTA. There was excellent correlation among the tested techniques.

Accuracy of Carotid Lumen Measurements by Non-Contrast SNAP MRA

Haining Liu, Jie Sun, Niranjan Balu, Daniel S. Hippe, Thomas Hatsukami, Chun Yuan

Purpose: Simultaneous non-contrast angiography and intraplaque hemorrhage MRI (SNAP) (1) is a high-resolution 3D non-contrast MRA approach based on phase-sensitive inversion recovery (PSIR). (1). SNAP MRA has been shown to reduce flow artifacts (1) and may provide improved non-contrast lumen measurements. However, the accuracy of SNAP luminal measurements has not been compared against widely used clinical standards. The aim of this study was to compare carotid lumen area measurements between non-contrast MRA methods SNAP and 3D time-of-flight (TOF) using contrast enhanced magnetic resonance angiography (CEMRA) as the reference standard.

Methods: Eleven subjects with 16-79% stenosis by duplex ultrasonography on at least one side were enrolled in the study after obtaining informed consent. All study procedures were approved by the University of Washington Institutional Review Board. Bilateral carotid arteries were scanned using a dedicated carotid coil for SNAP and 3D TOF, and a body coil for CE-MRA. Scan parameters were: CEMRA: TR/TE: 5.46/1.69ms, FOV: 350 (Foot-head [FH] direction)×350(Right-Left [RL] direction)×64(Anterior-Posterior[AP] direction)mm^3, resolution: 0.8×0.8×0.8mm^3. SNAP: TR/TE: 9.8/4.72ms, inversion time(TI) 500ms, FA: 11°, FOV: 160(FH)×160(RL)×32(AP)mm^3, resolution: 0.8×0.8×0.8mm^3. 3D TOF: TR/TE: 24/4.86ms, FA: 20°, FOV:160(AP)×160(RL)×46(FH)mm^3, resolution: 0.6×0.6×2.0 mm^3. Images were first reformatted to axial slices with a slice thickness of 2mm. Slices centered on the carotid bifurcation were reviewed (roughly 10 slices above and 10 slices below the bifurcation). A custom-designed image analysis software (2) was used to outline lumen contours independently on each MRA sequence and lumen areas were calculated. The degree of stenosis for each artery was calculated as the ratio of the minimum lumen area to the lumen area of the most proximal slice covered in the CCA, approximately 20 mm proximal to the bifurcation. Statistical Analysis: Agreement was summarized using the intraclass correlation coefficient (ICC). Bias and agreement were also evaluated qualitatively using Bland-Altman plots (differences vs. means). Bland-Altman limits of agreement (mean difference ±1.96*standard deviation of differences) were also calculated.

Results: A total of 15 stenotic arteries were reviewed. Of 298 slices reviewed, 8 slices were excluded because the lumen was partially outside the FOV on SNAP. The degree of stenosis was not calculable in two arteries because a disease-free reference site was not available within the FOV. As shown in Table 1, agreement in lumen area measurements by SNAP and CE-MRA was excellent (ICC: 0.94). Agreement between TOF and CEMRA was lower for lumen area (ICC 0.83, p<0.001). SNAP measurements tended to be larger than on CEMRA (mean difference: 2.9 mm^2) and TOF measurements tended to be smaller than on CEMRA (mean difference: -2.5mm^2). Although there was no significant difference in stenosis measurements by either SNAP (P=0.39) or TOF (P=0.42) relative to CEMRA (Fig 1 and Table 2), the ICC was excellent for SNAP (0.93) but poor for TOF (0.47) due to flow artifacts in reference slices.

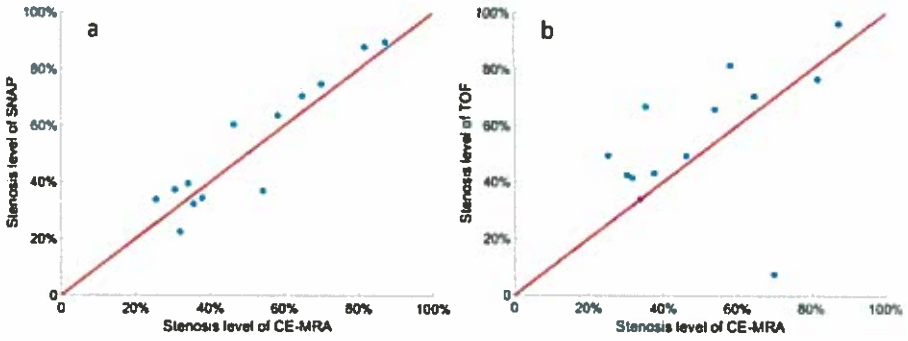

Fig 1: a) comparison of stenosis level between SNAP and CE-MRA; b) comparison of stenosis level between TOF and CE-MRA. Red line is unity line.

Conclusion: The excellent agreement with CE-MRA for both lumen area and stenosis measurements shows that SNAP is a promising non-contrast MRA sequence for lumen area measurements. Furthermore, the accuracy of non-contrast SNAP MRA was higher than clinically used non-contrast 3D-TOF MRA. SNAP MRA can potentially serve as a non-contrast sequence for clinical use.

Table 1. Lumen area measurements

Segment	No. of Slices	Lumen area (mm^2)			ICC with CEMRA (95% CI)	
		TOF	SNAP	CE-MRA	TOF	SNAP
All	290	30.29±15.03	35.69±18.09	32.82±15.81	0.83 (0.79-0.86)	0.94 (0.92-0.95)
With Plaque	136	27.90±16.49	34.81±21.83	31.72±18.12	0.81 (0.75-0.86)	0.94 (0.91-0.95)
Without Plaque	154	31.06±14.53	34.93±16.15	32.39±14.74	0.87 (0.84-0.91)	0.95 (0.94-0.97)

Table 2. Stenosis measurements

Methods	Mean of stenosis level	Difference with CEMRA	P value	ICC(95%c CI)
SNAP	53%±23%	2%±8%	0.39	0.93(0.78-0.98)
TOF	56%±23%	5%±23%	0.42	0.47(-0.09-0.80)
CEMRA	51%±21%			

References: (1) Wang J et al, MRM, 2013; (2) Kerwin et al, TMRI, 2007

Cardiac and Respiratory Motion-Resolved Free-Running Whole-Heart Coronary MRA of Patients Using 5D XD-GRASP Reconstruction

Giulia Ginami[1], Simone Coppo[1], Li Feng[2], Davide Piccini[1,3], Tobias Rutz[4], Ricardo Otazo[2], Daniel Sodickson[2], Matthias Stuber[1,5], and Jerome Yerly[1,5]

[1]University Hospital (CHUV) and University of Lausanne (UNIL), Lausanne, Switzerland, [2]Center for Advanced Imaging Innovation and Research (CAI2R), Department of Radiology, New York University School of Medicine, New York, NY, United States, [3]Advanced Clinical Imaging Technology, Siemens Healthcare, Lausanne, Switzerland, [4]Division of Cardiology and Cardiac MR Center, University Hospital of Lausanne (CHUV), Lausanne, Switzerland, [5]Center for Biomedical Imaging (CIBM), Lausanne, Switzerland

INTRODUCTION: Free-running self-navigated techniques (1-2) enable time-resolved evaluation of both cardiac function and coronary anatomy throughout the entire cardiac cycle. The intrinsic random undersampling of the cardiac phases and sensitivity to respiratory motion of these techniques, however, often lead to streaking artifacts. To overcome these hurdles, *5D* (x-y-z-cardiac-respiration) *XD-GRASP* (eXtra-Dimensional Golden-angle Radial Sparse Parallel MRI) has successfully been applied to reconstruct cardiac and respiratory motion-resolved 3D volumes in healthy adult subjects (3). Here, the potential of this approach was assessed in patients with confirmed coronary artery disease.

METHODS: **Data acquisition:** Data acquisition was performed in N=4 patients with myocardial infarction using a prototype free-running (non ECG-triggered) bSSFP 3D golden-angle radial trajectory (2) on a 1.5T scanner (MAGNETOM Aera, Siemens Healthcare, Erlangen, Germany). An additional superior-inferior (SI) projection was acquired at the beginning of each data segment (4), and was used for respiratory motion detection. Data were acquired during ≈14 minutes in free-breathing with the slow infusion of contrast agent (Gadovist, 0.03 ml/sec, 0.1 ml/kg). Imaging parameters of the free-running, fat-saturated acquisition were as follows: TR/TE 3.1/1.56ms, FoV $(220mm)^3$, voxel size $(1.15mm)^3$, matrix dimension $(192)^3$, flip- angle 90°, data segments 5'749, lines per segment 22, total acquired lines 126'478. **Image reconstruction:** A 1D respiratory motion signal (Figure 1b) was extracted (5) and images were reconstructed using: ***a)*** "*4D reconstruction*", where the 1D respiratory signal was used to correct for respiratory motion in the SI direction (5). The recorded ECG signal was used to sort the data into 15-20 3D cine frames (duration 100ms, view sharing 80%, ≈12'000 radial lines per frame). Finally, images were reconstructed with a standard re-gridding algorithm (2). ***b)*** "*5D XD-GRASP*", where the 1D respiratory and ECG signals were used to sort data into 6 different respiratory phases or bins (Figure 1c) and into ~20 cardiac phases (80ms duration, 50% view sharing), respectively. The cardiac- and respiratory-resolved images with dimensions of 192×192×192×20×6 were then reconstructed by solving (3): $\arg\min_m \|F \cdot C \cdot m - s\|_2^2 + \lambda_1 \|D_1 m\|_1 + \lambda_2 \|D_2 m\|_1$, where F represents the NUFFT operator, C the coil sensitivity maps, m the 5D image set to be reconstructed, s the sorted radial k-space data, D_1 and D_2 the finite difference operators applied along the cardiac and respiratory dimension, respectively, and λ_1 = 0.02-0.04 and λ_2 = 0.02-0.04 the regularization parameters, which were empirically selected. **Image quality assessment:** A diastolic 3D cine frame was selected from the *4D reconstruction* and compared with a diastolic 3D cine frame selected from an end-expiratory position of the images reconstructed with *5D XD-GRASP*. Two experienced reviewers scored the reconstructed volumes with grades ranging from 0 (non visible) to 4 (sharply defined), by considering overall image quality, sharpness of the myocardium, and coronary delineation. Visible coronary vessel length was quantified by using the software described in (6).

RESULTS: Data acquisition and reconstruction was successful in all cases; *5D XD-GRASP* provided 3D volumes resolved for both cardiac and respiratory motion (Figure 1). All the quantified results, as summarized in Table 1, confirmed the improvement in image quality, sharpness of the myocardium, and coronary visualization when the *5D XD-GRASP* approach was used for image reconstruction, with respect to the *4D reconstruction*.

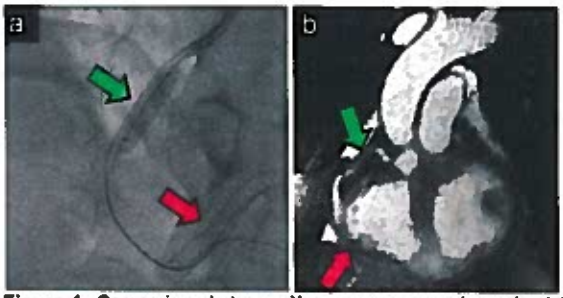

Figure 1: Comparison between X-ray coronary angiography (a) and 5D XD-GRASP (b) in one of the patients. The signal void in b (green and red arrows) confirms the presence of two stents in the RCA.

		4D Reconstruction	5D XD-GRASP
LAD	Length (cm)	4.9 ± 2.1	5.8 ± 3.2
	Grading	0.8 ± 0.8	1.4 ± 1.1
RCA	Length (cm)	3.9 ± 2.7	6.1 ± 3.7
	Grading	1.3 ± 0.7	1.8 ± 1.0
LCX	Length (cm)	1.1 ± 1.3	2.3 ± 2.2
	Grading	0.8 ± 0.7	0.9 ± 0.3
Myocardium	Grading	1.4 ± 0.3	2.3 ± 0.3

Table 1: Quantitative results, which confirm a trend for an improvement of both myocardial delineation and coronary depiction when 5D XD-GRASP is used when compared to the 4D reconstruction.

DISCUSSION and CONCLUSIONS: *5D XD-GRASP* has been successfully applied in a clinical setting and in a small cohort of patients. A major advantage of the *5D XD-GRASP* approach is that it reconstructs images in different cardiac and respiratory phases, and does not require any model for motion correction, as is the case for the 4D reconstruction. While 1D SI motion correction performs well for some subjects and specific locations of the anatomy, it only corrects for respiratory motion in the SI direction and does not account for the more complex 3D respiratory motion of the heart. Furthermore, *5D XD-GRASP* enables the reconstruction of cardiac- *and* respiratory-motion resolved datasets at the same time.

REFERENCES: *1)* Pang et al, MRM 2014 ; 72(5) 1208-17 *2)* Coppo et al, MRM 2015 ; 74 1306-16 *3)* Feng et al, Proc. Intl. Soc. Mag. Reson. Med. 2015 #27, *4)* Stehning et al, MRM 2005, 476 :480 *5)* Piccini et al, MRM 2012; 68 571-579 *6)* Etienne et al, MRM 2002, 48 :658-666.

Image Quality of Lower Extremity QISS MRA in Patients with Peripheral Artery Disease: Comparison with CTA

Akos Varga-Szemes, MD, PhD[1], Shivraman Giri, PhD[2], Giuseppe Muscogiuri, MD[1], Carlo N. De Cecco, MD[1], Pal Suranyi, MD, PhD[1], U. Joseph Schoepf, MD[1], Thomas M. Todoran, MD[3]

[1]Division of Cardiovascular Imaging, Department of Radiology and Radiological Science, MUSC; [2]Siemens Healthcare; [3]Divison of Cardiology, Department of Medicine, MUSC

Purpose: To evaluate the qualitative and quantitative image quality of the non-contrast quiescent interval single-shot (QISS) MRA in patients with peripheral artery disease (PAD).

Methods: Twenty patients (67±6 years, 11 male) with PAD referred for a clinically indicated lower extremity CTA (SOMATOM Force, Siemens AG, Forchheim, Germany) were consented for a non-contrast research lower extremity MRA on a 1.5 clinical scanner (MAGNETOM Avanto, Siemens AG, Erlangen, Germany) using an investigational prototype QISS sequence (FOV 400x260mm^2, TR/TE 3.5/1.4ms, flip angle 90°, acquisition length 144mm). Contrast to noise ratio (CNR) based on the vascular and peri-vascular signal was measured according to an 18-segment model. The segmental vascular enhancement and the image noise were rated on five-point scales (1-poor/non-diagnostic, 5-excellent) by two readers. Additionally, the number of non-diagnostic segments were counted and compared between CTA and QISS-MRA.

Results: A total of 360 segments were evaluated. The average CNR measured in QISS-MRA images was 63.4±17.5. QISS-MRA vascular enhancement ratings by the two readers were 3.7±0.5 and 3.8±0.4, respectively, while the CTA readings were 4.0±0.4 and 4.1±0.5, respectively, resulting in no significant difference between the two modalities. QISS-MRA image noise ratings were 3.4±0.7 and 3.6±0.5, respectively, while those for CTA were 4.0±0.5 and 4.2±0.5, respectively. Excellent inter-reader agreement was found in image quality ratings (κ>0.8). Thirty-one segments (8.6%) in CTA were excluded from the analysis due to stent artifacts (11), total occlusion (14), or heavy calcification (6) and 26 segments (7.2%) were non-diagnostic in MRA due to major image artifacts (12) or total occlusion (14). Five out of the six heavily calcified segments were diagnostic in QISS MRA.

Conclusion: In this study, image quality of the non-contrast QISS-MRA was comparable to that of contrast enhanced CTA. In certain circumstances, such as in heavily calcified segments, QISS-MRA provides superior lumen visibility compared to CTA. Such a non-contrast technique may have potential advantage in patients with severe renal disease.

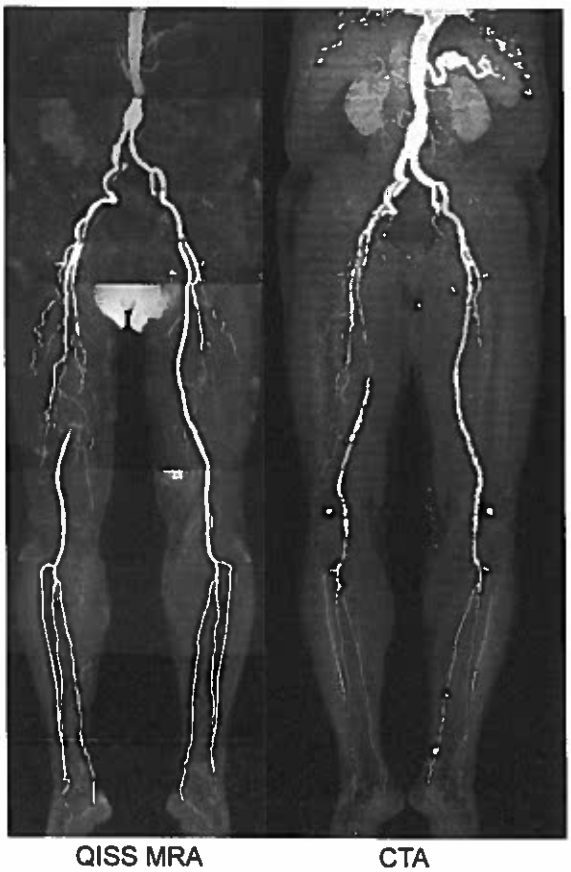

QISS MRA CTA

References:

Edelman RR, Sheehan JJ, Dunkle E, Schindler N, Carr J, Koktzoglou I. Quiescent-interval single-shot unenhanced magnetic resonance angiography of peripheral vascular disease: Technical considerations and clinical feasibility. Magn Reson Med 2010;63:951-8.

Hodnett PA, Koktzoglou I, Davarpanah AH et al. Evaluation of peripheral arterial disease with nonenhanced quiescent-interval single-shot MR angiography. Radiology 2011;260:282-93.

Non-contrast compressed sensing whole-heart coronary MRA at 3T: First results in twenty healthy volunteers

Masashi Nakamura[1], Teruhito Kido[1], Hitoshi Miki[2]

1) Ehime University Hospital, 2) Ehime Prefectural Central Hospital

Purpose:

The purpose of this study was to evaluate the diagnostic quality of Compressed sensing (CS) Whole-heart coronary magnetic resonance angiography (WHC-MRA) compared with conventional WHC-MRA.

Methods:

Twenty healthy volunteers underwent both conventional navigator gated WHC-MRA and navigator gated WHC-MRA with a prototype sequence using CS. We respectively assessed acquisition times, scores of image quality, and the visualized vessel lengths.

Results:

The mean effective scan time was 3 min 45 sec for CS WHC-MRA and 15 min 06 sec for conventional WHC-MRA ($p<0.001$). CS WHC-MRA received scores above 3 (good quality for diagnosis) in almost all segments. The average visible vessel lengths were shown no significant differences.

Conclusions:

CS WHC-MRA could shorten the scan time considerably while maintaining diagnostic image quality compared with conventional WHC-MRA.

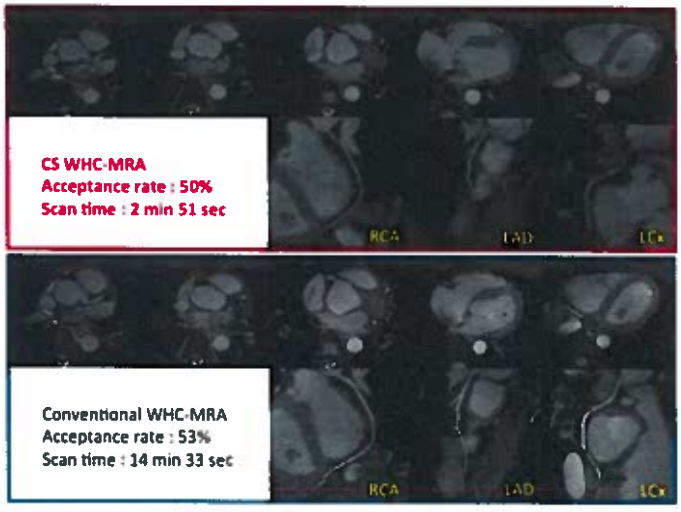

Evaluating Peripheral Artery Disease with ECG Gated Flow Spoiled-Fresh Blood Imaging Non Contrast-MRA

BZ Cooper[1], R Singh[1], M Grimaldi[1], R Griffith[1], PV Viswanath[2], E Wilson[1]
[1]Pocono Medical Center, [2]Pace University

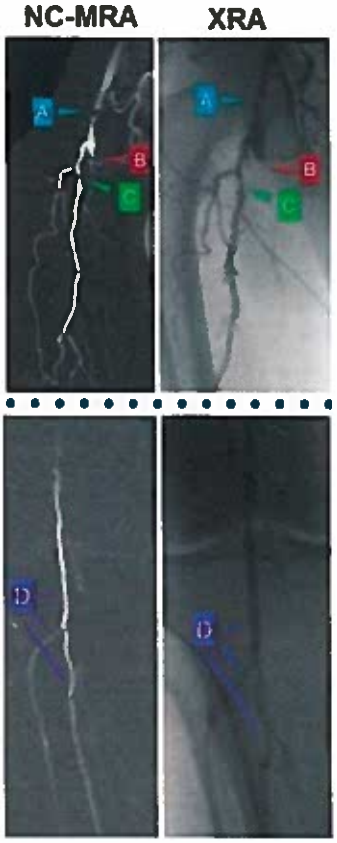

PURPOSE: Lower extremity PAD is the third leading cause of atherosclerotic cardiovascular morbidity[1]. The benefit of a noninvasive, non-contrast diagnostic tool to comprehensively assess peripheral vessels in patients with peripheral artery disease (PAD) is clear[2]. Non Contrast-Magnetic Resonance Angiography has been used to evaluate PAD but its ability to accurately detect the severity of stenosis and occlusion has not been well documented in the literature. The purpose of this work is to evaluate the sensitivity, specificity and accuracy of Flow Spoiled-Fresh Blood Imaging Non Contrast-Magnetic Resonance Angiography (NC-MRA) in the detection of clinically significant (>50%) stenosis, occlusions, reconstitution of flow and identification of target vessels for revascularization. In addition, a new automatic ECG algorithm was implemented, which determines the optimal systolic and diastolic phase used for triggering.

METHODS: This study was approved by the Western Institutional Review Board. Ten (10) patients with symptomatic PAD who were referred for lower extremity angiography (XRA) underwent NC-MRA of the bilateral lower extremities using a 1.5 Tesla MRI (Vantage Titan™, Toshiba) immediately prior to undergoing XRA. A three-station runoff was performed using Delay Tracker, removing the need to run an additional preparation scan previously required in FBI run-off imaging. Appropriate flow-spoiling gradient pulses on the readout axis were used to optimize the separation of arteries and veins. Source, subtracted and MIP data sets were reviewed in order to define image quality (IQ), disease location, and severity. Severity of stenosis of arterial segments as demonstrated by NC-MRA and corresponding XRA were scored using a 4 point scale; No stenosis (<50%), Moderate stenosis (50-79%), severe stenosis (>80%) and occluded. IQ was assessed with a three point scale (1-Poor/inadequate, 2-Acceptable, 3-Excellent). Sensitivity, specificity, positive predictive value (PPV), negative predictive value (NPV) and accuracy were calculated.

RESULTS: 216 segments were evaluated. The sensitivity, specificity, PPV, NPV and accuracy in the detection of stenoses (>50%) was 95.0%, 94.2%, 73.1%, 99.1%, 94.3%. The sensitivity of NC-MRA in the detection of occlusions, reconstitutions and identification of target vessels was 100%, 92.3% and 40.0%. Diagnostic information provided by MRA was sufficient in 9/10 patients. MRA provided additional valuable information that was not provided by XRA in 6/10 patients. The average Quality of MRA images was 2.72 (165-3, 42-2, 9-1). Average time for three-station runoff was 44 (Max 56/Min 30) minutes.

CONCLUSION: We have demonstrated that NC-MRA is a valuable diagnostic imaging modality that may be used to comprehensively assess the severity and location of PAD. NC-MRA may be used as a guide in preoperative planning of interventional procedures. The limitations of NC-MRA include its limited ability to confidently identify target vessels when revascularization is needed and its limited ability to image severity of disease within a vascular stent.

REFERENCES: (1) Fowkes FG et al. Lancet 2013; 382(9901):1329-40. (2) Pollak AW et al. *Circ Cardiovasc Imaging* 2012;5:797-807.

Figure 1: NC-MRA and XRA images of the same patient at corresponding locations (A) Severe stenosis Common Femoral Artery (B) Occlusion of Superficial Femoral Artery (C) Moderate stenosis Deep Femoral Artery (D) Reconstitution of popliteal artery and three target vessel for revascularization.

We acknowledge the support of Toshiba America Medical Systems

Initial Experience Using Accelerated Velocity Selective ASL for Non-Contrast Volumetric MRA in Complex Geometries

James H. Holmes[1] Patrick A. Turski[1], and Kevin M. Johnson[2]

Departments of [1]Radiology and [2]Medical Physics, University of Wisconsin-Madison, Madison, WI

Purpose: Non-contrast MRA has been widely shown using arterial spin labeling (ASL) based methods where labeling planes can be identified and blood velocities are sufficiently high. However, these methods have typically suffered in complex geometries without well-defined labeling planes or in cases of slow or complex flow patterns. Moreover, these techniques fail to depict venous structures due to the outflow rather than inflow of blood. Velocity selective ASL has been suggested as a possible solution for evaluating perfusion in these situations. In these techniques, a T_2 magnetization preparation is introduced and images are acquired with and without flow sensitizing gradients. The subtraction of these images produces angiographic images which have been previously used to image the slow flowing blood in the peripheral vasculature [1,2]. With recent advances in image acquisition and preparation modules, an opportunity exists to apply this technique to complex vascular territories. In this work, we show preliminary experience using a B0, B1 and eddy current insensitive velocity selective ASL preparation with a minimal delay and 3D radial readout for non-contrast MRA/MRV to facilitate usage in challenging vascular territories.

Methods: Preparation modules were introduced into a 3D radial gradient echo imaging sequence. The volumetric velocity selective ASL preparation pulse was achieved using a symmetric, adiabatic BIR-8 preparation module and motion sensitizing gradients with a V_{enc} of 2 cm/s [3]. Preparation pulses were played out periodically followed by acquisition of 159 radial lines of a 3D radial trajectory with variable density in the readout direction [4]. A 3 s delay was added after each segment of 159 imaging projections to allow for T_1 recovery. Labeling and non-labeling preparation pulses were then interleaved to reduce bulk motion sensitivity. A normal volunteer was imaged under IRB consent with a clinical 3 T MR system (MR750, GE Healthcare, Waukesha, WI) using a 32-channel head coil (Nova Medical, Wilmington, MA, USA). Total acquisition time was 8.5 min with 10,000 radial lines sampled per labeled and unlabeled image volume. The effective sampled k-space radius was 320 points resulting in an acceleration of 16x due to angular undersampling. Scan coverage included an FOV of 22 x 22 x 18 cm^3 with an isotropic acquired voxel size 0.69 mm.

Fig. 1 Non-contrast velocity selective ASL MRA images from a volunteer reformatted as orthogonal MIPs allowing simultaneous visualization of arterial and venous structures.

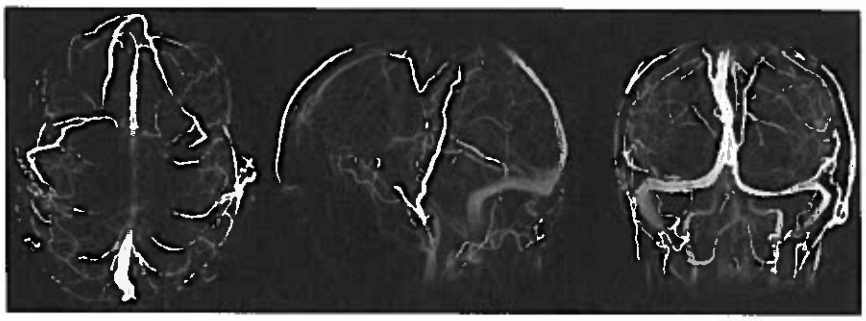

Results: Figure 1 shows Maximum Intensity Projection (MIP) images from a volunteer imaged without the administration of contrast. A high level of contrast is visible between moving and stationary spins. In particular, this can be observed in the venous structures demonstrating a high level of conspicuity of the deep cerebral and cortical veins. Images show the ability to capture simultaneous visualization of the rapidly flowing blood in the carotid arteries and the slow moving blood found in the sagittal sinus and draining veins. In this case, lower signal is observed above the nasal cavity due to signal loss in the images acquired without flow sensitizing gradients.

Conclusion: This work reports on initial experiences using a velocity selective ASL preparation pulse in combination with an isotropic high resolution 3D radial acquisition for non-contrast MRA outside of the peripheral vasculature. Images appear to provide a method to image venous structures without the need for contrast and with limited artifacts due slow flow. Improvement to the visualization of arterial structures may be realized with a less motion sensitive T_2 preparation and is an ongoing investigation.

References: [1] Fan et al. MRM, 62:1523-1532(2009) [2] Zhang et al. JMRI 43:364-372(2016) [3] Guo et al. MRM 73:1085-1094(2015) [4] Johnson et al. MRM 70:1241-1250(2013)

Session 7

Contrast Agent/Ferumoxytol

MRA and Non-Contrast CT Fusion: Initial Applications in TAVR Workup and Patients with Implanted Devices

Yoshida Takegawa, MD[1,2], Kim-Lien Nguyen, MD[1,3], Fei Han, PhD[1,2], Peng Hu, PhD[1,2], J. Paul Finn, MD[1,2]

[1]Diagnostic Cardiovascular Imaging Laboratory, [2]Department of Radiology, [3]Division of Cardiology, David Geffen School of Medicine at UCLA, Los Angeles, CA

Purpose: Whereas MRA provides excellent intraluminal contrast, it is insensitive to vascular calcification and fails to image indwelling metal devices due artifact. CT is exquisitely sensitive to calcium and can image a variety of indwelling hardware devices. However, in many patients, including some TAVR candidates, renal impairment makes iodinated contrast media and many gadolinium agents undesirable or contraindicated. We hypothesize that in patients where ferumoxytol is a suitable alternative to CTA, calcification and hardware devices may be accurately displayed over luminal anatomy by fusing non-contrast CT and ferumoxytol enhanced MRA (FEMRA) images. In a proof-of-concept study, we aim to demonstrate the accuracy of fusing both modalities.

Methods: Seven patients who were TAVR candidates and two patients with implantable device underwent FEMRA and also had non-contrast CT. CT and MR DICOM data were processed using Mimics software V18.0 (Materialize, Leuven, Belgium). Regions of interest (ROIs) on CT, which represent vascular calcification and implanted leads and devices, were isolated and registered to the FEMRA data. The ROI coordinates were registered in 3-dimensions on a Cartesian grid (x, y and z). Calcification voxels, pacing coil voxels and pacing box voxels were registered to the original FEMRA images and the fused images were marked as point ROIs using a DICOM viewing software (OsiriX®, Geneva, Switzerland). The location of each ROI from both sets of images were compared and evaluated.

Results: All patients had vascular calcification to varying degrees. One pacemaker patient (67 years, F) was evaluated pre-TAVR and another (78 years, F) was evaluated post-TAVR (Figure 1). Of the device patients, fifty-four ROIs were defined in case 1 and 30 ROIs in case 2. No significant offset errors were noted between the original FEMRA and fused FEMRA for case 1 (x= 0.75 (2.50 – 0.28) mm, y= 0.13 (0.23 – 0.00) mm, z= 1.58 (2.56 – 0.00) mm) and case 2 (x= 0.66 (1.40 – 0.00) mm, y= 0.05 (0.13 – 0.00) mm, z= 0.56 (1.50 – 0.00) mm). In all cases, the vascular calcification and implantable devices were fused successfully with the 3D FEMRA data. Volume rendered images clearly demonstrate the pacemaker lead and generator along with its positional relationship to vascular and intracardiac structures (Figure 1).

Conclusion: By fusing non-contrast CT and FEMRA, the locations of luminal anatomy, vascular calcification, and implantable devices can be accurately defined, thereby addressing the respective limitations of MR and CT for vascular and cardiac imaging.

Figure 1. Non-contrast CT (top left), FEMRA (middle left), and fused FEMRA (lower left) images are displayed in the left panel. The volume-rendered FEMRA image with calcium overlay (middle) belongs to a 78-year-old female with peripheral arterial disease, chronic renal failure, calcific aortic stenosis, and sick sinus syndrome status post a cardiac pacemaker who had successful TAVR placement. FE-MRA demonstrates the presence of a 23-mm Edward Sapien XT aortic bioprosthesis (top right, red arrows) and regions of signal void in the left upper chest, corresponding to the device generator (top right, green arrows). 3D color volume-rendered FE-MRA of the same patient with defined vessel borders and cardiac anatomy (lower right).

MRI with Ferumoxytol Across the Age Spectrum: Acute and Short-term Single Center Safety Experience

Kim-Lien Nguyen, MD[1,3], Takegawa Yoshida, MD[1,2], Fei Han, PhD[1,2], Ihab Ayad, MD[5], Gary M. Satou, MD[4], Brian L. Reemtsen, MD[6], Isidro B. Salusky, MD[7], Peng Hu, PhD[1,2], J. Paul Finn, MD[1,2]

[1]Diagnostic Cardiovascular Imaging Laboratory, [2]Department of Radiology, [3]Division of Cardiology, [4]Division of Pediatric Cardiology, [5]Department of Anesthesiology, [6]Division of Cardiothoracic Surgery, [7]Division of Pediatric Nephrology, David Geffen School of Medicine at UCLA, Los Angeles, CA

Purpose: We aim to summarize our single-center safety experience with the off label use of ferumoxytol for MRI and to compare the effects of ferumoxytol on monitored physiologic indices in patients under anesthesia with those of gadofosveset trisodium.

Materials and methods: Consecutive patients who underwent ferumoxytol-enhanced (FE) MRI exams between 2013 and 2016 were included. Adverse events (AEs) were classified according to the Common Terminology Criteria for Adverse Events v4.0. In a subgroup of patients examined under general anesthesia, recording of blood pressure, heart rate, oxygen saturation and end-tidal CO2 was performed. For comparison, a comparable group of patients who underwent gadofosveset-enhanced (GE) MRI under anesthesia with similar monitoring was also analyzed.

Results: 250 unique patients (148 adults and 102 children; 278 injections), ages 2 days to 94 years, underwent FE-MRI. No ferumoxytol-related severe, life threatening, or fatal AEs occurred acutely or at follow-up (16.1±9.4 months). Two patients developed ferumoxytol-related nausea, which was classified as a mild AE. In both the ferumoxytol and gadofosveset groups who had anesthesia, no AEs occurred. Between group (FE-MRI vs GE-MRI, Figure 1A) and within group (FE-MRI, Figure 1B) variations of physiologic indices were not statistically different (p>0.05). No significant change in blood pressure or heart rate (p>0.05) was noted between slow infusion of ferumoxytol (n=113) vs bolus injection (n=145) (p>0.05). Five patients had two or more FE-MRI exams.

Conclusions: In our single center experience encompassing 250 unique patients (278 injections) over a period of 3 years, no serious acute or short-term AEs occurred with the diagnostic use of ferumoxytol. Because of the modest population in our single center study, firm conclusions cannot be drawn about the generalizability of our results and thus vigilance and monitoring are recommended to mitigate potential rare adverse reactions.

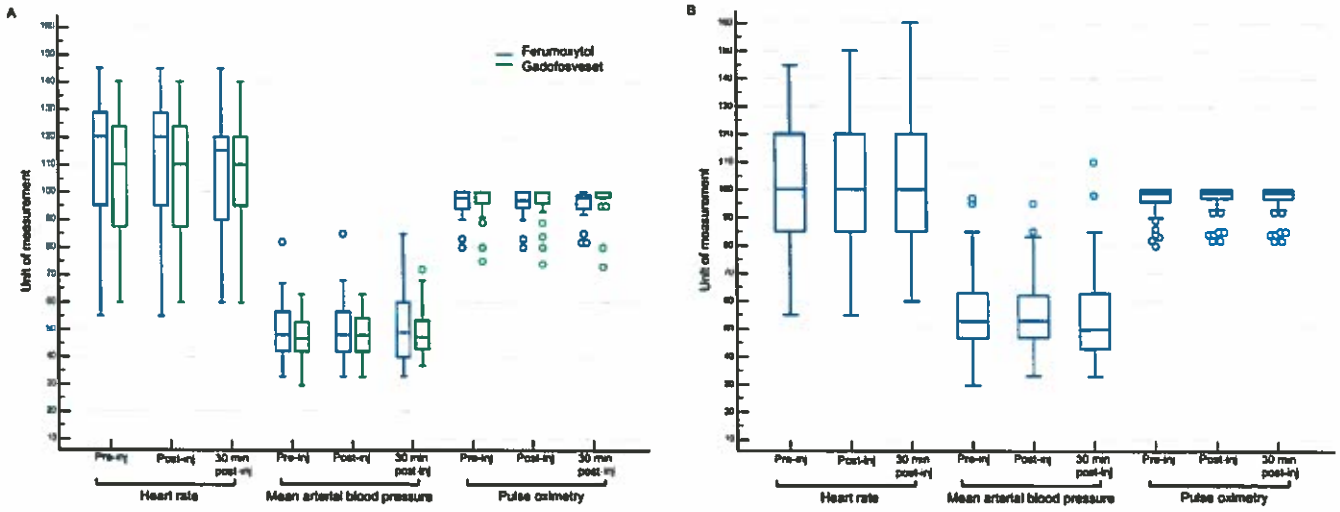

Figure 1: Comparison of hemodynamic and pulse oximetry measures in patients who had ferumoxytol-enhanced MRI exams and gadofosveset-enhanced MRI exams. ***Panel A*** summarizes the HR (bpm), MAP (mmHg), and pulse oximetry (%) distribution of all patients undergoing FE-MRI. Variations in HR, MAP, and oximetry were not statistically significant (ANOVA p>0.05). ***Panel B*** compares the HR, MAP, and pulse oximetry distribution between a comparable group of patients undergoing FE-MRI (n=23, ages 3 days to 13 years, 43% female) and GE-MRI (n=23, ages 2 days to 12.6 years, 43% female) under general anesthesia. *ANOVA*, analysis of variance; *bpm*, beats per minute; *HR*, heart rate; *MAP*, mean arterial blood pressure.

Experience with Ferumoxytol-enhanced magnetic resonance angiography (FeMRA) using standard MRA sequences in patients with advanced renal failure - a case series of 31 patients

Martin Hennessy [1], Sokratis Stoumpos [1], Patrick Mark [1,2], David Kingsmore [1,2], Alex Vesey [1], Aleksandra Radjenovic [2], Giles Roditi [1,2]

1 NHS Greater Glasgow & Clyde, Glasgow, UK

2 British Heart Foundation Glasgow Cardiovascular Research Centre, Institute of Cardiovascular and Medical Sciences, University of Glasgow, UK

Purpose

All angiographic modalities have drawbacks in frail patients with advanced renal failure. CT and invasive angiography both use ionising radiation and iodine-based contrast agents while the latter carries the risk of procedural complications such as vessel damage. Ultrasound and non-contrast MRA techniques avoid radiation but do not reliably answer clinical questions. Gadolinium-based contrast agents (GBCA) are avoided for contrast-enhanced (CE) MRA due to concerns regarding NSF. Ferumoxytol (an ultrasmall superparamagnetic iron oxide compound) can be used as a MRI contrast agent and we have been assessing its diagnostic utility in patients for whom there is no safer or effective alternative imaging modality, using standard CE-MRA sequences.

Methods

Patients with advanced renal failure - including those on renal replacement therapy - and a clinical indication for imaging were offered FeMRA on a Siemens MAGNETOM Prisma 3.0 T. The imaging protocol used the same sequences as our usual CE-MRA protocol with GBCAs comprising dynamic, first pass and high resolution imaging where required. This includes 1 mm isotropic resolution FLASH: TR 2.88 msec, TE 1.04 msec, Flip angle 20 degrees . The scans were qualitatively assessed by radiologists with a vascular expertise and patient management planned.

Results

In all 31 consecutive patients, ferumoxytol was well tolerated with no adverse reactions. There was suboptimal image quality in the abdomen for one patient who could not comply with breath holding. In all other cases, excellent vascular contrast for both arterial and venous evaluation with excellent image quality. FeMRA has allowed the planning of renal transplantation, assessment for angioplasty targets in patients with peripheral vascular disease, planning of renal arterial stent, obviated invasive diagnostic arteriography in detection of endoleaks and allowed assessment of failing dialysis fistulae with identification of peripheral (Fig 1) and central (Fig 2) venous stenoses. Variant vascular anatomy has been demonstrated (Fig 3.) In addition, non-vascular applications were explored, both by design (assessment of a complex renal cyst) and by coincidence (incidental renal tumour discovered).

Discussion

Use of ferumoxytol continues to yield valuable diagnostic information in patients with advanced renal failure in whom other imaging modalities are either contra-indicated or carry significant risk. While work is needed to optimise dosing and protocols, our experience shows that standard GBCA MRA protocols can yield diagnostic quality images. FeMRA has the potential to redress the inequalities from which patients with advanced renal failure suffer with regards to safe and available imaging techniques.

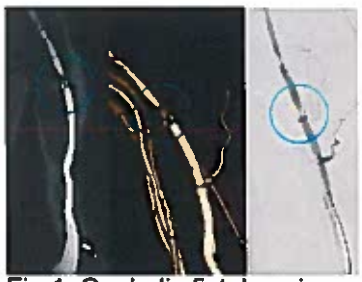

Fig 1: Cephalic fistula vein stenosis on FeMRA and DSA

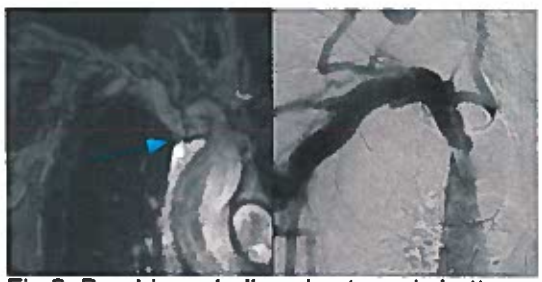

Fig 2: Brachiocephalic vein stenosis better seen on FeMRA than DSA

Fig 3: Double IVC

Improved Image Quality of Ferumoxtyol-enhanced 4D Flow MRI Compared to Gadofosveset Trisodium.

Nicholas S Burris MD[1,3], Kanae Mukai MD[1,2], Michael D Hope MD[1]
[1]University of California San Francisco, Department of Radiology
[2]University of California San Francisco, Department of Cardiology
[3]University of Michigan, Department of Radiology

PURPOSE: Blood pool contrast agents yield stable intravascular concentrations during the long scan times (8-15 minutes) required for three-directional phrase contrast MRI (4D Flow)[1]. Gadofosveset (Albavar), a gadolinium-based compound, and ferumoxytol (Feraheme), an iron-based compound, are both blood pool agents with high relaxivity values and long intravascular half-lives, although unlike gadofosveset, ferumoxytol can be safely administered to patients with renal insufficiency.[1,2] Additionally, ferumoxtyol has been shown to improve contrast between the left ventricular blood pool (LVBP) and myocardium, allowing for accurate segmentation of the endocardial border and calculation of ventricular volumes from 4D Flow magnitude data.[3] The purpose of this study was to compare image quality parameters in the left ventricle and ascending aorta between the blood pool contrast agents gadofosveset and ferumoxytol.

METHODS: Over a 9-month period we prospectively enrolled 20 patients scheduled to undergo MRA imaging of the chest. Clinical MRA imaging was performed on the same 3T GE scanner using either ferumoxytol (0.1 mL/kg)(n=10) as an off-label MR contrast agent for patients with renal insufficiency (GFR<30) or gadofosveset trisodium (0.12 mL/kg)(n=10) for patients with adequate renal function (GRF >30). 4D Flow data was acquired immediately after clinical MRA, and data was reconstructed and visualized using proprietary software (Arterys). Signal-to-noise ratio was measured in the tubular ascending aorta (SNR_{AO}) and LV blood pool (SNR_{LV}) on magnitude images, during diastole by two-point ROI method using the formula S/σ_{air} where S is mean ROI pixel intensity and σ_{air} is the standard deviation of pixel intensity in air. Contrast-to-noise ratio between LVBP and LV myocardium (CNR_{LV}) was calculated using the formula $(S_{myo} - S_{blood})/\sigma_{air}$ during diastole at the level of the basal interventricular septum. Group means were compared using unpaired t-tests assuming unequal variance.

RESULTS: Mean patient age was 63.6 ± 16.3 years, and ferumoxytol patients were significantly older (70.5 ± 15.3 vs. 56.7 ± 14.6 y, p=0.05). The majority of patients were male (13/20) with average BMI of 28.8 ± 4.2 kg/m^2. Average 4D Flow acquisition time was 11:20 ± 2:10 min, and did not significantly differ between contrast agents. Signal-to-noise ratios in the ascending aorta and LV were significantly higher with ferumoxytol compared to gadofosveset (SNR_{AO}: 73.0 ± 13.2 vs. 37.2 ± 5.0, p=0.03 and SNR_{LV}: 72.8 ± 14.1 vs. 36.0 ± 5.0, p=0.03). Similarly, contrast-to-noise ratio between the LV myocardium and blood pool was significantly higher with ferumoxytol (41.8 ± 8.3 vs. 11.0 ± 9.0, p<0.01).

CONCLUSION: Ferumoxytol resulted better 4D Flow image quality compared to gadofosveset, with an approximately two-fold increase in SNR in the ascending aorta and LV as well as a several fold increase in CNR between the LVBP and LV myocardium, improving delineation of the endocardial boarder. Ferumoxytol is an ideal contrast agent for 4D Flow MRI, especially in patients with renal dysfunction where gadolinium contrast agents are contraindicated.

REFERENCES:

1. Bock J, Frydrychowicz A, Stalder AF, et al. 4D phase contrast MRI at 3 T: effect of standard and blood-pool contrast agents on SNR, PC-MRA, and blood flow visualization. *Magn Reson Med.* 2010;63(2):330-338.
2. Finn JP, Nguyen KL, Han F, et al. Cardiovascular MRI with ferumoxytol. *Clin Radiol.* 2016.
3. Hanneman K, Kino A, Cheng JY, Alley MT, Vasanawala SS. Assessment of the precision and reproducibility of ventricular volume, function, and mass measurements with ferumoxytol-enhanced 4D flow MRI. *J Magn Reson Imaging.* 2016.

Preferred Format: Oral
Potchen Award: Eligible

Susceptibility Weighted Imaging of Arteries and Veins with using Ferumoxytol

E. Mark Haacke, PhD[1,3], Jean-Christophe Brisset PhD[2], Saifeng Liu PhD[3], Zeynep Demir[2], Yulin Ge MD[2]
[1]Department of Radiology, Wayne State University, 3990 John R, Detroit, MI 48201 USA, [2]Department of Radiology, New York University School of Medicine, New York, NY 10016 USA, [3]The MRI Institute for Biomedical Research, Waterloo, Ontario, Canada

Purpose: Microvascular abnormalities have been increasingly identified as the basis of many neurovascular and neurodegenerative disorders[1]. Imaging the cerebral venous system is currently achieved using susceptibility weighting imaging (SWI)[2,3]. However, SWI is unable to image arteries since arterial blood has the same susceptibility as the surrounding tissue (due to the lack of deoxygenated hemoglobin). This study was designed to evaluate the ability of SWI to image both the arterial and venous systems with ultra-high-resolution at 3T and 7T with the injection of an ultra-small-superparamagentic-iron-oxide (USPIO) agent, Ferumoxytol (a negative blood pool contrast agent).

Methods: Pre- and post-Ferumoxytol (2 or 4 mgFe/kg) SWI was performed on two healthy volunteers at both 3T and 7T MR. In order to obtain ultra-high resolution images (0.11x0.22x1.25mm), an asymmetric gradient-echo SWI sequence was used with the following image parameters: TR = 35ms, TE1 = 8ms, TE2 = 16ms and flip angle = 10° for a 13 min acquisition time for each echo. SWI data were processed using a high-pass filter with a 96x96 kernel since we were interested only in the small structures, i.e., the vessels.

Results: This USPIO driven MR angiography and venography (MRAV) approach successfully enhanced both the venous and arterial systems. The visibility of the arteries in the basal ganglia and cerebellum was improved as well as in the periventricular area (Figure 1). Exploiting the flow effect at short echo time (8ms), pre-USPIO MRAV maximum intensity projection allows arterial vasculature to be highlighted pre-contrast (Figure 1A). Small artery blooming was seen on post contrast MRAV, more prominent at longer TE (Figure 1D TE=16ms) than at low TE (Figure 1C TE=8ms). Small arteries (diameter=200~400μm) were seen 1.5~2 times bigger on post-contrast MRAV with TE=16ms (Figure 1D). Some very small cortical arteries can also be seen.

Conclusion: We have demonstrated the feasibility to generate ultra-high-resolution MRAV using USPIO-enhanced SWI. This could represent a powerful new tool in detecting microvascular abnormalities not visible on conventional MRA.

Keywords: USPIO, MRI, SWI, Susceptibility, blooming effect, arteriogram, venogram, angiogram, MRAV

Figure 1: Pre-contrast TE=8ms data (A) shows arteries on the MIP due to the time of flight effect and (B) shows veins on the mIP conventional SWI due to the stronger susceptibility of deoxyhemoglobin (but no arteries). Post-Ferumoxytol (2mg/kg) SWI (C) shows both veins (blue arrows) and arteries (red arrows). With the blooming effect, the vessels appear bigger on the images post-contrast (yellow arrows) at TE=8ms (C) and even bigger at longer TE = 16ms (D).

References

1. Brown, W.R. & Thore, C.R. Review: cerebral microvascular pathology in ageing and neurodegeneration. *Neuropathol Appl Neurobiol* **37**, 56-74 (2011).
2. Ge, Y., Grossman, R.I. & Haacke, E.M. Susceptibility weighted imaging in multiple sclerosis. in *Susceptibility weighted imaging in MRI* (eds. Haacke, E.M. & Reichenbach, J.R.) 249-264 (Wiley&Sons Inc, Hoboken, 2011).
3. Haacke, E.M., Xu, Y., Cheng, Y.C. & Reichenbach, J.R. Susceptibility weighted imaging (SWI). *Magn Reson Med* **52**, 612-618 (2004).

Session 8

Contrast Enhanced MRA

Evaluation of Four Injection Strategies for High Spatial Resolution Gadobenate Dimeglumine-Enhanced MR Angiography

Gregory J. Wilson and Jeffrey H. Maki
University of Washington, Department of Radiology, Seattle, WA, USA

Introduction: Contrast-enhanced MR angiography (CE-MRA) utilizes arterial water T_1 shortening during passage of intravenously injected contrast agent. Circulation of the contrast agent (*ie*, first-pass and subsequent dilution during recirculation) causes arterial signal intensity to vary throughout the acquisition. This signal modulation can cause image artifacts and blurring, such that the true image resolution may be limited by the bolus profile. Higher image resolution could be obtained by creating a signal intensity profile that is constant throughout the acquisition.

Such a signal intensity plateau can be created by tailoring the injection profile to a patient's individual hemodynamics using a test bolus and linear system theory.[1] Alternatively, one could utilize a one-size-fits-all, standardized injection that prolongs the signal enhancement. In any case, a steep signal enhancement upslope is desired to reduce ringing artifacts and venous enhancement. This study was conducted to evaluate signal intensity profiles from tailored injection profiles (TIPs) and standardized injections.

Methods: 19 (of eventual 40) subjects have been enrolled in this IRB-approved study. Each subject received a test bolus and one of four full-bolus injections (randomized), with total dose of 0.1 mmol/kg gadobenate dimeglumine (Bracco Diagnostics, Milan). Injection parameters (Table 1) were designed to provide 20 sec of signal enhancement (except the non-diluted, single-phase injection that represents a "typical" clinical injection). Bolus profiles were measured at 3T with a thick-slice, <1.5 sec temporal resolution, 3D SPGR acquisition with CE-MRA contrast parameters (TR = 3.5 ms, TE = 1.5 ms, flip angle = 30°), covering the entire aorta to reduce inflow signal. Signal intensity profiles were measured from a single ROI placed in the supra-celiac abdominal aorta.

Table 1. Summary of the four injection protocols.

Injection Type	Contrast (0.1 mmol/kg)	Test Bolus	Full Bolus
Non-diluted, Single-phase*	non-diluted	1 mL @ 1.6 mL/s	Remaining mL @ 1.6 mL/s
Diluted, Single-phase	diluted to 40mL	2 mL @ 2 mL/s	38 mL @ 1.6 mL/s
Diluted, Bi-phasic	diluted to 40mL	2 mL @ 2 mL/s	9 mL @ 3.3 mL/s and 29 mL @ 1.4 mL/s
Diluted, TIP	diluted to 40mL	2 mL @ 2 mL/s	Varied (TIP algorithm)

*typical injection for comparison

Results: Example full-bolus signal intensity profiles are shown in Figure 1. The non-diluted, single-phase injection shows a peaked signal intensity profile with no "plateau" phase. The three diluted injections show elongated signal enhancement phases with reduced peak signal enhancement (eg, peak height *vs.* recirculation tail) compared to the "typical" injection.

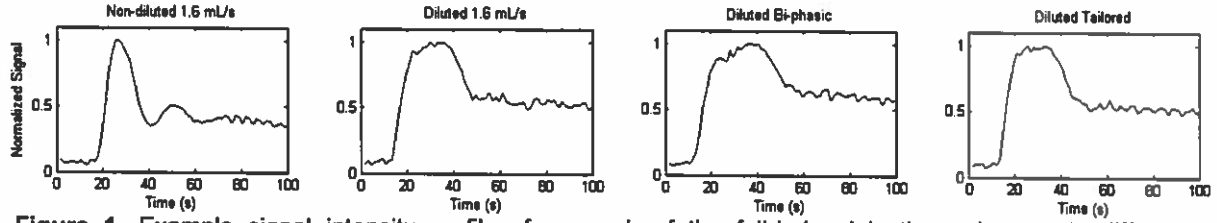

Figure 1. Example signal intensity profiles from each of the full-bolus injection schemes (4 different subjects). The first three injection profiles (from left) are standardized. The "tailored" injection profile (right) is patient-tailored using the TIP algorithm.[1]

Discussion: Elongated injection profiles provide longer signal enhancement with somewhat reduced peak signal intensity. Constant signal enhancement will produce sharper CE-MRA images by reducing bolus profile blurring. In addition, gadolinium contrast agent relaxivity effects limit the reduction of peak signal intensity such that resulting CE-MRA images will have sufficient signal-to-noise.[2,3] Multi-phasic injections (Diluted Bi-phasic and Diluted Tailored) allow a steeper enhancement upslope, allowing earlier acquisition start and thus less venous enhancement. Finally, the TIP algorithm provides a patient-specific injection profile to reduce patient variability and optimize the use of contrast agent dose.

Acknowledgments: Research funding provided by Bracco Diagnotics.

References:

1. Wilson GJ, Maki JH. J Magn Reson Imaging, Apr 19 (2016). [Epub ahead of print]
2. Wilson GJ, Woods M, Springer CS Jr, Bastawrous S, Bhargava P, Maki JH. *Magn Reson Med.* Dec;72(6):1746-54 (2014).
3. Wilson GJ, Springer CS, Bastawrous S, Maki JH. *Magn Reson Med,* Jun 14 (2016). [Epub ahead of print]

The impact of injector based contrast agent administration in time-resolved MRA

Johannes Budjan[1], Ulrike Attenberger[1], Hubertus Pietsch[2] and Gregor Jost[2]

[1] Department of Clinical Radiology and Nuclear Medicine, University Medical Center Mannheim, Germany
[2] MR and CT Contrast Media Research, Bayer Pharma AG, Berlin, Germany

Introduction: Time-resolved contrast enhanced MR-angiography (4D-MRA) allows the visualisation of the vascular contrast agent (CA) passage at high temporal resolution and with large volume coverage. This allows a simultaneous evaluation of anatomical and functional parameters. Dynamic information about arterial and venous blood flow is of high importance in the evaluation of various vessel pathologies, such as in the functional analysis of vascular malformations or in the evaluation of vessel stenoses. Thus, 4D-MRA is increasingly used in several clinical applications. The use of time-resolved acquisition techniques makes the bolus timing less critical and CA administration more straightforward compared to static MRA. Although the use of power injectors ensures a standardized and well-controlled injection, hand injections are still frequently used for MRA procedures. The aim of the present study was to compare power injector based CA administration with hand injection in 4D-MRA under highly standardized conditions in an animal model.

Methods: Thoracic-abdominal 4D-MRA (TWIST, TR/TE/α = 2.4ms/0.87ms/25°) was performed two times on 6 anesthetized Göttingen minipigs. Gadobutrol (Gadovist, Bayer Pharma AG) was injected at a dosage of 0.1 mmol/kg body weight followed by 20 ml saline either by manual injection or by using a power injector (MRXperion, Bayer Pharma AG; flow rate = 2 ml/s) in randomized order. The injection was started after the completion of the reference scan and 24 image stacks with an image update-time of 2s were acquired. A quantitative comparison of vascular signal enhancement was performed in the subtraction images by ROI measurements in the descending aorta (level of truncus pulmonalis), the renal arteries and the inferior vena cava (above kidneys).

Results: The time-resolved analysis of the signal enhancement representing the bolus curve revealed higher peak enhancements in all three anatomical regions for the automated injection compared to hand injection. Additionally, different bolus shapes between the two injection methods were found. Power injector use results in a compact first-pass bolus shape that is clearly separated from the second pass bolus (recirculation). For the manual injection the first-pass bolus is disrupted into two peaks, i.e. a dominating first peak closely followed by second peak with lower signal intensity (Fig.1). This leads to a prolonged first-pass bolus that fills the gap (i.e. the signal decline) seen between first and second-pass when using the power injector.

Discussion: In 4D-MRA a well-defined bolus shape is essential for functional analysis of blood flow. Manual hand injections are operator dependent and have no control about the precise injection rate. However, most important for 4D-MRA is the short interruption during manual injection when switching from the CA administration to saline by changing the syringes on the i.v. tubing. At this moment the tubing is still filled with CA which is subsequently administered by the saline flow. This short time delay results in a disrupted CA administration and leads to an additional vascular bolus peak. The resulting highly undefined bolus profile can substantially impair flow analysis and potentially reduce the diagnostic information of 4D-MRA. In contrast, automated CA administration using a power injector enables the continuous administration of CA that results in a well-defined vascular bolus shape. Therefore, the use of power injectors should be recommended for 4D-MRA.

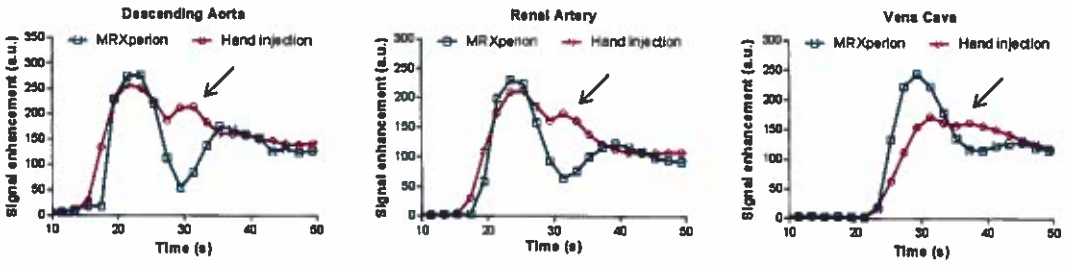

Fig1: Representative bolus shapes for CA administration either by hand or by the use of the power injector MRXperion. The additional first pass peak (arrow; introduced by hand injections) which is visible in the aorta, the renal arteries and the vena cava degrades the diagnostic opportunities in functional flow analyses. (a.u.: arbitrary units)

Injection Rate Optimization for CE-MRA: Predictions using Modulation Transfer Function Analysis

Toshimasa Clark[1,2], Gregory J. Wilson[2] and Jeffrey H. Maki[2]
1 – University of Colorado, Department of Radiology, Denver, CO, USA
2 - University of Washington, Department of Radiology, Seattle, WA, USA

Introduction: Optimization of CE-MRA involves a complex interplay between pulse sequence duration, bolus timing, contrast recirculation, and the subsequent R1-related increase and R2*-related reduction of vascular signal intensity. Often, little consideration is given to the contrast bolus itself, frequently injected over a duration much shorter than the acquisition time in belief that high contrast concentration improves SNR, thereby improving image quality. In reality, faster injection rates do not necessarily increase vascular signal intensity, but instead serve to decrease the bolus duration and effectively drop vascular signal intensity towards the end of the acquisition, essentially functioning as a low pass filter and causing blurring. This work attempts to quantify the effects of this multitude of variables through the analysis of the modulation transfer function (MTF) and suggest a framework for determining optimal CE-MRA injection strategies.

Methods: A computer-based CE-MRA model was developed (Matlab), able to model variable contrast injection rate and amount, as well as physiologic and image acquisition parameters over a wide gamut. Intra-arterial gadolinium concentration was predicted using Verhoeven's model with recirculation, with R1 and R2* calculated at each time point based on measured blood relaxivity (1,2). The MTF phantom consisted of a computer-generated swept sine wave designed in the fashion of test patterns used in the resolution testing of optical equipment. Its wavelength varied from 10,000 voxels to under 0.4 voxel, decreasing logarithmically. Using this model, contrast quantity, cardiac output, and MR imaging parameters such as B_0, TR, TE, acquisition time, spatial resolution and FOV can be infinitely varied and modulation transfer curves generated to determine the injection rates resulting in optimal resolution (defined as modulation dropping to 50% of its maximum - MTF_{50}) and image contrast (defined as area under MTF curve). A minimum SNR threshold of 10 was set to ensure adequate image quality. Specific simulations were performed for renal and carotid artery CE-MRA. We also present example patients who underwent carotid CE-MRA with slow effective injection rates.

Results: Figure 1 demonstrates a typical MTF curve for renal CE-MRA parameters, being a measure of resolution vs. spatial wavelength. Figure 2 shows corresponding MTF_{50} and AUC plots, suggesting in this case optimal contrast injection rates just below 1 mL/sec (peak AUC, minimum MTF_{50}). Optimal resolution (MTF_{50}) for renal and carotid CE-MRA is predicted for injection rates between 0.5-0.9 mL/sec and 0.2-0.3 mL/sec, respectively, dependent on contrast volume. Optimal image contrast (AUC) requires slightly faster injection rates. Administered contrast volume has more influence than does cardiac output. Simulated vessel phantom and clinical carotid CE-MRA exams at an effective contrast injection rate of 0.5 mL/sec demonstrate increased resolution.

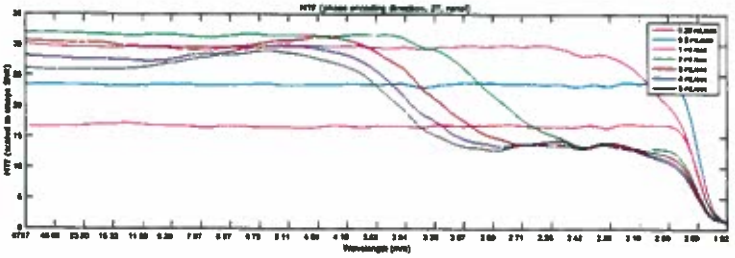

Figure 1. MTF curve, phase encoding direction, typical renal CE-MRA parameters, 3T. Effects of different contrast injection rates. Height of plateau to left can be thought of as SNR, with dropping amplitude as move right signifying resolution loss (related to bolus dropping off). Ultimate achievable resolution determined by pulse sequence parameters (x intercept to right).

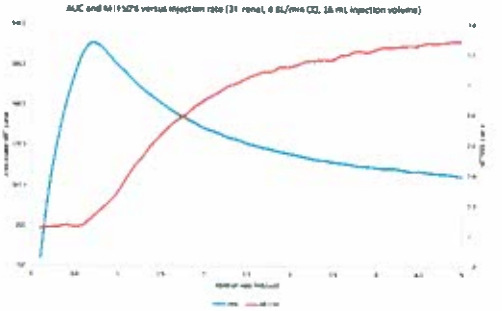

Figure 2. Renal CE-MRA simulation demonstrating MTF_{50} and AUC vs. Injection rate. Peak AUC represents best contrast, minimum MTF50 highest resolution.

Discussion: The relationship between vascular signal intensity and blood gadolinium concentration is highly non-linear, with increasing gadolinium concentration not necessarily leading to increased signal intensity. Higher injection rates such that the bolus "runs out" during the acquisition rely purely on recirculation to maintain R1 enhancement during peripheral k-space acquisition, and this modeling suggests that this leads to subtle, but significant resolution loss. Slower injections appear to optimize resolution by virtue of a longer injection duration, allowing for greater uniformity of R1 enhancement throughout k-space acquisition. Interestingly, this increased resolution comes with only a minimal SNR loss due in part to the non-linearity of R1 relaxivity and the R2* degradation seen as gadolinium concentrations increase. This work suggests optimal image resolution and contrast is achieved at intuitively slow effective injection rates (0.2-0.9 mL/s, dependent on imaging parameters).

References:

(1) Wilson GJ, Woods M, Springer CS Jr, Bastawrous S, Bhargava P, Maki JH. *Magn Reson Med.* Dec;72(6):1746-54 (2014).
(2) Wilson GJ, Springer CS, Bastawrous S, Maki JH. *Magn Reson Med,* Jun 14 (2016). [Epub ahead of print]

Basic Consideration of Contrast Bolus Dispersion and Pre-Clinical MRA Investigation of Dependencies on Cardiac Output Parameters and on Injection Rates

Gregor Jost[1], Harald Kramer[2], Martin Rohrer[1], [1]Radiology, Bayer Pharma AG, Berlin, Germany, [2]Department of Clinical Radiology, University Hospital Munich, Germany

Purpose: To validate basic principles of contrast agent bolus behavior in MRA by standardized animal experiments.

Methods: Three healthy anaesthetized minipigs were imaged with a 2D T1w GRE "test-bolus" sequence to assess SI changes in the superior vena cava, the pulmonary artery as well as the ascending aorta after administration of GBCA with different injection protocols. In addition 2D-Phase Contrast blood flow measurements were performed at the level of the descending aorta. Cardiac output was influenced by modification of anesthesia or application of cardiac stressors.

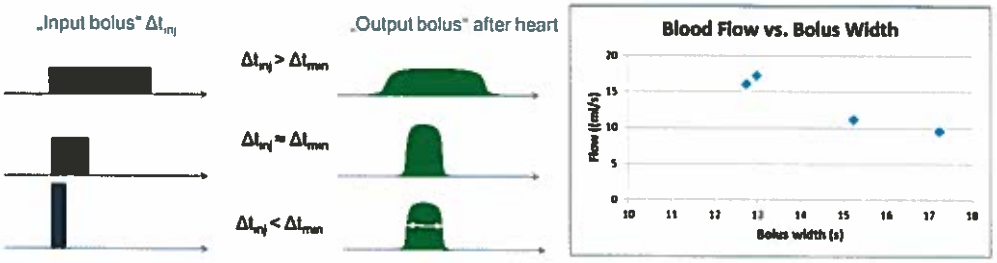

Fig1. (Left) Impact of injection time (Δt_{inj}) and minimum broadening time (Δt_{min}) on the bolus profile. (Right) Correlation of blood flow and bolus width for different cardiac outputs.

Results: If injection time is long compared to the minimum cardiac broadening time / cardiopulmonary passage, the characteristics of the input bolus will be transferred to the arterial system. I.e. the aortic bolus profile is basically independent of the bolus dispersion during heart-lung passage and widely independent of blood flow / cardiac output.(Figure 1)

If injection time is short compared to minimum broadening time the input bolus will not be transferred to the arterial system. I.e. the aortic bolus profile strongly depends on the bolus dispersion during heart-lung passage and blood flow / cardiac out.

The PC based blood flow measurements estimating the cardiac output correlates well with the bolus width/ bolus broadening.

Conclusion: Depending on the ratio of injection time and minimum cardiac bolus broadening the bolus profile before the cardiopulmonary passage is transferred to the arterial system. Cardiac output parameters as well as individual cardio-vascular parameters estimated by 2D PC-MRI correlate well with bolus geometry. The impact of injection time vs. minimal bolus broadening time is a valid assumption.

References: Kramer 2014 SMRA

MASE: Model-Based Angiogram Separation for Highly Accelerated, Motion-Resistant Dynamic Contrast Enhanced Magnetic Resonance Angiography

Eun Ji Lim[1], Jaeseok Park[1]

[1]Department of Biomedical Engineering, Sungkyunkwan University, Suwon, Korea, Republic of

Introduction: The objective of this work is to develop a novel, model-based angiogram separation method (MASE) for highly accelerated, robust DCE MRA even in the presence of subject motion and measurement noise. To this end, we propose a new, DCE signal model, which consists of stationary background ($\mathbf{X_0}$), DCE signals of interest ($\mathbf{X_{DCE}}$), and motion-induced signals ($\mathbf{X_M}$). Then, $\mathbf{X_{DCE}}$ and $\mathbf{X_M}$ signals are enforced to lie in the subspaces that are constructed using concentration time-course related single compartment recirculation (SCR) model and motion-mimicking (rotational, translational, random) synthetic model, respectively. Robust DCE angiogram is extracted by integrating the proposed signal model into a constrained optimization problem with sparsity and low rank priors under the framework of compressed sensing.

Methods: We model DCE signals in x-t space in the presence of noises $\mathbf{N}$: $\mathbf{X} = \mathbf{X_0} + \mathbf{X_{DCE}} + \mathbf{X_M} + \mathbf{N}$: **1) Concentration Time-Course Model:** A concentration time-course can be described by the single compartment recirculation (SCR) model [1], while stationary tissues remain nearly identical over the entire dynamic phases. Despite the nonlinearity of the concentration time-course, we hypothesize that it can be delineated by linear superposition of a few temporal bases found using singular value decomposition (SVD) of the SCR model-based synthetic data: $\mathbf{D} = \mathbf{U_D}\mathbf{\Sigma_D}\mathbf{V_D^H}$ where $\mathbf{D}$ is the row-vectorized (concentration time-course), stacked (row-wise) simulation data, $\mathbf{U_D}$ is the spatial basis, $\mathbf{V_D}$ is the temporal basis, $\mathbf{\Sigma_D}$ is the singular value matrix. Since $\mathbf{D}$ is substantially correlated in the temporal direction, the concentration time-course can be synthesized using only a few principal eigenvectors $\mathbf{V_r}$ from $\mathbf{V_D}$. **2) Motion-Mimicking Model:** Motion induced signals are synthesized by employing all possible variations of background pixels that potentially emulate translational, rotational, and random motions [2]. It is because the neighboring pixels share similar distribution across time frames while showing strong correlations inversely proportional to the distances between pixels. A subspace, in which motion-induced signals are located, can be learned from the residual images between the background mean and the synthesized images by using SVD and then taking the left singular vectors: $\mathbf{M} = \mathbf{U_M}\mathbf{\Sigma_M}\mathbf{V_M^H}$ where $\mathbf{M}$ is the row-vectorized, stacked residual data. $\mathbf{U_M}$, $\mathbf{V_M}$ and $\mathbf{\Sigma_M}$ are the left, right singular vectors and the singular value matrix, respectively: Given the considerations above, the proposed DCE signal model is reduced to: $\mathbf{X} \cong \mathbf{X_0} + \mathbf{U_D}\mathbf{V_r} + \mathbf{U_M}\mathbf{U_M^H}(\mathbf{X} - \mathbf{X_0}) + \mathbf{N}$. **3) MASE:** The proposed angiogram reconstruction from undersampled k-t space is performed by solving the following constrained optimization problem with sparsity prior: $\min_{\mathbf{U},\mathbf{X_M}} \|\varphi_1(\mathbf{U})\|_1 + \lambda_M \|\varphi_2(\mathbf{X_M})\|_1$ s.t. $\mathbf{d_r} = \mathbf{F_u}(\mathbf{AUV_r} + \mathbf{BX_M})$ where $\mathbf{A} = \mathbf{U_M}\mathbf{U_M^H} + \mathbf{I}$, $\mathbf{B} = \mathbf{U_M}\mathbf{U_M^H}$, $\mathbf{I}$ is the identity matrix, λ_M is the balancing parameter between $\mathbf{X_{DCE}}$ and $\mathbf{X_M}$, $\mathbf{d_r}$ is the measured, residual (k-t space) between the reference and DCE data, and $\mathbf{F_u}$ is the Fourier undersampling operator, and $\varphi(\cdot)$ is a sparsifying transform function. Then, DCE angiograms are reconstructed by a product of $\mathbf{U}$ and $\mathbf{V_r}$. **4) Data acquisition:** DCE MRA data was acquired at 3T whole-body MR scanner (MAGNETOM Verio, Siemens Medical solutions) using TWIST (TR/TE=2.5ms/0.94ms, FA=25°, matrix size= 320x240x144, 20 phases). The acquired images were Fourier transformed and then decimated to generate random undersampling for image reconstruction.

Results: Figure 2 compares the proposed MASE with conventional dynamic CS [3] and k-t RPCA [4] at R = 40. Among the competing methods, the proposed MASE clearly delineates time-varying DCE angiograms with the lowest level of background artifacts and noise.

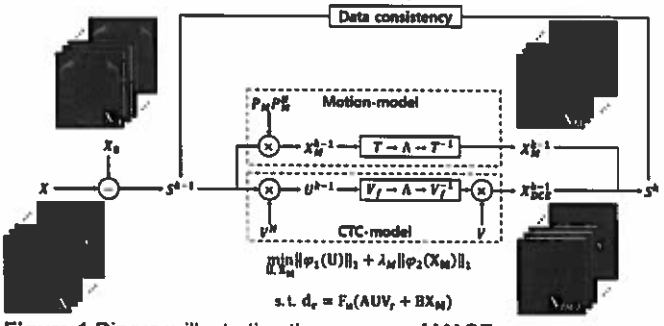

Figure 1 Diagram illustrating the process of MASE.

Conclusion: We successfully demonstrated the feasibility of the proposed MASE in DCE MRA with increasing reduction factors. In this work, DCE angiogram signals and motion-induced artifacts are directly modeled and reconstructed, while the other signals that do not lie in the subspace of DCE angiogram tend to be neglected. It is expected that the proposed MASE would enable a rapid, robust DCE MRA and widen its applications in a clinical routine.

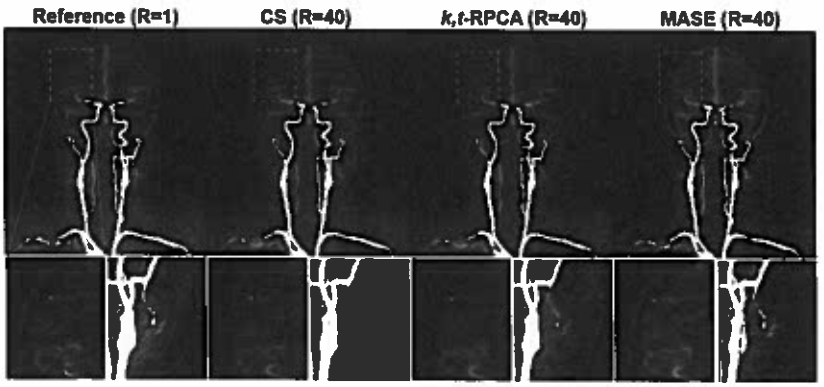

Figure 2 Comparisons of reconstruction methods for DCE MRA of the reference (conventional subtraction-based method), CS, k-t RPCA, and the proposed MASE (R=40) : MIP DCE angiograms and magnified ROI (bottom)

References: [1] Johnson G, et al. MRM 2004. [2] Suhyung P, et al. ISMRM 2016. [3] Rapacchi S, et al. MRM 2014. [4] Trémoulhéac B, et al. TMI 2014.

Purpose:

An IRB approved and HIPAA compliant retrospective review of 560 Pulmonary MRA cases performed for the primary diagnosis of pulmonary embolism (PE) was performed to determine the prevalence of direct and indirect findings of PE.

Materials and Methods:

After local IRB approval a retrospective review of 560 CE-MRA exams performed for the primary diagnosis of pulmonary embolism was performed with enumeration of the findings of PE. There were 30 patients with at least one PE reviewed. The indirect findings studied included the following: high T2W signal intensity pulmonary infarction, perfusion defects, pleural effusion, enhancing parietal pleura, enhancing pleural effusion, pulmonary venous stasis, vessel wall enhancement, and atelectasis.

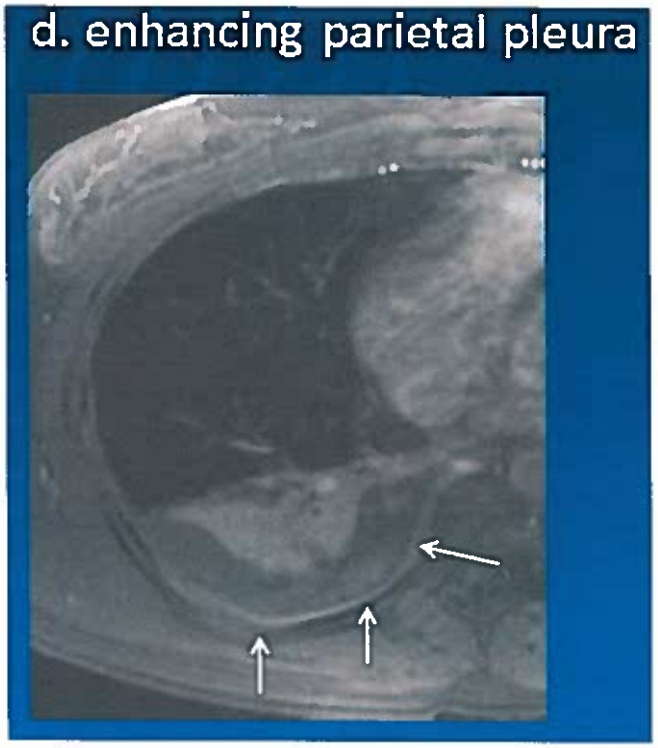

Results:

The indirect findings: 15/60 high T2W signal intensity pulmonary infarctions, 43/60 perfusion defects, 13/60 pleural effusions, 6/60 enhancing parietal pleura, 3/60 enhancing pleural effusion, 20/60 pulmonary venous stasis, 8/60 vessel wall enhancement, and 6/60 atelectasis.

Conclusion:

There are indirect findings of pulmonary embolism found at contrast enhanced pulmonary MRA. We describe here our preliminary results regarding the indirect findings of PE that are also seen at CTA along with new observations that are unique to MRA. Knowledge of these indirect findings can assist in helping to localize PE and determine its likely presence when the PE is small or in the process of dissolution from thrombolysis.

High Efficiency Coronary MRA with Non-Rigid Cardiac Motion Correction

Jianing Pang [1], Yuhua Chen [1,2], Zhaoyang Fan [1], Christopher Nguyen [1], Qi Yang [1], Yibin Xie [1], Debiao Li [1,3]

[1] Biomedical Imaging Research Institute, Cedars-Sinai Medical Center, Los Angeles, CA, USA
[2] Computer and Information Science, University of Pennsylvania, Philadelphia, PA, USA
[3] Bioengineering, University of California, Los Angeles, CA, USA

Purpose: Coronary arteries are challenging structures to image using MRI due to the small caliber, tortuous course, and continual motion. Current prospective ECG-triggering and navigator gating techniques tend to have low scanning efficiency, long scan time, and time-consuming setup. Both respiratory [1-3] and cardiac [4-5] motion correction techniques have been proposed to address such limitations. In this work, we proposed a new cardiac motion correction framework based on 4D coronary MRA [6], with retrospectively selected cardiac acceptance window, non-rigid cardiac motion registration, and iterative, motion corrected reconstruction.

Methods: MR data was collected using a contrast-enhanced spoiled gradient echo sequence with 3D radial trajectory and retrospective cardiac and respiratory self-gating. Affine respiratory motion correction was performed and 16 cardiac phases were reconstructed. Next, the quiescent phases were selected and registered to a common reference phase using a symmetric diffeomorphic model [7]. Then, motion-corrected reconstruction was accomplished by iterative inversion of the encoding operator [8]. The reconstruction program was written in MATLAB. Healthy subjects (N=13) were scanned using a clinical 3T scanner (Verio, Siemens): TR/TE=6.0/3.7ms, flip angle=15°, FOV=$(320mm)^3$, matrix size=320^3, number of lines=99,994, scan time=10min, contrast enhancement with a 0.2 mmol/kg Gd-BOPTA (MultiHance, Bracco) injected at 0.3mL/s. Two images were reconstructed for each subject: conventional gating (Gating), which combined data directly from a contiguous quiescent window, and the proposed method, which accepted all phases with minimal intra-phase motion and combined them with inter-phase cardiac motion correction (Moco). The scan efficiency, coronary sharpness, and apparent signal-to-noise ratio (aSNR) were compared using paired Student's t-test with a significance level of 0.05.

Results: The mean aSNR for Gating and Moco were 11.89±3.76 and 13.9±5.21, respectively. Moco led to a significant improvement in aSNR (P=0.005). Moco also led to significant improvements in sharpness of LM (P=0.007), proximal RCA (P=0.04), middle RCA (P=0.02), and proximal LAD (P=0.04), over Gating. The mean scan efficiencies for Gating and Moco were 18.8% ± 6.0% and 40.9% ± 9.7%, respectively. Moco led to a significant improvement in scan efficiency (P<0.001). The numbers are summarized in Fig. 1. Fig. 2 shows images from two example subjects.

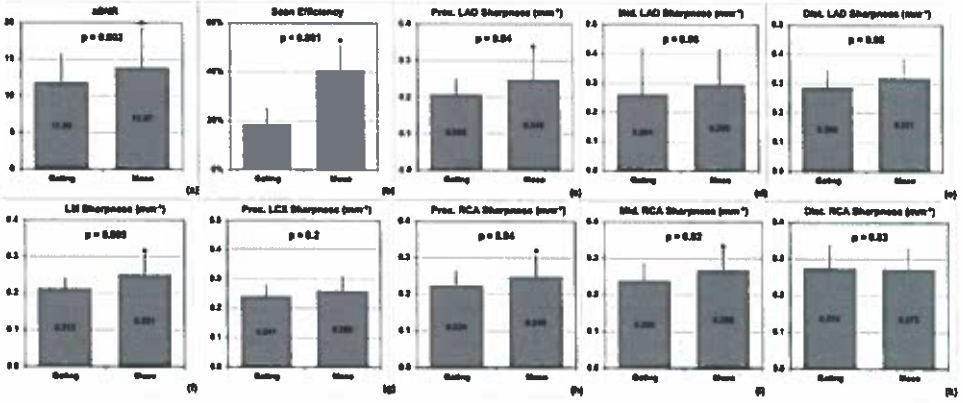

Figure 1 Comparisons of image quality metrics and scan efficiency

Conclusion: The proposed cardiac motion correction framework significantly increased the scan efficiency of whole-heart coronary MRA, and improves image quality given the same available data. Future works will be focused on further optimizing the motion correction algorithm, and exploring the potential to further scan time reduction.

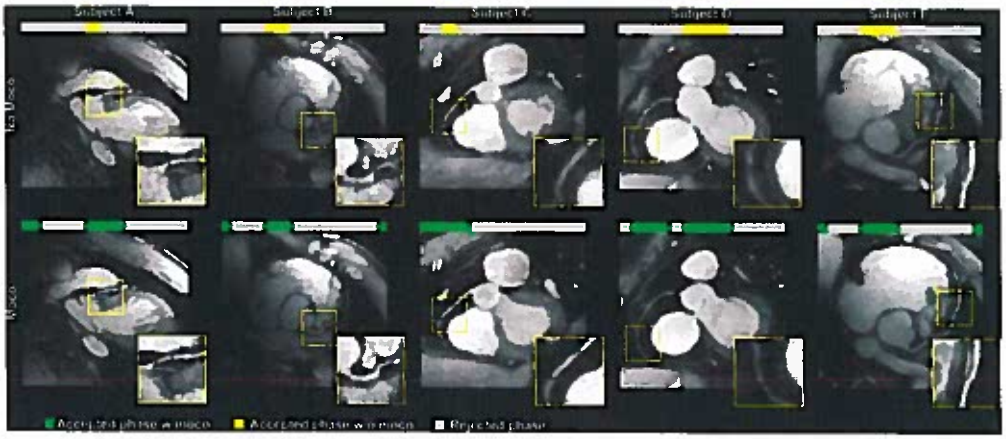

Figure 2 Example subjects comparing Gating (top) with Moco (bottom).

References: [1] Piccini MRM 2012;68(2):571 [2] Henningsson MRM 2012;67(2):437 [3] Pang MRM 2014;71(1):67 [4] Hardy MRM 2000;44(6):940 [5] Stehning MRM 2005;53(3):719 [6] Pang MRM 2014;72(5):1208 [7] Avants Med. Image Anal. 2008;12(1):26 [8] Schmidt MRM 2011;66(6):1541

Intravascular Agents for MR Venography in Children: a Comparison of Gadofosveset and Ferumoxytol.

Sarah N Khan MD, Takegawa Yoshida MD, J Paul Finn MD

Diagnostic Cardiovascular Imaging, Dept of Radiology, David Geffen School of Medicine, UCLA.

Purpose

Gadofosveset (Ablavar, Lantheus Medical Systems) has become popular for venographic imaging in children and adults [1] and is the only intravascular contrast agent approved by the U.S. FDA for MR angiography. With the imminent withdrawal from production of gadofosveset, there will be an unmet need for an intravascular agent with comparable imaging properties. Ferumoxytol (Feraheme, AMAG Pharmaceutials) has also shown promise as a steady state venous MR imaging agent in children [2,3]. However the relative performance of gadofosvoset and ferumoxytol has not been previously addressed. We compared the relative vascular enhancement, signal stability and adverse event rates of gadofosveset and ferumoxytol at similar molar dose levels for early and delayed phase venous imaging in children.

Materials and Methods

72 pediatric patients underwent MRI with ferumoxytol (N=34, 32 at 3.0T, 2 at 1.5T, mean age 5.2 ± 4.9 years, age range 3 days -16.2 years) or gadofosveset (N=38, 21 at 3.0T, 17 at 1.5T, mean age 3.7 ± 5.2 years, age range 1 day- 17.5 years) for a variety of clinical indications including pre- or post- organ transplant evaluation, venous access or congenital heart disease. High resolution MRA was performed at two or more time points post injection. The total administered Ferumoxytol dose was 4mg/kg. A subset of 12 age matched patients performed at 3.0T was selected from each group for detailed quantitative image quality and artifact evaluation and grading by two blinded pediatric radiologists. Vessels were divided into 18 venous segments depending on size and graded in the early venous phase (approximately 2 minutes post injection) and late venous phase (up to 40 minutes post injection) and scored according to: 1 = vessel not visualized or assessable due to poor image quality, 2 = vessel moderately well defined but only gross features (size/patency) are confidently assessable, 3 = vessel well defined and confidently assessable for structural pathology, 4 = excellent vessel definition with sharp borders such that fine details could be confidently evaluated. Signal to noise ratio (SNR) and contrast to noise ratio (CNR) calculations were performed in the portal vein and inferior vena cava for both the early and late venous phases.

Results

No adverse events were noted in any group with either agent. In all cases the reviewers were confident in their assessment and all images were considered diagnostic (score >= 2). Image quality grades were higher for Ferumoxytol (3.17 ± 0.39) compared to Gadofosveset (2.71 ± 0.58) in the early venous phase, and remained elevated for Ferumoxytol in the late venous phase (3.17 ± 0.62) but decreased for Gadofosveset (2.60 ± 0.57). In both venous phases, fewer artifacts were encountered for Ferumoxytol early venous (1.38 ± 0.68) than Gadofosveset early venous (1.46 ± 0.54); Ferumoxytol late venous (1.46 ± 0.45) and Gadofosveset late venous (1.65 ± 0.41). All vessels were graded higher with Ferumoxytol than Gadofosveset. Individual vessel grades for Gadofosveset typically decreased from the early venous phase to the late venous phase for all vessels except the tributaries of the superior and inferior pulmonary veins (1.92 ± 0.70 and 2.00 ± 0.75), the azygous vein (2.00 ± 0.88 and 2.06 ± 0.63), the middle hepatic vein (2.04 ± 0.92 and 2.05 ± 0.83), the internal iliac vein (1.68 ± 0.90 and 1.89 ± 1.05). In the early venous phase with respect to the portal vein, the SNR was: Ferumoxytol (135.37 ± 35.21) and Gadofosveset (114.65 ± 28.65); the CNR was Ferumoxytol (67.92 ± 31.84) and Gadofosveset (47.99 ± 23.63). In the late venous phase, the SNR was: Ferumoxytol (133.39 ± 28.53) and Gadofosveset (100.41 ± 23.39); the CNR was Ferumoxytol (52.06 ± 26.63); and Gadofosveset (35.06 ± 17.90).

Conclusions

Ferumoxytol produced higher diagnostic quality venous images in children over a wider time window compared to Gadofosveset, reflecting its more stable blood pool distribution.

References

1.Huang SY et al, Abdominopelvic and Lower Extremity Deep Venous Thrombosis: Evaluation With Contrast-Enhanced MR Venography With a Blood-Pool Agent. AJR 2013;201(1): 208-214.

2. Ruangwattanapaisarn N, Hsiao A, Vasanawala SS. Ferumoxytol as an off-label contrast agent in body 3T MR angiography: a pilot study in children. Pediatr Radiol 2015: 45(6):831-9. doi: 10.1007/s00247-014-3226-3.

3.Luhar A, et al. Contrast-enhanced magnetic resonance venography in pediatric patients with Chronic Kidney Disease: Initial Experience with Ferumoxytol. Pediatric Radiology, 2016 in press.

Session 9

Peripheral MRA

Time-Resolved Subtractionless Contrast Enhanced Dixon MRA of the lower legs on 1.5T

Marc Kouwenhoven[1], Silke Hey[1], Christine Nabuurs[1], Tim Leiner[2]

[1] Philips Healthcare, Best, Netherlands, [2] University Medical Center Utrecht, Radiology Dept., Netherlands

Purpose

Subtractionless Dixon used for first-pass stepping-table peripheral MRA has already shown to be higher in SNR and CNR, and is robust to motion [1]. The purpose of this work is to investigate the feasibility and potential benefits of time resolved subtractionless contrast enhanced MRA on 1.5T with viewsharing, Dixon and high acceleration factors in the lower legs. The novel approach was compared to conventional subtraction-based time-resolved MRA [2,3].

Methods

Seven patients with known or suspected peripheral vascular disease were examined on an Ingenia 1.5T scanner using the standard Anterior Body Coil and the built-in posterior coil. A single dose of Gadobutrol was used, with an injection speed of 1 mL/sec. 3D volumetric images were acquired with a FOV of 430 x 430 mm^2 and a volume thickness of 150 mm, using a dual-gradient-echo sequence with a $TE_1/TE_2/TR$ of 1.8/3.6/5.6 ms. Acquired spatial resolution was 1.1 x 1.1 x 2.0 mm^3, reconstructed to 1 x 1 x 1 mm^3. An eightfold acceleration (SENSE) was used, with a partial Fourier factor of 0.65, and an elliptical k-space shutter resulting in a net acceleration of 15.5x. Viewsharing was applied with a keyhole percentage of 15% and a peripheral sampling density of 25% [3,4], resulting in a 2.76 fold increase in temporal resolution (resulting in a total net acceleration factor of 43). The temporal resolution per dynamic phase was 5.5 sec, with a temporal footprint of 19.5 sec. A mask was acquired at the beginning of the acquisition, to enable comparison with conventional subtraction. 12-19 dynamic phases were acquired. Total scan time was 1:25-2:00 minutes. Water images were reconstructed using Dixon with a multi-peak spectral fat model [5]. Source modulus images were obtained from the first echo, allowing a comparison between water and subtracted modulus images from the same acquisition.

Results

In 1/7 patients (14%) significant motion was observed, corrupting the subtraction images; in a further 2/7 patients (28%) only mild motion was observed. Compared to the subtracted modulus images, the SNR in the unsubtracted Dixon water images was increased by a factor of 1.89 (SD 0.19) on average. The effect of bulk motion is shown in Fig. 1, where misregistration artifacts in the subtracted modulus images significantly increases the background signal. As can be seen from the water images in Fig. 1, the subtractionless Dixon method effectively eliminates these motion artifacts.

Discussion

Compared to the subtracted modulus images, the increase in SNR for the unsubtracted Dixon water images was a factor of 1.89 on average, which is in line with theoretical predictions [6]. No significant water-fat swap artifacts were observed, despite the echo spacing of 1.8 ms, which is relatively short for Dixon on 1.5T. The viewsharing and high acceleration factor allowed a sufficiently high temporal resolution with a relatively thick 3D volume, which facilitates easy planning.

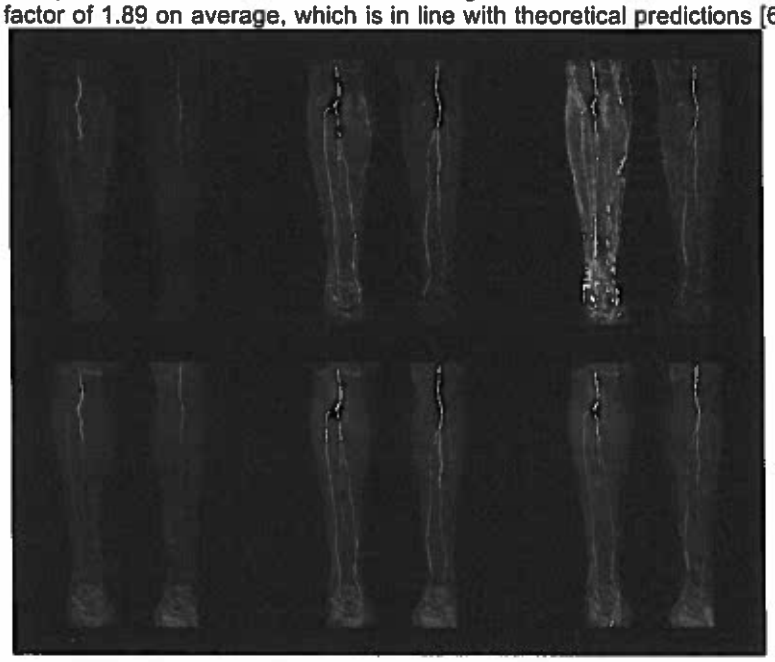

Fig. 1. Coronal MIPs of subtracted modulus images (top row) and of unsubtracted Dixon water images (bottom row) from a patient with significant motion especially towards the end of the acquisition. 3 selected dynamic phases are shown; 20 seconds (left column), 58 seconds (middle column) and 1:46 (right column).

Conclusion

The feasibility of time-resolved subtractionless MRA with viewsharing, Dixon and parallel imaging with a high acceleration factor has been demonstrated in this work on patients at 1.5T. The main advantages of the subtractionless method are nearly doubled SNR and the elimination of misregistration artifacts due to bulk patient motion. Both advantages can contribute to better clinical imaging, since the main indication for time-resolved MRA of the lower legs is for patients with critical limb ischemia, which often find it difficult to lay still for a longer period, and in which it can be important to visualize small (collateral) vessels.

References

1) Leiner T, et al. Eur Radiol 2013;23(8):2228-2235. 2) Andreisek G, et al. Radiology 2007;242(2):610-620.

3) Voth M, et al. Invest Radiol 2009;44(9):627-633. 4) Lim RP, et al. Am J Neuroradiol 2008;29(10):1847-1854.

5) Eggers H, et al. Magn Reson Med 2011;65(1):96-107. 6) Stinson EG, et al. Magn Reson Med 2015;74:81-92.

Accurate path length measurement in pulse wave velocity calculations improves inter-technique agreement

Jonathan R Weir-McCall, Arsh Thakur, Deirdre B Cassidy, Faisel Khan, Helen M Colhoun, J Graeme Houston

Division of Cardiovascular and Diabetes Medicine, University of Dundee, UK

Background: Pulse wave velocity is a well established marked of arterial stiffening with important prognostic implications. Carotid femoral pulse wave velocity (cf-PWV) is the most commonly used technique for the measurement of PWV, however MRI has become increasingly prominent due to its ability to measure directly the central aortic PWV (MRI-PWV). The two techniques show a high correlation, but with a significant and consistent bias across studies.(1,2) It is not clear whether this is due to inaccuracies in distance measurement in cf-PWV, the lower temporal resolution of MRI-PWV or different elastic properties throughout the arterial tree leading to this systematic bias. The aim of the current study was to evaluate whether the differences between cf-PWV and MRI-PWV can be accounted for by inaccuracies of currently used distance measurements.

Methods: 80 study participants underwent cf-PWV, whole body MR angiography and aortic PWV measurements. cf-PWV was performed using a Sphygmocor device (Atcor Medical, West Ryde, Australia), and a proximal (carotid to sternal notch) and distal (sternal notch to umbilicus and umbilicus to femoral) measure with final distance being the proximal distance subtracted from the distal distance. MR-PWV was calculated from the ascending aorta to the abdominal aorta using phase contrast sequences at the level of the right pulmonary artery and diaphragm with a transit time technique. Whole body MRA was performed on a 3T scanner (Tim Trio, Seimens, Erlangen) using an up titring (10ml then 15 ml) dual bolus contrast injection of gadoterate meglumine (Dotarem, Villepont) and a 4 station acquisition protocol, from which a curved MRP was generated from the carotid to the femoral arteries. From this, distances from the bifurcation of the common carotid to the aortic arch (proximal measurement), and from the aortic arch to the bifurcation of the common femoral artery (distal measurement) were measured. After subtracting the proximal from the distal measurement, this MRA derived distance was then used to recalculate the cf-PWV to give an MRA-PWV.

Results: MR-PWV showed moderate correlation with cf-PWV ($R=0.39$, $p<0.001$) but showed a consistent bias with a significantly lower MR-PWV than cf-PWV (MR-PWV= 8.8 ± 3.4 vs. cf-PWV=10.77 ± 2.67ms^{-1}, $p<0.001$). When cf-PWV was recalculated using the inter-arterial distance from the whole body MRA, correlation between the two techniques improved ($R=0.46$, $p<0.001$), with loss of the bias between the measures (MR-PWV=8.41 ± 3.43 vs. MRA-PWV 8.96 ± 2.15 ms^{-1}, $p=0.14$). When the two components of the carotid-femoral distance measurements were compared, the discrepancy in distance measurements was due to both an underscoring of the proximal distance (mean diff = -63.6 ± 26.6mm, $p<0.001$) and an overscoring of the distal measurement (30.4 ± 52.2mm, $p<0.001$).

Conclusion:
Differences in PWV measurement between carotid-femoral PWV and MRI measured central aortic PWV can be predominantly explained by inaccuracies introduced by the use of simple surface measurements to represent the convoluted arterial path between the carotid and femoral arteries.

1. Hickson SS, Butlin M, Graves M, Taviani V, Avolio AP, McEniery CM, et al. The relationship of age with regional aortic stiffness and diameter. JACC CVI 2010;3(12):1247–55.
2. Parikh JD, Hollingsworth KG, Kunadian V, Blamire A, MacGowan GA. Measurement of pulse wave velocity in normal ageing: comparison of Vicorder and magnetic resonance phase contrast imaging. BMC Cardiovascular Disorders; 2016;16(1):50.

A physiological model for arterial spin labeling reactive hyperemia in calf muscles: assessing microvacular dysfunction in the presence of arterial stenoses

Hou-Jen Chen [a], Graham A. Wright [a,b]

[a] *Department of Medical Biophysics, University of Toronto, Toronto, Ontario, Canada*
[b] *Physical Sciences Platform and Schulich Heart Research Program, Sunnybrook Research Institute, Toronto, Canada*

Purpose: To characterize and interpret arterial spin labeling (ASL) reactive hyperemia of calf muscles for better understanding of the microcirculation in peripheral arterial disease (PAD).

Methods: The mid-calf reactive hyperemia was recorded with single- slice flow-sensitive alternating inversion recovery (FAIR) in the right leg of 7 healthy subjects aged under 30 and 8 patients with PAD (15 legs scanned in total). The healthy subjects underwent 1, 2, 3, and 5 minutes of arterial occlusion via cuff inflation on their thigh. Each cuffing was separated by at least 15 minutes of rest. The patients only underwent 2-min cuffing. Imaging was performed at 3T (MR 750 by GE) with an 8-channel cardiac receive array placed in the calf region. The responses were characterized by empirical indices, i.e. peak and time-to-peak (TTP), and model-derived indices. The model incorporated arterial properties, oxygen transport, tissue metabolism, and vascular regulation mechanisms. Specificially, the modeled arteriolar relaxation is caused by intravascular ATP released by the red blood cells in the early phase of ischemia and interstitial adenosine accumulated in the prolonged ischemia, leading to an ischemic duration-dependent vasodilation in the reperfusion phase. The model behavior was simulated in the cases of normal circulation, stenoses, microvascular dysfunction, and combined diseases. Five free parameters, including the baseline perfusion (f_r), arterial resistance (R_p) and time constant (τ_p), and the sensitivity to ATP (g_{ATP}) and its' response time (τ_{ATP}), were used to generate reactive hyperemia for best fit to the acquired patients' responses. For healthy subjects' responses, adenosine parameters were included as free parameters whereas arterial resistance was kept constant.

Results

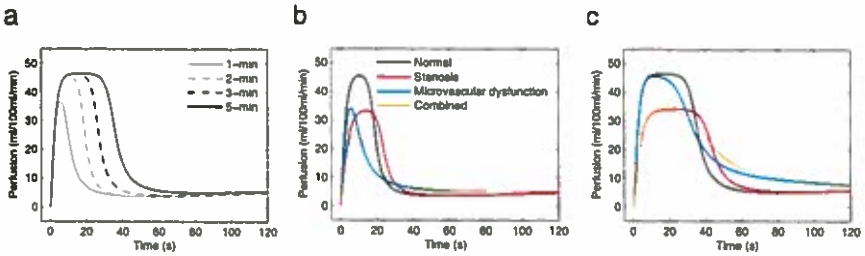

Fig 1. The simulated effect of ischemic duration on normal reactive hyperemia (a). The simulated influences of arterial stenoses and microvascular dysfunction on reacitve hyperemia induced by 2-min (b) and 5-min (c) ischemia.

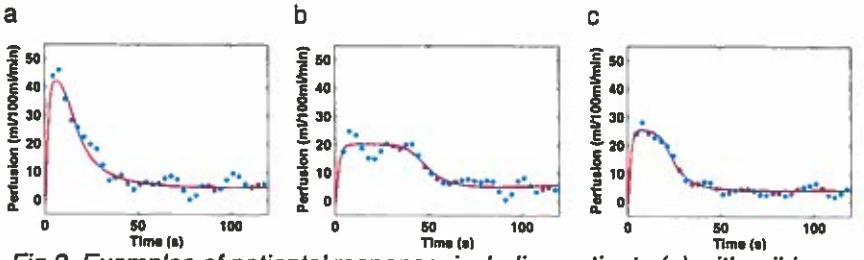

Fig 2. Examples of patients' response, including patients (a) with mild disease, (b) affected by stenoses but compensated by microvascular function through extending hyperemia, and (c) affected both by stenoses and microvascular dysfunction.

The model demonstrated distinct effects between arterial stenoses and microvascular dysfunction on reactive hyperemia, and indicated a higher sensitivity of 2-minute thigh cuffing to microvascular dysfunction than 5-minute cuffing (Fig. 1). Reasonable fit was achieved despite very different responses in the patient group (Fig. 2). The recorded perfusion responses in patients were better differentiated from the normal subjects using the model-based analysis rather than characterization using the apparent peak and TTP of the responses (Fig. 3).

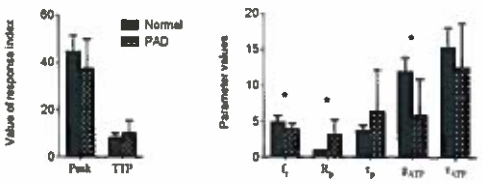

*Fig 3. Empirical (left) and model-derived (right) indices characterizing reactive hyperemia after 2-min ischemia in healthy subjects vs PAD patients. * indicates statisticaslly significant differences.*

Conclusion

This work demonstrates a novel analysis method and facilitates understanding of the physiology involved in ASL reactive hyperemia. ASL reactive hyperemia with model-based analysis may be used for noninvasive microvascular assessment in the presence of arterial stenoses, allowing us to look beyond the macro-vascular disease in PAD. A subgroup who will have poor prognosis after revascularization among the patients with critical limb ischemia may be associated with more severe microvascular diseases, which may potentially be identified using ASL reactive hyperemia.

Comparing DARC to Conventional MR Lymphangiography: Evaluating Venous Suppression and Quantifying Lymphatic Signal Loss

Beth Ripley, Gregory J. Wilson, Neeraj Lalwani, Jeffrey H. Maki
University of Washington, Department of Radiology, Seattle, WA, USA

Purpose: Lymphedema is a chronic and debilitating disease. Emerging microsurgical therapies such as lymphaticovenous anastomosis are associated with improved outcomes over more conservative management.[1] MR lymphangiograms (MRL) can facilitate appropriate selection of surgical candidates by providing spatially accurate maps of damaged lymphatic channels. MRLs, however, are difficult to interpret, particularly in cases of venous contamination after selective lymphatic injection. We have developed a technique called Dual Agent Relaxation Contrast MR Lymphangiography (DARC-MRL) that allows for the unambiguous separation of lymphatics and veins by leveraging the intravascular R2* effects of an USPIO (ferumoxytol) to reversibly suppress any signal within veins.[2] Our initial clinical experience is described here.

Methods: 43 consecutive patients imaged with DARC-MRL were compared to 43 matched patients who underwent conventional (no ferumoxytol) MR lymphangiography. In both cases, lymphatic opacification was achieved by intracutaneous (i.c.) administration of approximately 1 ml contrast agent (gadobenate dimeglumine) into each webspace (hand or foot). For DARC-MRL, ferumoxytol 5 mg/kg was administered i.v. prior to i.c. gadolinium to facilitate venous suppression at extended echo times (TEs). For DARC, the shortest mDixon TE pair (typical TE_1 5.8 ms, TE_2 7.0 ms) required for blood pool suppression was determined and DARC-MRL performed at that TE pair. Two radiologists graded conventional and DARC-MRL exams for location and degree of venous contamination. Additionally, the time course for maximal lymphatic opacification, as well as the amount of DARC lymphatic signal suppression due to longer TE times, was determined.

Figure 1. Conventional MRL (A) with significant venous enhancement (arrowheads). DARC-MRL (B) showing no veins (different patient). Short-TE MRV/MRL (C) same patient as (B) shows veins and lymphatics, allowing us to calculate lymphatic signal loss related to lengthened TE.

Results: 42/43 conventional MRL cases exhibited some degree of venous contamination, with 56% of cases severe enough to impair confident identification of lymphatics distal to the elbow/knee. By contrast, venous contamination was present in less than 10% of DARC MRL studies, and was not considered problematic for any case (Fig. 1). Secondary to the longer TE's, DARC lymphatic signal (Fig 1B) was reduced to 52±17% of the short-TE lymphatic signal (Fig. 1C; MRV/MRL). However, there were no cases where lymphatics were graded significantly suppressed due to R2*-related signal loss. The time course to maximal lymphatic opacification was determined for DARC-MRL studies, with MRL's at 25 and 50 minutes adequately capturing lymphatic filling, facilitating creation of a clinical protocol requiring < 1 hour.

Discussion: DARC-MRL reliably suppresses venous signal through TE elongation as compared to conventional MRL. This comes at the cost of approximately 50% of the lymphatic signal due to R2* effects. However, given the excellent resultant tissue contrast, this degree of signal loss did not impair identification of lymphatics. The loss of lymphatic signal implies R2* in the lymphatics is quite high, suggesting a lower dose of i.c. injected gadolinium may be beneficial for this technique. Time course analysis revealed that DARC MRLs are only required at 25 and 50 minutes, which allows us to inject ferumoxytol outside of the magnet and reduce the on-magnet time to less than 1 hour.

References

1) Damstra RJ, Voesten HGJ, Van Schelven WD, Van Der Lei B. *Breast Cancer Res Treat.* 2009;113(2):199-206.
2) Maki JH, Neligan PC, Briller N, Mitsumori L, Wilson GJ. *Curr Probl Diagn Radiol* 2016 45(3):174-9.

Feasibility of Time-Resolved 3D Contrast-Enhanced MR Angiography with Single-Echo Dixon Background Suppression at 3.0T

Eric G. Stinson, Joshua D. Trzasko, James F. Glockner, Phillip M. Young, Stephen J. Riederer
Mayo Clinic, Rochester, MN, USA

Purpose: Dixon-based background suppression for contrast-enhanced MR angiography (CE-MRA) has recently been reported to reduce motion sensitivity[1] and improve signal-to-noise ratio (SNR)[2] when compared to subtraction-based background suppression. Most work in this area has used dual-echo Dixon techniques, where images at two different echo times are used to obtain separate images of only water signal and only fat signal. Single-echo Dixon techniques[3-7] assume that system imperfections are known *a priori* or may be estimated, and require an image at only a single echo time to create the water and fat images. This provides the potential for reduced scan time or improved temporal resolution in a time-resolved exam while retaining an SNR improvement over subtraction[2]. While the feasibility of time-resolved CE-MRA with dual-echo Dixon has been shown at 1.5T[8], time-resolved single-echo Dixon CE-MRA has not been reported. The purpose of this work is to report on the feasibility of time-resolved 3D single-echo Dixon CE-MRA at 3.0T.

Methods: *Theory:* The phase-constrained signal equation for a spoiled gradient echo acquisition at echo time t is shown in Eq. 1, where $\theta(t)$ is the chemical shift-induced phase, $\phi(t) = \gamma \Delta B_0 t$ is the phase due to magnetic field inhomogeneity, ϕ_0 is the shared initial phase of W and F, the real-valued water and fat signals, and $N(t)$ is zero-mean Gaussian noise. By constraining W and F to be real with shared initial phase, ϕ_0, there are 4 unknown quantities[9]. Further, under the assumption that ΔB_0 and ϕ_0 are known or can be estimated[4,10], real-valued W and F can be reconstructed from a single complex measurement (Eq. 2). *In vivo Feasibility Experiment:* An IRB-approved experiment was performed on the calves of a healthy volunteer at 3.0T to evaluate the feasibility of highly accelerated time-resolved single-echo Dixon CE-MRA. Scan parameters are shown in Table 1. Single-echo images were generated according to Eq. 2 using regularized maximum likelihood estimates of ΔB_0 and ϕ_0 obtained from the post-contrast dual-echo images using a graph cuts-based optimization procedure.

$$G(t) = \left(W + Fe^{i\theta(t)}\right)e^{i(\phi(t)+\phi_0)} + N(t) \quad \textbf{(Eq. 1)}$$

$$\begin{bmatrix} W \\ F \end{bmatrix} = Re\{A^*A\}^{-1}Re\{A^*G\} \quad \textbf{(Eq. 2)}$$

$$\text{where } A = e^{i(\phi(t)+\phi_0)}\begin{bmatrix} 1 & e^{i\theta(t)} \end{bmatrix}$$

Results: Time-resolved single-echo Dixon maximum intensity projections (MIPs) and images are shown in Figure 1A,C. Fat/water separation was successful for all time frames. Late phase subtraction MIPs and images are shown for comparison in Figure 1B,D. Red arrowheads show motion-induced errors in the subtraction images that are not present in the Dixon images. Yellow arrows show improved depiction of small superficial subcutaneous veins within the fat in the Dixon images.

	Dual-Echo	Single-Echo
TR/TE$_1$/TE$_2$ (ms)	5.6/2.3/3.5	4.9/2.8/--
FA/BW (°/kHz)	18/±62.5	18/±62.5
FOV (cm)	34×34×16	34×34×16
Res. (mm)	1.4×1.4×1.6	1.4×1.4×1.6
SENSE R	R$_y$×R$_z$ = 1×1	R$_y$×R$_z$ = 4×2
Update Time	--	11.1 s

Table 1: Imaging parameters for Dixon CE-MRA. (reported as SI×RL×AP)

Discussion: Feasibility of time-resolved single-echo Dixon CE-MRA has been shown with highly accelerated imaging of the calves. Future work will investigate further reduction of update time with alternative sampling strategies, improved image quality through advanced reconstructions, theoretical analysis of accelerated Dixon SNR, and applications to other anatomies.

References: [1]Leiner T. Eur Radiol 2013;23:2228. [2]Stinson EG. MRM 2015;74:81. [3]Ma J. JMRI 2008;27:881. [4]Xiang Q-S. ISMRM 2001. #789. [5]Eggers H. ISMRM 2012. #1199. [6]Paltiel Z. SMRM 1985. #172. [7]Patrick J. SMRM 1985. #174. [8]Kouwenhoven M. ISMRM 2016. #886. [9]Bydder M. MRI 2011;29:216. [10]Stinson EG. ISMRM 2016. #2673.

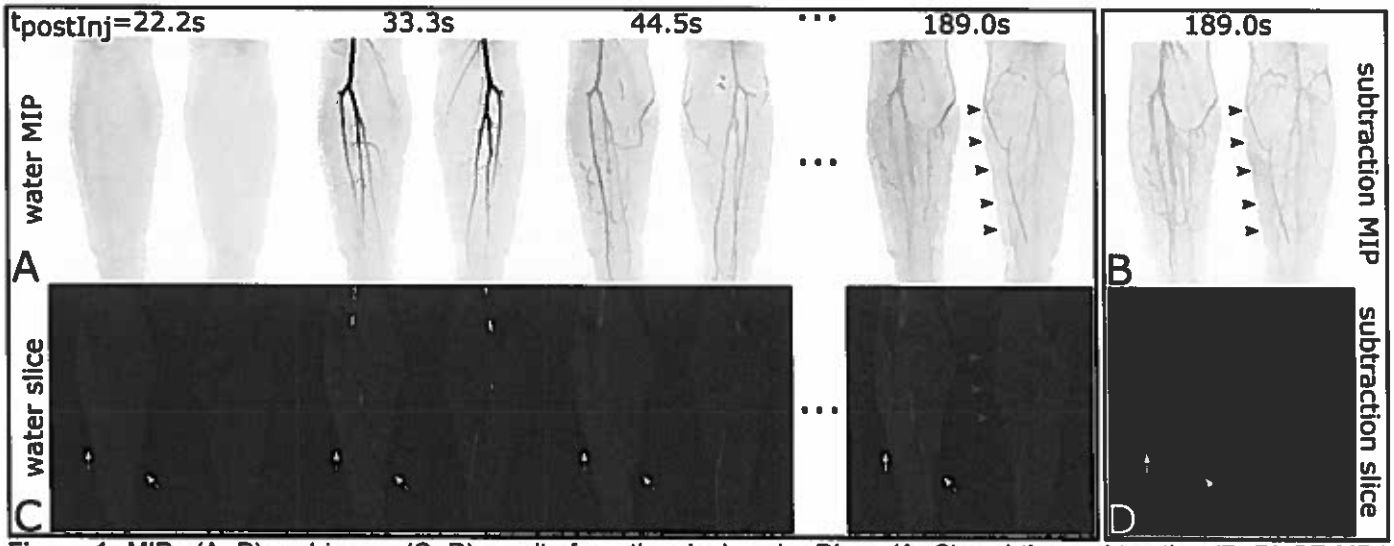

Figure 1: MIPs (A, B) and image (C, D) results from the single-echo Dixon (A, C) and time-subtraction (B, D) CE-MRA reconstructions. Red arrows show a motion-induced subtraction artifact in (B) and (D), while the Dixon images (A, C) are unaffected. Yellow arrows show that small superficial subcutaneous veins are well seen in the Dixon CE-MRA images (C).

Dual-echo, Dual-Bandwidth QISS FLASH with Enhanced Background Suppression for Peripheral Artery MRA at 3 Tesla

Robert R. Edelman[1,2], Shivraman Giri[3], Jianing Pang[3], Ioannis Koktzoglou[1,4]

[1]Radiology, NorthShore University HealthSystem, Evanston, IL, [2]Radiology, Northwestern University, Chicago, IL, [3]Siemens Healthcare, Chicago, IL, [4]Radiology, University of Chicago, Chicago, IL,

Purpose: Quiescent-interval slice-selective (QISS) MRA has proven to be an efficient and accurate non-contrast technique for the evaluation of peripheral arterial disease [1]. However, compared with CEMRA (which uses a short-TE, high-bandwidth 3D fast low angle shot (FLASH) readout), the balanced steady-state free precession (bSSFP) readout used for QISS is more sensitive to susceptibility effects. In certain circumstances (e.g. imaging near a metallic hip prosthesis or at 3 Tesla near an air-containing bowel loop or ferromagnetic clip), the image quality can be degraded by local signal loss as well as banding artifacts. To address this concern, we have previously reported a QISS sequence using a FLASH readout. The combination of a short TE and high sampling bandwidth without chemical shift-selective fat suppression minimize susceptibility artifacts. However, the high bandwidth worsens the signal-to-noise ratio (SNR), while the short TE and lack of fat suppression combine to reduce vessel conspicuity on maximum intensity projection (MIP) images. In order to overcome these limitations, we implemented a prototype dual-echo, dual-bandwidth QISS FLASH sequence which allows for enhanced background suppression.

Methods: Subjects were scanned on a 3 Tesla MRI system (MAGNETOM Verio, Siemens Healthcare, Erlangen, Germany) with IRB approval. The pulse sequence used the following imaging parameters: 40 slices with thickness = 3-mm, in-plane resolution 1.1-mm, TE_1 = 1.7 ms with bandwidth 930 Hz/px, TE_2 = 3.9 ms with bandwidth 395 Hz/px, bipolar gradients, no fat suppression, flip angle = 30°, 2- 4 shots, in-plane FOCI pulse. Image sets for both echoes were reconstructed and a mask image was created by taking the absolute difference of the two image sets. The mask image was scaled so that fat signal matched that in the 1st echo image, and then subtracted from the 1st echo image. The same process was used for the 2nd echo image, also with mask scaling. MIPs were then created from the difference images.

Results: Small vessel detail was obscured in the unprocessed 1st echo images due to the high signal intensity of adipose tissue and fat-containing bone marrow. The absolute difference mask image showed high fat signal and moderate muscle signal, with negligible signal from blood vessels. Of additional note, regions of altered magnetic susceptibility manifested in the mask image as distinctive bright regions. After processing, background signal was greatly reduced (particularly with the 1st echo), resulting in improved small vessel detail in the projected difference images (**Figure**).

Discussion: Dual-echo QISS MRA overcomes limitations of the standard QISS sequence by allowing the acquisition of a background-suppressed short-TE, high bandwidth 1st echo image that is insensitive to susceptibility artifacts, simultaneously with a low-bandwidth, 2nd echo image that provides competitive image quality to standard QISS. Unlike a dual-echo Dixon technique, the choice of TE is less restrictive and there are no fat/water phase swaps. By distinguishing regions of altered magnetic susceptibility, the mask image may have additional value for highlighting ferromagnetic clips or other metallic implants that might be inconspicuous in the QISS MRA. Given that the use of multiple shots increases scan time compared with standard single-shot QISS, the technique is best reserved for areas where there is concern for potential susceptibility artifacts using a bSSFP readout.

References: 1. Edelman RR et al. MRM 2010;63:951. **Funding:** 1R01HL130093, 1R21HL126015.

Session 10

New MRA Techniques

Automatic bolus detection for dynamic contrast enhanced imaging with sparse sampling

R. Marc Lebel[1,2], Naren Nallapareddy[3], Sajan G. Lingala[3], Linda B. Andersen[2], Richard Frayne[2], Krishna S. Nayak[3]

[1]GE Healthcare, Calgary, Canada; [2]Radiology, University of Calgary, Canada;
[3]Electical Engineering, University of Southern California, USA.

Purpose: Sparse sampling and constrained reconstruction has been used to achieve dynamic contrast enhanced (DCE) imaging with high spatial and temporal resolutions; several k-space sampling trajectories have been developed specifically for this purpose [1, 2]. A beneficial feature of some trajectories is the ability to retrospectively define the temporal resolution, enabling variable frame rates and reliable detection of unpredictable physiology. This feature is achieved via binning data acquired over intervals defined after the acquisition. In DCE imaging, rapid first-pass contrast agent dynamics could be reconstructed at a high frame rate while the gradual washout period could then be resolved at a lower frame rate. However, effectively leveraging this ability requires precise knowledge of the bolus arrival time (BAT). *The purpose of this work is to quickly and accurately estimate the BAT of the contrast agent*, which will be used to define variable temporal resolution reconstruction windows suitable for time-resolved angiography and DCE.

Methods: In-vivo data were acquired on a 3T GE MR750; phantom data on a 3T GE HDxt using a DCE flow phantom (Shelley Medical, London, Canada) [3]. A Cartesian radial sampling trajectory was incorporated into the vendor supplied 3D SPGR sequence [1]. This trajectory acquires spokes in the two phase-encode directions while fully sampling the readout; the center of k-space was acquired at the end of each spoke. Data were acquired continuously before, during, and several minutes after the contrast injection.

The BAT was estimated in five steps: (1) extracting the frequently sampled central line of k-space. (2) Determining the readout location with the most reliable MR signal change over time. (3) Computing the rate of signal change over a 9 sec sliding window. (4) Locating the first inflection point in the slope, which corresponds to the first large positive peak in the rate of change. (5) Regress the signal to baseline (the average signal from the start of scan to 5 sec prior to the peak slope). The time when the regressed signal intersects the baseline corresponds to the BAT.

The estimated BAT was compared with the first time frame when the bolus could be seen in subsequently reconstruction images. A variable temporal resolution was employed with a 2.5 sec resolution surrounding the estimated arrival time and a lower temporal resolution (between 5 and 20 sec) elsewhere.

Data were acquired in 5 patients and in 4 phantom trials.

Results: The proposed method was able to correctly identify the bolus arrival in the five patients evaluated (Fig. 1) and in the DCE phantom (not shown). The error in estimated arterial BAT equalled the 2.5 sec temporal resolution of the images. This accuracy is limited by how frequently the central k-space line was acquired but was sufficient for defining the temporal windows for subsequent image reconstruction. The BAT estimation process requires approximately 100 msec and so has minimal impact on the total reconstruction time.

Conclusion: The proposed method effectively detects a contrast bolus, thus providing modern sparse reconstruction methods with the information necessary for automatic selection of frame rates. Additionally, the need for a test-bolus and subsequent estimation of patient-specific timing delays could be eliminated, improving workflow efficiency and reducing acquisition errors.

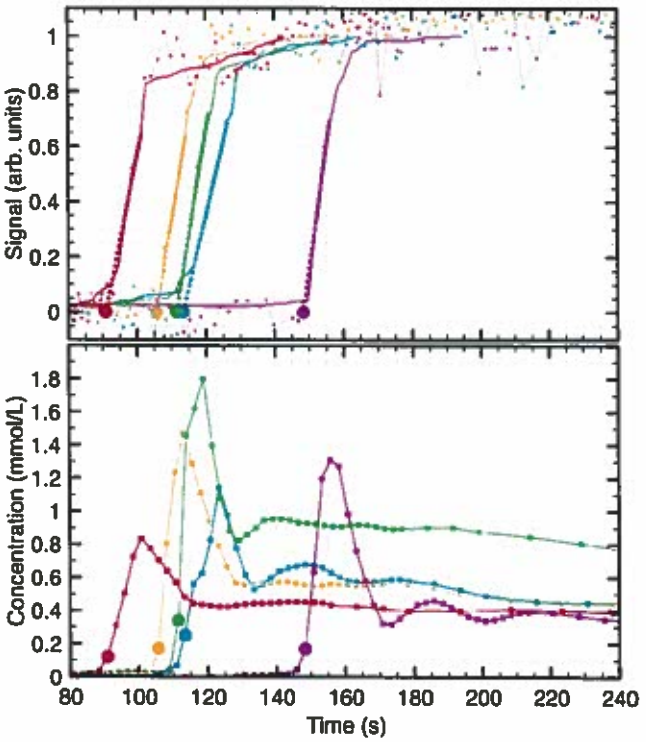

Figure 1: (top) Center of k-space intensity versus time in five patients. The region of maximum slope is regressed to baseline to locate the BAT (circles). (bottom) Arterial time-intensity curves from images reconstructed at a variable frame rate surrounding the estimated arterial bolus arrival time confirm accurate bolus detection

References:

[1] Zhu Y., *et al.* GOCART: GOlden-angle CArtesian randomized time-resolved 3D MRI. Magn Res Imag. 2016.

[2] Cheng JY, *et al.* Variable-density radial view-ordering and sampling for time-optimized 3D Cartesian imaging." ISMRM Workshop on Data Sampling and Image Reconstruction, 2013.

[3] Driscoll B., *et al.* Development of a dynamic flow imaging phantom for dynamic contrast-enhanced CT. Med. Phys. 2011.

A customizable numerical k-space simulation of dynamical MRAs using Physiologic Biofeedback and an Analytical Fourier Transformation Model.

Keigo Kawaji Ph.D.[1], Charles G. Cantrell, MS.[2,3], Satoshi Tamura, Ph.D.[4], Hui Wang Ph.D.[5], Timothy J. Carroll, Ph.D.[2], and Amit R. Patel MD.[1]

1 – Medicine, and 2 – Radiology, The University of Chicago. 3 - Biomedical Engineering, Northwestern University. 4 – Electrical and Information Engineering, Gifu University, Japan. 5 - Philips Healthcare, Cleveland OH.

Purpose: Validation experiments for the optimization of k-space acquisition and view ordering can be a resource-consuming, and therefore a very challenging process. A generalizable k-space simulation of MRA protocols is highly desirable, particularly in the evaluation of the effects of k-space interleaving and view ordering in dynamic MRA sequences. We present a simulation approach that incorporates 1) physiologic feedback, and 2) an analytical Fourier Transform (aFT) model (1,2). This combined model is subsequently applied in an exhaustive validation and optimization of four radial interleaving strategies associated with dynamic MRAs.

Theory: The biofeedback-based aFT model exploits defined k-space contributions of 3D ellipsoid and rectangular blocks, allowing for rapid numerical simulation of any angiographic MR protocol as a superpositioned sum of these shapes over time. In a dynamic MRA protocol, a simple feedback converts measured physiologic time-volume MRA data (i.e. the LV volume curve, blood pool intensity, T1/R1, T2/R2, etc.) into dynamic properties measured using the acquired k-space.

Methods: The above model is used in a comparative evaluation between four alternative radial interleaving approaches in an echo-temporal cine-Cardiac MR protocol (3). These were: a) pseudo-random, b) MoPS with pseudo-Golden Angle (GA) (3), c) temporally-periodic GA, and d) temporally aperiodic GA (4). The simulation was employed to quantitatively analyze the extent of variability in the radial spoke distribution with the aperiodic GA approach that is sensitive to the acquisition window size (i.e. R-R cycle in a cine-CMR sense; NOT real-time imaging). This window size was varied between 300 and 600 consecutive spokes. Next, a power spectrum analysis in the spatio-temporal frequency (x-f) domain was examined using this dynamic simulation phantom by comparing i) MoPS interleaving using a pseudo-GA/5 (22°) with 15ms temporal window and a per-echo sliding window, ii) aperiodic GA interleaving with an optimized acquisition window of size 595 echoes per R-R interval, iii) nSC-periodic GA (111.246°), and iv) aperiodic GA matched to the 540 echo-window (4) employed in i) and iii). Reconstruction errors were measured in the uniform left ventricular blood-pool.

Results: The figure below shows the biofeedback and aFT-based simulation model of the heart. **Top left)** Using pseudo-random interleaving, the pair of power spectrum plots show the relationship between the number of echoes between cycled radial streaks (nSC), and showing the nSC < 32 cutoff for proper separation of streak from physiologic frequencies. **Bottom left)** GA approach's dependence on the acquisition windows size 300-580 radial spokes. **Right)** Comparison of four interleaving approaches; the error measured inside the LV blood pool ROI was significantly lower from i) MoPS-interleaved reconstruction compared to ii-iv) GA-derived reconstructions (Mean error values were: MoPS w. pseudo-GA/5: 1.1%; GA (optimized 595 TRs): 1.7%; nSC-periodic GA (with nSC=30): 1.4%; GA (matched to MoPS at 540 TRs): 2.4%. pairwise $p<0.0005$ [MoPS vs each]). Additionally, the average LV Blood-pool ROI error from an exhaustive 10000 pseudo-random interleaving simulation was 1.8±0.02%; each simulation required ~8 sec using previously described GPU hardware (3). MoPS w. pseudo-GA/5 interleaving significantly outperformed other interleaving approaches.

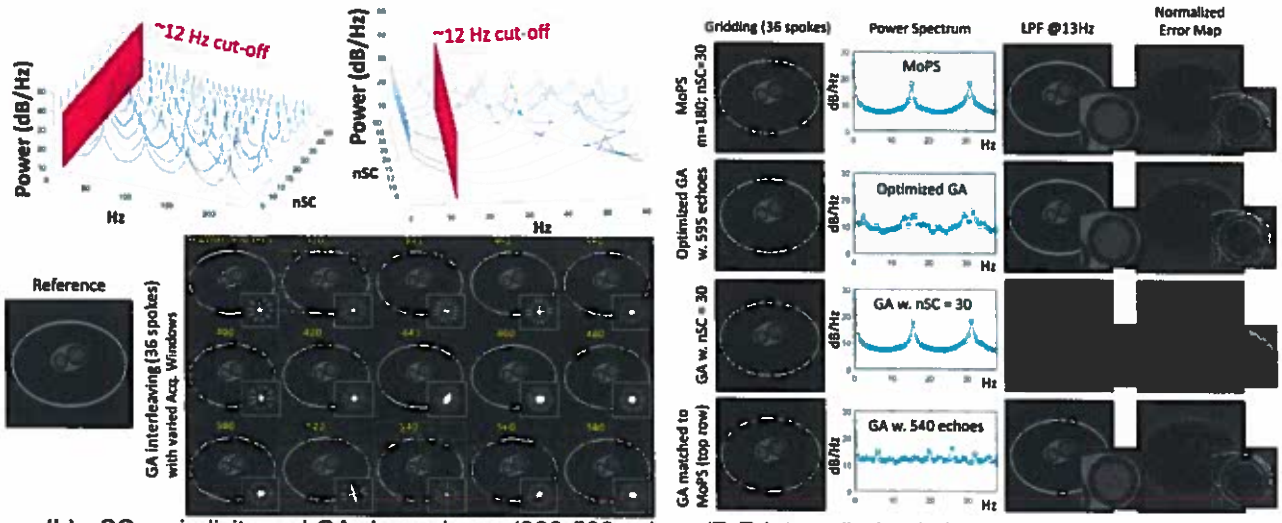

Figure: (L) nSC periodicity and GA-dependence (300-580 echoes/R-R interval) simulation; (R) 4x interleave comparisons.

Discussion: A customizable simulation model using biofeedback and aFT is presented to examine k-space view ordering in dynamic MRA acquisitions. This simulation - which can be employed efficiently in an exhaustive manner - can empirically validate theory-based acquisition properties and enable fair comparisons of different interleaving techniques.

Acknowlegements: NCATS ITM Pilot Award - CTSA UL1 TR000430; and AHA Predoctoral Fellowship Award 14PRE20380810.

References: 1. Ngo et al. MRM 2015, In Press. 2. Han et al. Proc. ISMRM 2016, pp3197. 3. Kawaji et al. Proc. ISMRM 2016, pp3123. 4. Kawaji et al. PLoS ONE 2015, journal.pone.0112020.

Comprehensive Wideband Cardiovascular MRI for Imaging Patients with an Implantable Defibrillator

KyungPyo Hong[1], Jeremy Collins[2], Daniel Lee[3], Bradley Knight[3], Rod Passman[3], James Carr[2], and Daniel Kim[2]
[1]Bioengineering Department, University of Utah, Salt Lake City, Utah, USA, [2]Radiology Department, Northwestern University, Chicago, Illinois, USA, [3]Internal Medicine (Cardiology), Northwestern University, Chicago, Illinois, USA

Purpose: Cardiovascular MR (CMR) is a proven modality for a comprehensive evaluation of cardiac health (function, perfusion, viability) and is particularly useful for identification of arrhythmogenic substrates in electrophysiology applications. Patients with an implantable defibrillator may benefit from CMR for guiding advanced therapies or procedures. Despite the fact that recent studies have shown that CMR can be performed safely in patients with an implantable defibrillator[1], CMR is generally not performed due to considerable image artifacts induced by defibrillator's generator (i.e., 2-6 kHz center frequency shift). Other than cine MRI with FLASH readouts, standard CMR methods produce considerable image artifacts in patients with a defibrillator. As an extension to previous wideband MRI studies[2-4], we sought to compare the performance between standard and wideband protocols in patients with a defibrillator who underwent clinical CMR.

Methods: Standard and wideband MRI protocols at 1.5T (Avanto, Siemens) used identical imaging parameters that are typically used in CMR, except the wideband RF pulse (inversion pulse for LGE; saturation pulse for perfusion and T1 mapping). We enrolled 10 patients (age = 58 ± 19 yrs) with a defibrillator who were scheduled to undergo clinical CMR. Immediately following the clinical pulse sequence, we performed the corresponding wideband pulse sequence (pulse sequence was not randomized due to priority given to clinical CMR). Perfusion imaging was performed in a short-axis plane with administration of 0.075 mmol/kg of Gadavist. Second perfusion scan was conducted immediately after the first perfusion scan with the same injection. T1 mapping scans were performed before and after contrast agent administration. LGE scans were performed approximately 10 min after contrast agent administration. For qualitative image analysis, three readers, who were blinded to pulse sequence types and each other, scored the image quality (1-5:worst-best) and image artifacts induced by the device (1-5:most-least). For statistical analysis, Wilcoxon ranked sum test was performed to compare the mean scores ($p < 0.05$ was considered significant).

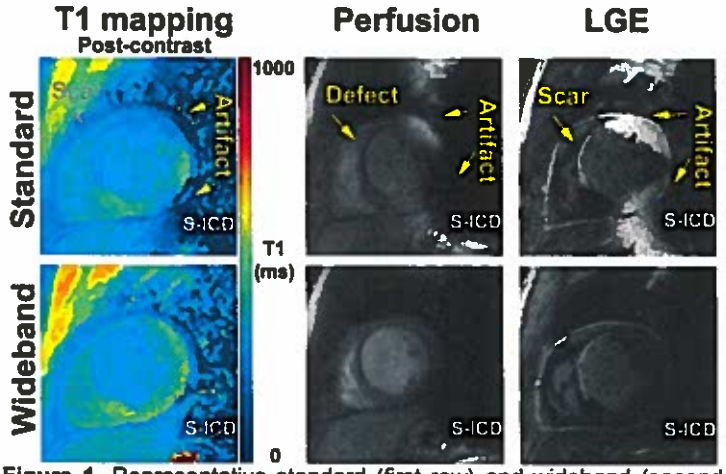

Figure 1. Representative standard (first row) and wideband (second row) T_1 map (left), perfusion (middle), and LGE (right) images in a patient with a subcutaneous ICD (S-ICD). White arrows point to image artifacts induced by S-ICD.

Table 1. Summary of qualitative analysis by three radiologists. Values represent mean ± standard deviation.

Item	Acquisition	Standard	Wideband	p-value
Image Quality (1-5:Worst-Best)	Perfusion	3.4 ± 1.0	4.5 ± 0.6	< 0.0001
	LGE	2.7 ± 1.1	3.8 ± 1.2	
	T_1 mapping	2.8 ± 1.1	4.1 ± 1.0	
Image Artifact (1-5:Most-Least)	Perfusion	3.3 ± 1.1	4.4 ± 0.7	
	LGE	2.4 ± 1.0	3.9 ± 1.0	
	T_1 mapping	2.8 ± 1.2	4.3 ± 1.0	

Results: Figure 1 shows representative standard and wideband perfusion, LGE, and post-contrast T_1 maps in a patient with a subcutaneous ICD. Compared with standard images, wideband images show significantly suppressed image artifacts. Compared with standard methods, each of the wideband perfusion, LGE, and T_1 mapping methods produced significantly better image quality ($p < 0.0001$) and fewer image artifacts ($p < 0.0001$) over 10 patients (Table 1).

Conclusion: This study demonstrates the feasibility of a wideband CMR protocol for a comprehensive evaluation of cardiac health in patients with an implantable defibrillator.

References: [1] Nazarian, S., et al., *Circulation* 2006;114:1277-1284. [2] Hong, KP, et al., *ISMRM* 2016. Proceeding No. 3133. [3] Ranjan, R, et al., *Europace* 2015;17:483-488. [4] Hong, KP, et al., *MRM* 2015;74:336-345.

Beyond the gadolinium-based contrast agents (GBCAs) injection: Long-term biodistribution and excretion

Jean-Sébastien Raynaud, PhD, Eric Lancelot, PharmD, PhD. Guerbet, Roissy CdG Cedex, France

Purpose

To ascertain the existence of a deep compartment for gadolinium storage in the body and assess whether the GBCAs used in radiology or cardiology present the same pharmacokinetic profile.

Methods

A meta-analysis of the available clinical and preclinical pharmacokinetic data about gadolinium in plasma, urine and bone was performed. The rate constants of the distribution (α), elimination (β), and residual excretion (γ) phases were determined from the plasma concentration and the renal excretion rate time curves. Gadolinium concentrations in murine bone and bone marrow were also studied.

Results

All GBCAs displayed a residual excretion phase of gadolinium in healthy volunteers. Gadoteric acid was cleared five times faster than linear GBCAs (γ=0.107 h^{-1} vs. 0.020±0.008 h^{-1}, respectively). Similar results were obtained from animal studies. A strong correlation was shown between the γ values of the GBCAs and their thermodynamic stability constants (R^2=0.9764). Faster gadolinium clearance from murine bone was also observed with gadoterate meglumine acid and gadoteridol (0.131-0.184 day^{-1}) than with linear GBCAs (0.004-0.067 day^{-1}). Both macrocyclic GBCAs displayed a similar half-life (3-5 days) as ^{14}C-gadodiamide, whereas ^{153}Gd-gadodiamide was characterized by a more prolonged residence time in bone (158 days).

Conclusion

This meta-analysis revealed that all GBCAs present a residual excretion, reflecting the existence of a deep compartment of distribution. Gadoterate meglumine undergoes a much faster residual excretion than linear GBCAs. The bone may represent a reservoir for gadolinium dissociation, long-term accumulation, and slow release into the blood stream, especially when using linear GBCAs. Dechelation may participate substantially in Gd deposition in bone.

Statistical approach to derive angiograms from multi-contrast MR images

Dahan Kim[1], Oliver Wieben[2-4], Patrick Turski[2], and Kevin Johnson[3].
Depts. of Physics, Radiology, Medial Physics and Biomedical Engineering, University of Wisconsin – Madison, USA

Purpose: MR angiography is a valuable tool for characterizing cerebrovascular disease and is often performed in combination with other vascular imaging methods such as 4D-flow MRI(1, 2). However, MR angiography sequences often suffer from artifacts which mimic disease and lead to errors in segmentations of vessels. Contrast-enhanced MR angiography (CE-MRA) suffers from overlapping venous structures, such as in the cavernous sinuses. TOF MRA and PC MRA suffer from signal loss in regions of slow or turbulent blood flow(3). These errors can be resolved by utilizing the complimentary information that exists across multiple scans acquired for angiography and structural imaging. For example, contrast enhanced T1-weighted black blood (BB) images delineates the vascular lumen with excellent negative contrast. However, BB MR images alone fail to distinguish vessels from calcification, hemosiderin and air filled cavities. We present an innovative paradigm that utilizes the available MR images of differing contrasts. We apply Bayesian statistics to fully extract complimentary information providing improved vessel segmentation.

Theory: The proposed technique aims to determine the probability that a particular voxel is vessel (v) given its intensity values in black blood (X_{BB}), CE-MRA (X_{MRA}), and PC angiogram (X_{CD}) images, namely $P(v|X_{BB}X_{MRA}X_{CD})$. This probability is not readily available, but Bayesian statistics allows its calculation in terms of probabilities that are easier to estimate from training data based on a human observer. From Bayesian statistics, probability $P(v|X_{BB}X_{MRA}X_{CD})$ can be written as

$$P(v|X_{BB}X_{MRA}X_{CD}) \sim P(v)l(v|X_{BB})l(v|X_{MRA})l(v|X_{CD}) \quad \text{(Eq. 1)}$$

where $P(v)$ is the probability reflecting *prior* knowledge of that voxel being vessel; and each of $l(v|X_{BB})$, $l(v|X_{MRA})$, and $l(v|X_{CD})$ is the vessel *likelihood* given the intensity value in the corresponding image. Since these likelihoods are in turn

$$l(v|X_{BB}) = P(X_{BB}|v), \quad l(v|X_{MRA}) = P(X_{MRA}|v), \text{ and } l(v|X_{CD}) = P(X_{CD}|v), \quad \text{(Eqs. 2)}$$

the probability of our interest can be written in terms of simple probabilities as

$$P(v|X_{BB}X_{MRA}X_{CD}) = P(v)\frac{P(X_{BB}|v)P(X_{MRA}|v)P(X_{CD}|v)}{P(X_{BB})P(X_{MRA})P(X_{CD})} \quad \text{(Eq. 3)}$$

with normalization constants in the denominator. Unlike $P(v|X_{BB}X_{MRA}X_{CD})$, the three probabilities $P(X_{BB}|v)$, $P(X_{MRA}|v)$, and $P(X_{CD}|v)$ that appear on the right-hand side can be obtained from gold standard segmentation of vessels in a training dataset and thus offer a quantitative and reliable way to estimate the desired probability $P(v|X_{BB}X_{MRA}X_{CD})$. Once this vessel probability is determined for every voxel in the image volume, a global threshold can be applied to yield angiogram that utilizes vessel likelihood information available from all three image types.

Methods: As a multi-contrast MR exam, a set of T1-weighted BB MRI, CE-MRA, and 4D flow intracranial scans were performed on human subjects with known neurovascular disease, using a 3T scanner (MR750, GE Healthcare, WI, USA) with a 32-channel head coil (Nova Medical, MA, USA). 3D BB were collected utilizing a DANTE(4) prepared spin echo sequence with 0.75x0.8x0.8mm^3 resolution, while CE-MRA and 4D flow were acquired with 3D radial sequences(5) with 0.6mm isotropic spatial resolution. BB MRI and CE-MRA images were first registered to the 4D flow magnitude image using 3D rigid registrations with mutual information (MI) metric(6) using open-source software ANTS (Advanced Normalization Tools) (7). Since computation of likelihood statistics requires knowledge of where the vessels are (see Eq. 2), vessels were first manually segmented from a set of test subjects. This was achieved using manual segmentation using a custom MATLAB script that displays the co-registered BB MRI, CE-MRA, and 4D-Flow CD images side-by-side, over 100 axial slices spanning much of the brain vasculature. The likelihood probabilities $P(X_{BB}|v)$, $P(X_{MRA}|v)$, and $P(X_{CD}|v)$ were then calculated from the manually segmented vessels. Calculations of $P(X_{BB})$, $P(X_{MRA})$, and $P(X_{CD})$ were performed using a separate mask that excludes air filled cavities over the same volume. Finally, the vessel probability $P(v|X_{BB}X_{MRA}X_{CD})$ was determined for each voxel from its intensity values X_{BB}, X_{MRA}, and X_{CD}, using Eq.3 for the case of $P(v)$=1 of no prior information.

Results and Conclusions: The normalized likelihoods $\frac{P(X_{BB}|v)}{P(X_{BB})}$, $\frac{P(X_{MRA}|v)}{P(X_{MRA})}$, and $\frac{P(X_{CD}|v)}{P(X_{CD})}$ show higher vessel likelihoods for lower values of BB, and higher likelihoods for higher values of CE-MRA and 4D-Flow CD, as expected. Figure 1 shows an example of angiograms in the internal carotid artery, where CE-MRA is challenging due to uptake in the cavernous sinuses. Bayesian angiograms correctly depict just the artery excluding the venous pool. This is in contrast to CE-MRA, BB, and 4D-flow angiograms which are limited by background enhancement, air cavities, and noise respectively.

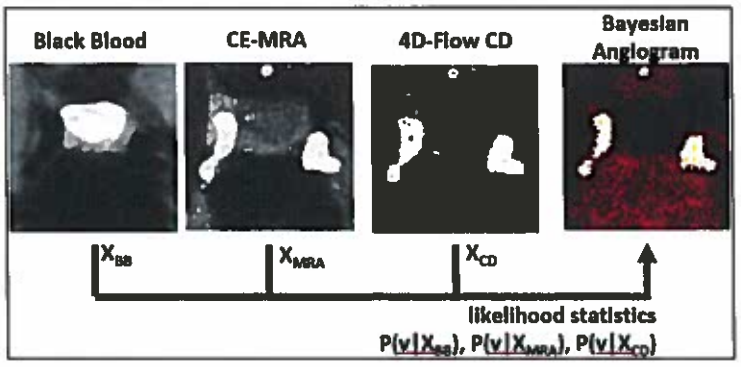

Figure 1. An example of a Bayesian angiogram in internal carotid artery, showing exclusion of cavernous sinuses where CE-MRA is challenging due to contrast uptake. Bayesian angiograms utilize intensity values from all three images of differing contrasts, and fully extracts their complementary information to produce the final angiogram reflecting the vessel likelihoods from each image.

References 1. Edjlali et al, Stroke. 2014;45(12):3704-6
2. Hasan et al. Stroke. 2013;44(2)
3. Huston et al. Radiology. 1991;181:721-30
4. Li et al. Magn Resn Med. 2012;68(5):1423-38
5. Johnson et al. Magn Reson Med. 2008;60(6):1329-36
6. Kim et al. ISMRM 2016.
7. Avants et al.Penn Image Computing Science Lab.2009.

Acceleration of Simultaneous TOF MR Angiography and BOLD MR Venography

Won-Joon Do[1], Seung Hong Choi[2], and Sung-Hong Park[1]
[1] Magnetic Resonance Imaging Laboratory, Department of Bio and Brain Engineering, Korea Advanced Institute of Science and Technology, Daejeon, Korea
[2] Department of Radiology, Seoul National University Hospital, Seoul, Korea

Purpose: To accelerate data acquisition for simultaneous time-of-flight MR angiography (TOF MRA) and blood oxygenation level-dependent MR venography (BOLD MRV).

Introduction: Both TOF MRA and BOLD MRV can depict different brain diseases effectively. However, it is not common to acquire both MRA and MRV, since both of them require relatively long scan times. In this study, we propose an efficient method to acquire TOF MRA and BOLD MRV within a clinically applicable scan time, by combining compatible dual-echo arteriovenography (CODEA), a novel sequence enabling simultaneous acquisition of TOF MRA and BOLD MRV [1], with Generalized Autocalibrating Partially Parallel Acquisitions (GRAPPA), a novel parallel imaging method (PI) to accelerate MRI pulse sequence [2].

Methods: All scans were performed using a 3T Siemens Trio MRI scanner with a 12-channel coil. One male volunteer was scanned with imaging parameters as follows. Matrix size = 384 X 288 X 80, FOV = 240 X 180 X 80 mm^3, phase resolution = 66 %, slice oversampling = 30 %, slice partial Fourier = 6/8, BW= 150 / 50 Hz/pixel, TE1 / TE2 = 3.04 / 25 ms, and TR = 40 ms. Total scan time was 9 min 56 sec without GRAPPA (Full) and was 5 min 26 sec with GRAPPA acceleration factor of 1.84. Echo specific k-space reordering scheme was adopted to 3D GRE dual echo sequence [1]. First 33% of first echo was not acquired to minimize TE1. Echo specific k-space reordering scheme was adopted on first phase encoding (PE1) direction to implement two different excitation pulses (Fig 1.a). A ramp profile excitation pulse with flip angle of 25° was implemented for TOF MRA in the first echo, whereas a flat profile excitation pulse with flip angle of 15° was implemented for BOLD MRV in the second echo.

In order to apply GRAPPA along PE1 direction, we used uniform subsampling mask (x2) with 16 reference lines (Fig 1. B). The acquired data was reconstructed with GRAPPA reconstruction algorithm. Data retrospectively sampled from the full data were also compared with the full and down-sampled data. The normalized mean square error (MSE) was calculated to quantitatively measure the differences between the full image and the down sampled images.

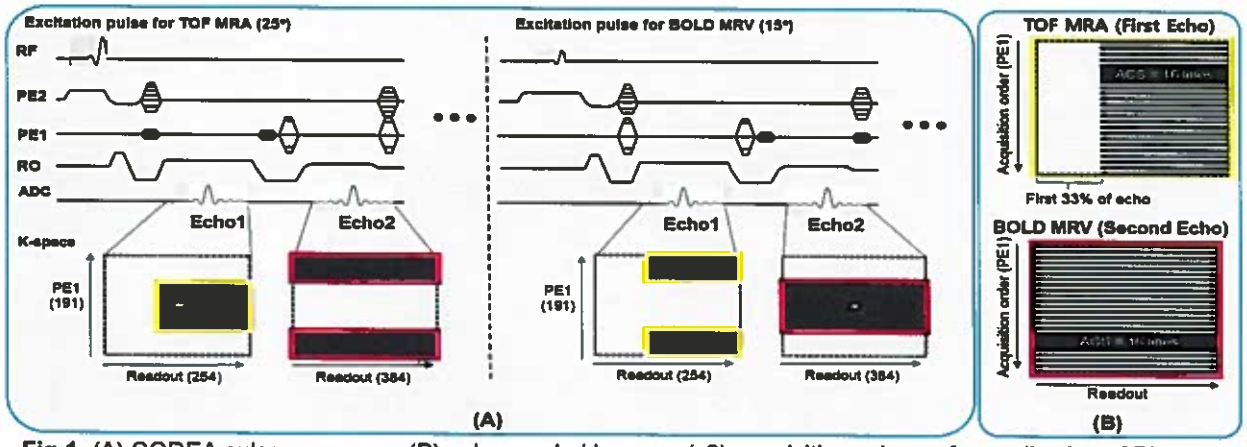

Fig 1. (A) CODEA pulse sequence. (B) sub-sampled k-space (x2) acquisition scheme for application of PI.

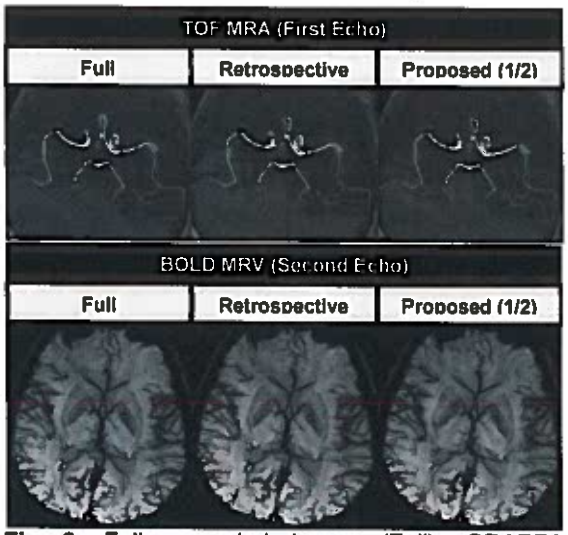

Fig 2. Fully sampled image (Full), GRAPPA reconstruction image from retrospective down sampling (Retrospective), GRAPPA reconstruction image from actual down-sampled acquisition

Results and Discussion: Arteries and veins were clearly shown in simultaneously acquired TOF MRA and BOLD MRV, respectively. GRAPPA reconstructed images of both the retrospective down sampling and the actual down sampling visually well preserved the detailed structures and contrast compared to those of the full sampling (Fig 2). The normalized MSE between the fully-sampled and the down-sampled images was 0.004 and 0.013 for TOF MRA and BOLD MRV respectively, which were negligible.

In the futue, the proposed approach will be tested and optimized with acceleration factor above 2 for GRAPPA and also for another acceleration technique, compressed sensing.

Conclusion: We could acquire TOF MRA and BOLD MRV simultaneously in ~5 min using CODEA in combination with GRAPPA. This improvement not only reduces image acquisition time, but also provides more clinical information in a limited scan time.

Reference: 1. Park et al. MRM 61:767-774.
2. Griswold et al. MRM 47:1202-1210

Derivation and Validation of Synthetic ECV Calculation from Blood Pool T1 values at 3T MRI

Ozair Rahman[1], Michael Markl[3], Alex Barker[3], Benjamin Freed[2], James Carr[1], Jeremy Collins[1]
[1]Northwestern University, Department of Radiology, Chicago, IL USA
2Northwestern University, Department of Cardiology, Chicago, IL USA
3Department of Biomedical Engineering, Northwestern University, Chicago, IL USA

Purpose: Myocardial gadolinium extracellular volume fraction (ECV) quantification with T1 mapping is a clinically useful tool in diagnosis and prognosis of cardiac pathology. As originally described ECV calculation requires a recent laboratory hematocrit (HCT_{lab}), which is impractical in the clinical routine and has slowed adoption of this technique. Recently, Treibel et al described a relationship between blood pool T1 values and the hematocrit using 1.5T MRI. Such a relationship has not been described at 3T. The purpose of this study was to derive the relationship between blood pool T1 and laboratory hematocrit at 3T and apply this derived formula to a validation cohort.

Methods and Materials: Retrospective study of 80 consecutive patients (mean age 62.6±22.1years) who underwent cardiac MR (CMR) at 3T (Magnetom Skyra, Siemens Medical Systems, Erlangen, Germany) pre- and 12-25-minute post-contrast T1 mapping using a modified Look-Locker inversion recovery (MOLLI) sequence with a 5(3)3 scheme with single shot steady state diastolic readouts at a single center between April 4th, 2015 to February 3rd, 2016. Patients were randomly split into derivation and validation subgroups with equal health and disease representation. Data was motion corrected with in-line T1 parametric map generation quantifying blood pool T1 values in the Left Ventricle (LV)(Xue et al., 2012). Linear regression was used to derive a reliationship between LV blood pool R1 and lab hematocrit. ECV quantification was calculated with laboratory (ECV_{lab}) and synthetic (ECV_{syn}) hematocrit using the tool developed by Kellman et al. All data is presented as mean±SD. Two sided, paired Student's t-test was calculated for between group differences; $P<0.05$ considered to be statistically significant

Results: Proof of concept, 80 subjects (24 women, 62.7 +- 15.5 years) were randomly assigned to derivation (N=50) (mean age 65.7± 23.8 years) and validation (N=30)(mean age 63.8±22 years) cohort. A linear relationship between HCT_{lab} and Left Ventricle $R1_{Blood}$ ($R^2=0.09$) was used to create a synthetic ECV and Hct formula: $(239\times[1/T1_{Blood}]) + 0.2815$, and applied to the validation cohort. Myocardial ECV_{syn} fractions calculated from LV blood T1 values were similar to those derived from laboratory-determined hematocrit. A fit curve was calculated and applied to the validation cohort and depicting high correlation ($R^2=0.95$). A bland-altman plot was performed to assess agreement between ECV calculations and lab vs synthetic hematocrit in the derivation cohort (Figure 1A and Figure 1B).

Conclusion: ECV calculations from synthetic and laboratory HCT were similar, suggesting that this technique may be a feasible alternative to routine blood draws in patients and conventional ECV calculations. (Figure 1)

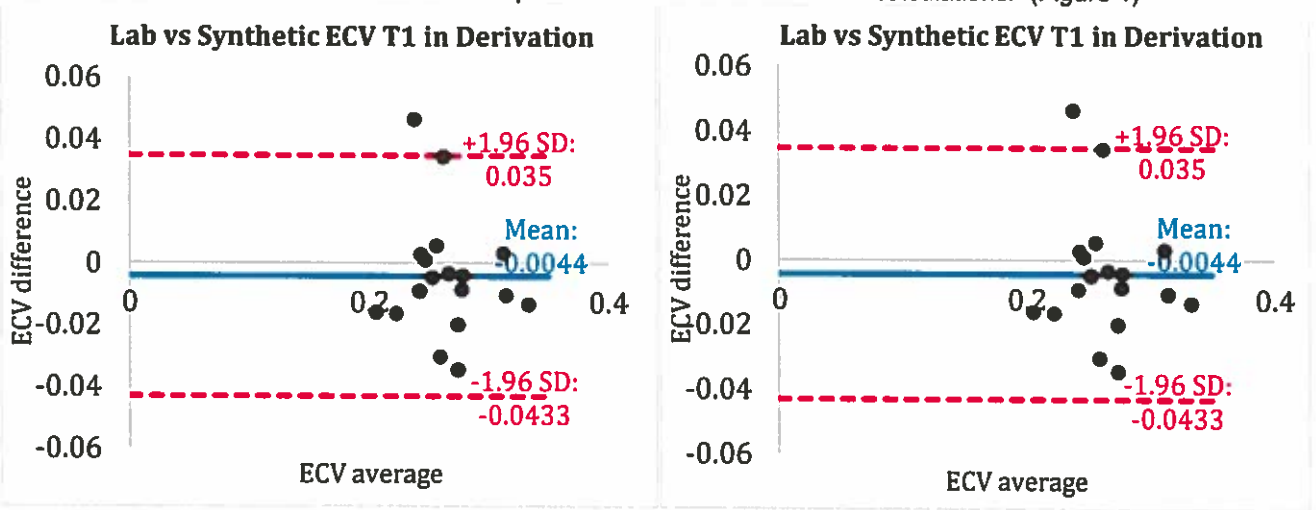

Xue, H., Shah, S., Greiser, A., Guetter, C., Littmann, A., Jolly, M. P., . . . Kellman, P. (2012). Motion correction for myocardial T1 mapping using image registration with synthetic image estimation. *Magn Reson Med, 67*(6), 1644-1655. doi: 10.1002/mrm.23153

A proper orthogonal decomposition approach towards merging CFD and 4D-PCMR flow data

Ali Bakhshinejad[1], Ahmadreza Baghaie[2], Vitaliy L. Rayz[1,3] and Roshan M. D'Souza[1]

[1]Department of Mechanical Engineering, University of Wisconsin-Milwaukee
[2]Department of Electrical Engineering, University of Wisconsin-Milwaukee
[3]Department of Neurosurgery, Medical College of Wisconsin

Purpose: To investigate use of Proper Orthogonal Decomposition (POD) to reconstruct accurate hemodynamic velocity profiles by merging patient specific Computational Fluid Dynamic (CFD) simulations and noisy *in-vivo* time resolved phase contrast magnetic resonance (4D-PCMR) imaging.

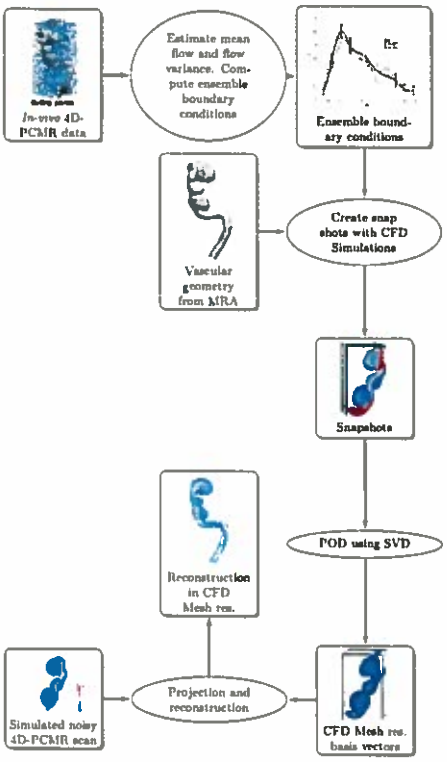

Figure 1: Hemodynamic velocity reconstruction using POD

Methods: The overall approach is as shown in the Figure 1. Boundary Conditions (BCs) are sampled from the raw 4D-PCMR flow data at several cutting planes at the inlet. After computing the mean flow and the flow variance, an ensemble of BCs is created assuming a normal distribution of flow measurement error. Note that in this study *in vivo* 4D-PCMR data is used only to generate BCs for the numerical phantom. Using these ensemble BCs along with patient specific geometry obtained from Magnetic Resonance Angiography (MRA), an ensemble of CFD simulations is conducted and the velocity profiles (snapshots) at each time step for all simulations are collected in a matrix $[X]$. Next, a set of basis vectors that span all possible solutions near the actual flow are generated by executing a Singular Value Decomposition (SVD) of $[X]$ as $[U][\Sigma][V]^T = SVD([X])$. This is the POD approach applied to flow problem. The matrix $[U]$ contains the left eigen vectors of $[X]$ which form the basis vectors of the solution space. The simulated 4D-PCMR reading $[Y]$ is then projected onto the basis as $[\alpha] = [U]^T [Y]$. An estimate of the actual flow is then reconstructed as $\left[\hat{Y}\right] = [U] \cdot [\alpha]$.

Results: An ensemble of 6 different CFD solutions was obtained by randomly perturbing the average time varying inlet flow BCs obtained from a raw 4D-PCMR data set. One of the 6 solutions was randomly selected as the ground truth. Gaussian noise was added to this solution to simulate the 4D-PCMR acquisition process. The remaining 5 solutions in the ensemble were used to construct the basis vectors. The noise-free estimate of the actual flow was obtained using the process described above. The result thus obtained was compared to the ground truth by computing the error. Figure 2a shows the magnitude of ground truth velocity profile at a particular cross-section. Figure 2b shows the noisy velocity after adding Gaussian noise with variance of 0.3 m/s. Figure 2c shows the reconstructed velocity profile using POD. Figure 2d compares the magnitudes of the ground truth, the noisy velocity, and the recovered velocity at a sample line indicated in Figure 2a.

Conclusion: The results indicate that the POD method has the potential to merge CFD and *in-vivo* 4D-PCMR to accurately reconstruct actual hemodynamic profiles. This will enable accurate estimation of clinically relevant derived parameters such as wall shear stresses (WSS) and pressure gradients.

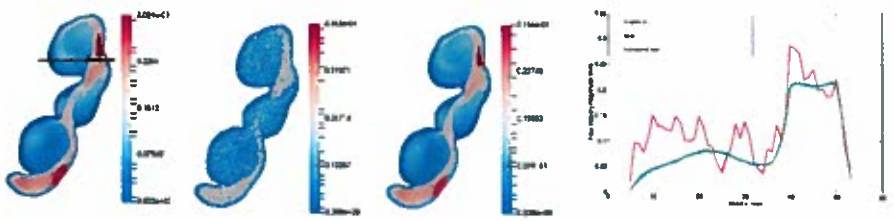

(a) (b) (c) (d)

Figure 2: Reconstructing hemodynamic velocities using POD. (a) Ground truth. (b) Noisy signal. (c) Reconstructed velocity profile. (d) Velocity magnitude comparison between ground truth, noisy and POD-based reconstruction along a 1-D section shown in (a)

Black-blood ultra short echo time (UTE) imaging of the thoracic vessels

Jean Delacoste[1], Helene Feliciano[1], Giulia Ginami[1], Ruud B. van Heeswijk[1], Davide Piccini[1,2], and Matthias Stuber[1,3]
[1]Department of Radiology, University Hospital (CHUV) and University of Lausanne (UNIL), Lausanne, Switzerland, [2]Advanced Clinical Imaging Technology, Siemens Healthcare, Lausanne, Switzerland, [3]Center for Biomedical Imaging (CIBM), Lausanne, Switzerland

Purpose: Ultra-short echo time (UTE) sequences are well suited for magnetic resonance angiography (MRA), as they are robust against flow dephasing (1). Their capacity to image short T_2 components may allow calcification to be identified in atherosclerotic plaques (2) and can also improve image quality in the lungs (3). In vivo examination of the vessel wall can also benefit from the use of black-blood imaging. In this work, in order to improve MRA of the thoracic vessels, we implemented and tested a 3D radial UTE sequence combined with a black-blood preparation module.

Methods: Motion-Sensitized Driven Equilibrium (MSDE) preparation (4) was implemented and added to a prototype 3D UTE sequence. The UTE acquisition was performed with a segmented 3D radial spiral phyllotaxis trajectory (5). An iterative algorithm (6) was used to retrospectively detect respiratory motion allowing reconstruction of motion-suppressed 3D image volumes gated to end-expiration with isotropic resolution covering the whole thorax. Different gradient moments used within the MSDE module result in preferential suppression of different flowing spins, depending on their velocity. This is indicated by the field of speed (FOS), defined as the velocities for which a phase shift of 2π will be induced (7). In each experiment, 3 datasets were acquired, using FOS values of 10, 20 and 30 cm/s. In addition, a reference dataset was obtained without motion-sensitizing gradients. This novel method was tested in 5 healthy volunteers using a 3T clinical MRI scanner (MAGNETOM Prisma, Siemens Healthcare, Erlangen, Germany). Acquisition parameters were echo time TE=0.05 ms, repetition time TR=5.4 ms, readout bandwidth=401 Hz/px, radio-frequency excitation angle=5°, field-of-view FOV=$(250mm)^3$, matrix size=192^3, voxel size=$(1.3mm)^3$ and 398 segments each consisting of 44 readouts. ECG triggering in diastole was used to acquire segments every other heart beat, to allow time for magnetization recovery. The signal-to-noise ratio (SNR) in the lumen was evaluated in 4 locations: the right pulmonary artery, left pulmonary artery, ascending aorta and descending aorta. The average SNR over all locations was compared for the 4 acquisition protocols. The standard deviation across the 4 ROIs was computed for each volunteer as measure of the interluminal variability. Statistical significance was assessed using a Student's t-test with p-values lower than 0.05 considered statistically significant. Additionally, two higher resolution datasets (reference and FOS=10 cm/s) were acquired in one volunteer with TE/TR=0.05/5.6 ms, readout bandwidth=399 Hz/px, radio-frequency excitation angle=5°, FOV=$(250mm)^3$, matrix size=256^3, voxel size=$(1mm)^3$, and 814 segments each consisting of 44 readouts. Composite datasets were also generated by subtracting motion-sensitized datasets from the reference datasets.

Results: The average lumen SNR was significantly lower with all FOS values when compared to the reference datasets. A FOS of 30 cm/s resulted in significantly higher signal (7.8) than that of 10 cm/s (5.8, p=0.05). However, no significant difference was measured between 10 (5.8) and 20 cm/s (6.2, p=0.6). Interluminal variability was significantly lower compared to reference datasets (2.7) with FOS of 10 cm/s (0.7, p=0.0009) and 20 cm/s (0.7, p=0.002) and the suppression of blood signal could be observed in all vessels despite their different orientations and locations in the FOV. The aortic wall could consistently be visualized with the proposed technique, as can be notably seen in the higher resolution data (figure 1b). The composite datasets, obtained by subtraction, yielded a bright signal from all flowing structures in the FOV. Notably, blood signal was enhanced, which allowed visualization of the vessels without requiring contrast injection (figure 1c).

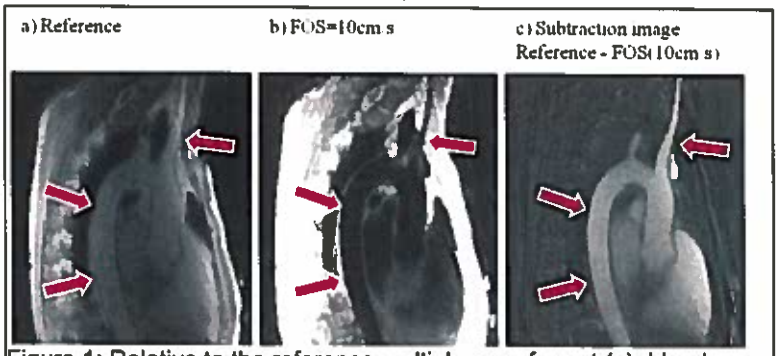

Figure 1: Relative to the reference multiplanar reformat (a), blood signal is suppressed in the black-blood prepared image (b) in the aorta and right common carotid artery (arrows). The aortic wall can be well identified over its entire length. In the subtraction image (c), the signal from vessels is highlighted with respect to other tissues.

Conclusion: High resolution 3D isotropic black-blood UTE imaging is enabled with the proposed technique and the results confirmed the significant decrease in signal from the arterial lumen. The optimal range of FOS values was determined to be inferior to 30 cm/s. With the small sample size, no significant difference could be measured between values of 10 and 20 cm/s and further studies are needed to assess the optimal parameter settings. Attenuation of flowing spins was successfully obtained in the entire FOV. This may not easily be obtained with conventional double-inversion techniques where the blood-pool in the imaged volume needs to be fully replaced between magnetization preparation and imaging. Additionally, the enhanced signal from blood vessels in the subtraction images could potentially deliver additional diagnostic information without requiring contrast injection.

Acknowledgements: This work was supported by the Swiss National Science Foundation grants 320030_143923 and 326030_150828 as well as a grant from the Fondation BCV.

References: 1. Nielsen et al. MRM 1999;41:591–599. 2. Chan et al. JCMR 2010;12:17. 3. Bergin et al. Radiology 1991;179:777–781. 4. Okada et al. J Comput Assist Tomogr 1998;22:364–371. 5. Delacoste et al. ISMRM; 2015, #1455. 6. Ginami et al. MRM 2015;75:1594-1604. 7. Nguyen et al. JMRI 2008;28:1092–1100.

Session 11

Vessel Wall MRI

Quantification of abdominal aortic aneurysm wall thickness using registration-based level set segmentation of 3D black-blood MR images

Yan Wang, Evan Kao, Florent Seguro, Farshid Faraji, Jing Liu, David Saloner
Department of Radiology and Biomedical Imaging, University of California, San Francisco

Purpose: Analysis of abdominal aortic aneurysm (AAA) geometric features plays an important role in medical treatment. The 3D patient-specific geometries can facilitate the assessment of rupture risk, which is normally based on aneurysm size, shape, volume and growth[1]. We propose a reproducible and efficient technique to segment and measure the vessel wall of AAA in 3D black-blood magnetic resonance imaging.

Method: 1) Segmentation: The proposed method (Figure 1) consists of co-registering the contrast enhanced MR angiography and black-blood MR images, and segmenting both the inner and outer wall using geometric active contours (GAC) and registration-based geometric active contour (RGAC), respectively. Solving the gradient flow can minimize the energy functional of the GAC model as follows: $\frac{\delta\phi}{\delta t} = \mu\left[\Delta\phi - div\left(\frac{\nabla\phi}{|\nabla\phi|}\right)\right] + \lambda\delta(\phi)div\left(g\frac{\nabla\phi}{|\nabla\phi|}\right) + vg\delta(\phi)$, where μ, λ and ν are weight coefficients and g the edge indicator function. The energy formulation from the RGAC model is used to estimate the outer wall: $E = rE_{registration} + gE_{GAC} + sE_{similarity}$, where r, g and s are positive regulation parameters, and E_{gac} controls the contour of the segmentation moving to the local minimization of the image. $E_{similarity}$ represents that the segmentation result should be similar to the reference image and $E_{registration}$ controls the registration of two neighbouring images[2]. 2) Measurement: Cross sections of the inner wall orthogonal to its centreline are generated at 1mm intervals. The wall thickness is defined as the distance between the outer wall and the inner along the ray projected from the centreline to the inner wall. The maximum wall thickness, area, maximal radius, and minimal radius for each cross section were calculated. The proposed segmentation technique was tested on 19 AAA patients. To validate our technique, an experienced radiologist also manually segmented those cases.

Results: The average Dice and CV values reached 89.79±2.46%, which demonstrated that comparable and stable segmentation was achieved with the proposed method compared to manual segmentation. The Bland-Altman and linear regression for the manual and the proposed method generated inner, outer and vessel wall volumes with Bias±1.96std (0.02±0.03, 0.05±0.03 and 0.01±0.07, respectively) and P value (0.85, 0.73 and 0.73, respectively) demonstrating good agreement between manual and the proposed segmentation. The maximal wall thickness, the inner, and the outer wall area are shown in Figure 2, respectively. The proposed segmentation method requires less time than other semi-automated methods, and is an order of magnitude faster than fully manual segmentation.

Conclusion: The proposed segmentation provides a reproducible and efficient way to obtain AAA geometry, and the measurement gives an accurate and repeatable way to get the maximal AAA diameter, a key parameter in surgical planning.

References: 1. Brady et al., Circulation. 2004. 2. Wang et al., Physics in medicine and biology. 2005.

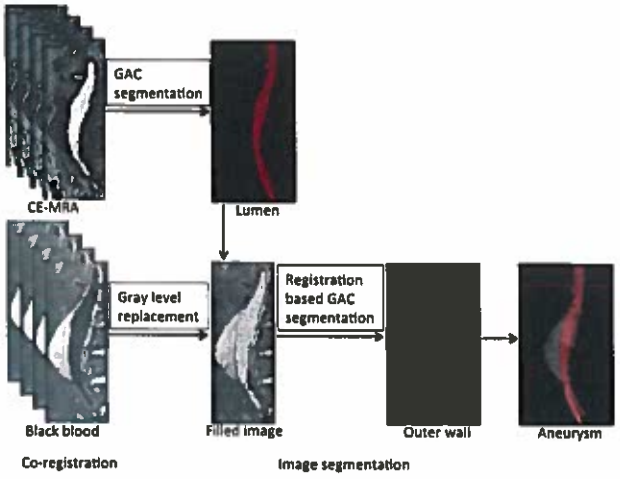

Figure 1: Inner and outer wall segmentation scheme.

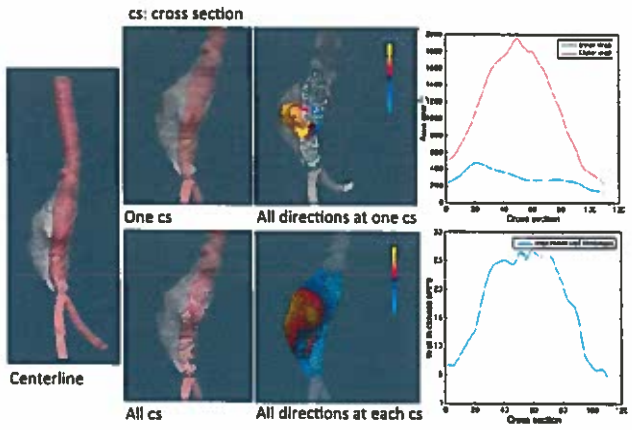

Figure 2: Wall thickness and area measurement at each cross section.

Multi-contrast Acquisition in a Single Sequence (MASS) for Carotid Atherosclerosis Evaluation and Quantitative T1 Mapping

Haikun Qi[1], Huiyu Qiao[1], Xinlei Pan[1], Zechen Zhou[2], Yishi Wang[1], Hujun Chen[1]
[1] Center for Biomedical Imaging Research, School of Medicine, Tsinghua University, Beijing, China
[2] Philips Research China, Shanghai, China

Purpose

Characteristics of atherosclerotic plaque, such as intraplaque hemorrhage (IPH) and heavy plaque burden, are considered to be the indicator for vulnerable plaque. However, complicated multi-contrast MR acquisitions are needed to evaluate these features (1), which require long scan time and are difficult to analyze because of misregistration between scans. Thus, the purpose of this study is to propose a Multi-contrast Acquisition in a Single Sequence (MASS) for carotid atherosclerosis evaluation, which can produce multiple T1 contrasts for IPH detection, plaque burden quantification and T1 mapping of the plaque.

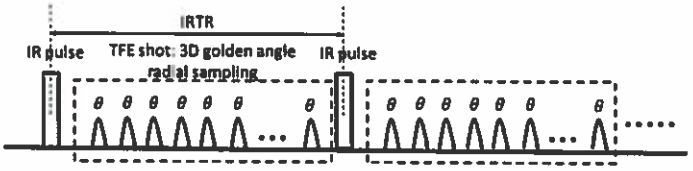

Fig. 1: Schematic diagram of the proposed IR 3D golden angle radial sequence.

Methods

Sequence Design: The proposed sequence consists of an IR preparation pulse and a 3D radial sampling acquisition (Fig. 1). Spokes of the same TI in different IRTRs conform to the golden angle distribution (2), to achieve uniform distribution of acquired spokes for reconstruction. For fat suppression, water excitation pulse was used in the acquisition. *MR Imaging:* After institutional review board approval, 2 healthy volunteers and 2 patients with carotid atherosclerosis were scanned on a 3T MR scanner (Philips, Achieva). The imaging parameters of MASS were: FOV=100mm isotropic; voxel size=0.8mm isotropic; readout=224 (2x oversampling); TR/TE=11.5/4.7ms; flip angle=10°; TFE factor (N) =151; IRTR=2000ms; scan duration=5min. The QIR-TSE (3) and SNAP (4) sequences were carried out as reference. *Image reconstruction:* After selection of starting spoke number n and temporal width TW, Sliding window and KWIC (5) were used together for reconstruction. Image contrast is dominated by the central parts of k-space. The resulting image intensity is thus determined by averaging the signal at spoke number of n to n+TW-1. T1 mapping was performed using images reconstructed with n from 1 to N-TW+1, and TW=15 (10 frames). The last frame was used to correct the phase errors in the inverted signal. Specific contrasts were also reconstructed with optimized n and narrow TW, including strong T1W contrast for IPH detection, and near-zero lumen contrast for vessel wall. *Image Analysis:* To evaluate the performance of MASS in IPH detection and plaque burden measurements. The reconstructed images of strong T1W contrast and vessel wall were compared with histology validated sequences, SNAP and QIR-TSE separately. The reconstructed vessel wall contrast images of MASS were reformatted into axially oriented 2mm slices as QIR-TSE. The images from the two sequences were matched based on carotid bifurcation. Lumen and outer wall were drawn by a reviewer on MASS and QIR-TSE images without knowing the method generating the images. The plaque burden measurements were compared between MASS and QIR-TSE by Mann-Whitney t-test and intra-class correlation coefficients (ICCs).

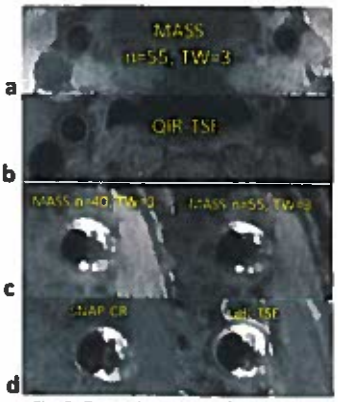

Fig. 2: Example images of a healthy volunteer and the patients with IPH from MASS (a, c) displaying contrasts for vessel wall and IPH. Corresponding QIR-TSE and SNAP images (b, d) are also shown for comparison.

Results

Both MASS and SNAP successfully detected the IPH of the left carotid artery in one patient (Fig. 2c, d). The images of optimized contrasts by MASS for the patients and a healthy volunteer are shown in Fig. 2a, c, compared with SNAP and QIR-TSE (Fig. 2b, d). The quantitative T1 map results of the patient with IPH are shown in Fig. 3. Although, flow artifacts may induce estimation error in the juxta-lumen region, the IPH area shows obviously decreased T1. The mean T1 values of IPH and muscle were 402ms and 1213ms, respectively. Plaque burden measurements for all the data were summarized in Table 1. No significant difference was found between MASS and QIR-TSE (P>0.05). And the ICCs (>0.9) indicates a good agreement between the two methods.

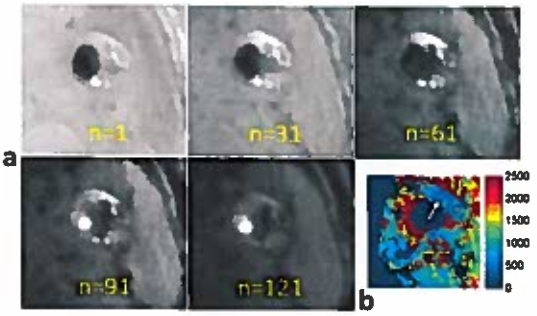

Fig. 3: T1 mapping results of the patients with IPH. a: The selected images of different T1 contrasts from by MASS with TW=15. b: The resulting T1 map.

Discussion

This study initially proved the feasibility of the proposed Multi-contrast Acquisition in a Single Sequence (MASS) in IPH detection, plaque burden measurements, and quantitative T1 mapping of atherosclerotic plaque. MASS may be a one-stop solution for 3D volumetric plaque imaging by providing inherently co-registered multi-contrast images in a single scan within short scan time (5 min).

Table 1: Comparison of plaque burden measurements.

Measures	Protocol		P	Agreement	
	QIR-TSE	MASS		ICC	95%CI
LA(mm2)	34.2±11.4	35.6±12.1	0.51	0.900	(0.824, 0.944)
WA(mm2)	54.2±24.6	58.9±30.9	0.78	0.916	(0.846, 0.953)
MaxT(mm)	3.2±1.6	3.0±1.6	0.48	0.931	(0.879, 0.961)
MeanT(mm)	2.0±0.8	2.1±0.9	0.96	0.939	(0.892, 0.965)

Values are mean±SD; LA for lumen area; WA for wall area; MaxT for maximum wall thickness; MeanT for mean wall thickness. P was estimated by Mann-Whitney test between MASS and QIR-TSE (P<0.05 is significant).

References

[1]. Saam T, et al. Radiology. 2007;244:64-77. [2]. Rachel W, et al. MRM. 2009;61:354-363. [3]. Vasily L, et al. MRM. 2002;48:899–905. [4]. Wang J, et al. MRM. 2013;69:337-345. [5]. Song H K, et al. MRM. 2000;44:825-832.

Post-Contrast Black-blood HASTE Imaging: Initial Results with Ferumoxytol.

Eun-Ah Park, MD[1,2], Takegawa Yoshida, MD[1], Sarah Khan, MD, J. Paul Finn, MD[1]

[1]Department of Radiological Sciences, David Geffen School of Medicine, University of California at Los Angeles, Los Angeles, CA 90095 and, [2]Department of Radiology and the Institute of Radiation Medicine, Seoul National University Hospital, Seoul, 110-744, Korea

Purpose: Despite a plethora of creative magnetization preparation schemes, reliable black blood imaging has proved evasive in clinical practice, because most techniques are flow dependent. The purpose of this study was to assess the reliability of black-blood Half-Fourier Single-shot Turbo Spin-echo (HASTE) imaging following ferumoxytol, as a complement to bright blood MR Angiography and based wholly on the relaxivity of ferumoxytol.

Materials and Methods: Our institutional review board approved this retrospective study protocol and written informed consent for the off label use of ferumoxytol was obtained in all patients. Forty-two patients underwent clinically indicated ferumoxytol-enhanced MR angiography of the thorax and abdomen. In all cases, pre-contrast black-blood HASTE images with dual-inversion prepulses were acquired in multiple planes and repeated following ferumoxytol administration, without the dual-inversion pulses. Quantitative measurements including homogeneity index (defined as standard deviation of the left atrial signal intensity) and signal-to-noise ratios (SNRs) for all of the central cardiovascular structures in the thorax were measured on the black blood images. Qualitative image quality scores for assessing complete suppression of blood signal were also evaluated in a 3-point scale by two readers: 3 = complete on all slices; 2 = incomplete on some slices and; 1 = incomplete on all slices. Results were compared using Wilcoxon-signed rank test.

Results: No adverse reactions to ferumoxytol were noted. Compared to pre-contrast black-blood images, ferumoxytol-enhanced black-blood images showed significantly better mean values of homogeneity indices (156.0±89.9 vs. 27.5±10.8, p <0.001) and lower intraluminal SNRs for all cardiovascular regions (overall, 28.4±41.9 vs. 7.1±6.3, p <0.001), indicating more effective blood signal suppression. Qualitative image scores showed virtually complete blood suppression in ferumoxytol images (overall, 2.9±0.2 vs 1.8±0.6 for gadofosveset, p <0.001). In multiple patients, ambiguity about the nature of intraluminal signal on pre-contrast HASTE images was resolved on post-ferumoxytol images (fig 1).

Conclusion: Black-blood HASTE imaging using ferumoxytol provided complete and reliable, flow independent blood signal suppression both quantitatively and qualitatively, without the need for magnetization preparation pulses.

References:

1. Neuwelt EA, Hamilton BE, Varallyay CG, et al. Ultrasmall superparamagnetic iron oxides (USPIOs): a future alternative magnetic resonance (MR) contrast agent for patients at risk for nephrogenic systemic fibrosis (NSF)? Kidney Int 2009;75:465-474.

2. Wei Li, et al. Lower Extremity Deep Venous Thrombosis: Evaluation with Ferumoxytol-enhanced MR Imaging and Dual-Contrast Mechanism—Preliminary Experience. Radiology 2007;242(3):873-881.

Figure 1.

A 3 year old female with Kawasaki Disease and giant coronary artery aneurysms, partially thrombosed. The left column shows sagittal and coronal pre-ferumoxytol HASTE images with high signal both within the patent lumen (arrowheads) and the upper thrombosed portions of the left coronary artery. The right column shows the corresponding post-ferumoxytol HASTE images with complete signal suppression within the patent lumen and persistent high signal superiorly due to thrombus. The middle column shows bright blood (MUSIC) images for reference, complementing the post-ferumoxytol HASTE images.

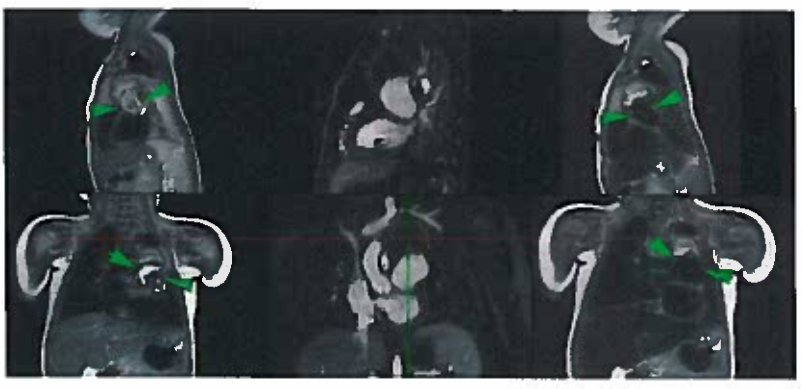

Scan-Rescan Reproducibility of Intraplaque Hemorrhage Volume Measured Using a Semi-Automatic Method with SNAP MRI

Jin Liu, Jie Sun, Thomas S. Hatsukami, William S. Kerwin, Niranjan Balu,
Daniel S. Hippe, Amy Wang, and Chun Yuan
University of Washington, Seattle, WA, United States

Purpose

Intraplaque hemorrhage (IPH) is a high-risk feature of atherosclerosis that is associated with accelerated plaque progression [1, 2]. IPH can be identified as hyperintense areas on T1-weighted MRI, due to T1 shortening effect caused by the formation of methemoglobin [3]. Improved contrast between IPH and other tissues on highly T1-weighted images results in good reader reproducibility in determining the presence of IPH [4-5]. However, the scan-rescan reproducibility of IPH volume measurement has not been reported. Simultaneous non-contrast angiography and intraplaque hemorrhage (SNAP) MRI has been recently developed to concurrently increase IPH-to-wall contrast and improve flow-suppression efficiency [6], which may improve reproducibility of IPH volume measurement. In this study, we sought to: 1) develop a SNAP-based semi-automatic method for time-efficient characterization of IPH; 2) establish scan-rescan reproducibility of IPH volume quantification.

Methods

Study Population: Thirty-three asymptomatic patients with carotid atherosclerosis were scanned twice within one month with SNAP (TR/TE = 10/4.8 ms, flip angle = 11°, inversion time = 500 ms, field-of-view = 160×160×32 mm^3, number of signal averages = 2, and scan time = 5.3 minutes). The acquisition spatial resolution was 0.8 mm isotropic, which was reduced to 0.4 mm after zero-filling interpolation. *Semi-automatic Processing:* **1)** Intensity normalization: The signal intensity ratio (SIR), defined for each voxel as the ratio of the signal intensity on phase corrected SNAP image to the sternocleidomastoid muscle (SCM) signal intensity on the reference SNAP image, was used for semi-automatic detection of IPH. **2)** 3D region-of-interest (ROI): After intensity normalization, a 3D cuboid ROI was defined interactively on the 3D image volume of SNAP. The 3D ROI included any hyperintense vessel wall areas if present. After processing one scan, the 3D ROI was automatically mapped to the paired scan, which was achieved by local rigid registration (MATLAB, R2015a). **3)** IPH detection and volume quantification: ROIs with ≥ 8 voxels (acquisition resolution) above a hyperintensity threshold were recorded as IPH present based on SIR. IPH volume (voxel size × number of voxels above a hyperintensity threshold) was calculated for each ROI with IPH present. *Hyperintensity Threshold:* An experienced reviewer read each scan independently and recorded IPH presence by visually inspecting whether there were distinct hyperintense signals within the carotid wall on SNAP as compared to SCM. A hyperintensity threshold was obtained through receiver operating characteristic (ROC) curve analysis and maximizing the sum of sensitivity and specificity for IPH detection, using the manual determination of IPH as the reference standard. *Statistics:* Cohen's kappa and the intraclass correlation coefficient (ICC) were used to evaluate the reproducibility of IPH detection and IPH volume measurement, respectively (R software, version 3.0.2). For both kappa and ICC, 95% confidence intervals were calculated and expressed in brackets. Pearson's correlation coefficient was calculated between time interval and within-subject coefficient of variation (CV) of IPH volume.

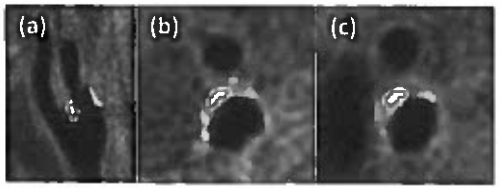

Figure. Automatically segmented IPH volume (red contours) using the hyperintensity threshold in longitudinal view (a) and axial views in Scan 1 (b) and Scan 2 (c) at the same location (blue line). Interval: 7 days.

Results

The time interval between two scans was 7.8 ± 8.9 days. *Hyperintensity Threshold:* An optimized threshold was found to be 1.4 times the mean intensity of SCM in the reference image. *Manual IPH detection:* Of the 66 arteries, the manual review found IPH on both scans of 13 arteries (19.7%) and on only one scan of 2 arteries (3.0%), resulting inter-scan kappa of 0.91 (0.79-1.0). *Semi-automatic IPH detection*: 12 arteries (18.2%) had IPH on both scans and 1 artery (1.5%) had IPH on only one scan, resulting inter-scan kappa of 0.95 (0.85-1.0). *Semi-automatic IPH volume quantification:* Using the hyperintensity threshold, IPH volume showed excellent scan-rescan reproducibility with ICC of 0.96 (0.87-0.99) (one example showed in **Figure**). *Impact of time interval:* There was no significant correlation between scan-rescan time interval and CV of IPH volume ($r = 0.27$, $p=0.395$).

Discussion and Conclusion

The scan-rescan reproducibility of IPH volume has not been previously reported. Reasons may include insufficient number of IPH plaques in previous studies, inconspicuous IPH boundaries, and uncertain biological stability of IPH signals. In this study, a semi-automatic method was developed based on SNAP, which can perform objective quantification of IPH volume with minimal human input. Scan-rescan reproducibility of IPH volume is high, suggesting SNAP as a reliable MRI sequence for IPH volume quantification and future IPH volume progression study.

References

[1] Michel JB, et al. Eur Heart J, 2011;32(16):1977-85. [2] Takaya N, et al. Circulation, 2005; 111(21): 2768-75. [3] Bradley WG, et al. Radiology, 1993;189(1):15-26. [4] Yamada N, et al. AJNR, 2007;28(2):287-92. [5] Qiao Y, et al. AJNR, 2011;32(3):454-9. [6] Wang J, et al. MRM, 2013;69(2):337-45.

Relating MRI characteristics of peripheral arterial lesions to guidewire puncture forces

Purpose
Percutaneous vascular interventions (PVI) offer a minimally invasive treatment for peripheral arterial disease (PAD), but carry a risk of immediate technical failure. A frequent mode of failure is the inability to enter chronic total occlusions (CTOs) with a guidewire. Current imaging of PAD lesions is extremely limited. Physicians can only base their revascularization decisions on target lesion location, length and degree of calcification. We aim to improve PAD lesion imaging using MRI. Further, we relate MRI characteristics to the amount of force a guidewire takes to puncture peripheral CTOs (as a surrogate for immediate failure).

Methods
We excised 50 PAD lesions from 7 amputation patients. We imaged lesions at high resolution (75μm^3 voxels) with T2-weighted (T2W) and Ultrashort Echo Time (UTE) sequences at 7 Tesla. We validated MR images (n=15) with microCT and histology. We classified chronic total occlusions (CTOs) (n=25) by their MR signal characteristics as "soft" (those with signals indicating fat, thrombus, microchannels, or loose fibrous tissue), "hard" (those with collagen and/or speckled calcium signals), or "calcified" (those with calcified nodule signals). A 2kg load cell advanced the back-end of a 0.035" stiff guidewire at a fixed displacement rate (0.05mm/s) through the CTOs, and the forces required to cross each lesion were measured.

Results
MRI accurately differentiated PAD lesions based on associated puncture force. The guidewire could not enter "Calcified" CTOs (n=6) at all. "Hard" CTOs (n=9) required a puncture force of 1.71N ± 0.51. "Soft" CTOs (n=25) required 0.43N ± 0.36. "Hard" CTOs required statistically higher puncture forces compared to "soft" CTOs ($t(11) = 6.875$, $p < 0.001$).

Conclusion
MRI characteristics of PAD lesions correlate with guidewire puncture forces, an important aspect of crossability. Future work will determine if clinical MRI scanners can be used to predict PVI success in patients.

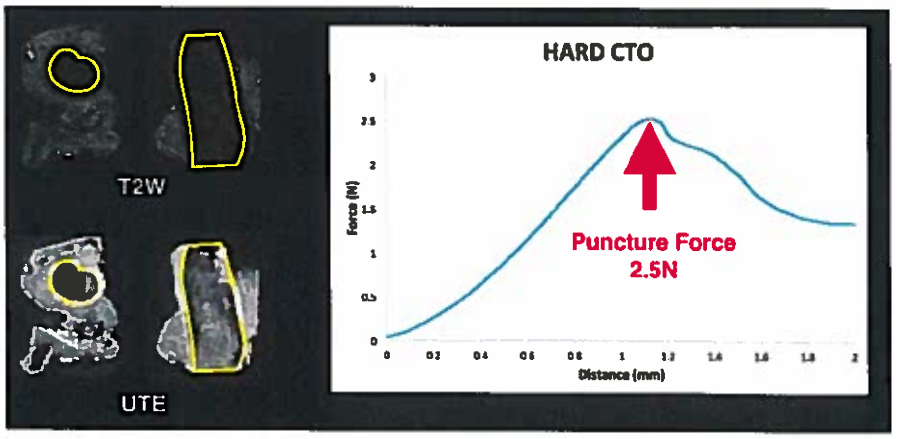

Figure: Non-calcified hard chronic total occlusion required 2.5N puncture force. The yellow highlights a completely occlusive plug of collagen within the vessel in both axial and coronal views. This lesion would likely fail PVI because the puncture force required exceeds the force at which clinical chronic total occlusion wires buckle (0.02-0.13N).

Hemodynamic vascular biomarkers at the site at which sidewall intracranial aneurysms occur at the paraclinoid internal carotid artery determined using patient-specific computational fluid dynamic simulation based on MR imaging

Tomoya Watanabe[1], Haruo Isoda[2, 1], Yasuo Takehara[3], Masaki Terada[4], Takehiro Naito[5], Chiharu Tanoi[6], Takafumi Kosugi[7], Yuki Onishi[8], Atsushi Fukuyama[1]

[1]Department of Radiological and Medical Laboratory Sciences, Nagoya University Graduate School of Medicine, [2]Brain & Mind Research Center, Nagoya University, [3]Department of Radiology, Hamamatsu University Hospital, [4]Department of Diagnostic Radiological Technology, Iwata City Hospital, [5]Department of Neurosurgery, Kasugai Municipal Hospital, [6]Department of Neurosurgery, Iwata City Hospital, [7]Renaissance of Technology Corporation, [8]Department of Mechanical and Environmental Informatics, Tokyo Institute of Technology, Graduate School of Information Science and Engineering

PURPOSE

Evaluation of hemodynamics is important, as hemodynamics is involved in the initiation, growth, and rupture of intracranial aneurysms. We performed computational fluid dynamics (CFD) based on magnetic resonance (MR) data of patients with and without paraclinoid internal carotid artery (ICA) aneurysms to qualitatively and quantitatively evaluate the distribution of vascular biomarkers at the aneurysm initiation sites of the paraclinoid ICA.

METHODS

This study was approved by our Institutional Review Board. Informed consent was obtained from all patients. This study included 35 patients who were followed up for aneurysms using 3D time of flight MR angiography (3D TOF MRA) and 3D cine phase contrast (PC) MR imaging (MRI). Fifteen out of 35 patients had an intracranial aneurysm in only one side of the paraclinoid ICA. The 15 affected ICA's were included in Group A with the 15 unaffected contralateral ICA's in Group B. 20 out of 35 patients had no aneurysms in the paraclinoid ICA and 33 out of 40 paraclinoid ICAs free of arteriosclerotic lesions were included in Group C. We created vascular geometries in STL format obtained from 3D TOF MRA and used them as the geometries for CFD analysis. For the pre-aneurysm geometries in Group A, we deleted aneurysm from the geometry obtained from 3D TOF MRA. Temporal volume flow rate (VFR) for each vessel during one cardiac cycle was calculated from 3D cine PC MR data set and this was used as a boundary condition for CFD analysis. The wall shear stress (WSS), spatial WSS gradient (SWSSG), oscillatory shear index (OSI), gradient oscillatory number (GON), aneurysm formation indicator (AFI), and streamlines were visualized from the analyzed results, and we qualitatively evaluated their distributions at the intracranial aneurysm initiation location. We also calculated the maximum WSS and SWSSG, and normalized those values using WSS of petrous ICA for both WSS and SWSSG and the mean blood flow travel distance for SWSSG. The normalized highest WSS and SWSSG were called nh-WSS and nh-SWSSG respectively. We investigated the statistical differences between Group A and Group C, and between Group B and Group C using the Mann-Whitney U test, and between Group A and Group B using the Wilcoxon signed rank test. A p-value less than 0.05 was considered statistically significant. The Bonferroni multiple-comparison correction was performed, and the p value was adjusted. We also performed ROC analysis.

RESULTS

In the qualitative evaluation, high WSS, SWSSG, and GON distribution were observed adjacent to the aneurysm initiation site in Group A. In addition, high WSS and SWSSG were observed at similar locations in Group B and Group C. In the quantitative evaluation, nh-WSS and nh-SWSSG were significantly higher in Group A than in Group C, and nh-SWSSG was significantly higher in Group A than in Group B. Using the ROC analysis, an nh-WSS threshold of 6.34 had a sensitivity of 0.92, specificity of 0.47 and an accuracy rate of 1.38; an nh-SWSSG threshold of 22.96 yielded a sensitivity of 0.83, specificity of 0.80 and an accuracy of 1.63.

Appropriate hemodynamics constantly remodels the vascular wall and helps to keep it in good condition. Inappropriate hemodynamics, however, may lead to mural cell apoptosis and subsequently vascular remodeling on the outward protrusion (aneurysm). Because the same tendency regarding distribution of biomarkers was seen in groups with and without aneurysms in the ICA in this study, it was thought that there was a threshold value in WSS and SWSSG that led to the initiation of aneurysms. We hypothesized that aneurysms occurred locally from the sites with highest WSS and/or SWSSG, and focused on the WSS and SWSSG as the regions of highest interest.

CONCLUSIONS

High WSS and SWSSG locations were observed at the aneurysm initiation sites of the pre-aneurysmal ICA and the groups where future aneurysms occurred had significantly higher nh-WSS and nh-SWSSG than the groups where no aneurysm occurred. Our findings indicated that nh-WSS and nh-SWSSG were good biomarkers for aneurysm initiation in the paraclinoid ICA.

Vessel Wall Analysis of Dissecting Aneurysm of Vertebral Artery Using 3T MRI

Keiji Igase, Daisuke Shoda, Nari Tei, Ichiro Matsubara, Takanori Ohnishi, Kazuhiko Sadamoto
Department of Neurosurgery, Washokai Sadamoto Hospital, Matsuyama, Japan

(Introduction) It has been difficult to acquire the information as to the vessel wall of intracranial arteries because of the smallness of relevant arteries and thinness of those vessel walls. Recently 3T MRI has shown up and the new technology enabling vessel wall of intracranial arteries to be clearly delineated has also developed. Using this new method we have evaluated the wall of dissecting aneurysm (AN) of the vertebral artery (VA).

(Methods) Consecutive 11 patients (mean age: 53.6 years old; Male 6 and Female 5) with a dissecting aneurysm of vertebral artery diagnosed with 3T MRI during 1 year (April 2015 to March 2016), who underwent 3T MRI, were enrolled in this study. All patients underwent 3T MRI (SIGNA HDxt: GE healthcare), with which both two images of 3D-TOF and T1-CUBE, which is one of 3D-FSE sequence created by GE healthcare, were obtained. We classified dissecting aneurysm to 3 types depending on the appearance on TOF-MRA, VA occlusion, Irregular wall, and AN like appearance. Subsequently we evaluated differences on T1-CUBE image in the aspect of intensity, appearance, and existence of intimal flap.

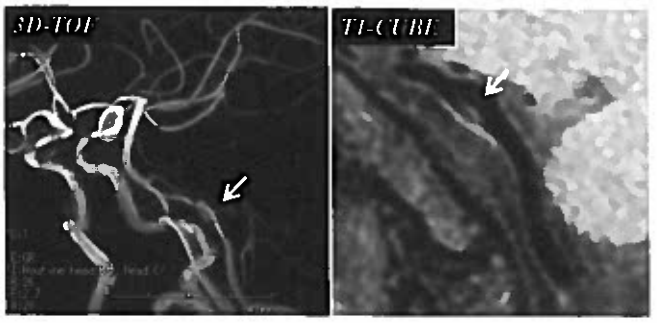

(Results) Breakdown of 3 types was VA occlusion 1, irregular wall 4, and AN like appearance 6. On the T1-CUBE image vessel wall of the lesion in 9 cases disclosed high-intensity, whereas that in 2 cases iso-intensity. Out of 6 cases with AN like appearance 4 cases revealed intimal flap like structure (Figure), which may imply that the laceration of internal elastic layer has been sustained, accordingly cases with AN like appearance might be better to be carefully managed in a clinical setting.

(Conclusion) New sequence of T1-CUBE could obviously delineate the vessel wall of dissecting aneurysm of vertebral artery and provide some valuable information depending on the appearance on TOF-MRA. Further investigation would be necessary to confirm these results.

ADC measurement of Carotid Atherosclerotic Plaque Using Motion Insensitive 3D DW-SOS Technique

Seong-Eun Kim[1,2], John A Roberts[1,2], Gerald S Treiman[3,4], Bradley D Bolster[5], Dennis L Parker[1,2] and Scott McNally[1,2]

Utah Center for Advanced Research[1], Depart of Radiology[2], Depart of Surgery[3], University of Utah
Department of Veterans Affairs[4], VASLCHCS
Siemens Healthcare[5]

PURPOSE

DWI has the potential to provide complementary information that will allow better discrimination of plaque components. The ADC values in different components within atherosclerotic plaques suggest that DWI might provide a tool for discriminating intraplaque hemorrhage (IPH) and lipid necrotic core from other components.[1,2] However, the current 3D DWI sequences based on multi-shot techniques are commonly limited by inconstant phase variance between each shot induced by motion.[3]

METHOD

A motion insensitive 3D diffusion weighted driven equilibrium Stack of Stars (3D DW-DE SOS) sequence was implemented.[4] To test the feasibility of this technique to visualize and assess plaque composition, 22 patients with carotid disease and 3 normal subjects were recruited and underwent 3T carotid MRI with a custom carotid coil. IPH was detected in 17 patients. The imaging parameters in DWI were: FOV=152x152 mm^2, 2 mm slice thickness, TE/TR = 2.05/8.0ms, 32 slices/slab, b =20, 450 s/mm^2. The resultant in-plane spatial resolution was 0.6x0.6 mm^2. The total imaging time was 3 min 20 sec. The ADC map was calculated and displayed using IDL. ADC values were obtained for the normal wall segments on 3 adjacent slices of the common carotid artery on 3 normal subjects. ADC values in the plaque of the 22 subjects were measured at 3 different slice locations within the plaque.

RESULTS

Table 1	Symptomatic	Asymptomatic	IPH+	IPH-
ROI(number)	42	87	60	69
ADC ($10^{-3}mm^2/s$)	0.65±0.14	0.98±0.16	0.67±0.13	1.05±0.12

The mean and standard deviation of the vessel wall ADC for normal wall was $1.48\pm0.11\times10^{-3}$ mm^2/s. The ADC measurements of patients were summarized in Table 1. Symptomatic plaque had significantly lower ADC than asymptomatic ($p<.001$). Plaque with IPH had significantly lower ADC than with no IPH ($p<.001$). Fig 1 shows one example ADC measurements in a patient with bilateral carotid IPH. The mean ADC of symptomatic hemorrhage on the right ($0.38\times10^{-3}mm^2/s$) was lower than ADC on the asymptomatic left side ($0.83\times10^{-3}mm^2/s$).

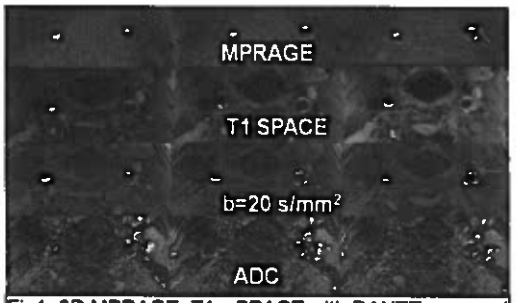

Fig1. 3D MPRAGE, T1w SPACE with DANTE prep and DWI of b=20s/mm^2 and ADC maps from a patient with a bilateral hemorrhage which is indicated by red (symptomatic) and green (asymptomatic) arrows.

CONCLUSION

Our sequence was able to yield high resolution ADC maps that could provide clear ROI selection for important plaque components. Our measured ADC values match the values reported in recent in-vivo studies.[1,2] The ADC values of the normal carotid wall compared with the lower ADC values in IPH lipid and hemorrhage suggest that ADC measurements may be of substantial value in plaque component discrimination. We believe that this 3D SOS technique can be used to further investigate the ADC in other plaque components.

REFERENCE

1.Kim SE, et al. JMRI. 2011;34:1167. 2. Young VE, et al. Neuroradiology. 2010; 52:929.
3.Xie Y, et al. J Cardio MR 2014,16:67 4. Kim SE, et al. Proceeding of ISMRM 2016

Non-contrast 3D Black Blood MRI for Abdominal Aortic Aneurysm Surveillance: Comparison with CT Angiography

Chengcheng Zhu[1], Bing Tian[1], Joe Leach[1], Qi Liu[2], Jianping Lu[2], Luguang Chen[2], David Saloner[1], Michael Hope[1]

1. Department of Radiology and Biomedical Imaging, UCSF, San Francisco, CA, USA
2. Department of Radiology, Changhai Hospital, Shanghai, China

Purpose: Current management of abdominal aortic aneurysm (AAA) disease is based on the maximal diameter of the aneurysm, and intervention is recommended when the AAA has a diameter larger than 5.5 cm. CTA is the gold standard for AAA imaging, but requires radiation and iodinated contrast, and is therefore not the preferred modality for serial monitoring. 3D black blood MRI [1] is a promising tool for AAA monitoring as it does not require radiation or iodinated contrast agent and has excellent soft tissue contrast that allows characterization of the aortic wall and intra-luminal thrombus (ILT). AAAs with fresh ILT (hyper-intense on T1-weighted MRI) can progress two times faster compared with those without fresh ILT [2]. This study aims to 1) validate 3D MRI for quantifying AAA dimensions using CTA as a reference standard, and evaluate its inter-observer reproducibility; 2) compare MRI and CTA for evaluating ILT composition.

Methods: 28 patients (24 male, age 72±9) with AAA disease underwent 3T MRI and CTA scans within an average interval of 11 days. Two T1-weighted 3D sequences were acquired: 1) Our previous developed blood suppressed fast-spin echo sequence (DANTE-SPACE) [1]: TR/TE: 800ms/20ms, 1.3mm isotropic resolution; 2) 3D GRE (VIBE): TR/TE 4.2ms/1.2ms, 1.3x1.3x2.6mm. CTAs were acquired using clinical protocols with ~0.8mm isotropic resolution. ***Image analysis:*** Two experienced radiologists measured the maximal diameter of the AAAs using multi-planar reconstruction (MPR) on both the black blood MRI images and the CTA images. ILT and psoas muscle signal intensities were recorded. ILT signal ratio (ILT_r) was calculated as $Signal_{ILT}/Signal_{Muscle}$. ILTs were characterized as fresh (hyper-intense, ILTr>1.2) or old (iso-intense).

Results: There is an excellent agreement between black blood MRI and CTA for diameter measurements (ICC>0.99, CV<5%). Both MRI and CTA are highly reproducible (ICC>0.99, CV<2.5%). ILT shows homogeneous signal at CTA, but heterogeneous signal on MRI. **Three types of ILT composition were classified: (1: predominantly fresh ILT; 2: mixture of fresh/old; 3: predominantly old ILT)** There was good agreement for identifying fresh ILT using FSE and GRE, however, only moderate agreement was found for the ILT_r quantification (Pearson r=0.31).

Discussion and Conclusions: To our knowledge, this is the first study comparing 3D black blood MRI against CTA for AAA imaging. MRI provides accurate and reproducible AAA dimension measurements as validated by CTA. It also provides unique information of ILT composition that is closely related to progressive AAA disease. 3D black blood MRI can be used as a non-invasive tool for AAA Surveillance and ILT evaluation, and has the potential to improve patient risk stratification.

References: 1. Zhu C et al, MRI 2015; 2. Nguyen VL et al. Eur J Vas Endovasc Surg 2014.

Type 1: Predominately Fresh ILT

Type 2: Mixture of Fresh and Old ILT

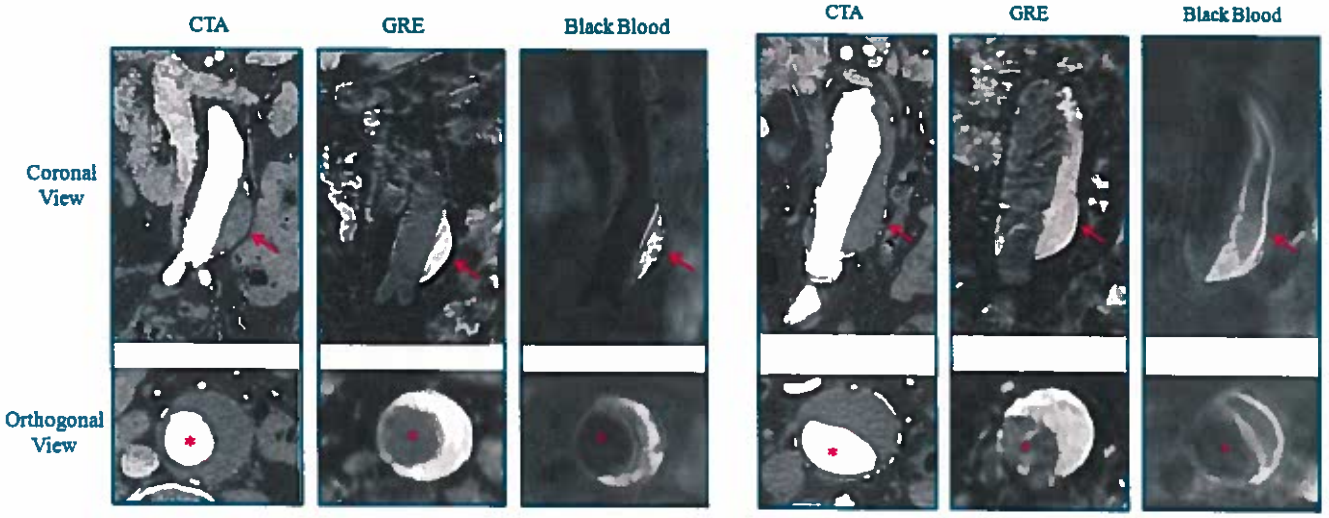

Session 12

Future Directions

Can signal averaging combined with undersampling and compressed sensing improve sensitivity? A fluorine-19 study

Emeline Lugand[1], Jerome Yerly[1,2], Tom Hilbert[1,3,4], Roberto Colotti[1], Tobias Kober[1,3,4], Matthias Stuber[1,2], Ruud B. van Heeswijk[1]

[1]Radiology, University Hospital of Lausanne (CHUV); [2]Center for Biomedical Imaging (CIBM); [3]Advanced Clinical Imaging Technology (HC CMEA SUI DI BM PI), Siemens Healthcare; [4]LTS5, EPFL, Lausanne, Switzerland

Purpose - To improve the detection of weak MR signals, their sampling can be repeated and the intensity averaged in order to obtain a higher signal-to-noise ratio (SNR), although this will often lead to a prohibitively long acquisition time. To address this limitation in fluorine-19 (^{19}F) MRI, several studies have investigated the use of compressed sensing (CS) [1,2]. In these studies, an undersampled acquisition is averaged several times and reconstructed with a CS algorithm in order to enhance the sensitivity of the acquisition per unit time. Unfortunately, besides showing the denoising effects of the CS algorithm itself, it has not been demonstrated that the combination of averaging and undersampling results in improved sensitivity. This indeed appears to be counterintuitive: averaging increases the sample count, while undersampling decreases it, resulting in no net sample gain (Fig.1). However, when undersampling is performed with a pattern that fully samples the k-space center and gradually undersamples the k-space periphery, the signal intensity information that is stored in the center is fully retained. Thus, the goal of this study was to demonstrate that the combination of signal averaging with this specific undersampling regime improves the sensitivity per unit time compared to a fully sampled dataset, when both are reconstructed with CS.

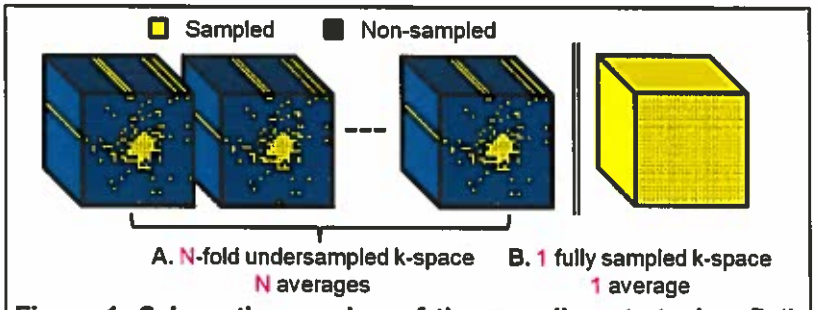

Figure 1. Schematic overview of the sampling strategies. Both 3D k-spaces A and B have the same sample count: while B is fully-sampled with each line acquired once, A is N-fold undersampled with its k-space center fully sampled and its periphery gradually undersampled, but with each line acquired N-times.

Methods - Images were acquired at 3T (MAGNETOM Prisma, Siemens Healthcare, Germany) with an isotropic 3D TSE sequence, voxel size of $(0.5\text{mm})^3$ and matrix size of 64x64x64. A phantom was made of 5 syringes of agar gel mixed with PFPE (perfluoropolyether, Celsense Inc) at different ^{19}F concentrations (1.05/0.52/0.26/0.13/0M, from tube n°1 to tube n°5, Fig. 2A), which were embedded in a tube with agar gel. Fully sampled images were acquired with 1 and 16 signal averages (NA). While the dataset with NA=1 remained fully sampled, the NA=16 acquisition was retrospectively undersampled using a variable density distribution (Fig. 1) with an acceleration factor (AF) of 16, thus leading to an identical hypothetical acquisition time for both datasets. A previously published CS algorithm [1,4] was used to reconstruct both the fully sampled (1NA-1AF) dataset (here thus behaving like a denoising filter) and the undersampled dataset (16NA-16AF). Images were compared in two ways: first, the visibility of all tubes with PFC was compared qualitatively by visual inspection. Second, for quantitative comparison a linear regression of the known concentration C versus the signal intensity S within the same image was performed, and the uncertainty of the slope was calculated.

Results – The CS algorithm effectively denoises the fully sampled dataset (Fig. 2B vs. D). Furthermore, while in the 1NA-1AF image the third and fourth tubes are hardly distinguishable from the noise (Fig. 2D), all four tubes are clearly visible in the 16NA-16AF image (Fig.2, arrows). The uncertainty of the slope of the concentration-signal fit was 9% for the 1NA-1AF, and 6% for the 16NA-16AF images.

Discussion - Averaging the center of k-space with CS rather than sampling k-space uniformly allowed for better visualization of lower ^{19}F concentrations. We therefore posit that the superior image quality in the low-SNR regimes is due to the higher SNR in the combined averaged-undersampled k-space points. This improves the performance of the image fidelity constraint of the CS algorithm and enables an improvement of the sensitivity per unit time.

References
[1] Kampf, JMR 2010
[2] Zhong, MRM 2012
[3] Lustig, MRM 2007
[4] Yerly, MRM 2015

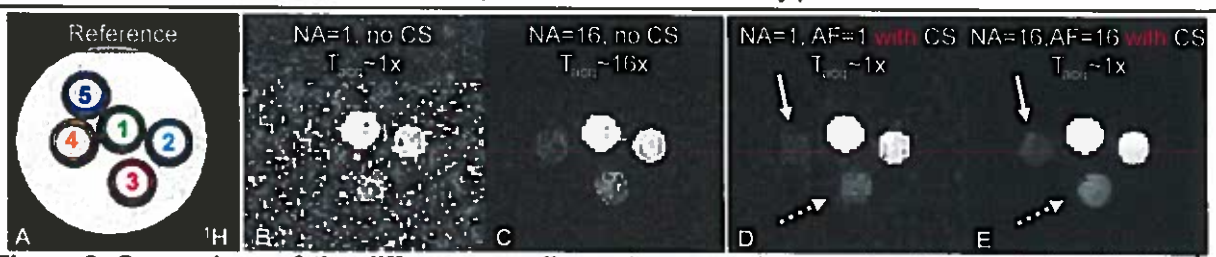

Figure 2. Comparison of the different sampling schemes and reconstruction methods. A) Axial ^{1}H reference image where the circles indicate the position of the tubes from the highest concentration (1) to the lowest (5). **B-C)** ^{19}F images with NA=1 and NA=16. **D-E)** CS-reconstructed versions of B&C without (AF=1) and with undersampling (AF=16). Arrows indicate the differences in reconstruction fidelity at low SNR.

A calibration-free method to estimate blood oxygen saturation

Juliet Varghese[1], Rizwan Ahmad[2], Lee C. Potter[2], Orlando P. Simonetti[3]
[1]Department of Biomedical Engineering, [2]Department of Electrical and Computer Engineering, [3]Department of Internal Medicine, The Ohio State University, Columbus, Ohio, USA

Purpose: A non-invasive means to measure oxygen saturation (O2 sat) in the cardiac chambers and vessels would be useful in the diagnostic evaluation of congenital heart disease, heart failure and pulmonary hypertension. T2 based magnetic resonance (MR) oximetry techniques have been limited by the need for a technique/patient specific, extensive in vitro calibration procedure [1, 2]. We have developed a novel calibration-free oximetry technique to estimate O2 sat from blood T2 [3]. In this study, we sought to determine if the use of a reference measurement of arterial blood T2 and its corresponding O2 sat provide greater accuracy in the calibration-free estimation of venous O2 sat.

Methods: A porcine model was studied across a range of O2 sat levels with a graded hypoxemia experiment (n =7). At each hypoxemia level, four distinct T2 maps of blood in the left and right ventricle were acquired in a short axis view. Each map was acquired using a fixed inter-echo spacing (τ_{180} = 12, 15, 20 and 25 ms). A standard measurement of arterial and venous O2 sat and hematocrit was obtained from analysis of blood samples drawn by invasive catheterization. Venous O2 sat was estimated with the calibration-free MR oximetry (Figure 1) method by (i) constrained non-linear least squares fitting of four venous T2 measurements to the Luz-Meiboom (L-M) model (equation in Figure 1), and by (ii) joint fitting of eight blood T2 measurements (four each for arterial and venous blood) together with the measured arterial O2 sat. The results were then compared to the standard invasive measurement of venous O2 sat (Figure 2).

Results: The correlation with the invasive measurement was significant at $p < 0.001$ for venous O2 sat estimated with and without a reference arterial T2 and O2 sat (R^2 = 0.90 and 0.88 respectively). The bias between the invasive and MR oximetry method was much lower and not significant for O2 sat estimated with a reference (-0.2 ± 3.7%, p = 0.76) compared to O2 sat estimated without a reference (7.4 ± 4.7%, $p < 0.001$).

Discussion: The need for extensive calibration and difficulty in obtaining an accurate T2 measurement of flowing blood have hindered the use of MR oximetry in determining intra cardiac O2 sat. We have overcome these limitations by exploiting blood T2 dependence on τ_{180}. A set of effective blood T2 measurements for a given blood pool, each at specific τ_{180}, can create the diversity of data required to estimate O2 sat along with the remaining nuisance parameters from the L-M model. This provides a framework for calibration-free, quantative MR oximetry in the heart. Our results showed that the accuracy of the technique is higher when a patient-specific reference measurement of O2 sat is used. In patients, this can be obtained from a simple measurement of arterial O2 sat made using a finger pulse oximeter.

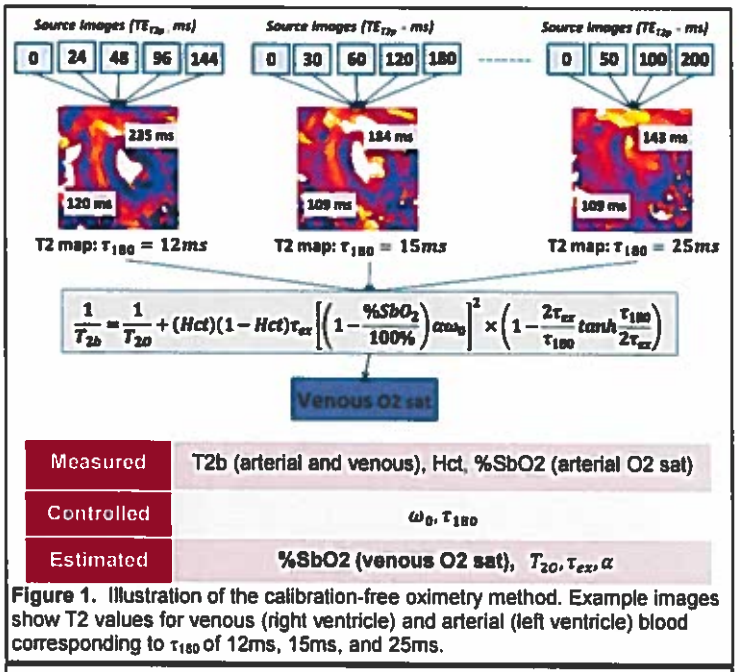

Figure 1. Illustration of the calibration-free oximetry method. Example images show T2 values for venous (right ventricle) and arterial (left ventricle) blood corresponding to τ_{180} of 12ms, 15ms, and 25ms.

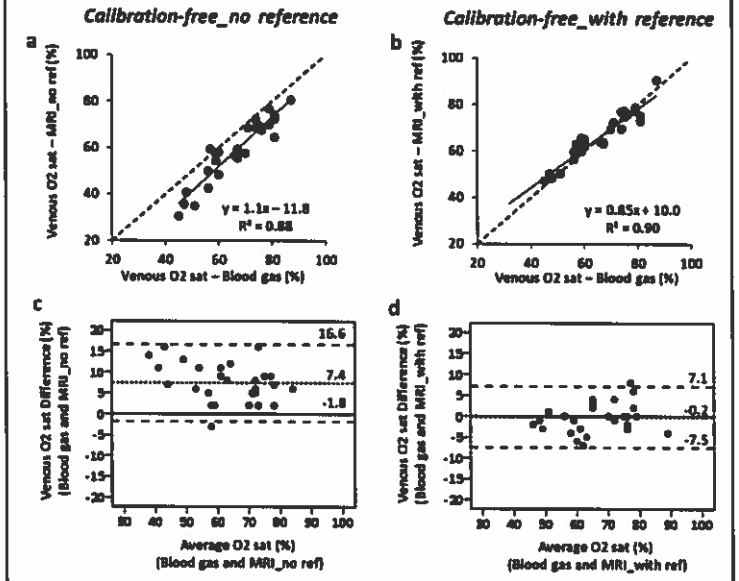

Figure 2. Regression (a,b) and Bland Altman plots (c,d) from the porcine study shows comparison of venous O2 sat estimated from calibration-free MR oximetry against reference blood gas measurements. A larger bias is seen in O2 sat values estimated without a reference measurement (Bias = 7.4 ± 4.7%, R^2 = 0.88). Venous O2 sat estimated with an arterial reference shows smaller bias and higher correlation (Bias = -0.2 ± 3.7%, R^2 = 0.90).

References: 1. Wright G.A, et. al. J Magn Reson Imaging. 1991;1:275-283. 2. Lu H. et. al. Magn Reson Med 2012;67:42–49 3. Varghese et al. JCMR 2016 18(Suppl 1):W29 [2]

Three-Dimensional Hemodynamics in Dilated Ascending Aorta With and Without Aortic Valve Stenosis and Regurgitation in Tricuspid Aortic Valve

Kenichiro Suwa[1], Ozair Abdul Rahman[1], Emilie Bollache[1], Michael J Rose[2], Amir Ali Rahsepar[1], James Carr[1], Jeremy D Collins[1], Alex J Barker[1], Michael Markl[1], [1]Department of Radiology, Northwestern University Feinberg School of Medicine, Chicago, IL, United States, [2]Department of Medical Imaging, Ann & Robert H. Lurie Children's Hospital of Chicago, IL, United States

Purpose: Altered hemodynamics and WSS in ascending aorta (AAo) with bicuspid aortic valve (BAV) is associated with aortopathy[1, 2]. Aortic valve stenosis (AS) and regurgitation (AR) in tricuspid aortic valve (TAV) are also associated with ascending aortic (AAo) dilatation[3, 4]. However, patients can develop AAo dilatation even with neither AS nor AR (no AS/AR). The purpose of this study was to characterize the differences in AAo flow patterns, velocity, flow eccentricity, and wall shear stress (WSS) between patients with AS, AR, and no AS/AR all with TAV and dilated AAo, and healthy controls using 4D flow MRI.

Methods: A total of 96 subjects with TAV identified via IRB-approved retrospective chart review were comprised of moderate to severe AS (n=8, 72±9 years, 8 men, mid AAo diameter [MAAd]: 41±2mm), moderate to severe AR (n=33, 62±14 years, 25 men, MAAd: 44±5 mm), no AS/AR (n=30, 63±9 years, 22 men, MAAd: 42±4 mm) and controls (n=25, 57±10 years, 19 men, MAAd: 33±4 mm). All subjects underwent in-vivo 4D flow MRI. AAo flow patterns were visualized with pathlines and were graded for the presence of vortex and helix flow using a 3 point scale (1, no vortex/mild helix [flow rotation < 180°]; 2, 1-2 large vortex/moderate supra-physiologic helix [flow rotation: 180° to 360°]; 3, more than 2 large vortex/prominent supra-physiologic helix [flow rotation > 360°]). Systolic peak velocities were quantified in 9 aortic segments. AAo flow eccentricity was evaluated by identifying regions with systolic peak velocities >1 m/s in 4 cross-sectional quadrants in the proximal, mid and distal AAo. Systolic peak WSS was calculated in 10 anatomic aortic segments.

Results: Patients with AS, AR, and no AS/AR showed significantly elevated vortex and helix flow compared to control subjects (Vortex: 2.0±0.5, 2.1±0.5, and 2.0±0.4, respectively vs. 1.4±0.5, p<0.05, Helix: 2.8±0.5, 2.3±0.8, and 2.3±0.9, respectively vs. 1.7±0.7, p<0.05). Peak velocities were significantly elevated in the patients with AS from root to distal arch compared to those with AR, no AS/AR, and controls. Peak velocities were significantly increased in AR patients in the aortic root and mid AAo compared to those with no AS/AR and controls (Fig. 1). Increased flow eccentricity was observed in the patients with AS in the mid and distal AAo, with AR in any part of AAo, and with no AS/AR in the proximal AAo, while controls demonstrated more uniform flow profiles (Fig. 2). As summarized in Fig. 3, significantly elevated WSS was observed in the patients with AS from AAo to arch compared to those with AR, no AS/AR and controls, and in those with AR in outer curvature of proximal AAo, both curvatures of distal AAo and arch compared to those with no AS/AR. Significantly lowered WSS was found in the patients with no AS/AR in the inner curvature of distal AAo compared to controls.

Conclusion: Patients with dilated AAo and no AS/AR exhibit similar abnormal AAo flow patterns than those with AS or AR, regardless of changes in peak velocity. The findings indicate that AAo dilatation is generally associated with aberrant flow patterns. Patients with AS or AR demonstrated higher velocity, eccentric flow and elevated WSS in AAo compared to those with no AS/AR, which may cause accelerated AAo dilatation. Further outcomes studies are warranted.

References: 1. Barker AJ et al, Circ Cardiovasc Imaging. 2012;5:457-466. 2. Bissell MM et al, Circ Cardiovasc Imaging. 2013;6:499-507. 3. Markl M et al, Circ. 2007;116:e336-e337. 4. Hiratzka LF et al, J Am Coll Cardiol. 2010;55:e27-e129

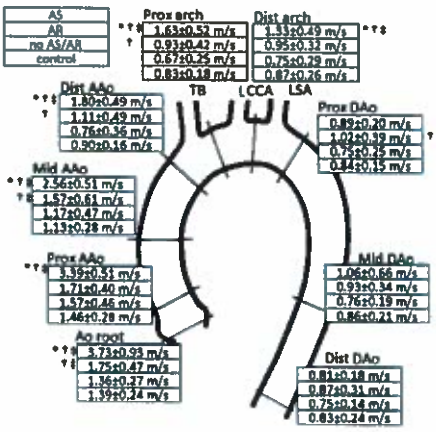

*p<0.05 vs AR only, †p<0.05 vs no AS/AR, ‡p<0.05 vs control

Figure 1. Systolic peak velocities in 9 analysis planes. AAo: Ascending aorta, DAo: descending aorta, TB: Brachiocephalic trunk, LCCA: left common carotid artery, LSA: left subclavian artery

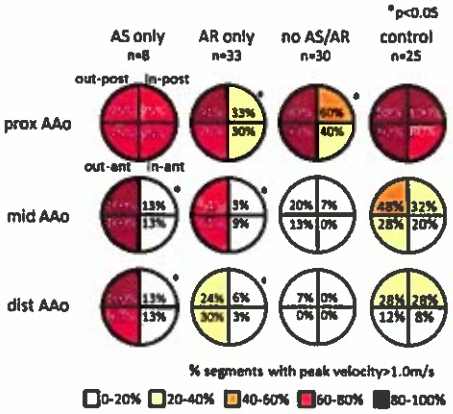

Figure 2. Aortic flow eccentricity. Decide visually if Peak velocity exceeds 1m/s or not in each quadrants of 3 analysis planes. prox: proximal, dist: distal

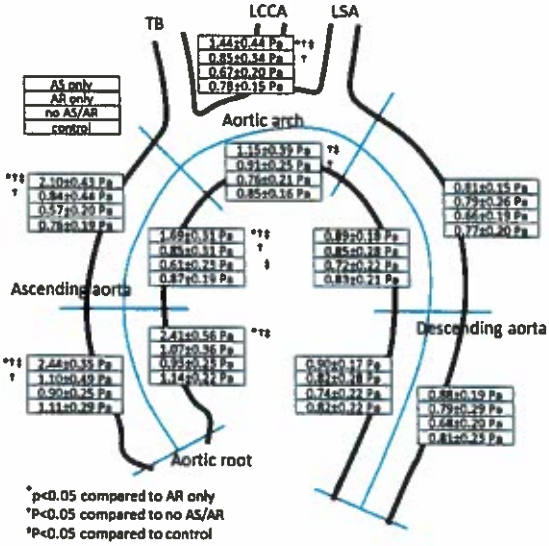

*p<0.05 compared to AR only
†P<0.05 compared to no AS/AR
‡P<0.05 compared to control

Figure 3. max 2% WSS in each segments at peak systolic phase on aortic wall. TB: Brachiocephalic trunk, LCCA: left common carotid artery, LSA: left subclavian artery.

4D Flow Imaging of the Placenta and Umbilical Cord in the Rhesus Macaque – Initial Experience

Jacob Macdonald[1], Sydney Skopos[2], Kevin Johnson[1], Chris Francois[3], Scott Reeder[3], Ian Bird[4], Dinesh Shah[4], Ted Golos[2], Oliver Wieben[1,3]

Departments of Medical Physics[1], Endocrinology & Reproductive Physiology[2], Radiology[3], Obstetrics & Gynecology[4]
University of Wisconsin, Madison, WI

Purpose: Vascular health of the placenta and supplying arteries is clinically assessed with echo imaging, but can suffer from user dependence, compromised echo windows, and is usually only possible in later stages of gestation. The NIH recently started the Human Placenta Project to investigate new approaches for the non-invasive assessment of placental health without ionizing radiation[1]. Irregular or compromised utero-placental blood flow is associated with pregnancies that result in hypertension/preeclampsia, fetal growth restriction, preterm birth, and stillbirth. Here we investigate the feasibility of 4D Flow MRI using a radially undersampled trajectory, PC VIPR[2,3], to assess vascular anatomy and hemodynamics of blood flow to the uterus, and hence placenta, without a contrast agent. In this feasibility study, a rhesus macaque was imaged, a model with several similarities to human placental development albeit with distinct differences[4,5].

Methods: One pregnant rhesus macaque was imaged on a 3.0 T scanner (Discovery MR750, GE Healthcare, Waukesha, WI) with a 32 channel cardiac coil. The rhesus had a gestational age of 112 days (early 3rd trimester). Placental imaging was performed with a time-averaged, un-gated PC VIPR acquisition (TR/TE=6.1/2.6ms; FA=8°; VENC=80cm/s; FOV=18x18x18cm^3; matrix=192x192x192; scan duration = 610s). The mother and the fetus were sedated with isoflurane, effectively eliminating fetal motion. Segmentation of maternal and fetal vessels (from the PC MRA images obtained by complex difference processing) and the placenta (from magnitude images) was performed and overlaid using the MIMICS software package (Version 17.0, Materialise, Leuven, Belgium). Time-averaged flow was measured and visualized at midpoints in the uterine arteries, uterine veins, and umbilical vessels using Ensight (Version 10.0, CEI Inc., Apex, NC). Feasibility of using PC VIPR to measure flow in the placental and fetal vessels was visualized, assessed, and quantified by a conservation of mass approach where flow to the placenta through the uterine arteries was compared against flow from the placenta through the uterine veins. A similar comparison was performed in the umbilical vessels.

Results: Fig. 1A shows the segmented maternal and fetal vessels. No contributions from the ovarian arteries were detected. Flow measures were 0.525 mL/s and 0.575 mL/s in the right and left (maternal reference frame) uterine arteries respectively, while flow was 1.11 mL/s in the right uterine vein. Flow was too slow in the left uterine vein to be detected. These flow measures represented excellent performance of the PC VIPR acquisition, as incoming flow to the placenta closely matched the outgoing flow. Unlike humans, who have a single lobe to their placenta, the rhesus macaque features two lobes, as was apparent in Fig. 1B. Of the two placental lobes, the right-hand lobe appeared to be dominant, with a greater volume and interfacing with the umbilical vessels. This dominance was reflected in the uterine vein flow, as the majority of the returning flow from the placenta passed through the right uterine vein. In the umbilical cord, one artery and one vein with measured flow of 0.69 mL/s and 0.75 mL/s respectively were identified through Ensight measurements. The rhesus macaque has two umbilical arteries, however, so the reduced arterial flow measurement is likely due to the second umbilical artery having low flow and not being detected. This is supported by the appearance of two umbilical arteries in the fetus (Fig. 2A) and a small cluster of velocity vectors in the direction of arterial flow outside of the two previously identified umbilical vessels in Ensight (Fig 2B).

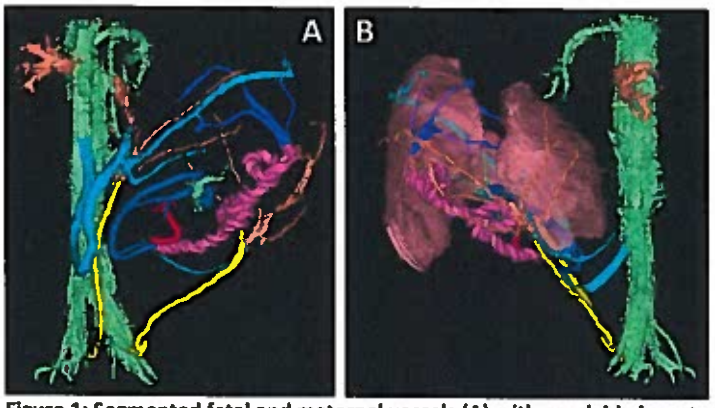

Figure 1: Segmented fetal and maternal vessels (A) with overlaid placenta (B). The umbilical vessels are in pink, while the uterine arteries and veins are in yellow and light blue respectively.

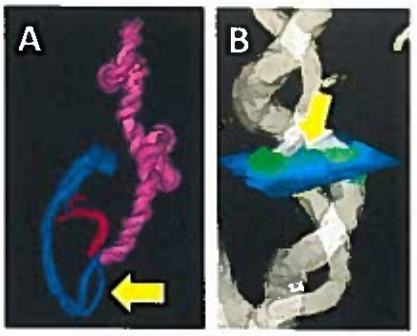

Figure 2: (A) Two umbilical veins and one umbilical artery in the fetus and (B) velocity vectors possibly indicating second umbilical artery.

Conclusion: To our knowledge, this is the first attempt to measure flow to the placenta with 4D flow MRI. The use of sedation for the mother and the motion robustness of a radial trajectory resulted in good quality vascular images not only of the uterine arteries, but also of the umbilical cord and the larger vessels in the fetus. At this point it remains unclear if the lack of visible flow contributions from the ovarian arteries is due to (1) measurement errors, (2) limits in spatial resolution, or (3) naturally low flow. Additional studies are warranted to further investigate the utility of this approach. Improved measurement and visualization of low-flow vessels may be possible by implementing a dual-VENC acquisition[6].

References: 1. nichd.nih.gov/research/HPP 2. Gu et al. Am J Neuroradiology. 2005;26(4):743-9. 3. Johnson et al. MRM. 2008;60(6):1329-36. 4. Dambaeva et al. Biology of reproduction. 2012;86(1):1-10. 5. Golos et al. International J Developmental Bio. 2010;54(2-3). 6. Nett et al. JMRI. 2012;35(6):1462-71.

Acknowledgements: We thank NIH CHD U01 HD087216 for funding and GE Healthcare for research support.

TWIST sequence for evaluation of the inferior epigastric artery prior to Deep Inferior Epigastric Perforator (DIEP) flap breast reconstruction

M.A. Aschauer, J. Gessl, D. Parvizi (2), M. Hasenhüttl, L.P. Kamolz (2)
Department of Neuroradiology, Vascular and Interventional Radiology and (2) Department of Plastic Surgery, Medical University of Graz, Austria

Purpose:
For ideal flap planning the origin of the vessel, anatomical variations, vessel diameter, anatomical course and the location, relative to the umbilicus is needed. The goal of this study was to test a new developed MRA sequence-protocol to identify and describe arteries of the anterior abdominal wall because using the described sequence by Prince et al. the arteries and veins could not be differentiated in all cases.

Methods:
Ten women underwent our standardized protocol from June 2015 to April 2016 with a Siemens 3-T Magnetom Prisma-Fit. Mean age 50.1 years (35-70). Preoperative imaging in prone position under breath hold as long as possible. Intravenous injection of gadolinium-based contrast agent (Gadobutrol), single dose 0.1 ml/kg body weight, 30 ml NaCl 0.9%, flow rate of 2 ml/s. Sequence parameter: repetition time (TR)/echo time (TE)/flip = 2.9/1.0/24.0 degrees. Bandwidth 645. Slice thickness 1.1 mm. Acquisition matrix 352/238. Start of series after individual analysis of contrast medium transit time to determine the most ideal moment for arterial imaging of the perforator vessels.



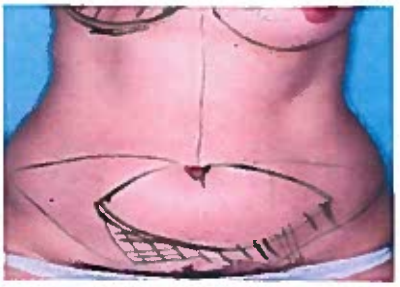

a) arterial phase b) arterial phase 3D SUB-MIP: measuring c) preoperative markings

Results:
- Vessel imaging was appropriate for flap planning in every study
- Length measuring of the inferior epigastric artery and its distribution distal the umbilicus was possible.
- Intraoperative identification of the perforators was easier / faster due to objective imaging. In seven cases (70%) the surgeon used the preoperatively selected vessels for the flap.
- In one case (10%) the surgeons decided preoperatively to perform a TRAM flap due to the suboptimal vessel situation, which was identified by MRA.
- In two patients (20%) the surgeons decided intraoperative to perform a TRAM flap due to the suboptimal vessel situation. Also in these two cases the MRA report described only gentle perforators.
- 3D reconstruction, however, is relatively complex and time consuming, as well is the measuring process.

Conclusion:
The tested sequence is robust and useful, but we will evaluate our sequence for imaging of renal arteries to compare with TWIST to get a higher resolution and fewer images.

Literature:
M.D. Agrawal, N.D.Thimmappa, J.V.Vasile et alJ. Reconstr. Microsurg.2015; 31:1-11

Poster Exhibition

Can we do without IV contrast? Role of advanced non-contrast imaging techniques to evaluate complex vascular anatomy

Kathan Amin, Dheeraj Gopireddy, Erin Kelly
John H Stroger, Jr Hospital of Cook County

Objectives: The intent of this exhibit is to review the role of advanced non-contrast techniques like T-SLIP (time spatial inversion pulse) and FBI (Fresh Blood Imaging) to evaluate complex vascular anatomy. Also, to emphasize on the importance of non-contrast MRA techniques especially considering the risk of NSF in CKD patients.

Methods: We retrospectively reviewed non-contrast MRA cases performed in our hospital over the last year and compared both these techniques. We paid close attention to the diagnostic quality, limitations and challenges associated with these techniques.

Results: Cases from normal individuals to patients with complex peripheral vascular disease, complex vascular malformations, vascular tumors and complex aortic dissections will be presented. Additionally cases related to venous thrombosis will also be discussed.

Discussion: Among the non-contrast MRA techniques Time of Flight and Phase contrast imaging has been popular but has many limitations. Newer 3D techniques like Fresh Blood Imaging (FBI) and T-SLIP (Time spatial inversion Pulse) use the intrinsic blood to produce high quality, versatile and robust images of the vessels. FBI is a 3D T2 weighted ECG gated partial Fourier fast advanced spin echo sequence, and is capable of imaging aorta and peripheral vessels. Moreover FBI acquires data in systole and diastole to eventually subtract the venous phase to produce bright arterial blood images. On the other hand T-SLIP technique is an arterial spin labeling variant which can be combined with 3D SSFP (steady state free precession) with in a targeted imaging region. T-SLIP tags blood as a tracer to obtain bright blood images after suppressing the back ground tissues. Both these techniques have strengths and limitations, they not only reduce the risk of NSF but also reduce cost, a target to keep in mind in the current healthcare landscape.

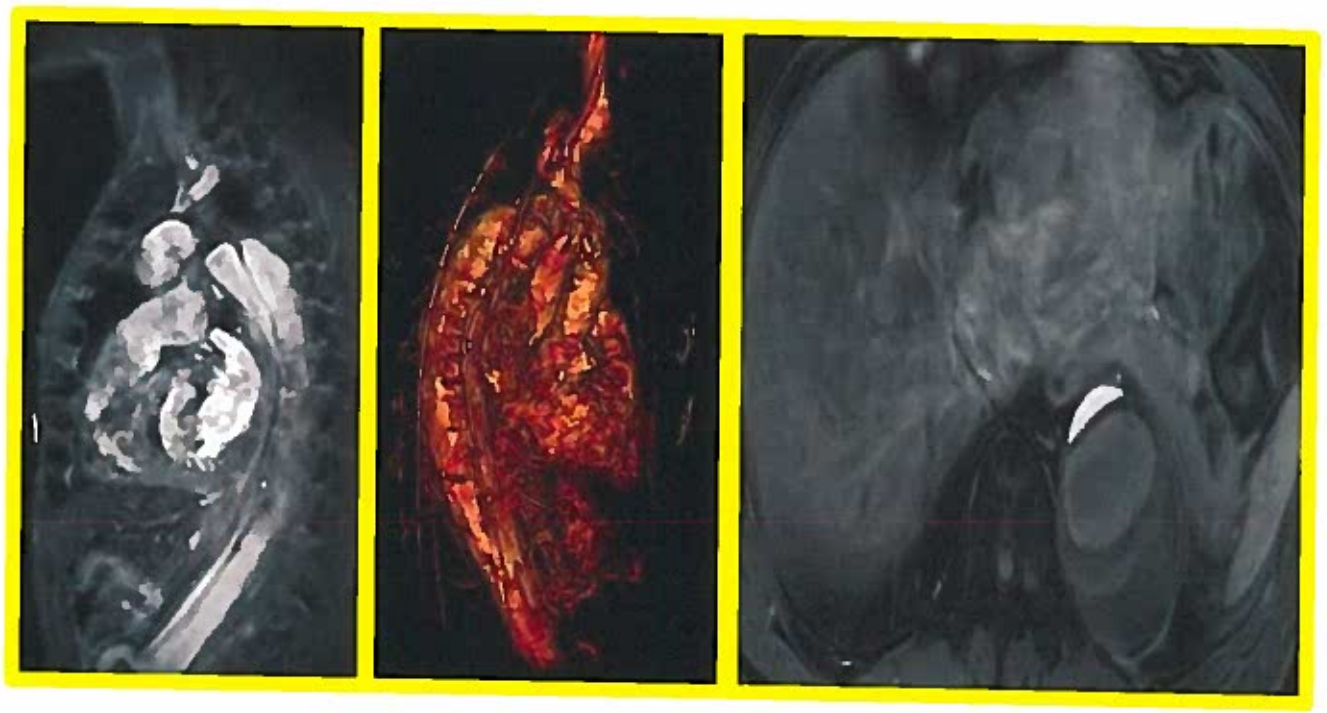

Towards acquisition of aortic k-t accelerated 4D flow MRI under 2 minutes

Emilie Bollache[1], Pim van Ooij[2], Alex J Barker[1], Michael Markl[1]

Department of Radiology, [1]Northwestern University, Chicago, USA; [2]Academic Medical Center, the Netherlands

Purpose: 4D flow MRI, which consists of acquiring three-directional velocity-encoded data in a 3D volume and throughout time, is limited by scan time. Respiratory gating allows to correct for breathing-related motion and is usually performed with a navigator tracking displacement of the diaphragm. However, 50% of the data are typically rejected by the navigator, leading to a doubling of the scan times, and, although recent k-space reordering strategies have allowed reducing rejection rates [1], a thoracic 4D flow MRI remains around an 8 minutes scan time when using acceleration techniques. Accordingly, our purpose was to test further k-space reordering strategies to allow 4D flow data acquisition of the aorta without the use of navigator gating to shorten the acquisition time, while restricting respiratory motion artefacts.

Methods: Two healthy volunteers (56, 62-yr old males) were recruited to test the following cartesian kyz-space reordering schemes: 1- original 'linear' line-by-line left-right filling; 2- filling from center to outer, calculating beforehand the distance from center of each k-space position ('in-out'); 3- filling from outer to center during the first 10 cardiac cycles then applying scheme #2 ('out-in-out'); 4- random filling. For each subject, the fully free breathing MRI included 4D flow data acquisition using each of the above k-space reordering schemes without navigator gating, followed by a conventional 4D flow sequence using a navigator placed on the lung/liver interface. Acquisition was performed with no contrast agent on a 1.5T MAGNETOM Aera scanner (Siemens) in a sagittal oblique aortic volume using k-t GRAPPA with an acceleration factor of R=5, prospective ECG gating and a Venc=150 cm/s; other parameters are summarized in Table 1. All datasets were preprocessed to correct for eddy currents, noise and aliasing using a custom software, and used to segment the aortic 3D volume (Mimics, Materialize) [2]. Then, 2D planes were extracted using Ensight (CEI) in both the ascending (AA) and descending (DA) aorta, at the level of the pulmonary artery. Finally, AA and DA borders were manually drawn for each cardiac phase, to compute peak systolic flow and net flow volume throughout the cardiac cycle (custom software). Regional AA and DA peak velocity was also estimated using maximal intensity projections [3].

	TR	TE, ms	FA	Spatial resolution	Nseg	Temporal res
Conventional	4.9 ms	2.5 ms	7°	2.25x2.25x2.4 mm^3	2	39.2 ms
4 tests	4.2 ms	2.3 ms	7°	2.25x2.25x2.7 mm^3	4	67.2 ms

Table 1: 4D flow parameters for acquisitions with (conventional) or no (testing 4 k-space reorderings) navigator. Nseg: number of segments.

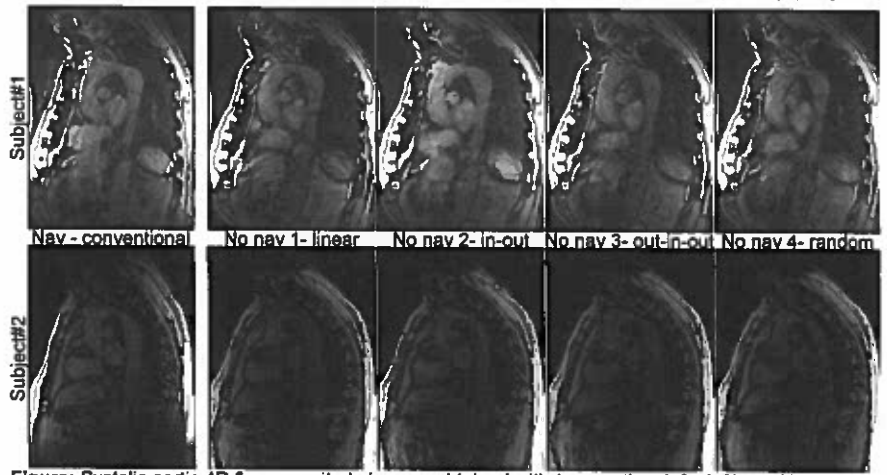

Figure: Systolic aortic 4D flow magnitude images obtained with (conventional, far left) or without (right, using 4 different k-space reordering schemes) respiratory navigator in each healthy volunteer.

Results: Scan time was 1:35 min for the 4 sequences with no navigator in subject#1, and 3:50 to 4:40 min in subject#2, who had a slower and more variable heart rate, i.e around twice as fast as the conventional 4D flow sequence using navigator. Images were of comparable quality between the 4 sequences using no navigator and exhibited no extreme respiration-related artefacts (Figure). Table 2 provides for each subject relative difference between conventional navigator 4D flow and each non-gated sequence, which was mostly below an absolute error of 10%. Overall, the best agreement was obtained with the 'in-out' k-space reordering.

Conclusion: The combination of k-t acceleration, efficient k-space ordering and decreased temporal resolution can reduce 4D flow scan time under 2 minutes. In this preliminary work, no respiratory gating aortic indices were within acceptable error to those obtained using navigator. Ongoing works include optimization to further shorten the scan time and enable acquisition during breath-hold and recruitment of more subjects to be able to study differences between k-space filling schemes.

References: [1] van Ooij et al. MRI 2015; [2] Schnell et al. J Comput Assist Tomogr 2016; [3] Rose et al. JMRI 2016.

	AA			DA		
	Vmax	Qmax	Qnet	Vmax	Qmax	Qnet
Subj#1	*linear*: -4%	*linear*: 1.5%	*linear*: 7%	*linear*: 4%	*linear*: 1.3%	*linear*: 14%
	in-out: -19%	*in-out*: -7%	*in-out*: 1.7%	*in-out*: -4%	*in-out*: -8%	*in-out*: -2%
	out-in-out: -0.6%	*out-in-out*: -8%	*out-in-out*: -1.7%	*out-in-out*: -6%	*out-in-out*: 13%	*out-in-out*: 10%
	random: -0.6%	*random*: -6%	*random*: 3%	*random*: 9%	*random*: 11%	*random*: 6%
Subj#2	*linear*: 9%	*linear*: -1%	*linear*: -7%	*linear*: -9%	*linear*: -15%	*linear*: 9%
	in-out: 2%	*in-out*: 0.4%	*in-out*: -8%	*in-out*: -1%	*in-out*: -12%	*in-out*: 6%
	out-in-out: 1%	*out-in-out*: 1.1%	*out-in-out*: -5%	*out-in-out*: -3%	*out-in-out*: -3%	*out-in-out*: 20%
	random: -7%	*random*: 6%	*random*: -7%	*random*: -9%	*random*: -10%	*random*: 11%

Table 2: Differences between the sequences with no navigator using 4 different k-space reordering schemes and the conventional navigator 4D flow (expressed in percentage of the value obtained using the conventional sequence), for each subject and index in the AA and DA. Vmax: peak velocity; Qmax: peak flow; Qnet: net volume.

Evaluation of myocardial edema in patients affected by acute myocardial infarction (AMI) and acute myocarditis (AM) using surface coils.

Federica Ciolina, Cristian Borrazzo, Nicola Galea, Rosa Ammendola; Marco Francone; Iacopo Carbone

Institution: Department of Radiological Sciences, Oncology and Pathology of Policlinico Umberto I, Sapienza University of Rome

Aim

To evaluate myocardial edema in patients affected by AMI and in patients with suspicious AM in terms of signal intensity (SI), signal to noise ratio (SNR) and contrast-to-noise ratio (CNR) using T2w-short-tau inversion recovery (STIR) sequences acquired with body coils and with both body coils and surface coils.

Material and methods

37 patients with diagnosis of AMI or with clinical suspicious of AM (average age 51±14,1) underwent a cardiac magnetic resonance (CMR) using a 1.5 T scanner (Magnetom Avanto; Siemens) equipped with high gradient system (32 channels body coil and surface coils).

T2-STIR sequences were acquired in short axis planes using body coil and both body and surface coils. Quality and quantity analysis were done comparing T2-STIR values, CNR and SNR obtained using body coils and both body and surface coils. All values were compared with T1 native.

Statistical analysis was done using t test and p values were considered significant with $p<0.005$.

Results

21(57%) patients with AMI (group A) and 16(43%) patients with suspicious of AM (group B) were evaluated.

T2-STIR values of SI obtained using body coil and using both body and surface coils resulted in group A of 244,28±28,74 vs 191,65±17,12, in group B of 201,4±65,13 vs 176,14±59,31 ($p<0,0001$).

SNR and CNR were in group A of 107 vs 8,7 and 48,7vs 3; in group B of 66,7 vs 7,8 and 26,7 vs 1,5 ($p<0,0001$). Native T1 mapping values measure in both groups confirmed the presence of edema (group A of 1101,38 ± 72,14; group B of 1087,2 ± 70,82 ($p<0,0001$).

Conclusion

Surface coils coupled with body coils enable a better detection and quantification of myocardial edema in patients affected by AMI and in cases with suspicious myocarditis.

Noninvasive Venous Pressure Measurement of Dural Arteriovenous Fistulas using 4D Flow MRI (Phase Contrast VIPR MRA)

Zachary Clark MD*, Leonardo Rivera BS**, Oliver Wieben PhD**, Kevin M. Johnson PhD**, Patrick Turski MD*
Affiliations: University of Wisconsin-Madison Departments of Radiology *, Medical Physics**

Purpose: Dural arteriovenous fistulas (DAVFs) are vascular malformations that can present aggressively with seizure, hypertensive encephalopathy, intracranial hemorrhage, or progressive myelopathy. Venous hypertension is the pathophysiologic mechanism thought to be responsible for aggressive presentation. Intraoperative ultrasound studies have shown that dural venous pressure is elevated in spinal DAVF patients with myelopathy (1). Venous pressure measurements of intracranial DAVFs have not been reported. 4D Flow MRI has emerged as a powerful tool to characterize the cerebrovasculature noninvasively. Previous work using phase contrast vastly undersampled isotropic projection reconstruction (PC VIPR) has demonstrated the feasibility of generating relative pressure maps from velocity data in blood vessels. This technique has been used to measure pressure noninvasively in cerebral aneurysms, the carotid artery, and across aortic coarctations (2-4). In this study we describe our initial experience measuring pressure noninvasively in the dural sinuses of normal subjects and patients with DAVFs. Our hypothesis is that venous pressure is elevated on the side of a DAVF compared to the contralateral side and the magnitude of the pressure differential correlates with the severity of symptoms.

Methods: 4D Flow MRI exams were obtained in ten normal control subjects to provide a reference database for normal variations in venous pressure and anatomy. Patients with unilateral DAVFs affecting the transverse/sigmoid sinus underwent a 4D Flow MRI (PC VIPR) as part of a previously reported constrained reconstruction technique termed HYPRFlow (5). The PC VIPR acquisition was used to generate relative pressure maps and streamlines. This approach is based on the Navier-Stokes equation, and assumes blood to be both incompressible and Newtonian (3). Pressure was compared between the DAVF patients and normal controls as well as between the side of the DAVF and contralateral side. All exams were conducted using IRB approved protocols.

Results: Our preliminary results confirm that dural sinus pressure is elevated on the side of the DAVF compared to the contralateral side. Venous pressure variations in the dural sinuses were more common in DAVFs compared to normal controls. Quantitative measurements of venous blood flow, velocity, and pulsatility are currently in progress.

Conclusion: Noninvasive pressure measurement of the dural sinuses using 4D Flow MRI (phase contrast MRA) of the dural sinuses is feasible in patients with DAVFs. Initial results support the hypothesis that DAVFs result in venous hypertension which may be the mechanism ultimately leading to increasing symptoms and aggressive presentation.

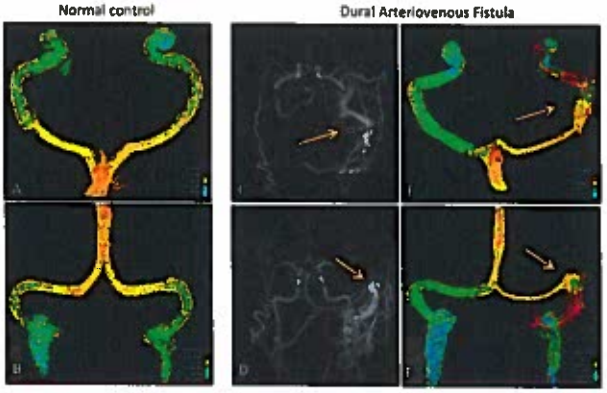

Figure 1. Relative pressure maps in a normal control patient in the axial (A) and coronal (B) plane as well as for a patient with a type IIa DAVF affecting the left transverse and sigmoid sinus (arrows). HYPRFlow images in the axial (C) and coronal (D) plane show the site of arteriovenous shunting (arrows) where there is increased pressure seen on the axial (E) and coronal (F) pressure maps.

References
1. Hassler et al *Hemodynamics of spinal dural arteriovenous fistulas* J. Neurosurg 70:360-370, 1989.
2. Moftakhar et al *Noninvasive Measurement of Intra-Aneurysmal Pressure and Flow Pattern Using Phase Contrast with Vastly under sampled projection Imaging*. AJNR 28:1710-1714, 2007.
3. Turk et al *Physiologic and Anatomic Assessment of a Canine Carotid Artery Stenosis Model Utilizing Phase Contrast with Vastly Undersampled Isotropic Projection Imaging*, AJNR 28:111-115, 2006.
4. Nett et al *Noninvasive Pressure Measurement with 4D phase contrast MRI in Patients with Aortic Coarctation* J Cardiovascular Mag Res 14 (Supp1):P106, 2012.
5. Clark et al *Accelerated Time-Resolved Contrast-Enhanced Magnetic Resonance Angiography of Dural Arteriovenous Fistulas Using Highly Constrained Reconstruction of Sparse Cerebrovascular Data Sets*, J. Inv Rad Jun;51(6):365-71, 2016.

3D analysis of Vessel Morphology

Imaged with ECG Gated Flow Spoiled-Fresh Blood Imaging Non Contrast-MRA

BZ Cooper[1], R Singh[1], R Griffith[1], M Grimaldi[1], PV Viswanath[2], E Wilson[1]
[1]Pocono Medical Center, [2]Pace University

Purpose: The morphologic assessment of peripheral vessels in patients suffering from peripheral arterial disease (PAD) is important in determining treatment options. Contrast and Non-Contrast MRA is becoming increasingly utilized preoperatively to assess the location and severity of vascular disease[1]. Whereas 2D quantitative angiography (QA) for the assessment of vessel diameter is standard, 3D quantitative angiography (QA) may provide more accurate measurements by minimizing inherent limitations of 2D measurements[2]. The aim of this study was to compare 3D to 2D analyses of diameter and implied area of vessels of the lower extremity arterial tree imaged with Non-Contrast MRA.

Methods: This study was approved by the Western Institutional Review Board. Five (5) healthy adult volunteers underwent Flow Spoiled-Fresh Blood Imaging (FS-FBI) Non-Contrast MRA (NC-MRA) of the complete arterial bed from the aorto-iliac bifurcation down to the distal run-off using a 1.5 Tesla MRI (Vantage Titan™, Toshiba) scanner. A three-station full runoff was performed on each volunteer. Image acquisition was performed at peak systole and peak diastole using auto-ECG. Appropriate flow-spoiling gradient pulses on the readout axis were used to optimize the separation of arteries and veins. 2D (McKesson Radiology Station ™) and 3D (Vitrea, Vital Images) workstations (WS) were used for uni-planar (UP) and bi-planar (BP) analysis of Maximum Intensity Projections (MIP). 15 arterial locations were assessed for each volunteer. All measurements were made at a uniform window width/level and at a uniform magnification. The transverse diameter (Tr) at each location was measured using a 2D WS (Tr2D). The transverse (Tr3D) and Anterior–Posterior (AP) diameter (AP3D) were measured using a 3D WS. The ratio of Tr2D to Tr3D, the ratio of the area implied by Tr2D (Ai2D) to the area implied by Tr3D ($Ai^{Tr}3D$), and the ratio of Ai2D to the area implied by Tr3D and AP3D ($Ai^{Tr\text{-}AP}3D$) were calculated. Under the null hypotheses of no difference between the 2D and 3D measurements, all these ratios should be equal to one. An F-test, based on an estimated linear regression model, was used to jointly test the hypotheses that the ratios are all equal to one for all 15 arterial locations. All statistical analysis were performed using STATA14.

Results: The null hypotheses of no difference between the 2D and 3D measures was easily rejected with a high degree of confidence for all ratios: Tr2D to Tr3D ($F(12, 48) = 5.59$, Prob > F = 0.0000), the ratio of Ai2D to $Ai^{Tr}3D$ ($F(12, 48) = 3.01$, Prob > F = 0.0033), and the ratio of Ai2D to $Ai^{Tr\text{-}AP}3D$ ($F(12, 48) = 3.01$, Prob > F = 0.0033). This suggests that the 2D measurement of the blood vessel area is significantly greater than that of the 3D measurement. The evidence also suggests that this is particularly true at the Internal Iliac Artery and the DFA arterial locations.

Conclusion: This preliminary study demonstrates significant differences between 3D and 2D assessment of vessel diameter and implied vessel area of arteries imaged with NC-MRA. Whereas assessing severity of stenosis and preoperative planning is usually performed with 2D analysis, future investigative work may show a benefit to using 3D analysis tools for the assessing vessel morphology.

References: (1) Cooper BZ et al. J Surg Res. 2001 Sep;100(1):99-105. (2) Ihara T et al. Ann Vasc Surg. 2013 Feb;27(2):154-61.

We acknowledge the support of Toshiba America Medical Systems

QISS non-contrast MRA for assessment of the iliofemoral arteries in TAVR candidates

Ferreira Botelho, Marcos P.[1]; Mohiuddin, Sohaib[1]; Collins, Jeremy D.[1]; Edelman, Robert R.[2]; Koktzoglou, Ioannis[2]; Carr, James C.[1]

1. Radiology, Northwestern University, Chicago, IL, United States. 2. Radiology, NorthShore University HealthSystem, Evanston, IL, United States.

Purpose: Transcatheter aortic valve replacement (TAVR) has emerged as an accepted therapeutic option for moderate and high-risk patients with severe aortic stenosis. Vessel caliber of the iliofemoral access site is part of routine pre-interventional assessment with CTA and catheter angiography. Non-contrast Quiescent Interval Slice-Selective (QISS) MR angiography has been proven useful for evaluation of lower extremity peripheral vascular disease, however its accuracy for quantifiying luminal sizes has not been studied. Our objective was to study the accuracy of QISS MRA compared to CTA as an alternative for pre-surgical planning in patients considered for TAVR.

Methods: We prospectively enrolled 5 patients considered for TAVR for this pilot study, as well as 7 other patients being evaluated for aortoiliac aneurysms or PAD. All patients had a CTA of the iliofemoral region obtained within 3 months. MR imaging was acquired at 1.5T. Non-contrast MRA was performed using 3 mm thick QISS, optimized for the pelvic and femoral vasculature, Cartesian sampling. Arteries were evaluated in 6 segments in each individual (bilateral common iliac, external iliac and common femoral arteries). A single reader compared the MRA images to CTA in terms of patency and severity of segments of stenosis, using minimal orthogonal measurements. Qualitative scores were also given in a 5-point Likert scale.

Results: Mean age of participants was 73 years, 9 males and 3 females. A total of 132 segments were compared. In two individuals with hip prosthesis the arterial segments with regional artifacts were excluded. There was no significant qualitative difference in visualization of the lumen between CTA and QISS MRA (4.8 vs 4.5, $p>0.05$). Severe or complete segmental stenoses were present in 2 of the patients, detected both by CTA and QISS. Mean luminal orthogonal luminal measurements were not statistically different (8.68 mm CTA vs 8.82 mm QISS, $p>0.05$). Measurements differences between CTA and QISS ranged from none (42% of all measurements) to 2 mm (8%).

Conclusion: QISS MRA and CTA have comparable accuracy for evaluation of luminal measurements and for detecting stenosis of the iliofemoral vasculature. The QISS MRA technique has great potential as an alternative to CTA for assessment of vascular disease in TAVR candidates.

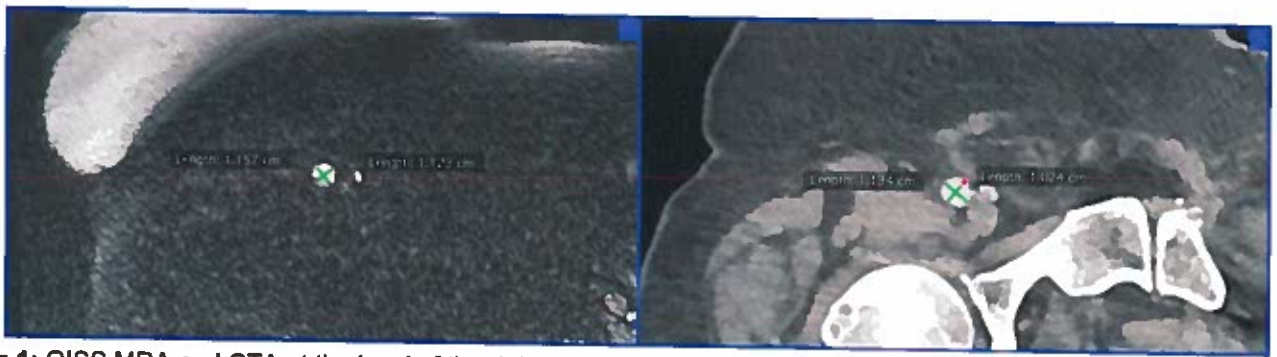

Fig 1: QISS MRA and CTA at the level of the right common femoral artery demonstrating similar measurements.

Summary of strategies for reduction of susceptibility artifacts in peripheral non-enhanced MRA

Shivraman Giri[1], Jianing Pang[1], Ioannis Koktzoglou[2,3] Robert R. Edelman[2,4]

[1]*Siemens Healthcare, Chicago, IL;* [2]*Radiology, NorthShore University HealthSystem, Evanston, IL,* [3]*Radiology, University of Chicago, Chicago, IL,* [4]*Radiology, Northwestern University, Chicago, IL, ,*

Purpose: Non-enhanced MR angiography (NEMRA) offers a viable alternative to computed tomography angiography (CTA) and Contrast-enhanced MR angiography (CEMRA), avoiding the need for ionizing radiation and iodinated or gadolinium based contrast agents. In NEMRA, different mechanisms are used in different anatomical regions to accentuate the signal from arteries while suppressing undesired signal from background muscle, adipose tissue, and veins. Of these, the Quiescent-interval slice-selective (QISS) MRA has proven to be an efficient and accurate non-contrast technique for the evaluation of peripheral arterial disease [1]. QISS is a 2D MR technique that uses regional saturation pulses to suppress signal from background and veins, and chemically shift-selective saturation to suppress signal from fat. While this approach has been robust in most patients, the use of bSSFP can lead to artifacts in regions of high susceptibility, such as those due to air in bowel loop or prosthetic implants. Some approaches have been proposed to overcome this limitation. Here we provide a summary of these techniques and their relative merit.

Methods: We evaluated the following four different prototype techniques at both 1.5T and 3T (MAGNETOM Avanto and Verio, Siemens Healthcare, Erlangen, Germany) to minimize susceptibility artifacts; so as to not suppress water spins in a magnetically inhomogeneous environment, fat-suppression pulse was turned off in each.

1. The first approach is based on the use of ultra-short echo (UTE) sequence for signal readout; at short TEs (on the order of 40 us), susceptibility-related dephasing is negligible. One disadvantage of this approach is that SNR of the UTE sequence is in general low.
2. The second technique is very similar to the UTE approach, in that it uses a GRE readout instead of bSSFP. The bandwidth is high at 930 Hz/px, giving a short TE=1.7 ms. By default, this approach also gives a short TR (~4.5ms). At such low TRs, there is not sufficient inflow of unsaturated arterial blood. To improve arterial conspicuity, we extend the TR to ~10 ms.
3. The third approach is based on the work by Bangerter et al. [2] that uses multiple-acquisition bSSFP, each with a different frequency offset to move the dark-bands, and combining them in different ways. For angiography applications, we found a MIP of multiple-frequency acquisitions to be useful.
4. The fourth approach is based on dynamically phase-cycled radial bSSFP (DYPR), where the RF phase cycle is continuously updated so that each radial spoke is acquired at a different frequency offset, and banding may be removed using standard gridding reconstruction.

Figure 1: CT image from a patient with hip implant

Results: Representative images from a patient with hip implant. Fig 1 shows anatomic CT image, Fig 2 shows MRA images acquired on 1.5T system. CEMRA was successfully acquired; NEMRA using standard QISS failed due to susceptibility artifacts. These were corrected using approach #2 described above.

Discussion: We have evaluated multiple approaches to minimize susceptibility-induced artifacts in NEMRA such as those from bowel loops and prosthetic implants. The choice of specific approach depends on application, although our current evidence suggests the use of GRE readout with high bandwidth works reliably at 1.5T. Due to imaging time considerations, we recommend full run-off protocol using standard QISS, and restricting the use of any of these techniques to stations affected by susceptibility artifacts.

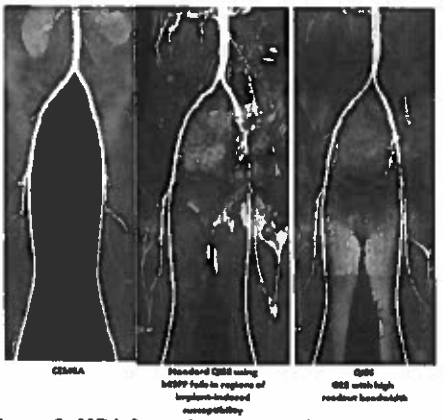

Figure 2: MRA from the same patient as in Fig 1 acquired on 1.5T system.

References: 1. Edelman RR et al. MRM 2010;63:951. 2. Bangerter et al. MRM 2004;51:1038. 3. Benkert et al. MRM 2015;73:182.

SECURE study: observational post-marketing study on the safety profile of gadoterate meglumine - Final results in 35,499 patients

Dr. Andreas Gottschalk, Prof. Dr. Bodo Kress

Department of Neuroradiology, Hospital Nordwest, Frankfurt, Germany

Purpose:

To prospectively assess the safety profile of gadoterate meglumine (DOTAREM®, Guerbet, France) and the incidence of Nephrogenic Systemic Fibrosis (NSF) in routine practice.

Methods:

A worldwide observational post-marketing study was undertaken to collect safety data in adults and children with or without renal impairment, who were scheduled to undergo routine contrast-enhanced Magnetic Resonance Imaging (MRI) with gadoterate meglumine. Demography, risk factors, indication(s) for MRI and occurrence of adverse events (AE) were recorded. A 3-month follow-up period was planned for patients with at least moderate renal impairment (eGFR<60 mL/min/1.73 m^2) in order to detect any suspicion of NSF.

Results:

A total of 35,499 patients were analyzed (female: 53.1%; mean age: 49.5 ± 17.9 years; range: 0-98 years). When documented, the most frequent indications for contrast-enhanced MRI were central nervous system (61.0%), whole body (25.2%), musculoskeletal system (14.3%) and angiography (4.1%). A majority of patients (61.9%) were reported without risk factors. The most frequent of the listed risk factors were any stage of renal impairment (14.7%) and hypertension (11.9%). A total of 70 AEs were observed in 44 patients (0.12%). Among them, 38 AEs reported in 32 patients (0.09%) were considered as adverse drug reactions, mainly urticaria (0.03%), nausea (0.02%) and vomiting (0.01%). Nine adult patients (0.03%) experienced serious AEs including 4 serious adverse drug reactions reported in 3 patients (<0.01%). Moderate to severe renal impairment was reported in 514 patients (1.4%), 92.6% of them were followed-up with no suspicion of NSF observed.

Conclusion:

This final analysis in 35,499 patients of all ages confirms the excellent safety profile of gadoterate meglumine in routine practice.

Improving Signal-to-Noise Ratio in Carotid MRI

JR Hadley, S McNally, M Beck, DL Parker
Departments of Radiology and Electrical Engineering, University of Utah

Introduction

Signal-to-Noise Ratio (SNR) can be increased in Magnetic Resonance Imaging (MRI), using several methods including sequence manipulation and hardware modifications. Of all the options for increasing SNR, radiofrequency (RF) receiver coils provide the most significant gain. Sensitivity of a coil to the signal in the imaging sample depends primarily on the geometry and position of the loop with respect to the sample. To achieve the highest SNR requires the coil to be in close proximity to the sample of interest and the coil geometry to be optimized. The coil must be small enough that it is not sensitive to regions outside the region of interest and large enough to pick up the signal at the required depth. Custom coils designed for a specific application typically provide much higher SNR than commercial coils that are designed for general purpose imaging of a broad range of body habitus. Coils that provide even small gains in SNR provide significant imaging improvement. For example, a specific-purpose (SP) coil that can provide a 40% SNR improvement over a general-purpose (GP) coil, can achieve the same image quality as the GP coil with a factor of 2 savings in scan time. Similarly, an SP coil that can provide a factor of 2 SNR improvement over a GP coil can achieve the same image quality as the GP coil with a factor of 4 savings in time. Increased SNR can be leveraged to improve image quality, temporal and spatial resolution, and enable or improve imaging functionality such as diffusion tensor imaging.

Carotid Artery Imaging Coils

The adult anterior neck, with its significant variation in shape and size does not have a commercially available high SNR GP integrated coil solution that is currently available for any of the major MRI manufacturers. Currently, the anterior neck elements of commercial head/neck coils have been positioned relatively far from the surface of the neck in order to accommodate all neck shapes and are used at the expense of substantially reduced SNR compared to coils that form well to the anterior neck anatomy.

Some research groups working on Carotid MRI are using coils that have been developed specifically for that application. However, these SP carotid coils have not provided consistently high SNR with full anterior neck coverage for all patients as required for standard clinical use. Bilateral anterior neck carotid coils fit closely up against most necks and can provide high SNR for a small segment of the carotid arteries. The first bilateral surface coil used for hi-res carotid imaging was the four-channel coil designed by Hayes et al (1) and a carotid coil based on the same concept is available commercially for several different MRI vendors (Machnet, Roden, The Netherlands). The size of this coil's high sensitivity volume and ease of positioning were improved by the eight-channel bilateral carotid coil design presented by Balu et al (2). This coil concept has been developed into a commercially available neck coil for Philips MRI systems (Shanghai Chenguang Medical Technologies, Shanghai, China). In addition, a six-channel carotid coil is currently available for General Electric MRI systems (NeoCoil, Pewaukee, Wisconsin, USA), and a 4-channel, unilateral, general-purpose coil that can be used for carotid imaging is available for Siemens MRI systems (Siemens Healthcare, Erlangen, Germany). Other variations of the bilateral carotid coil concept have been presented by Tate and Hu et al. (3,4). These coils provide high SNR over a small volume, but they must often be repositioned during the patient exam to place the coil's high signal sensitivity volume over the carotid bifurcation. In addition, these coils were not designed for integration with other head or neck coils, and require the removal of any existing head coils on the patient table to perform a cervical carotid imaging study. Comprehensive, simultaneous, high-resolution imaging of the head and neck, which should benefit patient stroke workup, is not possible with these coils. Neck coils developed by Beck et al. (5) have been developed with the intent to overcome many of the bilateral coil limitations, and have been designed specifically to be integrated with existing commercial head/neck and spine coils to provide high-resolution comprehensive imaging of the entire carotid artery.

Discussion

Many clinicians still use stenosis as their standard for patient treatment planning. However, current research shows that unstable plaque is a better indicator for treatment planning and is better identified by MR imaging providing information regarding lipid necrotic core, fibrous cap thickness and intraplaque inflammation and hemorrhage. Yet these imaging techniques have not become standard of care for carotid artery disease patients in everyday clinical practice. While researchers and clinicians have commented that adequate RF coils need to be developed for this purpose, the practical considerations required to implement these types of patient-specific coils and the resulting additional data need to be addressed by the medical community. This overview of RF coils currently available for carotid MRI is intended to stimulate further discussion of coil design features that are needed to move high-resolution carotid imaging into clinical practice and improve patient care for carotid artery diseases.

References: 1. Hayes CE et al. Surface coil phased arrays for high-resolution imaging of the carotid arteries. J Magn Reson Imaging 1996;6(1):109-112. 2. Balu N et al. Improvements in carotid plaque imaging using a new eight-element phased array coil at 3T. J Magn Reson Imaging 2009;30(5):1209-1214. 3. Tate Q et al. Increased vessel depiction of the carotid bifurcation with a specialized 16-channel phased array coil at 3T. Magn Reson Med 2013;69(5):1486-1493. 4. Hu X et al. An 8-channel RF coil array for carotid artery MR imaging in humans at 3 T. Med Phys 2016;43(4):1897-1906. 5. Beck et al. Interchangeable Patient-Specific Receive-Only Carotid Coils for Simultaneous Imaging with Radio Frequency Head Coils at 3 Tesla, ISMRM 2016, Singapore, p 2151.

Assessment of Velocity, Reynolds Stress Tensor, and Pressure Loss using Phase-Contrast MRI with Extended Velocity Encoding

Henrik Haraldsson[1], Sarah Kefayati[1], Sinyeob Ahn[2], Petter Dyverfeldt[3], Jonas Lantz[3], Tino Ebbers[3], and David Saloner[1]
[1] University of California, San Francisco, United States, [2] Siemens Healthcare, [3] Linköping University, Sweden

Purpose: Significant vascular stenosis results in inadequate perfusion distal to the lesion and is a major cause of mobidity and mortality. Although geometric measurements such as cross sectional area are used to grade these lesions, their hemodynamic impact is determined by the resulting pressure loss. Invasive catheterization is the gold standard to assess this pressure loss, but the method is expensive and associated with risks including dislodgement of thromboemboli, dissection, clotting, bleeding, and infection. Non-invasive methods are therefore attractive but have traditionally not accounted for turbulence, which may greatly impact the net pressure loss, and consequently provided inaccurate hemodynamic pressure. Recently, a method has been developed using phase-contrast MRI with extended velocity encoding to assess the Reynolds stress which allows measurement of pressure loss accounting for turbulence [1]. The purpose of this work is to evaluate the influence of turbulence on MRI-based pressure loss computation.

Methods: Gd-DTPA doped water was pumped through a pipe with a diameter of 15 mm and a cosine-shaped stenosis with a maximal area reduction of 75% at two constant flow rates. 2D phase-contrast MRI was used to quantify the flow rate as 26ml/s and 56ml/s, corresponding to Reynolds numbers (Re) of 2207 and 4753 based on the unconstricted diameter. Velocity and Reynolds stress were acquired using 3D phase-contrast MRI with extended velocity encoding [1] and used to compute the pressure loss using the Poisson pressure equation. The pressure loss was computed twice, once accounting for turbulence and once not accounting for turbulence (i.e. analogous to previous methods). Computational fluid dynamics (CFD) was used to calculate the pressure loss for the two flow rates by solving the Navier-Stokes equations in ANSYS CFX 16.0 and its results were compared to MRI measurements. CFD was performed with the time step of 50 μs, and global imbalances of mass and momentum < 0.1%, which ensured sufficient accuracy in simulation. Turbulent flow fluctuations were resolved using Large Eddy Simulation (LES). The LES technique has previously been validated against direct numerical simulations (DNS) for this type of flow [2].

Results: Velocities and Reynolds stress components acquired with MRI showed good visual agreement with CFD simulations. Low turbulence was seen for the 26ml/s flow rate resulting in a moderate pressure drop with little influence of the turbulence. However, at the 56ml/s flow rate, the proposed method which incorporates the measured Reynolds stress into the MRI-based pressure computation revealed an up to 40% greater pressure loss as compared to the conventional approach which assumes that the flow is laminar.

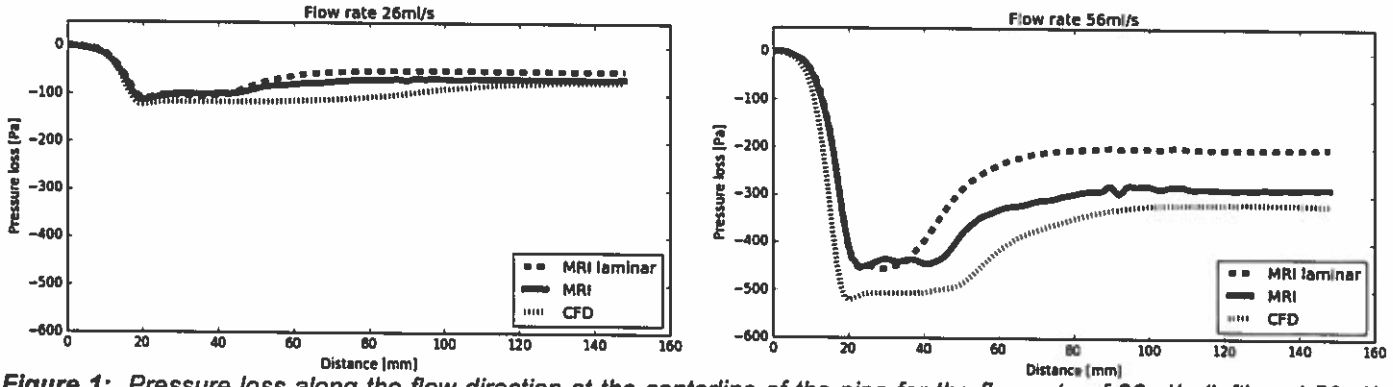

Figure 1: *Pressure loss along the flow direction at the centerline of the pipe for the flow rate of 26ml/s (left) and 56ml/s (right). The MRI-derived pressure loss accounting for turbulence is shown with solid lines whereas the conventional approach, assuming laminar flow, is shown with dashed lines. The corresponding results obtained with CFD are shown with dotted lines.*

Conclusion: Phase-contrast MRI with extended velocity encoding provides improved estimation of pressure loss by accounting for turbulence. The method could allow for non-invasive pressure measurements and provides a low-risk assessment of the clinical relevance of a stenosis.

References: [1] Haraldsson et al. Turbulence Tensor Quantification using ICOSA6 Flow Encoding. 27th Annual International Conference on Magnetic Resonance Angiography, Cincinnati; 2015.
[2] Gårdhagen et al. Large Eddy Simulation of Stenotic Flow for Wall Shear Stress Estimation - Validation and Application. WSEAS Trans. Biol. Biomed. 2011;8:86–101.

Finding optimal dose for Ferumoxytol-enhanced Magnetic Resonance Angiography (FeMRA)

Martin Hennessy [1], Sokratis Stoumpos [1], Patrick Mark [1,2], David Kingsmore [1,2],
Alex Vesey [1], Aleksandra Radjenovic [2], Giles Roditi [1,2]

1 NHS Greater Glasgow & Clyde, Glasgow, UK 2 British Heart Foundation Glasgow Cardiovascular Research Centre, Institute of Cardiovascular and Medical Sciences, University of Glasgow, UK

Purpose

The ultrasmall superparamagnetic iron oxide compound Ferumoxytol has been used in imaging for research and clinical applications. A commonly used dose is 4 mg/Kg although some work has suggested significantly higher doses may be required[1]. However, for clinical experience we suspected that for angiography, a lower dose could produce contrast and image quality sufficient for diagnostic imaging, especially as blood pool volume does not increase in a linear fashion with body weight. We set out to determine the relationship between Ferumoxytol dose and MRA signal and hence determine whether a dose of Ferumoxytol lower than 4 mg/Kg can produce diagnostic-quality imaging.

Methods

Patients with advanced renal failure and a clinical indication for vascular imaging were offered 3T FeMRA (Siemens MAGNETOM Prisma). Those patients patients undergoing aorto-iliac imaging were included in the analysis. All patients underwent FeMRA with 4 mg/Kg of Ferumoxytol (up to a maximum of 300 mg) as dilute, controlled infusion in divided aliquots . A T1w 3D FLASH breath-hold acquisition with isotropic 1.0 mm voxels was performed pre-contrast and following each increment of Ferumoxytol. Image analysis was performed using OsiriX MD (pixmeo, Sui.) Regions of interest (ROI) were placed on aorta, IVC, psoas muscle, abdominal fat, liver, spleen and background air then copied to identical locations on each post-contrast sequence. Mean signal in the ROI was recorded. Data were collated and signal graphed against Ferumoxytol dose with regression analysis. Qualitative assessment of the imaging was also performed.

Results

Successful imaging was performed in 31 patients of whom 26 had aorto-iliac imaging. Data points are plotted in Figure 1. The relationship between signal (Sig; arbitrary units) and dose was modelled by a quadratic expression: $Sig = a_0 + a_1 D + a_2 D^2$ The results of the model fitting are presented in Table 1, alongside predicted maximal signal in the aorta and IVC, and the dose that yields Sig_{max}. The dose that produces 90% of the predicted CNR values are denoted as D_{90}.

X	R^2	a_0	a_1	a_2	Sig_{max}	D_{max}	D_{90}
Aorta	0.56	44.21	80.10	-10.27	200.37	3.90	2.50
IVC	0.60	38.57	70.74	-7.61	202.90	4.65	3.01

To gain 90% of predicted maximum signal requires 2.5 mg/Kg (aorta) and 3.0 mg/Kg (IVC). That is, to gain the last 10% of maximum signal over 90% requires an additional 50% increase in dose. Image quality at 2.5 mg/Kg was considered sufficient by qualitative assessment in all patients.

Discussion

FeMRA has enormous imaging potential in patients with advanced renal failure. Imaging research and practice to date tends to use doses of 4 mg/Kg. We have demonstrated that although peak signal will be obtained at doses of 3.9 and 4.6 mg/Kg for aorta and IVC, respectively, there is little added signal at doses above 2.5 mg/Kg with image quality sufficient for diagnostic purposes. Lower doses are more cost efficient and may reduce any potential side effects of intravenous iron preparations.

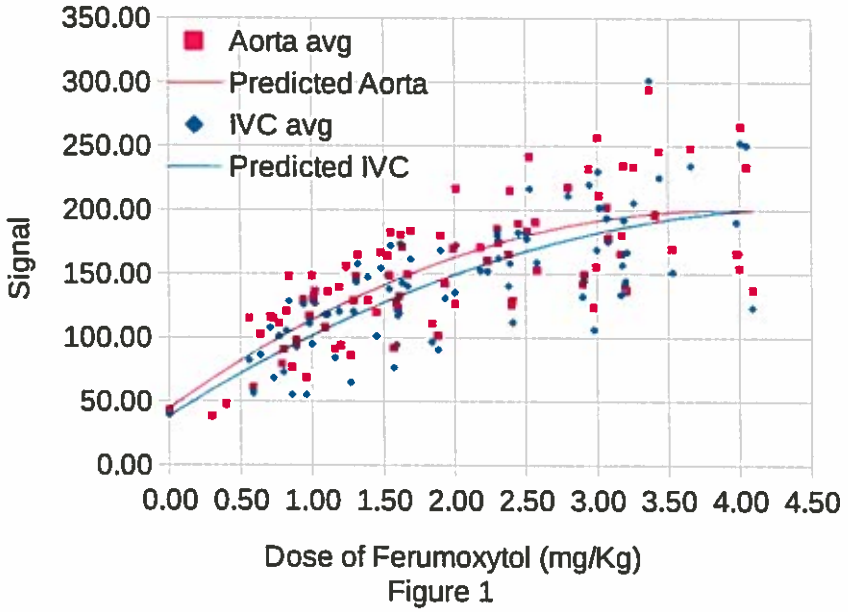

Figure 1

References: 1 Mathematical Optimization of Contrast Concentration for T 1 -Weighted Spoiled Gradient Echo Imaging. Reeder, S, Smith, R, Hernando D, Magnetic Resonance in Medicine (2016) 75:1556-1564

Title: 4D Flow Analysis of Renal Flow Changes due to Kidney Cancer

Carson A. Hoffman[1], Sylvana García-Rodríguez[2], Alejandro Roldán-Alzate[2,3], E. Jason Abel[4], Oliver Wieben[1,2], and Christopher J. Francois[2]

[1]Department of Medical Physics, University of Wisconsin, Madison, WI, [2]Department of Radiology, University of Wisconsin Madison, WI, [3]Department of Mechanical Engineering, University of Wisconsin Madison, [4]Department of Urology, University of Wisconsin Madison, WI

Purpose

Kidney cancer frequently invades and obstructs the venous system and inferior vena cava (IVC), which can change vascular flow patterns. Changes in renal hemodynamics due to kidney carcinoma have not been fully characterized. By utilizing 4D flow magnetic resonance imaging (MRI) to visualize and quantify changes in the arterial and venous renal systems, improved patient specific treatment decisions might be achievable.

Methods

Seven kidney cancer patients participated in the study. Imaging was performed on a clinical 3T scanner using 4D flow MRI with an undersampled radial acquisition, PC VIPR. Flow measurements were performed for both arterial and venous renal systems using in-house macros developed for Ensight (CEI Inc, Apex, NC). Prior to cancer treatment, eight flow values were measured at the supraceliac aorta (SC), suprarenal aorta (SR), left renal artery (LRA), right renal artery (RRA), superior inferior vena cava (SIVC), infra inferior vena cava (IIVC), left renal vein (LRV), and right renal vein (RRV). The reported renal flow measurements represent the total blood flow into and out of the kidneys.

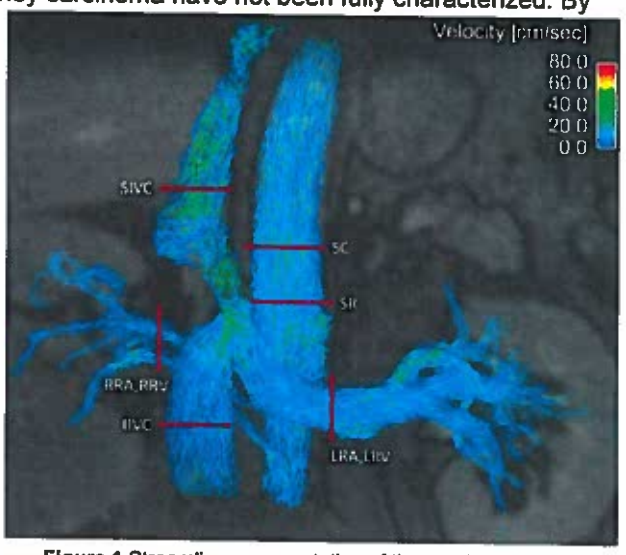

Figure 1 Streamline representation of the renal vascular system color encoded by velocity. Approximate plane placement for flow measurements are shown by the red lines. Tumor has grown into the IVC.

Results

An asymmetry in arterial renal flow was found to exist in all of the seven patients. In three of the patients arterial renal flow increased to the healthy kidney, and in four of the patients arterial renal flow increased to the cancerous kidney. In two of the three patients where tumor was found in the IVC, the IIVC flow values were greater than the SIVC. Two of the seven patients had a completely occluded IVC, which did not allow for IIVC measurements to be taken. Flow values not reported in Table 1 are a result of cancer-impeded flow or a low SNR from the 4D flow MRI.

Conclusion

Our pilot study demonstrates the feasibility to quantify hemodynamic changes due to kidney cancer using 4D flow MRI. Further improvements may be achieved by designing a protocol that utilizes a dual velocity encoding (VENC) scan, to improve visualization and flow quantification in slow flow regions. In relation to healthy volunteers, which show a symmetric flow of blood to the kidneys [1], a clear asymmetry change in blood flow was found in all patients. Preoperative knowledge of flow changes may enable surgeons to plan for alternative treatment approaches such as grafting or ligation of major vascular structures. Further investigation is needed to understand what causes the increase in blood flow to be directed to the healthy or cancerous kidney.

References

[1] Sylvana García-Rodríguez Diurnal Variation of Renal Blood Flow using 4D flow MRI. In Proceedings of the 24th Annual Meeting of ISMRM, Singapore, 2016. 0709.

TABLE 1 – Renal Flow Measurements (ml/min)

Age	Sex	Tumor Side	SC	SR	LRA	RRA	SIVC	IIVC	LRV	RRV	Tumor IVC
58	M	L	4185	2095	295	348	1514	657	142	286	–
50	M	R	2895	1595	488	176	739	1284	733	–	+
63	M	L	4173	2665	242	381	437	–	–	350	++
68	M	N	5892	2698	345	638	754	–	479	330	++
84	M	R	2716	2053	175	461	2035	1293	219	466	–
47	F	L	3674	1746	766	422	–	528	–	337	+
70	M	L	5911	3271	790	386	984	1163	–	208	+

SC - Supraceliac, SR - SupraRenal , LRA - Left Renal Artery, RRA - Right Renal Artery, SIVC - Superior Inferior Vena Cava, IIVC - Infra Inferior Vena Cava, LRV - Left Renal Vein, RRV - Right Renal Vein, Tumor IVC symbols : – No tumor in the IVC, + Tumor in the IVC, ++ Occluded IVC

Table 1 Flow measurements from seven patients with kidney carcinoma. All of the measurements reported are taken prior to cancer treatment.

Non-Contrast Dynamic MR Angiography with Arterial Spin Labeling in Children

Amber Pokorney[1], Houchun H. Hu[1], Niccolo Stefani[2], Jonathan M. Chia[2], Jeffrey H. Miller[1]
[1]Radiology, Phoenix Children's Hospital, Arizona [2] Philips HealthTech

Purpose: To evaluate a 4D dynamic non-contrast dynamic angiography MRI technique based on arterial spin labeling (ASL) called CINEMA (Contrast inherent INflow Enhanced Multi phase Angioraphy) in the assessment of the arterial neurovasculature in pediatric patients.

Methods: All studies were performed on two identical 3 Tesla MRI platforms (Ingenia, Philips HealthTech, R5.1.7) using 32-channel head coil arrays. Over the past year, the CINEMA technique [1, 2] has been successfully implemented in over 100 pediatric patients at our institution, ranging in age from newborns to teenagers. The CINEMA variant evaluated in this work was based on a pulsed ASL technique and had a scan time of 5-7 minutes. Briefly, the approach acquires paired control and labeled data sets. The latter contain blood signals that have been previously inverted (i.e., labeled) by inversion radiofrequency (RF) pulses. Multi-phase dynamic data are acquired by varying the start time of data acquisition from the time of RF inversion (i.e., label delay). Subtraction of labeled and control (non-labeled) data sets at each dynamic phase suppresses static tissues and yields an arterial-only angiography image.

Our pediatric protocol utilized a 3D segmented gradient echo EPI readout. Eighty axial slices were acquired with a resolution of 1.2x1.2x0.8 mm^3. Twelve dynamic (temporal) phases are typically acquired, starting with a label delay of 40-200 ms, followed by 100-120 ms intervals. In addition to CINEMA, 3D time-of-flight (TOF) with a resolution of 0.6x0.6x0.7 mm^3 were acquired in nearly all cases for comparison.

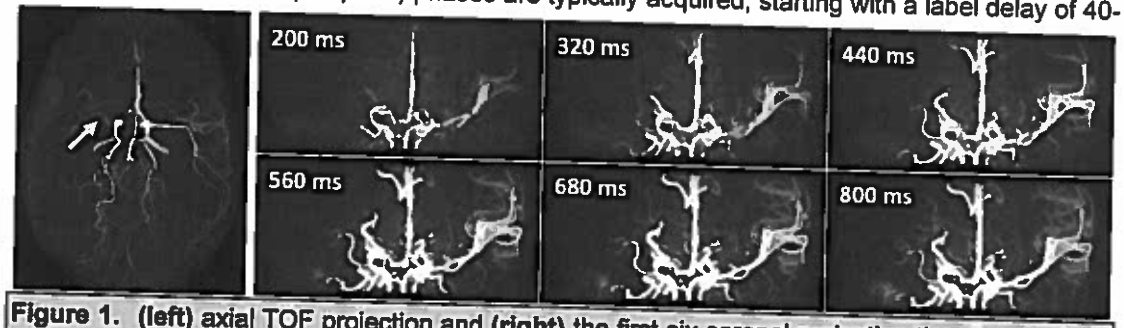

Figure 1. (left) axial TOF projection and **(right)** the first six coronal projection time frames from non-contrast CINEMA in a 13 months old child with Moyamoya disease.

Results: Figures 1 and 2 show exemplary results in a 13 months old and a 7 years old, respectively, both with Moyamoya disease. Axial TOF projections show compromised anterior and middle cerebral arteries on the right (Figure 1) and left (Figure 2) sides of the patients (arrows), respectively. The first six and four CINEMA dynamics corroborate TOF finding, and illustrate delayed arterial filling on the affected side through the coronal projections. Figure 3 shows CINEMA results in a 1 day old boy who presented with seizures. The 12 dynamics demonstrate an otherwise normal angiogram.

Figure 2. (left) axial TOF projection and **(right)** the first four coronal projection time frames from non-contrast CINEMA in a 7 years old Moyamoya patient.

Conclusion: Our data demonstrates the robustness and clinical utility of non-contrast CINEMA in pediatric neurovascular imaging. The technique is particularly useful in assessing patients with Moyamoya disease and asymmetric Circle-of-Willis flow and supplements conventional TOF imaging. Recently, we have further coupled TOF and CINEMA with quantitative 3D spiral pCASL[3] to evaluate perfusion deficits and cerebrovascular response in pediatric patients under an acetazolamide challenge. Additional work in evaluating CINEMA in the peripheral vasculature is also underway.

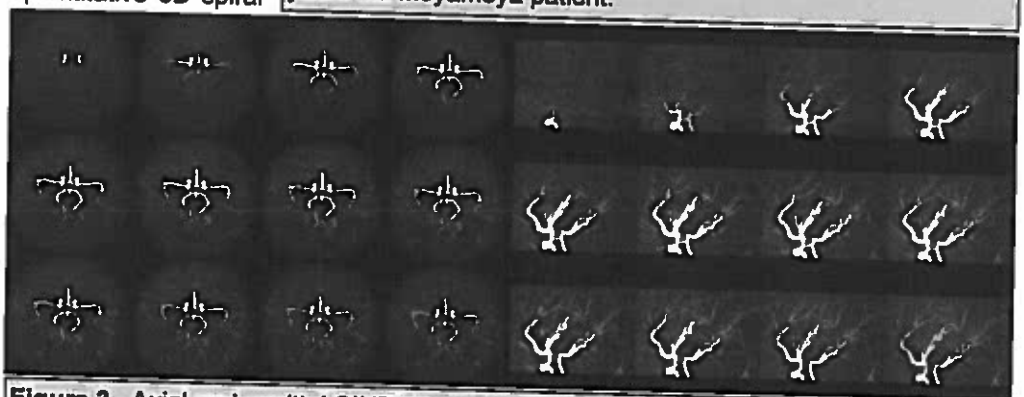

Figure 3. Axial and sagittal CINEMA projections in a one day old patient.

[1] Nakamura M, ISMRM 2013; #540. [2] Iryo Y, Radiology 2014; 271:193-9. [3] Li Z, MRM 2016; 75:266-73.

Non-Contrast, Flow-Independent, Relaxation-Enhanced MR Angiography with an Inversion Recovery and T2-Prepared 3D mDIXON Gradient-Echo Sequence: Preliminary Experience in Children

Amber Pokorney[1], Houchun Hu[1], Jonathan Chia[2], Dianna Bardo[1], Masami Yoneyama[3]
[1] Radiology, Phoenix Children's Hospital, Arizona [2] Philips HealthTech, Dallas, Texas [3] Philips Electronics, Tokyo, Japan

Purpose: To evaluate the feasibility and clinical utility of a non-contrast MRA technique using inversion recovery and T2-prepared magnetization preparation in conjunction with a 3D mDIXON water-fat separated gradient echo (i.e., FFE) pulse sequence in pediatric patients, primarily in neck/shoulder, extremity, abdomen, and pelvis imaging.

Methods: The 3D REACT (Relaxation-Enhanced Angiography without Contrast and Triggering) technique is based on a conventional mDIXON two-point water-fat **[1]** Turbo Field Echo (TFE) pulse sequence, with additional magnetization preparation by a non-volume-selective inversion pulse and a T2-prep module to suppress signals from static tissues, such as muscles and organs, and to enhance signal contrast between blood vessels and background **[2]**.

Over the past 3 months, we have successfully acquired REACT data on 11 pediatric patients, ranging in age from 5-11 years old. All imaging studies were performed on a 3 Tesla Philips Ingenia platform (R5.1.7) using anterior and posterior 32-channel coil arrays. Typical imaging parameters for the REACT sequence were: coronal orientation, 1.2-1.3mm voxel size, 120 2 mm over-contiguous slices, a T2-prep time of 50-90 ms with four 180° refocusing pulses, a TFE shot interval of 3 s, an inversion time of 105 ms, TR=3.9 ms, TE1/TE2=1.3/2.3 ms with bipolar readout, flip angle=12°, SENSE factor=2, TFE turbo factor=100, and linear k-space view order. Without respiratory triggering, the acquisition time is ~2-3 min; abdominal respiratory triggered cases take ~5 min.

Results: Several representative cases from our preliminary experience are shown. Figure 1 illustrates three REACT results in the lower extremity. One patient was evaluated for purulence from a left knee wound. The other patient was evaluated for knee joint effusion. While the peripheral vasculature of the popliteal trifurcation can be clearly observed, note also the clear depiction of hyperintense edema and effusion in the cases. Figure 2 illustrates non-contrast REACT results in the upper extremity and abdomen. Panels (A, B) show a comparison between REACT and a post-Gadolinium MRA acquired with a routine 3D mDIXON FFE method. Figure 3 illustrates a typical example of REACT in the subclavian region.

FIG1: (A) Partial maximum intensity projections (MIPs) of REACT coronally and sagitally of the left leg in an 11y female with a laceration from a vehicular accident. Note clear visualization of extensive edema in the subcutaneous adipose tissue anteriorly, cranially, and caudally (arrows). (B) Sagittal MIP in a 7y female with joint effusion. Note uniform fat suppression and low signal from muscle. (C) REACT MIP of the popliteal trifurcation in an asymptomatic 10y male.

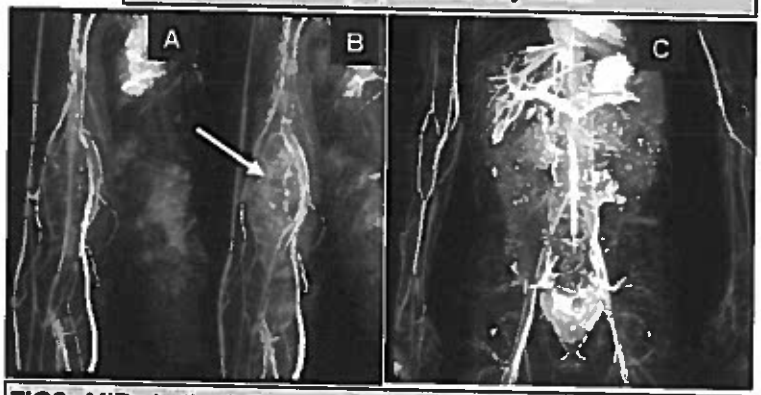

FIG2: MIPs in the left arm of a 4y female from (A) REACT and (B) post-Gd (4.5ml Dotarem) routine 3D mDIXON MRA. The patient has a mass in the triceps (arrows) of lymphatic origin. (C) Coronal MIP from respiratory-triggered REACT scan in an 8y female with an absent infrarenal inferior vena cava and diminished common iliac veins. The patient was contraindicative for Gd administration and has a history of renal failure. Note again uniform fat suppression across the large FOV.

Conclusion: Our preliminary experience with REACT in children suggests that the sequence is robust and capable of providing diagnostically useful MR angiograms with uniform fat suppression in large FOV body applications. The sequence has allowed some of the angiographic exams at our pediatric institution to be performed without Gd-based contrast agents. Efforts continue in optimizing the inversion recovery and T2-prep timings of the pulse sequence in children and in evaluating the sequence in a variety of vascular pathologies. Comparisons involving Gd-based results are underway.

[1] Leiner T, Eur Radiol. 2013;23:2228. **[2]** Yoneyama M, et al. ISMRM 2016; #2252.

FIG3: Coronal MIPs of REACT in a 12y male.

Comparison of flow measurements derived from 2D and 4D-MR velocimetry in a jugular vein phantom

Evan Kao[1,2], Sarah Kefayati[2], David Saloner[2]
[1]University of California – Berkeley, [2]University of California – San Francisco

Purpose: To assess the reliability of 2D MR velocimetry for measuring flow by comparing it to 4D MR velocimetry results.

Introduction: Blood flow is a common parameter used to assess the health of a vessel or graft. It is also used as a boundary condition for patient-imaging-based computational simulations. Therefore, accurate flow values are important to ensure reliable clinical evaluations or relevant numerical simulation results. 2D MR and 4D MR are both convenient methods for measuring the flow rate but each has uncertainties related to specifics of acquisition: 2D MR assumes through plane homogeneity and that the slice can be placed transverse to the vessel; 4D is lengthy and is SNR limited.

Methods: A silicone model of a jugular vein based on patient contrast-enhanced MR angiography data was attached to a flow pump apparatus providing steady flow. This model was chosen as it has a highly structured spatial velocity field. At six locations transverse to the vessel axis (**Figure 1**), 2D MR data was obtained at a spatial resolution of 0.8 x 0.8 mm with a 5mm slab thickness and 50 repetitions. The phantom was subsequently imaged using 4D MR velocimetry at a spatial resolution of 1.3 mm isotropic and temporal resolution of about 80 ms for 5 repetitions.

Flow profiles from the 2D flow data were extracted using Segment v2.0 [1]. The 4D flow data quantified by: 1) Segmenting the phantom geometry using VMTK, 2) slicing the 4D flow data using the flow through-planes from the 2D MR data, 3) clipping the through-planes with the phantom segmentation, and 4) calculating the flow from the velocity normal to the through-plane (**Figure 2**).

Results: The variability in the flow through repetitions (standard deviation < 2% of the flow) appears to be overshadowed by the variability in space, i.e., the choice of through-plane (max SD of 13% of the flow) (**Figure 3**). For smaller vessel cross-sectional areas, the 2D acquisition tends to overestimate the flow and has greater variability in space and lower variability with repetition relative to the 4D acquisition. Agreement between the 2D and 4D data is dependent on the segmentation used to provide the cross-sectional area from which flow is calculated.

Conclusion: The flow obtained by 2D and 4D MR varies with location. Potential sources of error are volume averaging which varies with vessel size, background phase offsets, and intravoxel phase dispersion in regions of large phase shear as occurs in the region with a central vortex. Flow models which provide highly structured flow fields are valuable tools in assessing the accuracy of flow measurements.

References: [1] S. Bidhult, M. Carlsson, K. Steding-Ehrenborg, H. Arheden, and E. Heiberg, A new method for vessel segmentation based on a priori input from medical expertise in cine phase-contrast Magnetic Resonance Imaging. In Proc of 17th Annual SCMR Scientific Sessions, New Orleans, USA, 2014.

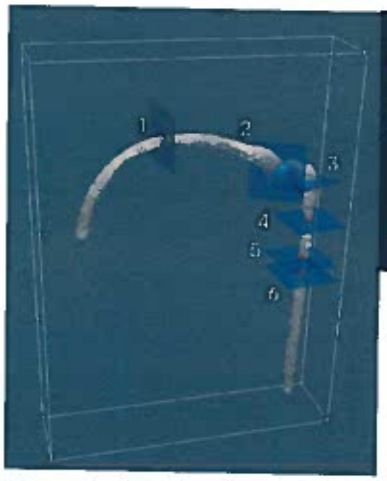

Figure 1. Visual representation of 2D and 4D flow data. (A) 2D flow data is represented as planes within the 4D flow data volume (represented by the box outline). A segmentation of the phantom created from the 4D flow magnitude data is also provided for reference.

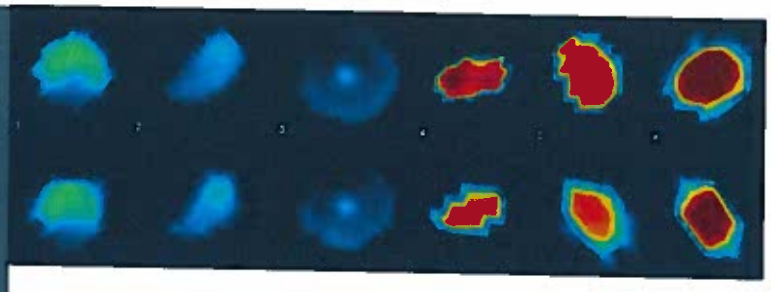

Figure 2. Comparison of 2D and 4D velocity data at 2D transverse planes. (Top Row) The velocity field at each transverse slice. Plane numbers correspond to those in Figure 1. (Bottom Row) Corresponding slices of the 4D volume are created at the same locations as those for the 2D flow data sets.

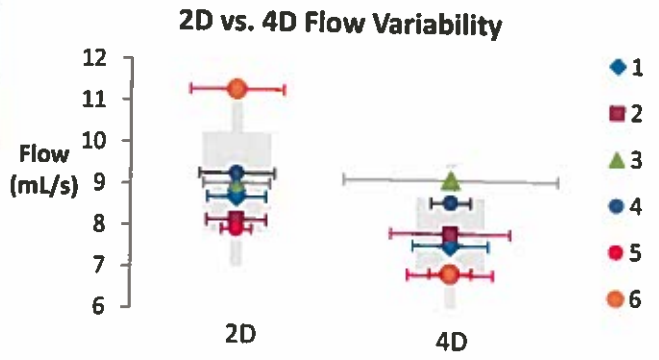

Figure 3. Repetition-averaged flow values and variability. In general, 2D data-derived flows appear to be greater than the 4D data-derived flows. The profile labels correspond to those in Figs 1 and 2. The horizontal error-bars represent standard deviation with respect to repetition for each through-plane flow (scale not shown). The thick vertical error bar represents the standard deviation with respect to location.

Comparison of biventricular strain derived from heart deformation analysis and speckle tracking echocardiography: a working definition of normal for a novel technique

Eric J. Keller, MA[1]; Kai Lin, MD[1]; Benjamin H. Freed, MD[2]; Peter Smith, MD[1]; Bruce S. Spottiswoode, PhD[3]; Maria Carr, RT[1]; Marie-Pierre Jolly, PhD[4]; Michael Markl, PhD[1,5]; James C. Carr, MD[1]; Jeremy D. Collins, MD[1]

[1]Department of Radiology, Feinberg School of Medicine, Northwestern University, Chicago, IL, USA.
[2]Department of Cardiology, Feinberg School of Medicine, Northwestern University, Chicago, IL, USA.
[3]Cardiovascular MR R&D, Siemens Healthcare, Chicago, IL, USA.
[4]Medical Imaging Technologies, Siemens Healthcare, Princeton, NJ, USA.
[5]Department of Biomedical Engineering, Northwestern University, Evanston, IL

Purpose: To assess the performance of prototype software for strain analysis in healthy volunteers.

Methods: 36 volunteers (48±15 years; 8 women) underwent cardiac magnetic resonance imaging (CMR) at 1.5T. CMR was repeated within 3-14 days for 16 subjects. 11 subjects underwent echocardiography immediately before or after CMR. Prototype heart deformation analysis (HDA) software was used to retrospectively quantify strain from segmented balanced steady state free precession (bSSFP) cinegraphic imaging with a temporal resolution of 39.2 msec. Myocardial contours were automatically generated on short axis images; long axis contours were drawn by two independent reviewers at end-diastole and propagated throughout the cardiac cycle using an automated algorithm. Echocardiographic strain was obtained via semiautomatic tracking of stable patterns of natural acoustic markers within the myocardium on short and long axis views.

Results: HDA feasibility was 100% (36/36) compared to 91% (10/11) for 2D STE. Inter-observer agreement was excellent for HDA (ICC>0.87, p<0.01). Healthy global peak systolic strain with HDA was found to be -25.0 (-24.0 - -26.1)% (LV circumferential), 60.5 (55.3 – 65.6)% (LV radial), -22.3 (-20.5 - -24.0)% (LV longitudinal), and -26.0 (-23.8 - -28.2)% (RV longitudinal). Inter-examination variability in strain measurements was low, ranging from 1.7 (1.0 – 2.4)% to 9.2 (7.6 – 10.5)%. HDA-derived circumferential and right ventricular longitudinal strain values were similar to 2D STE (p>0.05), but radial and left ventricular longitudinal strain values were significantly larger (p<0.05).

Conclusions: HDA prototype software enabled efficient, consistent, and retrospective quantification of myocardial strain from conventional bSSFP cine CMR data, demonstrating clinical feasibility.

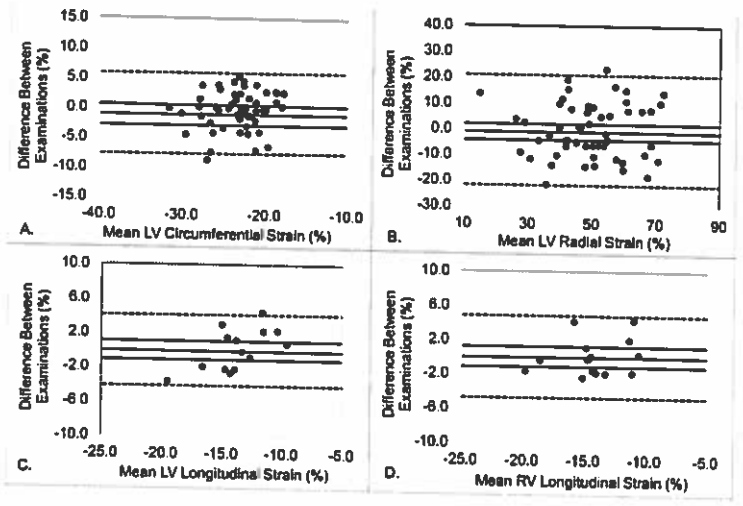

Figure 1: Bland-Altman plots for HDA-derived circumferential (A) and radial (B) regional and global strain values as well as LV longitudinal (C) and RV longitudinal (D) global strain values in 16 healthy volunteers who had identical CMR examinations 3-14 days apart. Solid lines represent mean and 95% confidence interval bias. Dotted lines represent 95% confidence intervals.

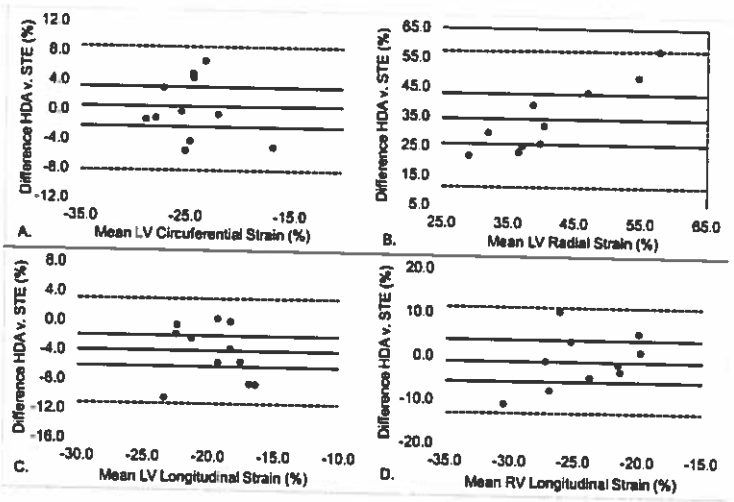

Figure 2 : Bland-Altman plots for agreement of paired 2D STE and HDA-derived circumferential (A) and radial (B) global strain values as well as LV longitudinal (C) and RV longitudinal (D) global strain values performed on the same day in 11 healthy volunteers. Solid lines represent mean and 95% confidence interval bias. Dotted lines represent 95% confidence intervals.

Post-Contrast Black-blood HASTE Imaging: Initial Results with Ferumoxytol.

Eun-Ah Park, MD[1,2], Takegawa Yoshida, MD[1], Sarah Khan, MD, J. Paul Finn, MD[1]

[1]Department of Radiological Sciences, David Geffen School of Medicine, University of California at Los Angeles, Los Angeles, CA 90095 and, [2]Department of Radiology and the Institute of Radiation Medicine, Seoul National University Hospital, Seoul, 110-744, Korea

Purpose: Despite a plethora of creative magnetization preparation schemes, reliable black blood imaging has proved evasive in clinical practice, because most techniques are flow dependent. The purpose of this study was to assess the reliability of black-blood Half-Fourier Single-shot Turbo Spin-echo (HASTE) imaging following ferumoxytol, as a complement to bright blood MR Angiography and based wholly on the relaxivity of ferumoxytol.

Materials and Methods: Our institutional review board approved this retrospective study protocol and written informed consent for the off label use of ferumoxytol was obtained in all patients. Forty-two patients underwent clinically indicated ferumoxytol-enhanced MR angiography of the thorax and abdomen. In all cases, pre-contrast black-blood HASTE images with dual-inversion prepulses were acquired in multiple planes and repeated following ferumoxytol administration, without the dual-inversion pulses. Quantitative measurements including homogeneity index (defined as standard deviation of the left atrial signal intensity) and signal-to-noise ratios (SNRs) for all of the central cardiovascular structures in the thorax were measured on the black blood images. Qualitative image quality scores for assessing complete suppression of blood signal were also evaluated in a 3-point scale by two readers: 3 = complete on all slices; 2 = incomplete on some slices and; 1 = incomplete on all slices. Results were compared using Wilcoxon-signed rank test.

Results: No adverse reactions to ferumoxytol were noted. Compared to pre-contrast black-blood images, ferumoxytol-enhanced black-blood images showed significantly better mean values of homogeneity indices (156.0±89.9 vs. 27.5±10.8, p <0.001) and lower intraluminal SNRs for all cardiovascular regions (overall, 28.4±41.9 vs. 7.1±6.3, p <0.001), indicating more effective blood signal suppression. Qualitative image scores showed virtually complete blood suppression in ferumoxytol images (overall, 2.9±0.2 vs 1.8±0.6 for gadofosveset, p <0.001). In multiple patients, ambiguity about the nature of intraluminal signal on pre-contrast HASTE images was resolved on post-ferumoxytol images (fig 1).

Conclusion: Black-blood HASTE imaging using ferumoxytol provided complete and reliable, flow independent blood signal suppression both quantitatively and qualitatively, without the need for magnetization preparation pulses.

References:

1. Neuwelt EA, Hamilton BE, Varallyay CG, et al. Ultrasmall superparamagnetic iron oxides (USPIOs): a future alternative magnetic resonance (MR) contrast agent for patients at risk for nephrogenic systemic fibrosis (NSF)? Kidney Int 2009;75:465-474.

2. Wei Li, et al. Lower Extremity Deep Venous Thrombosis: Evaluation with Ferumoxytol-enhanced MR Imaging and Dual-Contrast Mechanism—Preliminary Experience. Radiology 2007;242(3):873-881.

Figure 1.

A 3 year old female with Kawasaki Disease and giant coronary artery aneurysms, partially thrombosed. The left column shows sagittal and coronal pre-ferumoxytol HASTE images with high signal both within the patent lumen (arrowheads) and the upper thrombosed portions of the left coronary artery. The right column shows the corresponding post-ferumoxytol HASTE images with complete signal suppression within the patent lumen and persistent high signal superiorly due to thrombus. The middle column shows bright blood (MUSIC) images for reference, complementing the post-ferumoxytol HASTE images.

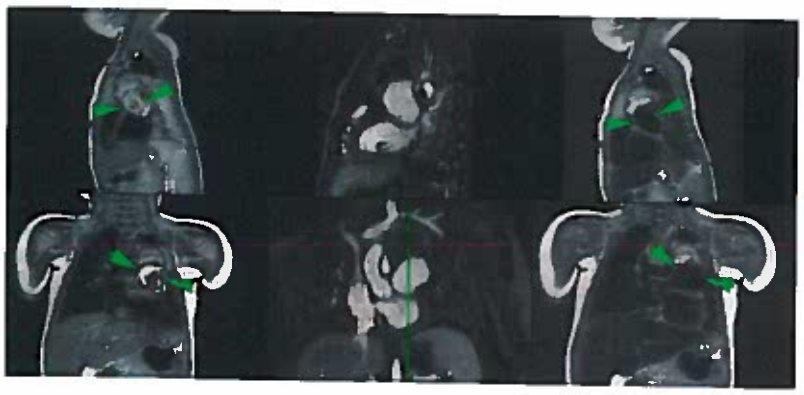

Usefulness of ultra-short echo time imaging for assessment of MR property of metallic stent:
An in-vitro phantom study

Jin-hee Jang[1], Yoon-ho Nam[1], Bum-soo Kim[1], Song Lee[1], Hyun Suk Choi[1], So-Lyung Jung[1], Kook-Jin Ahn[1], Taesub Chung[2]

The Catholic University of Korea[1], Yonsei University Medical College[2], Seoul, Korea

Purpose: Metallic stents are used in intracranial arteries, for various purposes: an assistant tool for coil-embolization, a treatment option of intracranial arterial stenosis and dissection, and aneurysm treatment by flow-diversion. To cover those variable clinical purposes and variability of size and anatomy, there are a variety of metallic stents those are commercially available. One of the major concerns after installation of metallic stents in intracranial arteries is proper imaging follow-up. Naturally, MR angiography has been one of the major options, after stenting of intracranial arteries[1, 2]. However, metallic stents had different MR properties, as compared with human body. It would be helpful to evaluate the property of installed stents, to clarity the effect of stent to MR signals. Susceptibility and radio-frequency (RF) shielding effects are two major sources that determine the signals in and around the metallic stents [3, 4]. In this paper, we validate the clinical utility of ultra-short echo-time (UTE) imaging as an efficient assessment tool for both susceptibility and RF shielding effect for metallic stents.
Methods: We used 7 different commercially available metallic stents those widely used for intracranial arteries (Table or figure). Stents were installed within the silicone tube of 3-mm luminal diameter. At 3T MRI, center out radial UTE images were obtained for 7 different metallic stents with following parameters: TE1/TE2/TR= 0.04/5/18ms, FA=10°, 0.75 mm iso voxel, 65,535 spokes. The susceptibility and RF shielding effects of the metallic stents were evaluated by utilizing phase difference between two echoes and UTE magnitude (which have negligible susceptibility effects), respectively. We classified metallic stents into two categories according to RF shielding effect (severe or acceptable, signal loss 50% cut off). Stents were also classified into two categories according to susceptibility effect (severe or acceptable). To validate the various MR characteristics of metallic stents to MRA, TOF MRA was obtained. After silicone tubes were connected to pulsatile flow pump, TOF-MRA was acquired with following parameters: TE/TR=3.55/22ms, FA=18°, 0.5 mm iso voxel. Stent was located parallel to B0, and flow velocity was calibrated into 50 cm/sec (confirmed by 2D PC, venc = 80 cm/sec). Comparison of relative in-stent signals (RIS) were done in control (unstented segment) and stented segments.

Table: Intracranial Stents approved in Korea

No.	Name	Structure	Material	Metal Coverage	Marker	SIZE
1	Enterprise 2	Laser-cut	Nitinol	upto 10%	Platinum	4mm x 23mm
2	LVIS Blue	Braided	Nitinol + 3 Tantalum strands	upto 28%	Platinum(90)/Iridium(10)	4.5mm x 23mm
3	PED	Braided	Platinum/Tungsten & 35NLT	30-35%	None	4mm x 35mm
4	LVIS Jr.	Braided	Nitinol + 3 Tantalum strands	upto 18%	Platinum(90)/Iridium(10)	3.5mm x 33mm
5	Wingspan	Laser-cut	Nitinol	not available	platinum	4mm x 15mm
6	Solitaire	Laser-cut	Nitinol	upto 6%	Platinum(90)/Iridium(10)	4mm x 20mm
7	Neuroform3	Laser-Cut	Nitinol	upto 11%	Platinum/Iridium	3mm x 20mm

Figure 1. Representative UTE images for acceptable RF shielding and susceptibility (A, stent 2) and severe RF shielding and susceptibility (B, stent 3).

Results: Stent 2, 4, 5 and 7 were considered acceptable RF shield effect (Group A) and others (stent 1, 3, and 6) were not (Group B). Based on difference map of two phase maps, stent 1, 2, 4, 5, and 7 had acceptable degree of susceptibility. Group A stents showed relatively preserved RIS (median 3.42, range 2.48-5.85) on TOF MRA (Figure 2). Group B Stents showed low RIS (median 1.08, range 0.42-1.12). RIS of unstented segment was 5.28. When flip angle was increased (36°), RIS of group A stents get higher (median 13.08, range 9.16-15.55) than standard FA. RIS of group B stents in TOF MRA with high FA had also increased (median 3.75, range 3.46-4.14), which were similar to the RIS of group A stents of standard FA.

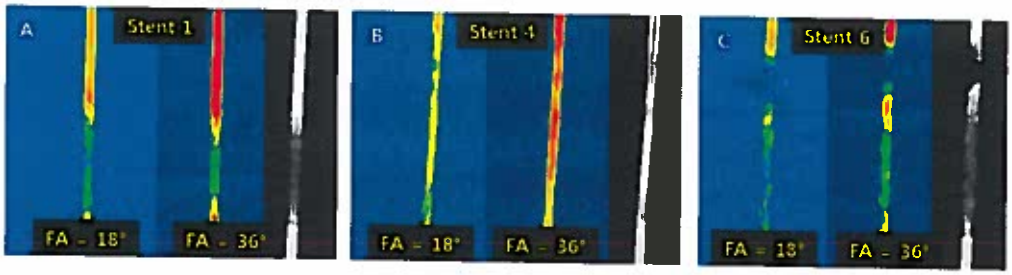

Figure 2. Standard and high flip angle TOF MRA of stents. Stent 1 and 6 were group B, severe RF shielding. Note the weak signal of stented segment in standard FA and restored RIS in high FA. Stent 4 was group B, and relatively preserved luminal signal on both standard and high FA.

Conclusion: UTE image was a feasible MR tool for MR property of metallic stents, especially for the assessment of RF shielding.

References

1. Seok JH, et al. *Korean J Radiol.* 2012;13:550-556, 2. Choi JW, et al. *Neurointervention.* 2011;6:71-77, 3. Wang Y, et al. *Magn Reson Med.* 2003;49:972-976, 4. Bartels LW, et al. *J Vasc Interv Radiol.* 2001;12:365-371

Fused Source and Subtraction Arterial Spin Labeled MRA of the Extracranial Carotid Arteries

Ioannis Koktzoglou[1,2], Ian G. Murphy[1,3], Robert R. Edelman[1,3]

[1]Radiology, NorthShore University HealthSystem, Evanston, IL, [2]University of Chicago Pritzker School of Medicine, Chicago, IL, [3]Northwestern University Feinberg School of Medicine, Chicago, IL

Purpose: Several nonenhanced methods have been proposed for MRA of the carotid arteries[1-6]. Of these methods, time-of-flight (TOF) remains the most widely available. Compared with TOF MRA, recent work has shown that nonenhanced arterial spin-labeled (ASL) MRA has the capability to reduce saturation effects, increase vascular contrast and improve image quality for displaying the carotid bifurcation and internal carotid arteries[7]. Nonetheless, a drawback of this subtractive method has been suboptimal image quality for portraying proximal vessels (including the aortic arch, brachiocephalic and subclavian arteries) due to respiratory motion and insufficient RF labeling at the inferior edge of the field of view. We evaluated whether the fusion of unsubtracted and subtracted images might address this deficiency.

Methods: This study was IRB approved and used informed consent. Imaging was done on a 3 Tesla MR system (MAGNETOM Verio, Siemens Healthcare). Using a combination of pseudocontinuous and pulsed RF spin labeling along with a segmented 3D Cartesian fast low-angle shot readout (TR/TE/flip = 5.8ms/3.7ms/5°, 1mm^3 resolution) in a manner previously described[7], nonenhanced carotid ASL MRA was performed in 15 subjects (8 volunteers, 7 patients). Reconstructions were performed with conventional subtraction of control and labeled data, and with the proposed "fusion ASL" approach that replaced the inferior portion of the field of view of the subtracted images with the corresponding voxels of the unsubtracted "control" images. To minimize step artifact at the junction of the two data sets (located at the upper edge of the pulsed RF label), data were gradually fused over a 1cm transition zone. Subtracted, nsubtracted control, and fused images were reviewed by a radiologist who scored thirteen arterial locations using a 4-point scale (1: non-diagnostic, 2: fair, 3: good, 4: excellent). Arterial-to-background contrast-to-noise ratio (CNR) was measured in the aortic arch, and in the proximal and mid common carotid arteries.

Results: The figure below shows the potential of fusion ASL reconstruction for improving display of proximal arterial segments. Compared to standard subtractive reconstruction, fusion ASL reconstruction provided significantly improved image quality for displaying the aortic arch (mean values of 2.3 vs 1.1, $P<0.0001$), brachiocephalic artery (2.9 vs 1.4, $P<0.001$), and left (2.8 vs 1.7, $P<0.01$) and right (3.0 vs 1.6, $P<0.001$) subclavian arteries. Fusion ASL reconstruction provided median CNR gains in the aortic arch, proximal and mid common carotid arteries of 2.2-fold, 1.6-fold and 1.4-fold, respectively.

Conclusion: Results show that the fusion of unsubtracted and subtracted images obtained during ASL-based MRA of the extracranial carotid arteries can improve the image quality and contrast-to-noise ratio of large proximal arteries, namely the aortic arch, brachiocephalic and subclavian arteries.

References: 1) Keller et al. Radiology 1989;173:572-532. 2) Blatter et al. AJR 1993;161:1269-1277. 3) Nishimura et al. Magn Reson Med 1987;4:193-202. 4) Kramer et al. Eur Radiol 2011;21:1667. 5) Takei et al. J Magn Reson Imaging 2012;35:957-962. 6) Koktzoglou et al. Magn Reson Med 2016;75:2072-7. 7) Koktzoglou et al. J Cardiovasc Magn Reson 2016;18:18.

Contrast Enhanced Pelvic Venography in the Workup of Cryptogenic Stroke

Kramer LA, Hasan KM University of Texas Health Science Center-Houston

Introduction: In the absence of ultrasound evidence of lower extremity deep venous thrombosis, magnetic resonance venography (MRV) of the pelvic venous system is utilized in our institution to evaluate for a source of emboli in patients with cryptogenic stroke and a right to left shunt(1). Because of the tortuosity of the pelvic veins and the presence of valves, flow artifacts due to turbulence are common and may simulate a clot on standard 2D time-of-flight (2DTOF) sequences. On noncontrast MRV studies, CINE fast gradient-echo sequence (CINE FGRE) has been utilized to identify flow artifacts in an effort to improve specificity. With the temporal efficiency of fast 3D TOF sequences and the availability of the intravascular agent, gadofosveset trisodium, contrast enhanced MRV (CEMRV) has been recently adopted as the standard protocol at our institution in cryptogenic stroke. The goal of this study was to determine if the CEMRV provides increased specificity over CINE FGRE in evaluation of the pelvic DVT.

Methods: We retrospectively reviewed consecutive pelvic MRV studies. Only patients with acute CVA, right to left shunt by echocardiogram and negative Doppler ultrasound evidence of lower extremity DVT were included in the study. Studies were performed using a 1.5 Tesla magnet. MRV was performed within 72 hours of onset of symptoms. Non-contrast MRV was obtained with a peripherally pulse triggered axial CINE FGRE pulse sequence (TR = 7.6 msec, TE = 4.6 msec, FA = 15 degrees; 8mm thick sections with no gap) in the axial plane. A conventional 2DTOF was performed utilizing an axial spoiled gradient-echo (SPGR) sequence (TR = 22.0 - 46.0 msec, TE = 6.9 msec, FA = 70 degrees; 4 -7 mm thick sections with no gap). Clots were identified on the 2DTOF sequence as rounded filling defects seen on two or more contiguous sections when their size and shape matched the CINE FGRE sequence over the cardiac cycle (figure 1) and were termed concordant round filling defects. Flow artifacts were identified on the 2DTOF sequence as rounded filling defects seen on two or more contiguous sections when their size and shape were smaller and varied over the cardiac cycle on the CINE FGRE sequence (figure 1) and were termed discordant round filling defects. Concordant linear defects were considered as valves. The common femoral, external iliac and common iliac veins in addition to lower portion of the inferior vena cava were evaluated for concordant and discordant filling defects. CEMRV was performed 5 minutes following an intravenous dose of 0.03 mmol/kg of gadofosveset trisodium using an axial fast 3D TOF sequence (TR = 4.8 msec, TE = 2.4 msec, FA = 10 degrees; 4 mm thick sections interpolated to 2mm) in the axial plane. On the CEMRV any round filling defect was considered positive for thrombi.

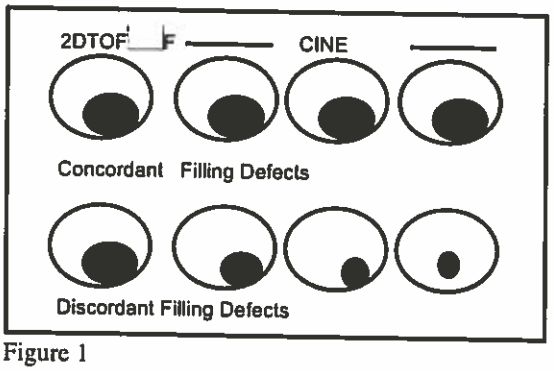

Figure 1

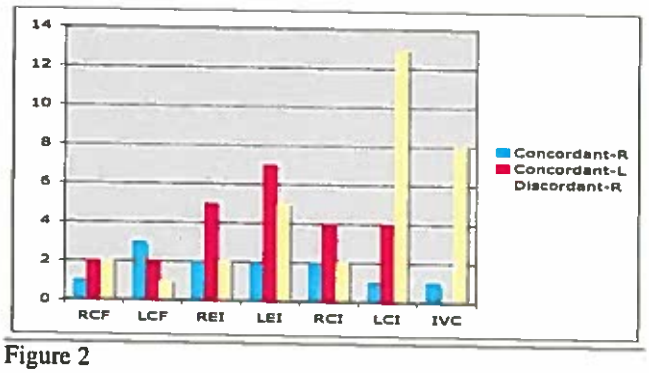

Figure 2

Results: A total 151 patients met inclusion criteria having an age range of 18 – 75 years (ave = 41 years). 43 patients underwent a noncontrast MRV and 108 patients underwent a CEMRV study. There we no patients having both CEMRV and noncontrast MRV sequences. On the noncontrast MRV a total of 4 patients (9%) had concordant round filling defects compatible with intravenous thrombus. No patients had filling defects on the CINE study, which were not seen on the 2DTOF sequence. 31 patients had discordant round filling defects (72%). A total of 11 patients (26%) had concordant linear filling defects compatible with venous valves. The number and distribution of concordant and discordant filling defects is seen in figure 2. Right Common Femoral = RCF; Left Common Femoral = LCF; Right External Iliac = REI; Left External Iliac = LEI; Right Common Iliac = RCI; Inferior Vena Cava = IVC; Concordant Round = Concordant-R; Concordant Linear = Concordant-L; Discordant Round = Discordant=R. On the CEMRV a total of 6 patients had positive filling defects (6%) in the following distribution: LCI (n=1), LCF (n=2), RFV (n=1), gonadal vein (n=1) and IVC (n=1).

Discussion/Conclusion: MRV is utilized to noninvasively evaluate the pelvic venous system in patients with cryptogenic stroke. The diagnosis of a DVT will implicate long-term anticoagulation therapy and therefore high sensitivity and specificity is critical to treatment planning. Although traditional 2DTOF sequences are very sensitive to intraluminal abnormalities, the extensive tortuousity of pelvic veins and the presence of valves cause flow artifacts resulting in low specificity. Flow artifacts will vary with velocity and therefore the size and shape can very over the cardiac cycle, which can be readily assessed with CINE sequences thereby improving specificity. Although CINE MRV and CEMRV were not directly compared in each subject, the decreased percentage of CEMRV positive cases suggests increased specificity over noncontrast MRV in the workup of cryptogenic stroke.

(1). Cramer SC, Rordorf G et al. Increased pelvic vein thrombi in cryptogenic stroke: Results of the Paradoxical Emboli from Large Veins in Ischemic Stroke (PELVIS) study. Stroke. 2004 Jan;35(1):46-50.

Endogenous assessment of diffuse myocardial fibrosis in patients with T1ρ-mapping

Joep W. van Oorschot JW[1,4], Fatih Güçlü[2], Sanne de Jong[3], Steven A. Chamuleau[2], Peter R. Luijten[1], Jaco J. Zwanenburg[1], Tim Leiner[1]

From the Departments of Radiology[1], Cardiology[2] and Experimental Cardiology[3], Utrecht University Medical Center, Utrecht, The Netherlands, and Philips Healthcare[4], Best, The Netherlands

Purpose: Recently, it was shown that a significantly higher T1ρ is found in compact myocardial fibrosis after chronic myocardial infarction. In this study, we investigated the feasibility of native T1ρ -mapping for the detection of diffuse myocardial fibrosis in patients with dilated cardiomyopathy (DCM).

Methods: T1ρ -mapping was performed on three explanted hearts from DCM patients at 3 Tesla (T). Histological fibrosis quantification was performed, and compared with the T1ρ -relaxation times in the heart. Furthermore, twenty DCM patients underwent an MRI at 1.5T. Native T1ρ -maps, native T1 -maps, and extracellular volume (ECV)-maps were acquired. Additionally, eight healthy volunteers were scanned for reference values.

Results: A significant correlation (Pearson r = 0.49; P = 0.005) was found between ex vivo T1ρ -values and fibrosis fraction from histology. Additionally, a significantly higher T1ρ -relaxation time (55.2 ± 2.7 ms) was found in DCM patients compared with healthy control subjects (51.5 ± 1.2 ms) (P = 0.0024). The relation between in vivo T1ρ -values and ECV-values was significant (Pearson r = 0.66). No significant relation was found between native T1 - and ECV-values in this study (P = 0.89).

Conclusions: This study showed proof of principle for the endogenous detection of diffuse myocardial fibrosis with T1ρ -MRI. Ex vivo and in vivo experiments showed promising results that T1ρ -MRI can be used to measure the extent of diffuse myocardial fibrosis in the myocardium.

Assessment of Intraplaque Hemorrhage Signal Changes on MRI

Jin Liu, Jie Sun, Thomas S. Hatsukami, William S. Kerwin, Niranjan Balu,
Daniel S. Hippe, Amy Wang, and Chun Yuan
University of Washington, Seattle, WA, United States

Purpose

Intraplaque hemorrhage (IPH) is a characteristic feature of high-risk atherosclerotic plaque [1]. Several studies have shown that presence of IPH stimulates plaque progression [2] and is a risk factor for cerebrovascular events [3]. Recently, serial studies have found that the IPH signal intensity changes in MRI exists [4] and differs between symptomatic and asymptomatic carotid arteries [5], which may be associated with plaque progression. However, no study has assessed the reproducibility of IPH signal intensity in MRI. Simultaneous non-contrast angiography and intraplaque hemorrhage (SNAP) MRI [6] provides inherent advantages for normalized signal measurement because of coil sensitivity corrected intensity and concurrently acquired reference image. This study aims to develop a signal intensity ratio measurement method based on SNAP, assess its reproducibility and explore IPH signal intensity ratio changes.

Methods

Study Population: Thirty-three patients with asymptomatic carotid stenosis or plaque were scanned twice with SNAP MRI within one month (time interval: 7.8±8.9 days). Based on time intervals, patients were divided into three exclusive groups: within one day, within two weeks and within one month. *SNAP MRI parameters:* TR/TE = 10/4.8 ms, flip angle = 11°, inversion time = 500 ms, field-of-view = 160×160×32 mm^3, spatial resolution = 0.8×0.8×0.8 mm^3 acquired and 0.4×0.4×0.4 mm^3 interpolated. *Image Analysis:* Adjacent muscle signal or fibrous tissue is widely used for intensity normalization in carotid MRI [6]. However, the background phase corrected SNAP image used for IPH detection is derived from highly T1 weighted image where muscle signal is close to zero. Therefore, for intensity normalization, we used adjacent sternocleidomastoid muscle (SCM) signal in the reference image, which is proton-density weighted and acquired simultaneously in SNAP imaging. The signal intensity ratio (SIR), defined as the ratio of signal intensity on phase corrected SNAP image to SCM signal intensity on the reference SNAP image, was calculated for each voxel. Maximum Signal Intensity Ratio (Max SIR) was recorded for all arteries. *IPH Analysis:* An experienced reviewer read each phase corrected SNAP scans independently and visually identified IPH presence for each artery. An optimized SIR threshold of 1.4 was obtained through receiver operating characteristic (ROC) curve analysis and maximizing the sum of sensitivity and specificity for IPH detection, using the manual determination of IPH as the reference standard. Each voxel with SIR > 1.4 was then classified as IPH+. Arteries with ≥ 8 IPH+ voxels (acquisition resolution) were classified as IPH present. In the IPH present arteries, max IPH SIR, mean IPH SIR (mean SIR of IPH+ voxels) were recorded. *Statistics:* The intraclass correlation coefficient (ICC) was used for evaluating the reproducibility of the max SIR within all arteries. In the IPH+ arteries, the within-subject coefficient of variation (CV) was calculated and the correlation between the within-subject CV and scan-rescan time interval was evaluated using Pearson's correlation coefficient (R software, version 3.0.2).

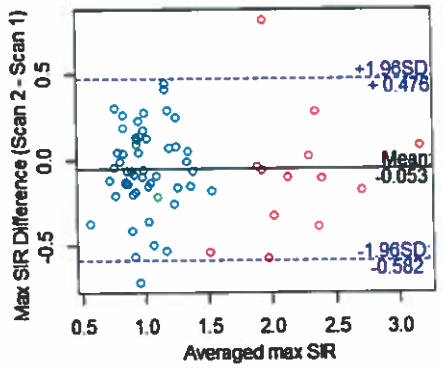

Figure 1 Bland-Altman plots of maximum SIR of carotid artery. Based on manual reading, blue dots are IPH- on both scans, red dots are IPH+ on both scans and green dots are IPH+ only on one scan.

Results

Out of 66 arteries, the max SIR of arteries showed good scan-rescan reproducibility, with an ICC of 0.88 (0.81-0.92) (**Figure 1**). By applying the SIR threshold of 1.4, 12 arteries were identified as having IPH on both scans (high agreement with manual review results with kappa of 0.93). There were significant to marginal correlation between scan-rescan time interval and within-subject variance of IPH max SIR (r=0.58, p=0.048) or IPH mean SIR (r = 0.57, p=0.055) (**Figure 2**).

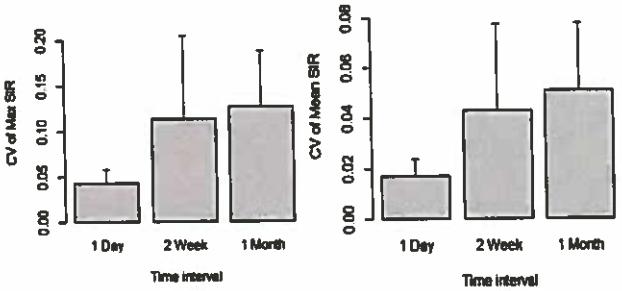

Figure 2 Within-subject coefficient of variation (CV) of max IPH SIR and mean IPH SIR against time interval of three groups (4 IPH+ arteries in each group). Error bars denote standard error.

Discussion and conclusion

Few studies have looked at the changes of IPH, which is hampered by the limited IPH incidence and lack of sensitive and reproducible biomarkers. While the size of IPH can be measured, the signal intensity of IPH might reveal additional significant information such as metabolic activities and IPH changes. Max SIR and mean SIR may provide an early marker for detecting changes in IPH, including the dissolution and incidence of IPH. IPH SIR variance tends to increase with time, which may be related to IPH changes and requires further study.

References

[1] Michel JB, et al. Eur Heart J, 2011;32(16):1977-85. [2] Saam T, et al. J Am Coll Cardiol 2013; 62(12):1081-1091. [3] Altaf N, et al. J Vasc Surg, 2008;47(2):337-42. [4] Sun J, et al. 84th EAS Congress, Austria 2016; p248. [5] Wang Q, et al. Int J Cardiovasc Imaging, 2010; 26(2), 323-32 [6] Wang J, et al. MRM, 2013;69(2):337-45.

4D Flow MRI of the Spinal Canal: First Results

U. Ludwig[1], K. Wolf[2], M. Menza[1], J. Hennig[1] and A. Krafft[1]

[1]Department of Radiology, Medical Physics, University Medical Center Freiburg, Germany
[2]Department of Neurology and Neurophysiology, University Medical Center Freiburg, Germany

Introduction

Within the spinal canal, dynamic factors of cerebrospinal fluid (CSF) flow and spinal cord movements have been recognized as possibly contributing factors on the development of spinal cord detoriation [1,2,3]. MRI-based 2D phase contrast (PC) imaging has been the standard imaging technique for studying cerebrospinal fluid (CSF) dynamics [4,5]. As CSF dynamics associated to lesions show a high temporal and spatial heterogeneity [4], a more complex approach is needed in order to understand the underlying biomechanics. The aim of this study was to evaluate the ability of 4D flow MRI in CSF dynamics in the cervical spine.

Methods

All experiments were performed on a 3T MAGNETOM Prisma (Siemens, Erlangen, Germany). One healthy, male volunteer (age: 31 years) with no history of neurological disorder or spinal trauma underwent MRI of the spine that included two 4D flow-sensitive acquisitions. The first 4D flow protocol employed velocity encoding in all three directions and collected data in 40 sagittal planes (i.e. in parallel to the spine's main direction) at an isotropic resolution of 1.25 mm^3. The second 4D protocol used an axial slice orientation (i.e. perpendicular to the spine's main direction) with a two-fold higher in-plane resolution and applied velocity encoding only along the through-plane direction. To compensate for the SNR drop due to the higher in-plane resolution the partition thickness was four-fold increased so that the voxel size was 0.6x0.6x5 mm^3. Both data sets used prospective ECG triggering and employed PEAK-GRAPPA acceleration (factor: 5, number of reference lines 20) [6] and acquired data with otherwise identical imaging parameters (TR = 9.2 ms, TE ~ 6.5 ms, 10 heart phases, 2/4 lines per phase, temporal resolution = 73.6 ms, concomitant field correction, total acquisition time ~12 min) including a venc value of 0.05 m/s. The 3D volumes of both protocols were positioned to cover the section of the spine ranging from vertebra C2-C7. Velocity data were derived from the subtraction of the phase images without and with velocity encoding. Further data processing was done in Matlab and visualization of the flow data with a web-based in-house developed software tool.

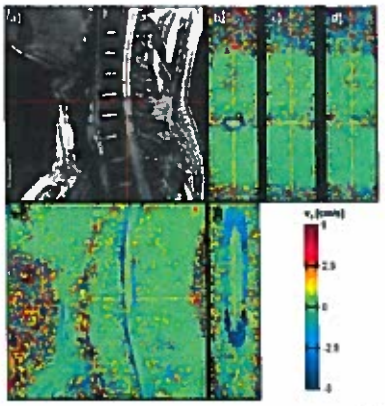

Figure 1: a) Sagittal magnitude image, b-d) velocity maps in b) head-feet, c) anterior-posterior and d) left-right direction. Corresponding e) sagittal and f) coronal velocity maps as marked by orange lines.

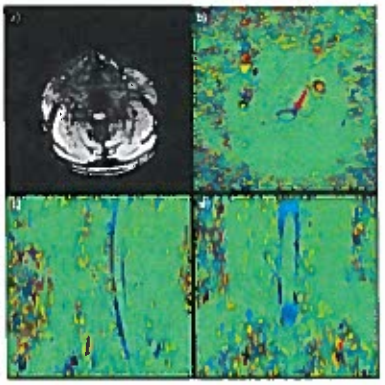

Figure 2: a) Original high-resolution axial magnitude image and b) corresponding velocity map. c) Sagittal and d) coronal reformatted velocity maps. Red arrow marks the area of the ROI for the time course (Figure 3).

Results

Figure 1 and 2 show representative velocity maps. CSF flow is mainly present along the direction of the spinal cord and barely visible in volunteer's left-right or anterior-posterior direction (Fig. 1). The CSF velocity approximately follows a sinusoidal pattern over the course of one heartbeat (Fig. 3). Maximum velocities in the range of 5-6 cm/s were measured so that unwrapping of high velocities (> venc) was required. The flow protocol with the high in-plane resolution revealed similar velocities and revealed that no CSF flow occurs in areas of branching nerves from the spinal cord.

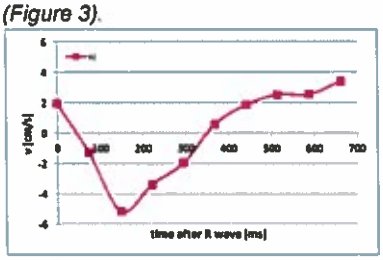

Figure 3: Exemplary time course in ROI (red arrow in Figure 2) following a sinusoidal profile with peak velocities of -5 to 5 cm/s.

Conclusion

Our data indicates that 4D flow MRI is able to measure CSF flow in the upper part of the spine (C2-C7) with high spatial and temporal resolution. Our initial findings will be used to further optimize our 4D flow protocol (number of velocity encoding directions, venc settings etc.). Future work will also include 4D flow measurements in patients with spinal cord stenosis.

References

1. Vavasour et al. Spine, 14(10): 2344-2354.
2. Chang et al. Spine, 39(26): 2136-2142.
3. Wolf et al. In Submission
4. Wagshul et al. J Neurosurg 2006;104:810–819
5. Haughton et al. AJNR 2003;24:169–176
6. Jung et al. JMRI 2008;28:1226-1232

Beyond high resolution: Prospectively motion corrected Time of Flight angiography with 150µm isotropic resolution at 7T under SAR constraints

H. Mattern, A. Sciarra, F. Godenschweger, D. Stucht, F. Lüsebrink, O. Speck
Department of Biomedical Magnetic Resonance, Otto-von-Guericke University Magdeburg, Germany

PURPOSE

Time of Flight (ToF) angiography benefits from increased SNR and prolonged T1 relaxation times at 7T [1]. With increasing spatial resolution motion artifacts are more likely and with increasing B0 fields the specific absorption rate (SAR) increases too, preventing the use of venous saturation (SAT). In this study, prospective motion correction (PMC) [2] is used to prevent motion artifacts and VERSE [3] plus sparse saturation [4] are used to reduce SAR and enable SAT.

METHODS

In this study, which was approved by the local ethics committee, one healthy male subject was scanned with a 32-channel head coil (Nova Medical, Wilmington, USA) at 7T (Siemens, Erlangen, Germany) after giving written informed consent. Each scan consisted of 4 slabs with 25 % overlap, 96 slices per slab and 196x147mm² FOV. Full brain angiograms without (product sequence) as well as with PMC and sparse saturation were acquired with TR/TE=50/6.63 ms; 25° TONE pulse; (0.25 mm)³ voxel size; GRAPPA 3; scan duration 48:05. Additionally, a motion corrected ToF with (0.15 mm)³ voxel size was acquired using TR/TE=35/6.63 ms, 23° TONE pulse; no GRAPPA acceleration; scan duration 2:14:21.

RESULTS

Axial Maximum Intensity Projections (MIP) with and without PMC plus sparse saturation are shown in Fig. 1a, b. The subject moved considerably during the extended scan time (motion range ~50-times larger than voxel size) leading to noticeable artifacts. PMC successfully prevented motion artifacts, improving image quality considerably. Sparse saturation suppressed the veins efficiently. In the (0.15 mm)³ axial MIP (see Fig. 1c) very small vessels, e.g. branches of the basal artery are clearly visible. Compared to the (0.25 mm)³ data, the higher resolution (0.15 mm)³ example provides a dramatically improved level of detail.

CONCLUSION

Prospective motion correction and adapted SAR management unleashes the full potential of ToF angiography at 7T leading to unprecedented high effective resolution.

ACKNOWLEDGEMENT

We would like to thank Sebastian Schmitter for his support. This work was supported by the NIH, grant number 1R01-DA021146.

REFERENCES

[1] Ladd ME. TMRI. 2007;18(2):139–152. [2] Maclaren J. et al. PloS one. 2012;7(11):e48088. [3] Conolly S. et al. JMRI (1969). 1988;78(3):440–458. [4] Schmitter S. et al. MRM. 2012;68(1):188–197.

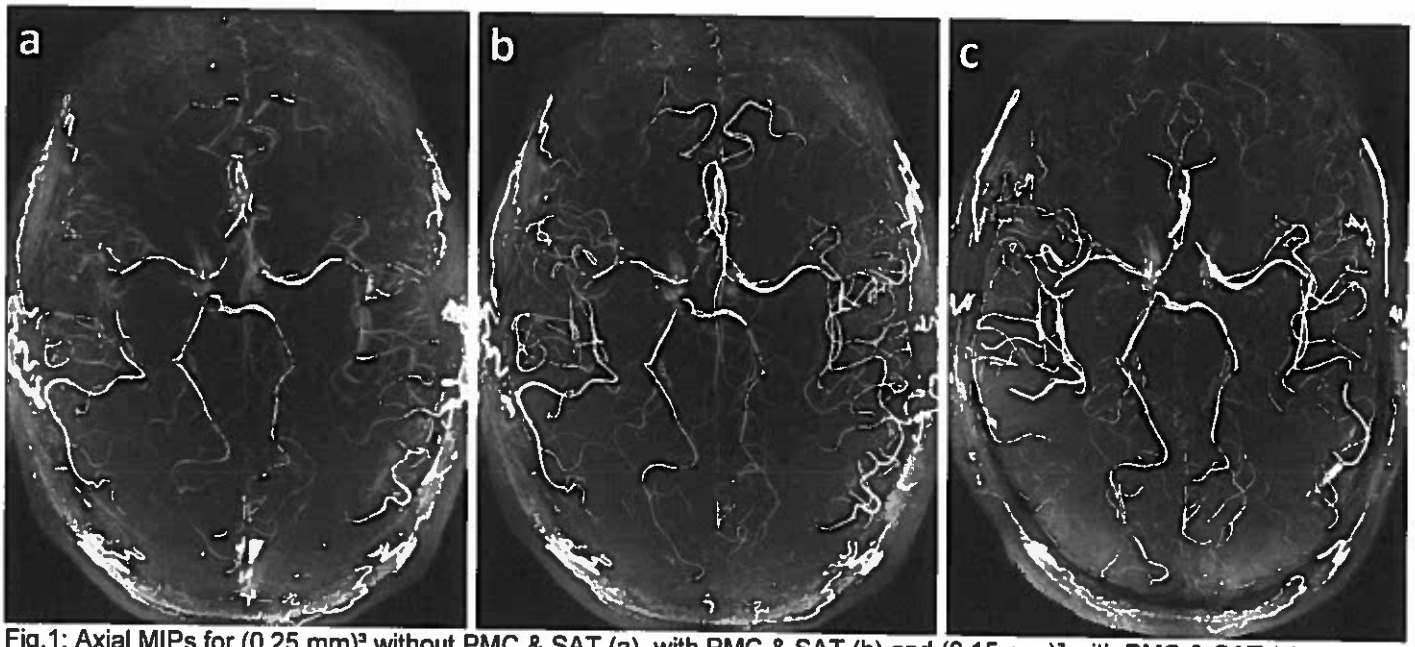

Fig.1: Axial MIPs for (0.25 mm)³ without PMC & SAT (a), with PMC & SAT (b) and (0.15 mm)³ with PMC & SAT (c)

Comparison of In Vitro 4D Flow MRI and CFD to Stereoscopic Particle Image Velocimetry

Rafael Medero[1,2], David Rutkowski[1,2], Margaret Weathers[1], Kevin Johnson[3], Alejandro Roldán-Alzate[1,2]
Departments of (1) Mechanical Engineering, (2) Radiology, (3) Medical Physics; University of Wisconsin-Madison

Purpose: Non-invasive assessment of blood flow is challenging. 4D flow MRI has shown promising results, assessing hemodynamics in different vascular territories. Computational fluid dynamics (CFD), a technique used extensively to simulate blood flow in different physiological conditions [1,2], has demonstrated good agreement with 4D flow MRI [3]. However, validation of 4D Flow MRI using a standard experimental method, such as stereoscopic particle image velocimetry (Stereo-PIV), has yet to be thoroughly investigated [4]. The purpose of this study is to compare velocity measurements through an in vitro carotid artery bifurcation model using 4D Flow MRI, Stereo-PIV and CFD.

Methods:

MR Imaging: A silicone phantom of a carotid artery bifurcation was connected to a perfusion pump and scanned on a clinical 3T scanner (Discovery MR 750, GE Healthcare, Waukesha, WI), using a wrist coil. 4D flow MRI was performed with a 5-pt radial-undersampled technique, PC-VIPR [5]. Imaging parameters were as follows: imaging volume: 24 x 24 x 24 cm; 0.625 mm acquired isotropic spatial resolution; TR/TE = 6.4/1.8 ms; VENC = 75 cm/s. MRI was performed while a solution of water and glycerol circulated through the model at 1 L/min. Gadofosveset trisodium (Ablavar, Lantheus Medical Imaging, N. Billerica, MA) was added to the solution to improve the signal to noise ratio.

4D Flow MRI Quantification: Vessel segmentation was performed in Mimics (Materialise, Leuven, Belgium), where a three-dimensional (3D) geometry was generated from the 4D Flow MRI complex difference images. The 4D Flow MRI dataset was visualized and quantified in Ensight (CEI Inc., Apex, NC). Velocity streamlines were generated, to display flow trajectories and characterize the velocity field in the three orthogonal directions within the whole volumetric domain.

Stereo-PIV Measurements: PIV was performed on the silicone phantom using a Flowmaster Stereo-PIV (2D3C) system (LaVision, Göttingen, Germany) that enables the measurement of all three velocity components (3C) within a 2D plane using two cameras. The system used data acquisition software DaVis 8.3.1 and is consisted of a dual-pulse 527 nm Nd:YLF laser perpendicular to two high speed cameras Phantom v341, with a resolution of 2560 x 1600 pixels, 4 megapixels, and frame rate of 402 Hz (Fig. 1 – bottom-left). A solution, seeded with polymer particles (diameter = 10 μm), of glycerol and water (55:45 glycerol/water) was pumped at 1 L/min through the model to match its refractive index (n = 1.41). Image preprocessing and vector post-processing was performed to improve the quality of the results by reducing the intensity fluctuation in the background due to reflections, and to eliminate spurious vectors.

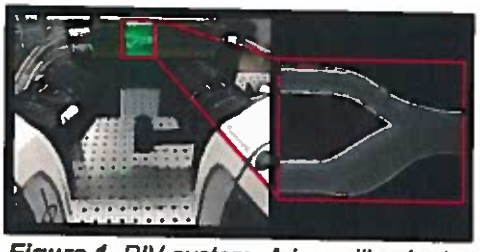

Figure 1. *PIV system. A laser illuminates fluorescent particles. Images from two high-speed cameras are simultaneously acquired to track the fluid flow.*

CFD Simulation: The segmented geometry from the bifurcation phantom was prepared in ANSYS workbench and imported into FLUENT (Ansys, inc Cannonburg, PA, USA) for a steady state simulation. Boundary conditions included inlet flow rate of 1 L/min, outflow conditions based on 4D Flow MRI data, and a rigid vessel wall. Fluid density and viscosity were set at 1100.7 kg/m^3 and 0.0033784 Pa·s, respectively.

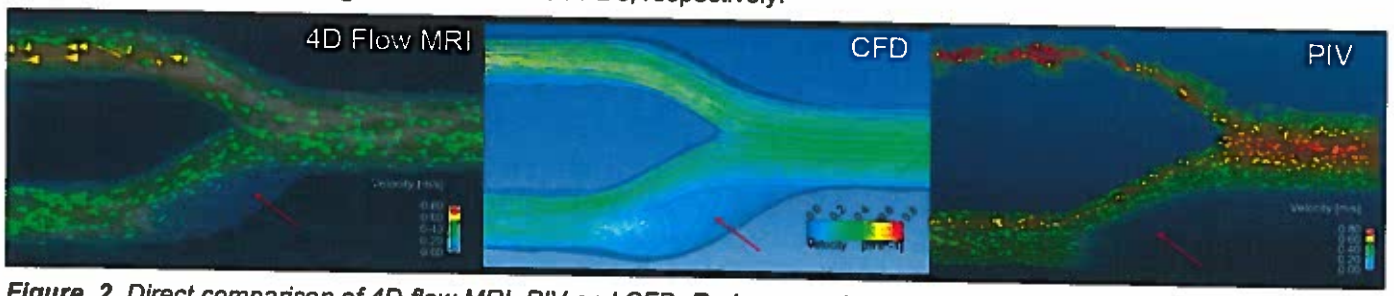

Figure. 2. *Direct comparison of 4D flow MRI, PIV and CFD. Red arrows show the recirculation zone.*

Results: Figure 2 shows similar velocity color coded streamlines acquired from 4D Flow MRI, CFD and stereo-PIV. Peak velocities as well as a recirculation (stagnant flow) region were found downstream of the bifurcation using the three methods.

Discussion: Streamlines showed similar flow trajectories, especially in the lower part of the bifurcation, where the diameter increases. The stereo-PIV system provides great insight into the velocity field within the model, using an excellent acquisition quality. Recirculation regions were well reproduced and measured, located at the bottom area of the bifurcation (red arrows, Fig. 2). Future work will focus on optimizing the particle illumination by the laser sheet to obtain superior image quality throughout the domain. In addition, 4D Flow MRI data will be compared with measurements performed using the FlowMaster Tomographic PIV that enables the instantaneous measurement of the three velocity components in a complete 3D measurement volume.

References: [1] Anderson, JR, IEEE. 2014; [2] Li, X, Bio-Med. Mater. Eng. 2015; [3] Roldán-Alzate, A., Journal of Biomechanics. 2015; [4] Kitajima, H., Journal of Biomechanics. 2008; [5] Johnson, K M., JMRI. 2010.

Optimization and Comparison of a Sliding Slab MRA Technique with Conventional MRA Protocols

Jason K. Mendes[1], John Roberts[1], Bradley D. Bolster[2] and Dennis L. Parker[1]
[1]Utah Center for Advanced Imaging Research, [2]Siemens Healthcare

Purpose: Improved SNR and spatial resolution make 3D MRA techniques desirable in many applications. While slab overlapping techniques (such as MOTSA[1]) combine many advantages of multi slice 2D and single slab 3D techniques, they still suffer from slab boundary artifacts. Sliding slab techniques such as SLINKY[2] and SLIPR[3] have shown greatly reduced slab boundary artifacts but have seen limited clinical adoption. However, with the desire for larger FOV imaging and increased spatial resolution, there is a renewed interest in sliding slab techniques[4-6]. We evaluate the ability of sliding slab techniques to replace current 2D and non-sliding 3D MRA techniques, with particular application to carotid artery imaging. Optimization of sequence parameters for the sliding slab techniques is also considered.

Methods: All imaging was performed on a Siemens PRISMA scanner. The sliding slab technique chosen was a SLIPR version of 3D radial stack of stars. Spatial resolution was 0.8mmx0.8mmx1.0mm with a FOV of 15cm in the slice direction. Tracking venous saturation and fat saturation was applied when possible.

Results: Figure 1 shows a comparison of a multi-slab 3D TOF sequence with an equivalent SLIPR technique. To keep boundary artifacts to a minimum, the TOF protocol utilizes a larger slab thickness (4.8 cm) while the SLIPR protocol uses a much thinner 8 mm slab thickness. As a result of the smaller slab thickness, there is improved inflow between excitation pulses resulting in better contrast to noise. In this case both protocols used sequence parameters optimized for the 3D TOF (in particular flip angle and TR) but these value are not optimal for the SLIPR protocol and further improvements can be expected with parameter optimization.

Conclusion: We have demonstrated feasibility of performing sliding slab for large FOV carotid artery MRA and shown improved results over a 3D TOF protocol. Future work includes comparing sliding slab versions of other MRA protocols such as QISS[7].

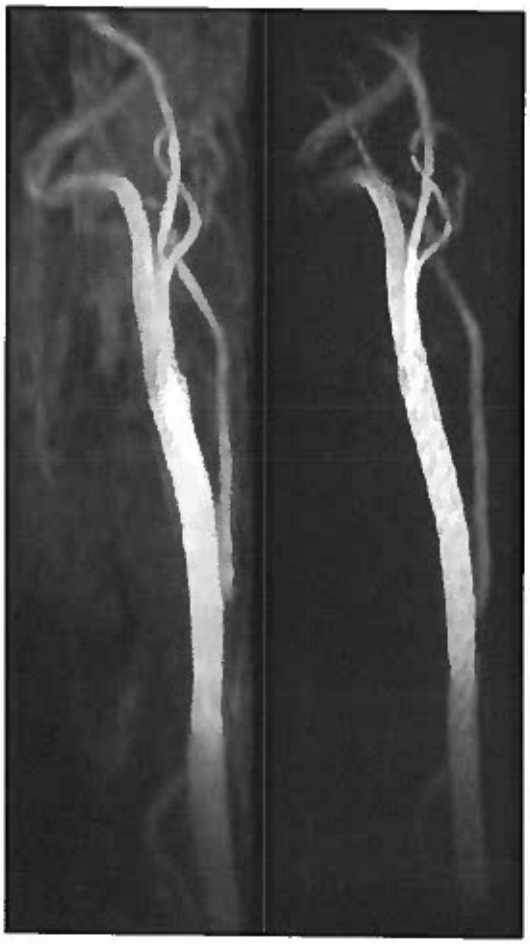

Figure 1: Carotid artery MRA from a 3D TOF sequence (left) and a SLIPR stack of stars sequence (right). Both sequences had similar acquisition parameters and scan times.

References: 1. Parker et al. MRM 1991;17:434, 2. Liu et al. 1998;8:905, 3. Parker e al. JMRI 1999;10:569, 4. Kwon et al. MRM 2015;74:727, 5. Choi et al. MRM 2015;73:1177, 6. Li et al. MRM 2016;75:729, 7. Edelman MR 2010;63:951.

TITLE: The Use of Cardiac Magnetic Resonance Imaging in Diagnosing and Characterizing Hypertrophic Cardiomyopathy

AUTHORS (LAST NAME, FIRST NAME): Ogele, Emmanuel[1]; Choudhury, Lubna[1]; Carr, James C.[1]; Collins, Jeremy D.[1]

INSTITUTIONS (ALL): 1. Feinberg School of Medicine, Northwestern University, Chicago, IL, United States.

PRESENTATION TYPE: Oral or Poster

CURRENT CATEGORY: Congenital Heart Disease

CURRENT SUB-CATEGORY: Clinical

ABSTRACT BODY:

Background : In Hypertrophic Cardiomyopathy (HCM), measurements of maximal myocardial thickness serve a critical role in diagnosis and risk stratification. CMR plays an increasingly significant clinical role. Maximum wall thickness is commonly measured at both MRI and TTE often with discrepancies. The purpose of this study is to examine the influence of slice obliquity on CMR-measured maximum myocardial thickness in the basal anteroseptum comparing 3-Chamber long-axis with short-axis CMR imaging and further, to assess the degree of agreement between long-axis measurements on TTE and MRI.

Methods: We performed a retrospective analysis of 50 consecutive patients (29 males and 21 females; age 58 ± 14) referred for CMR at Northwestern Memorial Hospital with asymmetric septal HCM. The 3-chamber (3Ch) balanced steady state free precession (bSSFP) images were cross-referenced with the short axis (SA) bSSFP cine stack to ensure correlation between measured myocardial regions. The basal anteroseptum was measured on the 3-chamber images in diastole using a line parallel with the mitral valve and on the short axis view, a line orthogonal to the myocardium at the region corresponding to that measured in the 3 chamber view. The angulation in degrees between the 3-chamber bSSFP slice position and the orthogonal measurement on short-axis images was recorded. In cases with significant discrepancy between 3Ch and SA, measurements of the basal anteroseptum were performed on parasternal long axis (PSL) images at TTE. Measurements were compared using the student's t-test, with a p-value of 0.05 considered significant.

Results: On aggregate, there was a difference between CMR derived 3Ch and SA myocardial thickness ($p<.0005$) with an average difference of 0.99 ± 1.4 mm. Angulation between 3Ch and SA images averaged 18 ± 15 °. There was a positive linear correlation between angulation and the difference noted between CMR derived 3Ch and SA measurements ($R^2 = .755$, $p = .012$. See Figure 1).12 subjects (24%) demonstrated at least a 1.5mm difference between CMR derived 3Ch and SA measurements corresponding to an angulation of 24.7°. 4 subject were reclassified below HCM diagnostic threshold after SA measurement. TTE measurements showed a close agreement with 3Ch measurements (mean TTE-3Ch = .85mm) while tending to overestimate the short axis measurements (mean TTE-SA = 1.69mm).

Conclusions: Angulation of long-axis imaging may explain differences between long-axis and short-axis measurements. Although the absolute difference averaged 0.99 mm in this study, the reliance on maximal myocardial thickness in the diagnosis of HCM is potentially significant, with nearly ¼ of subjects in our study demonstrating differences greater than 1.5 mm. 3Ch images agreed more with TTE measurements

suggesting similar challenges with angulation. Our results suggest that operators should minimize 3Ch angulation; keeping the angulation to < 20 as this corresponds to a difference of 1mm and is within the expected error of repeat measurement.

4D flow MRI of stented versus stentless aortic valve bioprostheses

Pim van Ooij[1], Laurens Wollersheim[2], Floortje van Kesteren[1,3], Jan Baan[3], Aart Nederveen[1], A Kaya[2], Bas de Mol[2], Nils Planken[1];Departments of Radiology[1], Cardiothoracic Surgery [2], Cardiology[3]
Academic Medical Center, University of Amsterdam, Amsterdam, The Netherlands

Purpose: Surgical aortic valve replacement is the standard treatment for patients with severe aortic valve stenosis and bioprosthetic valves are the predominant implant of choice. Traditional bioprostheses have a stented framework, facilitating easy implantation. However, this framework reduces the effective orifice area and obstructs laminar blood flow, increasing the valvular gradient. As an alternative, stentless bioprostheses have been introduced. Purpose of this study is to evaluate the hemodynamic performance of stented and stentless aortic valve bioprostheses using 4D flow magnetic resonance imaging (MRI), 1 year after surgical aortic valve replacement.

Methods: 30 patients with either a stented or stentless bioprosthesis (Mitroflow or Freedom SOLO) and comparable baseline characteristics underwent non-contrast enhanced 4D flow MRI at 1.5 Tesla scanner, 9 to15 months after implantation. Data analyses included quantitative comparison of mean and per voxel analyses of systolic peak velocity, wall shear stress and viscous energy loss in the ascending aorta during peak systole.

Results: Two patients were excluded due to claustrophobia and atrial fibrillation during scanning. Twenty-eight MRI scans (14 Mitroflow, 14 Freedom SOLO) were available for analysis. No statistical differences in mean hemodynamic parameters were found (fig 1). Per voxel analysis revealed significant lower flow velocities at the prosthesis level for stented prostheses and higher wall shear stress in the distal ascending aorta and aortic arch and more energy loss if compared to the stentless prostheses (fig 2).

Conclusion: The hemodynamic performance of the stentless and stented aortic valve prosthesis was comparable when assessed for average volume values in the ascending aorta. However there was a tendency towards lower peak velocities across the stentless prosthesis and a favorable flow profile with higher ascending aorta central lumen velocities and lower distal ascending aorta wall shear stress and viscous energy loss in the stentless prosthesis compared to the stented prosthesis at 1 year after implantation.

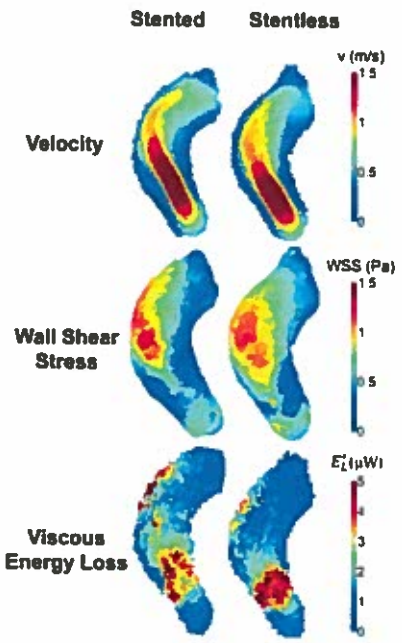

Figure 1

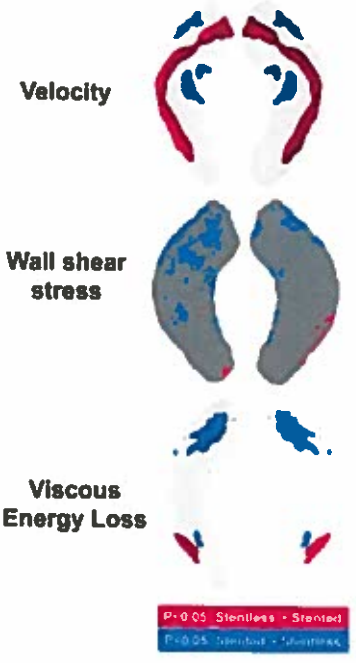

Figure 2

LVNC – Are we overdiagnosing this entity?

Polakova Mistinova Jana[1], Jurko Alexander[2], Bilicky Jozef[1]

[1]Radiology clinic of Medical Faculty Commenius University, Bratislava, Slovakia

[2]Pediatric cardiology ambulance, Martin, Slovakia

Noncompaction of the left ventricle (LVNC) is relatively rare, genetically conditioned cardiomyopathy. This disease causes, that the myocardium of the left ventricle has a typical two-layer character with a thicker noncompacted and thinner compacted layer. LVNC shows variability in its genetic pattern, pathophysiologic findings, and clinical presentations. The clinical presentations are ranging from asymptomatic patients to patients who develop ventricular arrhythmias, thromboembolism, heart failure or even sudden cardiac death.

Although there are many publication about LVNC, with echocardiographic and MRI criteria, but there is no „gold standard" for LVNC diagnosis, therefore is combined cardiac imaging best visualisation possibility available. At this moment is still unclear whether LVNC is more common diagnosis as supposed or it is new epiphenomenon of leftventricular dilatation. So there remains an open question if the current MRI criteria for LVNC are really not overdiagnosing patients with rather low risk.

Our retrospective study of 44 LVNC patients with genetically proven disease, showed not just that cardiac MRI offers great benefit in visualising the trabeculations in patients with noncompaction of the left ventricle, but also pointed out, that with current MRI criteria for LVNC we are truely overdiagnosing patients with simple morphological prominent trabeculation.

Key words: noncompaction of the left ventricle (LVNC), echocardiography, cardiac magnetic resonance

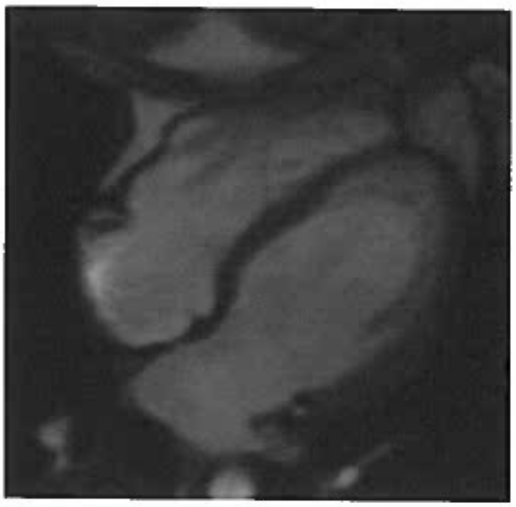

Picture 1. 4ch TrueFISP sequence, bilateral form of noncompaction cardiomyopathy.

T1 and T1* comparison in calculating synthetic hematocrit across multiple cardiac areas

Ozair Rahman[1], Michael Markl[3], Alex Barker[3], Benjamin Freed[2], James Carr[1], Jeremy Collins[1]
[1]Northwestern University, Department of Radiology, Chicago, IL USA
2Northwestern University, Department of Cardiology, Chicago, IL USA
3Department of Biomedical Engineering, Northwestern University, Chicago, IL USA

Purpose: Accurate and reliable ECV calculation has proven to be a vital tool in clinical practice. ECV calculation using blood pool T1 values has been described; however, T1* may be a more accurate technique to estimate blood pool T1 values. Importantly, blood pool T1* values may offer a more accurate technique for estimating the hematocrit as the T1* value assumes complete recovery of longitudinal relaxation between pulses. The purpose of this study was to systematically evaluate the accuracy of synthetic hematocrit estimation derived from blood pool T1 and T1* values across different blood pool regions, taking the lab hematocrit as the gold standard.

Methods and Materials: Retrospective study of 100 consecutive patients (mean age 55.3±16.4 years) who underwent cardiac MR (CMR) at 1.5T (Magnetom Avanto, Siemens Medical Systems, Erlangen, Germany). with pre and post contrast T1 modified Look-Locker inversion recovery imaging (MOLLI) with a 5-3-3 heart beat sampling – recovery – sampling schema and in-line T1 and T1* parametric map generation from motion corrected images at a single center between April 4th, 2015 to February 3rd, 2016. Pre and 12-25 minute post contrast MOLLI imaging was performed. T1 and T1* values were obtained from parametric maps in the: left atrium (LA), left ventricle (LV), descending thoracic aorta (Dao) and myocardium. Lab hematocrit was acquired by venipuncture at the time of the study. The extracellular volume fraction (ECV) was calculated as described in the SCMR consensus statement [1] HCT_{syn} was calculated based on its linear relationship with longitudinal relaxivity (1/T1) of blood. ECV quantification was calculated with laboratory (ECV_{lab}) and synthetic (ECV_{syn}) hematocrit.

Results: The venous hematocrit (38%±5%) was statistically significantly similar to T1 and T1* values calculated in the Left Atrium (LA), and the Left Ventricle (LV). T1 values in the Descending thoracic aorta (Dao) however, depicted significant difference (P<0.0001) when compared to lab (Table 1). This is in contrast to the T1* values calculated in the Dao which showed similar results (P=0.94) when compared to lab hematocrit.

Conclusion: In this study HCT_{syn} calculated from T1 and T1* values across multiple cardiac areas (LA, LV, DAo) represented consistently insignificant differences. But when comparing synthetic hematocrit calculation using T1 values derived from the Dao, to lab hematocrit, revealed significant differences. This can be partially explained by the differences in T1 and T1* in the presence of higher flow states. Important to note, however, is the calculation of ECV with T1 and T1* values from the DAo did not show a statistically significant difference when compared to ECV calculated from Lab Hematocrit. This illustrates the ability of the formula to compensate for irregularities calculated in HCT_{syn} and still be able to reliable quantify ECV_{syn}.

Table 1	T1	T1*
Left Atrium	38.7%±3%	38.7%±3.5%
Left Ventricle	38.7%±2.7	38.7%±3%
Descending Thoracic Aorta	44%±3.6%*	38.6%±3.1%
ECV	0.29±0.08	0.33±0.12

*statistically significant (P<0.5)

1. Moon JC, Messroghli DR, Kellman P, Piechnik SK, Robson MD, Ugander M, Gatehouse PD, Arai AE, Friedrich MG, Neubauer S, Schulz-Menger J, Schelbert EB, Society for Cardiovascular Magnetic Resonance I, Cardiovascular Magnetic Resonance Working Group of the European Society of C. Myocardial t1 mapping and extracellular volume quantification: A society for cardiovascular magnetic resonance (scmr) and cmr working group of the european society of cardiology consensus statement. *Journal of cardiovascular magnetic resonance : official journal of the Society for Cardiovascular Magnetic Resonance*. 2013;15:92

Reproducibility and observer variability of myocardial T2 mapping

Kenichiro Suwa[1], Amir Ali Rahsepar[1], Kai Lin[1], Jeremy Collins[1], James Carr[1], Michael Markl[1], [1]Department of Radiology, Northwestern University Feinberg School of Medicine, Chicago, IL, United States,

Purpose: Myocardial edema has demonstrated utility in the diagnosis and prognosis of heart disease[1]. Myocardial T2 mapping is useful to detect diffuse edema quantitatively[2]. Aim of this study was to investigate the between scan reproducibility and intra- and inter-observer variability for both global and regional myocardial T2 mapping.

Methods: Sixteen volunteers (50±17 years, 11men, left ventricular ejection fraction 57.3±7.6 %, LV Mass 108±41 g) underwent myocardial T2 mapping using a T2-prepared bSSFP pulse sequence with in-line rigid motion correction and parametric map generation. Basal, mid-chamber, and apical short-axis slices were obtained in the short axis orientation. T2 mapping was repeated in all subjects during a second visit separated by an average 17±5 days to assess between scan variability. T2 relaxation times were measured off parametric maps using the 16-segment AHA model and averaged to determine global T2 values. For intra-observer and inter-observer variability, analysis was repeated by the same observer 2 weeks after initial analysis and by an independent 2nd observer.

Results: Global T2 in scan 1/observer 1, scan 2/observer 1, scan 1/observer 2, and scan 1/observer 1 (2nd measurement) was 46.6±1.7 ms, 46.5±2.4 ms, 47.3±2.0 ms, and 46.6±1.9ms. Bland-Altman plots in intra-, inter-observer and inter-scan variability showed narrow limits of agreement both in global and regional T2, and we did not observe any systematic bias (Fig. 1). Intraclass correlation coefficients in intra-, inter-observer and inter-scan variability were 0.95, 0.87 and 0.82. Side-by-side comparisons of regional T2 were summarized in figure 2. Regional T2 values were highly reproducible except for 7 segments. Significant elevations were detected in apical anterior segment measured by observer 1 in 2nd reading, mid inferior segment, infero-septum, and apical segments measured by observer 2 compared to measurement in scan1 by observer 1 in 1st reading.

Conclusion: The between scan reproducibility of global myocardial T2 values between scans was excellent. Intra- and inter-observer variability of myocardial T2 relaxation times was small both segmentally and globally. Segmental between scan reproducibility was modest with limits of agreement of ±6.74 msec but no segments demonstrating significant differences between scans in healthy volunteers.

References: 1. Simonetti OP et al, Radiology. 1996;199:49-57. 2. Verhaert D et al, JACC Cardiovasc Imaging. 2011;4:269-278.

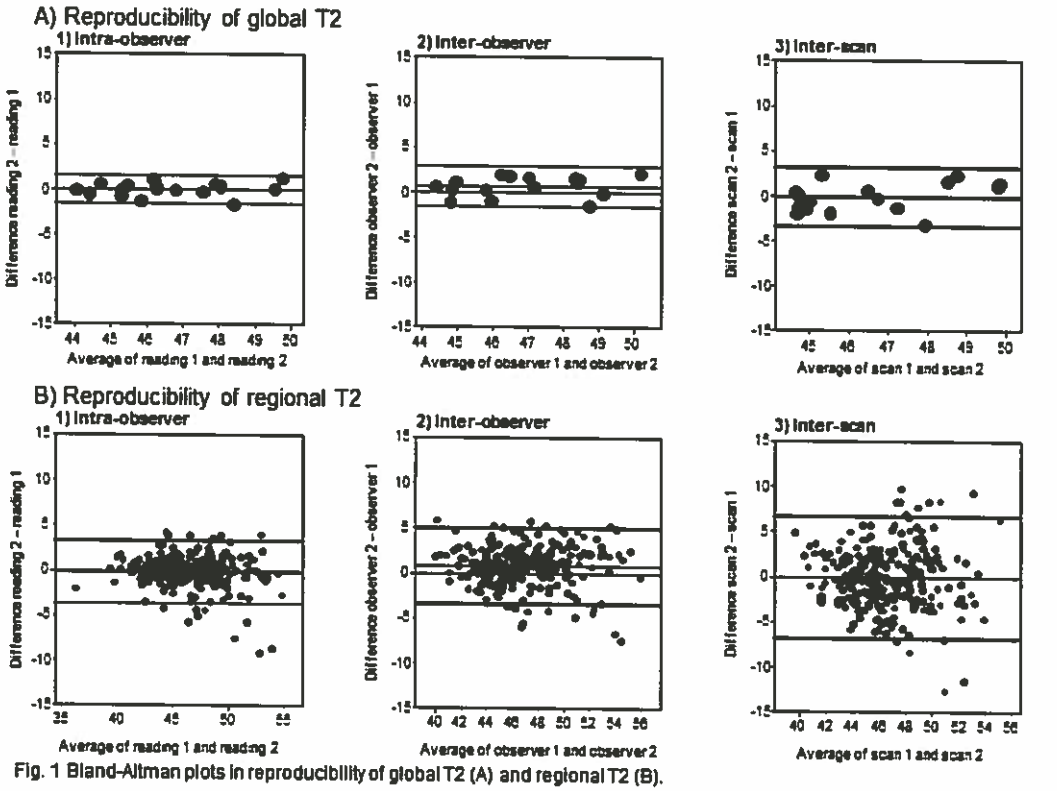

Fig. 1 Bland-Altman plots in reproducibility of global T2 (A) and regional T2 (B).

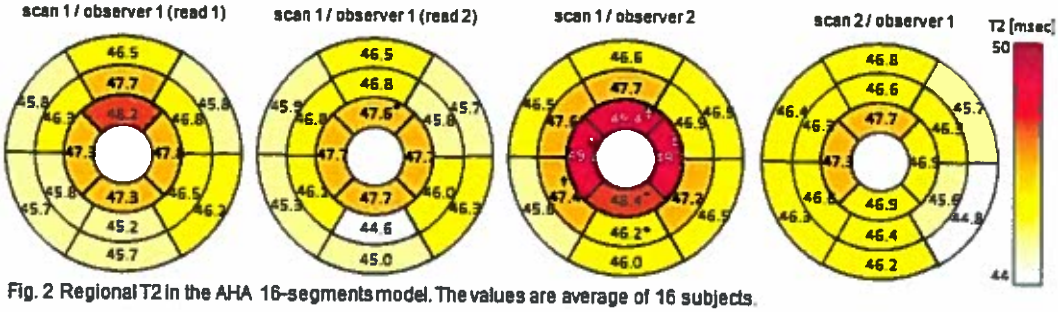

Fig. 2 Regional T2 in the AHA 16-segments model. The values are average of 16 subjects.

*P<0.05, †P<0.01, ‡P<0.001 compared to T2 in the same segment in scan1/observer1 (read 1).

High-Resolution Breath-Held Cardiac T_2 Mapping with SKRATCH: A Quantitative Comparison of Four Techniques in Healthy Volunteers

Emeline Lugand[1], Jerome Yerly[1,2], Helene Feliciano[1], Jerome Chaptinel[1], Ruud B. van Heeswijk[1]

[1]Department of Radiology, University Hospital (CHUV) and University of Lausanne (UNIL), Lausanne, Switzerland;
[2]Center for Biomedical Imaging (CIBM), Lausanne and Geneva, Switzerland;

Introduction - Radial T_2 mapping can be used to quantify myocardial edema and is robust against motion artifacts [1]. However, radial imaging generally results in a lower signal-to-noise ratio (SNR) than Cartesian imaging depending on the degree of undersampling (i.e. sparsity) of its k-space periphery, which consequently receives higher weights through the density compensation function (DCF) (Fig.1a), thus increasing noise and undersampling artifacts in the reconstructed images. Such noise amplification can be reduced by sharing the k-space periphery of the different T_2 weighted images (Fig.1b) [2]. Meanwhile, theT_2 map accuracy is maintained, since the contrast of an image is mainly determined by the k-space center. The k-space periphery sharing in turn allows for higher undersampling (Fig.1c) and a decrease in acquisition time. This undersampled radial cardiac T_2 mapping technique is named SKRATCH (Shared k-space RAdial T_2 Characterization of the Heart), and was previously described with navigator gating for high-spatial-resolution T_2 mapping [3], which allowed for the investigation of thin myocardium. In the present study, SKRATCH was implemented for high-spatial-resolution T_2 mapping within a single breath-hold. We developed four breath-held SKRATCH techniques and quantitatively characterized and compared their accuracy, uncertainty and robustness.

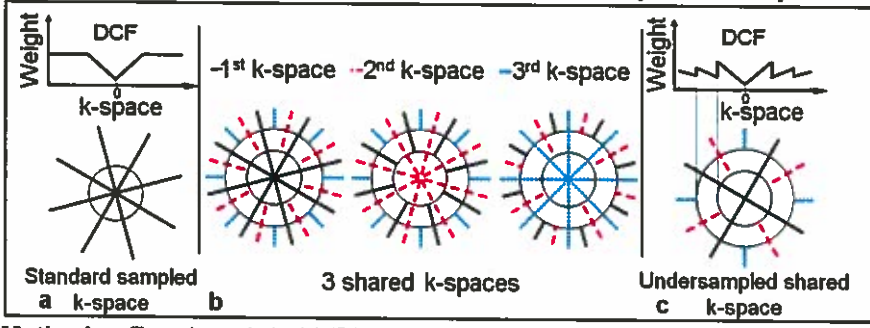

Figure 1. Schematic overview of the k-space sharing. a. A radial k-space shown below its DCF along one radial line. **b.** Three k-spaces with different contrast sharing their peripheries. The circles indicate the radii outside of which an extra k-space is added **c.** An undersampled and shared k-space. While the number of lines decreased, the periphery of k-space still has a higher sampling density than in a.

Methods - Four breath-held (BH) SKRATCH techniques were compared to each other and to a navigator-gated reference [2]. All of them consisted of an undersampled radial acquisition with a continuously increasing golden-angle, ensuring unique k-space coverage for a series of 4 T_2 preparation times (T_2Prep).The first two techniques used GRE acquisition with two different types of T_2Prep (0/30/45/60 ms and 0/30/45/∞ ms), where the infinite T_2Prep is approximated by a saturation preparation (SatPrep) [4]. For the third and fourth techniques, the GRE was replaced by a bSSFP acquisition. For all techniques, the resolution was 1.2x1.2x8mm^3. Data were acquired at 3T (Prisma, Siemens) in 16 healthy volunteers at the same mid-ventricular short-axis location. The mean segmental T_2 values (μ_{T2}, the accuracy), the relative standard deviations (σ_R = standard deviation/μ_{T2}, i.e. the uncertainty), and the total segmented myocardial areas were calculated. For the myocardial areas analysis, only volunteers with all segments analyzed were included.

Results –The mean segmental T_2 values of the breath-held SKRATCH T_2 maps closely matched those of the navigator-gated reference (Fig.2). The relative standard deviation σ_R slightly increased from 8±2% for the reference T_2 map to 10-12%. All segments were analyzed in both GRE techniques, while 17/96 segments were discarded from the analysis of both bSSFP techniques due to artifacts. The segmented myocardial areas remained constant compared to the reference area of analysis for all SKRATCH techniques except bSSFP without SatPrep, where it decreased by 14% (Fig.2).

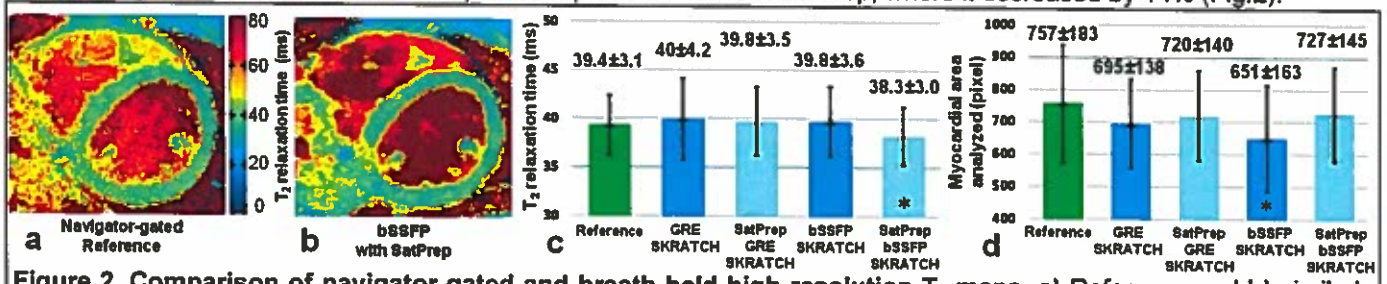

Figure 2. Comparison of navigator-gated and breath-held high-resolution T_2 maps. a) Reference and **b)** similarly homogeneous BH SKRATCH T_2 map. **c)** Comparison of the T_2 values and **d)** segmented areas, * = significant values.

Discussion - All breath-held SKRATCH techniques enable the acquisition of high-resolution T_2 maps within a single breath-hold and were highly similar to the navigator-gated T_2 maps. Both types of GRE-based T_2 maps were shown to be more robust against artifacts. Both SatPrep techniques resulted in a larger segmented myocardial area when compared to their respective protocol without SatPrep. In conclusion, the SatPrep GRE protocol appears to be the optimal protocol, since it is both robust and results in a large segmented myocardial area.

References - [1] van Heeswijk JACCCVI 2012 [2] Song MRM 2000 [3] Lugand ISMRM 23, 2015 [4] Akçakaya MRM 2015

preferred presentation: oral

section: cardiac structure and function / new imaging techniques

synopsis: While T_2 mapping with radial acquisition is robust against motion artifacts, it suffers from a low signal-to-noise ratio that is caused by the undersampling of the k-space periphery and the associated density compensation function. To overcome this, four different breath-held SKRATCH (Shared k-space RAdial T_2 Characterization of the Heart) techniques (GRE or bSSFP acquisition, saturation preparation on or off) were implemented. SKRATCH is based on the combination of the KWIC (k-space-Weighted Image Contrast) filter and undersampled acquisitions. The accuracy, uncertainty and robustness against artifacts of the four breath-held techniques were quantified and compared to a standard of reference.

Comprehensive blood flow measurements in ex vivo pig heart models using 4D flow MRI

Eva S. Peper[1], Alberto Leopaldi[2], Sjoerd van Tuijl[2], Nicky de Jonge[2], Gustav J. Strijkers[3], Arend de Weger[4], Aart J. Nederveen[1], Jurgen de Hart[2], Henk A. Marquering[1,3], Pim van Ooij[1]

[1]*Department of Radiology, Academic Medical Center, the Netherlands,* [2]*LifeTec Group, Eindhoven, the Netherlands,* [3]*Department of Biomedical Engineering & Physics, Academic Medical Center, the Netherlands* [4]*Department of Cardiothoracic Surgery, Leiden University Medical Center, the Netherlands*

Purpose: To investigate the feasibility of 4D flow MRI measurements in ex vivo pig heart models in human physiological conditions for the visualization of coronary blood flow and quantification of cardiac blood flow.

Methods: The pig hearts (n=5) were connected to the PhysioHeart platform [1] (LifeTec Group BV, Eindhoven, The Netherlands). For preparation, the pericardial sack was discarded and the azygotic vein and the superior and inferior caval vein were removed and ligated to close the right atrium. The pulmonary veins were removed to the level of the left atrium and ligated. After reinstating coronary perfusion and after defibrillation, the hearts started contracting to reach sinus rhythm. Physiological pre- and afterload pressures mimicking human conditions were subsequently applied to the left ventricle (5 liters pig blood per minute, 120/80 mm Hg systolic/diastolic pressure). The right ventricle was only subjected to a volume loading, resulting from ventricle filling with coronary venous blood. [2]. A retrospectively cardiac gated 4D flow MRI examination on a 3T scanner (Ingenia, Philips, Best, The Netherlands) was performed with a field of view of 150 x 150 x 150 mm^3; Non-interpolated spatial resolution of 2.3 x 2.3 x 2.3 mm^3; Echo time/Repetition time and flip angle of 2.2 ms/5.2 ms and 8°, respectively; VENC was 100 cm/s in x, y and z- direction. The number of cardiac phases was 24 and the scan was three times accelerated with k-t PCA (Gyrotools, Zurich, Switzerland) [3]. Scan time was approximately 12 minutes. Visualization of the data and quantification of blood stroke volume (SV) in and out the aorta, in and out the left atrium and in and out the pulmonary artery was performed in GTFlow (Gyrotools, Zurich, Switzerland). As a measure for robustness of the measurement, the difference in blood volume flowing in and out the heart was calculated as: $Difference = \frac{|blood\ volume\ in - blood\ volume\ out|}{(blood\ volume\ in + blood\ volume\ out)/2} * 100\%$

Results: Figure 1 shows pig heart #1 in the PhysioHeart platform and results from the pathline analysis at various time steps, focusing on different features of intra-cardiac (b,c), aortic (d) and coronary blood flow (e). The heart rates of the pig hearts are given in table 1. The heart rates remained stable during the acquisition. In general, the hearts remained viable for 3-4 hours. 4D flow MRI-measured stroke volumes in and out the hearts are given in table 1. Stroke volumes were 80 ml, and the difference in blood volumes flowing in and out the heart was 10%. This difference can be attributed to noise in the data and to manual vessel delineation which did not take vessel movement into account.

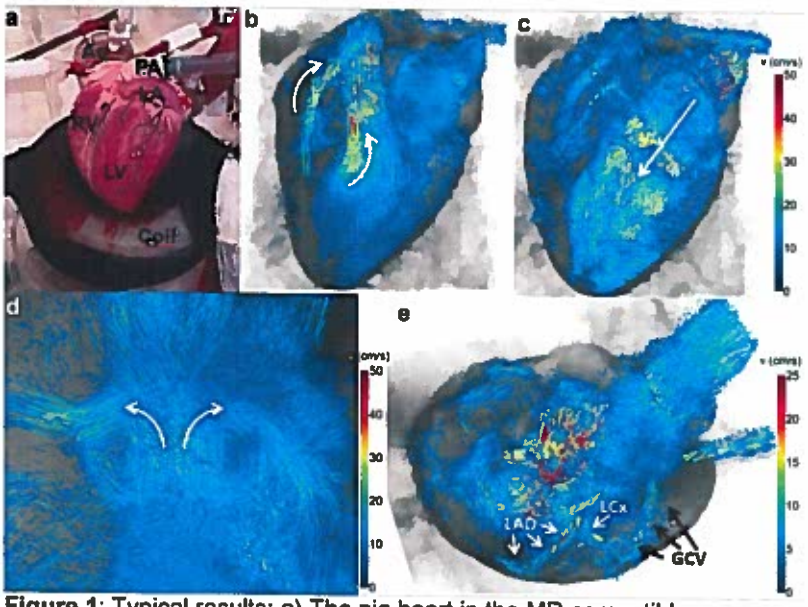

Figure 1: Typical results: a) The pig heart in the MR compatible PhysioHeart Platform. LV = left ventricle, RV = right ventricle, LA = left atrium, PA = pulmonary artery, Ao = Aorta. b) Intra-cardiac flow in the ejection phase. c) Intra-cardiac flow in the filling phase. d) Recirculating blood flow in the aortic sinuses. e) Flow in the coronary arteries. LAD = left anterior descending artery, LCx = left circumflex artery, GCV = great cardiac vein

Conclusion: In this study, results of 4D flow MRI in ex vivo beating pig hearts model were presented. The PhysioHeart platform allows for the visualization of intra-cardiac blood flow in high detail. The feasibility of flow visualization using 4D flow MRI in coronary arteries and veins was shown. These initial results encourage performing measurements in pig hearts adapted for pathophysiology such as the implantation of artificial valves or the simulation of stenosis to quantify fractional flow reserve. With the PhysioHeart platform, the assessment of pathophysiology and treatment effects is possible in a highly controlled fashion. The platform can be used for validation of 4D flow MRI and other novel cardiac MR sequences.

Table 1: Heart rate (HR, bpm) SV (ml) in and out the heart

	HR	SV in	SV out	Difference (%)
Heart #1	107	72	83	14
Heart #2	102	89	91	2
Heart #3	112	54	62	14
Heart #4	96	88	94	7
Heart #5	128	71	80	12
Mean ± SD	104±7	75±14	82±13	10±5

References: [1] de Hart, J. *et al. J. Artif. Organs* (2011) [2] Schampaert, S. *et al. Artif. Organs* (2013) [3] Pedersen, H. *et al. Magn. Reson. Med.* (2009). **Acknowledgement: STW Grant CARISMA 11630: PAPAVER**

A template of intra-cardiac blood velocity in ex vivo pig heart models using 4D flow MRI

Pim van Ooij[1], Alberto Leopaldi[2], Eva S. Peper[1], Sjoerd van Tuijl[2], Nicky de Jonge[2], Gustav J. Strijkers[3], Arend de Weger[4], Aart J. Nederveen[1], Jurgen de Hart[2], Henk A. Marquering[1,3]

[1]*Department of Radiology, Academic Medical Center, the Netherlands,* [2]*LifeTec Group, Eindhoven, the Netherlands*
[3]*Department of Biomedical Engineering & Physics, Academic Medical Center, the Netherlands*
[4]*Department of Cardiothoracic Surgery, Leiden University Medical Center, the Netherlands*

Purpose: To create cohort-averaged 3D maps of intra-cardiac velocity in ex vivo beating pig hearts models that can serve as a template to investigate flow behavior after flow-altering interventions such as valve implantation.

Methods: The pig hearts (n=5) were connected to the PhysioHeart platform [1] (LifeTec Group BV, Eindhoven). The set-up is described in detail in deHart et al. [1]. A retrospectively cardiac gated 4D flow MRI examination on a 3T scanner (Ingenia, Philips, Best, The Netherlands) was performed with a field of view encompassing the entire heart and parts of the inflow and outflow tubes. Field of view was 150 x 150 x 150 mm^3; Non-interpolated spatial resolution was 2.3 x 2.3 x 2.3 mm^3; Echo time/Repetition time and flip angle were 2.2 ms/5.2 ms and 8°, respectively; VENC was 100 cm/s in x, y and z-direction. The number of cardiac phases was 24 and the scan was three times accelerated with k-t PCA (Gyrotools, Zürich, Switzerland) [3]. The 3D cohort-averaged velocity map of the intra-cardiac velocity fields at the ejection phase and the filling phase was created according to previously published methodologies [4]. The ejection phase was defined as the time frame with the highest blood flow pumped out of the aorta. The filling phase was defined as the time frame with the highest blood flow pumped into the left atrium. First, a threshold was applied to the velocity magnitude to exclude velocity vectors with a magnitude lower than 0.1 m/s and a threshold was applied to the anatomical data to exclude regions outside the heart with low signal. Next, with rigid co-registration techniques, a 'shared' geometry was created for both the ejection phase and for the filling phase that represented the geometry of the five hearts. Subsequently, the velocity vectors were projected onto the shared geometry by nearest neighbour interpolation. Finally, the velocity vectors were averaged for the five hearts yielding the cohort-averaged 3D velocity map. Furthermore, a standard deviation (SD) and a coefficient of variation (CV = SD / mean) map were created to visualize the variability in velocity magnitude between the five hearts.

Results: In figure 1 the cohort-averaged velocity maps for the ejection and filling phase are displayed. In the ejection phase (figure 1a), the velocity vectors in the left ventricle are directed towards the aorta, and outflow out the aorta is clearly visible. The maximum intensity projections of the mean and the standard deviation show that the variability in velocity magnitude between the hearts was moderate compared to the mean (figure 1b and c), which was supported by the CV map (1d). The CV averaged over the geometry was 27%. For the filling phase (figure 1e), the velocity vectors show the filling of the left ventricle from the atrium. The maximum intensity projections of the mean and the standard deviation again show that the variability in velocity magnitude between the hearts was moderate compared to the mean (figure 1f and g). This was again supported by the CV map (1h), with an average CV of 32%.

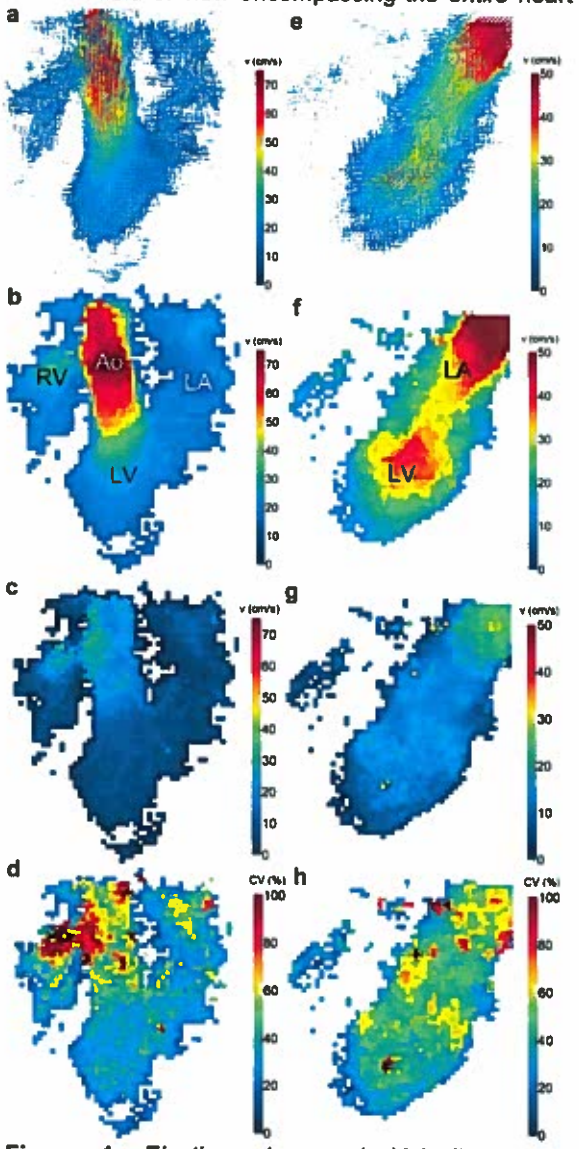

Figure 1: *Ejection phase: a) Velocity vectors averaged over the 5 hearts in the 'shared' geometry, b) maximum intensity projection (MIP) of velocity magnitude averaged over the 5 hearts, c) MIP of the standard deviation of the velocity magnitude for the 5 hearts; d) MIP of the CV e), f) and g) and h) identical as a), b), c) and d) for the filling phase. RV = right ventricle, LV = left ventricle, Ao= Aorta, LA = left atrium.*

Conclusion: In this study a template was created that can serve as a comparison tool for intra-cardiac velocity in the ejection and filling phase to investigate if flow patterns are altered in ex vivo pig hearts after interventions such as artificial valve implantation or after inducing cardiac ischemia.

References: [1] de Hart, J. *et al. J. Artif. Organs* (2011) [2] Schampaert, S. *et al. Artif. Organs* (2013) [3] Pedersen, H. *et al. Magn. Reson. Med.* (2009) [4] van Ooij P. et al. ISMRM 24 (2016): 0317 **Acknowledgement: STW Grant CARISMA 11630: PAPAVER**

Functional measurements with accelerated self-gated free-breathing 3D cardiac cine MRI

Yan Wang, Evan Kao, Liang Ge, Li Feng, Kanae Mukai, Karen Ordovas, David Saloner, Jing Liu
Department of Radiology and Biomedical Imaging, University of California, San Francisco

Purpose: Automatic segmentation provides essential and efficient tools for accurate functional measurements, especially because manual segmentation is impractical for analysing massive and complex 3D/4D data sets. We here propose an automatic segmentation based on the level set method to efficiently segment left ventricle (LV) and right ventricle (RV) on a 3D cardiac CINE data.

Method: 1) Data acquisition: We have proposed a highly accelerated free-breathing self-gated 3D CINE MRI to image the heart through the entire cardiac cycle[1]. The sequence was applied on 8 healthy volunteers (4 female, age 29.9±5.7 years, heart rate 62.0±8.5 bpm) on a 3.0T MR scanner (GE Medical Systems, Milwaukee, WI) with an 8-channel cardiac coil.3D bSSFP sequence with a golden-ratio based variable-density pseudo-random sampling strategy, CIrcular Cartesian UnderSampling (CIRCUS)[2], was applied, with FOV=34.0×25.5cm^2, TR/TE=4.1/1.7ms, FA=60°, BW=±125kHz, slice thickness of 4mm, image matrix=256×144, temporal resolution of 41 ms, and scan time of 2.5±0.3 minutes. Cardiac phases were reconstructed using a combined compressed sensing and parallel imaging method, k-t SPARSE-SENSE[3]. 2) Image segmentation: Automatic segmentation in 3D or 4D (3D+t) MRI data is difficult given the inherent noise associated with MRI data from inconsistent cardiac motion and inhomogeneous image gradient. The proposed method (Figure 1) consists of detecting the circular structures using the Hough transform, and segmenting both the LV and RV using the circular structure in the proposed elliptically refined level set. The energy formulation of this model is: $E = E_{data} + \alpha E_{shape}$, where E_{data} is the data attachment term and E_{shape} embeds the shape prior. We adopt this model with the Chan-Vese model[4] as the data attachment term:

$$E_{data}(c_1, c_2, C) = \mu \cdot Length(C) + \nu \cdot Area(inside(C)) + \omega_1 \int_{inside(C)} |I - c_1|^2 dxdy + \omega_2 \int_{outside(C)} |I - c_2|^2 dxdy,$$

where μ, ν, ω_1 and ω_2 are fixed positive parameters, I is the intensity of the image, and c_1 and c_2 are the average intensity inside and outside C, respectively.

Results: We have successfully acquired and segmented 3D CINE images from all 8 subjects. Figure 1 (left) shows the segmentation results in short axis view along multiple slices, using our proposed automatic segmentation algorithm on 3D cardiac CINE images. 3D visualization at end-diastolic phase is displayed (Figure 1, right). Figure 2 gives the measurements of volume and mass during the entire cardiac cycle.

Conclusion: In summary, we have developed an automatic 4D cardiac segmentation algorithm for improving cardiac function measurements applied on an accelerated free-breathing self-gated non-contrast-enhanced 3D CINE imaging.

References: 1. Liu J, et al., ISMRM, 2014, p429. 2. Liu et al., Quant Imaging Med Surg. 2014. 3. Feng L, et al., MRM, 2013;70(1):64-74. 4. Chan et al., J Vis Commun Image Represent. 2000.

Figure1: Automatic segmentation of LV and RV with the proposed method (left) and 3D visualization at end-diastolic phase

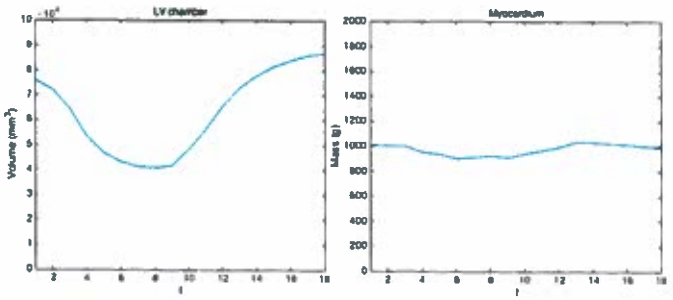

Figure 2: Left: volume measurement of LV chamber during the entire cardiac cycle. Right: myocardium mass measurement during the entire cardiac cycle.

Does correction of carotid-femoral pulse wave velocity distance measurements improve disease discrimination?

Jonathan R Weir-McCall, Arsh Thakur, Deirdre Cassidy, Faisel Khan, Shona Z Matthew, Helen M Colhoun, J Graeme Houston
Division of Cardiovascular and Diabetes Medicine, University of Dundee, UK

Purpose: Pulse wave velocity is a well established marked of arterial stiffening with important prognostic implications.[1] Carotid femoral pulse wave velocity (cf-PWV) is the most commonly used technique for the measurement of PWV, however relies on the use of surface measures of distance to represent the convoluted path of the underlying arterial tree introducing potential errors in PWV calculation. The aim of the current study was to assess whether recalculation of PWV using arterial centreline measurements derived from whole body MRA (MRA-PWV) improves the accuracy of PWV for identifying cardiovascular disease.

Methods: 109 study participants were recruited into one of 4 groups: T2DM with CVD (n=22), T2DM without CVD (n=38), CVD without T2DM (n=23) and a control group (G4: n=26). All participants underwent cf-PWV, cardiac MRI and whole body MR angiography. cf-PWV was performed using a SphygmoCor device (Atcor Medical, West Ryde, Australia). Physical distance for PWV calculation was calculated using a proximal (carotid to sternal notch) and distal (sternal notch to umbilicus and umbilicus to femoral) measure with final distance being the proximal distance subtracted from the distal distance. Whole body MRA was performed on a 3T scanner (Tim Trio, Seimens, Erlangen, Germany) using an up titring (10ml then 15 ml) dual bolus contrast injection of gadoterate meglumine (Dotarem, Villepont, France) and a 4 station acquisition protocol, from which a curved MRP was generated from the carotid to the femoral arteries. From this, distances from the bifurcation of the common carotid to the aortic arch (proximal measurement), and from the aortic arch to the bifurcation of the common femoral artery (distal measurement) were measured. After subtracting the proximal from the distal measurement, this MRA derived distance was then used to recalculate the cf-PWV to give an MRA-PWV.

Results:
PWV distance measurements were significantly lower using MRA arterial centrelines (mean diff = 87.5 ± 58.4mm, $p<0.001$) resulting in cf-PWV being significantly higher than MRA-PWV (cf-PWV= 10.91 ± 2.67 vs. MRA-PWV= 9.0 ± 2.19ms^{-1}, $p<0.001$). Despite this both measures showed a high degree of correlation ($R=0.89$, $p<0.001$). Neither cf-PWV ($F=1.86$, $p=0.14$) nor MRA-PWV ($F=1.73$, $p=0.17$) differentiated between the four groups. When the groups were combined into either having CVD (n=45) or no-CVD (n=64), a continued lack of difference between these groups was observed for both cf-PWV ($t=1.17$, $p=0.25$) and MRA-PWV (1.47, $p=0.14$). Neither cf-PWV ($R=0.06$, $p=0.52$) nor MRA-PWV ($R=0.04$, $p=0.66$) showed a significant correlation with indexed left ventricular mass.

Conclusion:
While there are significant inaccuracies in the distance measurement used for the calculation of cf-PWV, correction of this does not appear to improve discrimination between those with and without cardiovascular disease.

1 Ben-Shlomo Y, Spears M, Boustred C, *et al.* Aortic pulse wave velocity improves cardiovascular event prediction: an individual participant meta-analysis of prospective observational data from 17,635 subjects. *J Am Coll Cardiol* 2014;**63**:636–46. doi:10.1016/j.jacc.2013.09.063